Novel seeding techniques for generation of high repetition rate coherent nanometer FEL radiation

Dissertation
zur Erlangung des Doktorgrades
an der Fakultät für Mathematik, Informatik und Naturwissenschaften
Fachbereich Physik
der Universität Hamburg

vorgelegt
von
Georgia Paraskaki
aus
Kreta, Griechenland

Hamburg
2022

Gutachter der Dissertation: Prof. Dr. rer. nat. Wolfgang Hillert
Dr. rer. nat. Johann Zemella

Zusammensetzung der Prüfungskommission: Prof. Dr. rer. nat. Wolfgang Hillert
Dr. rer. nat. Johann Zemella
Prof. Dr. rer. nat. Markus Drescher
Dr. rer. nat. Velizar Miltchev
Prof. Dr. rer. nat. Daniela Pfannkuche

Vorsitzende/r der Prüfungskommission: Prof. Dr. rer. nat. Daniela Pfannkuche

Datum der Disputation: 03.02.2022

Vorsitzender
Fach-Promotionsausschusses PHYSIK: Prof. Dr. Wolfgang Hansen

Leiter des
Fachbereichs PHYSIK: Prof. Dr. Gunter HW Sigl

Dekan der Fakultät MIN: Prof. Dr. Heinrich Graener

Declaration of Authorship

Eidesstattliche Versicherung / Declaration on oath
Hiermit versichere ich an Eides statt, die vorliegende Dissertationsschrift selbst verfasst und keine anderen als die angegebenen Hilfsmittel und Quellen benutzt zu haben.

Hamburg, den 11.02.2022

Unterschrift der Doktorandin

"Learn what the rest of the world is like. The variety is worthwhile."

Richard P. Feynman,
Surely You're Joking, Mr. Feynman!: Adventures of a Curious Character.

Contents

Declaration of Authorship **v**

Abstract **xi**

Zusammenfassung **xii**

1 Introduction **1**
1.1 Motivation 1
1.2 Organization and scope of the thesis 4

2 Theory **7**
2.1 Accelerator physics 7
2.1.1 6D phase space 7
2.1.2 Transverse beam dynamics 8
2.1.3 Longitudinal beam dynamics and bunch compression 10
2.2 Synchrotron Radiation 13
2.2.1 Synchrotron radiation: bending magnets and insertion devices 13
2.3 FEL theory 15
2.3.1 Low-gain FELs (Oscillator FEL) 15
2.3.2 High-gain FELs (The single-pass FEL) 17
Self-amplified spontaneous emission (SASE) 20
Ming-Xie correction for 3D effects 21
2.4 Seeding theory 21
2.4.1 High-Gain Harmonic Generation 22
2.4.2 The optical klystron 26
2.4.3 Echo-Enabled Harmonic Generation 28
2.5 Gaussian Optics 32
2.5.1 Beam properties and propagation 32
2.5.2 Spectral and temporal properties 34
2.6 FEL Radiation Properties 35

3 HGHG seeding with an optical klystron **37**
3.1 High repetition rate seeded FEL with an optical klystron in high-gain harmonic generation 37

4 HGHG seeding with an oscillator starting with a low repetition rate seed laser **51**
4.1 Optimization and stability of a high-gain harmonic generation seeded oscillator amplifier 51

5 HGHG seeding with an oscillator starting from shot noise **67**
5.1 Advanced Scheme to Generate MHz, Fully Coherent FEL Pulses at nm Wavelength 67

6 Conclusions and Outlook **91**

A Numerical methods **95**
A.1 Simulating the FEL process with Genesis 1.3 95
A.2 Radiation field treatment with Ocelot 96

B Additional simulation results **97**
B.1 HGHG seeding with an optical klystron 97
B.2 HGHG seeding with an oscillator starting with a low repetition rate seed laser 101

Acknowledgements **117**

Abstract

High gain free electron lasers (FELs) generate radiation of unprecedented brightness and unique properties and have proven to be a useful tool for applications in a wide range of studies in physics, biology, medicine and chemistry. External seeding techniques have been experimentally demonstrated and aim to improve the intrinsically poor temporal coherence of a high-gain FEL starting from shot noise. Seeded schemes, like the high gain harmonic generation (HGHG), are based on frequency up-conversion and generate fully coherent radiation thanks to the external seed laser that initiates the process in the FEL. However, the dependence of the properties of the seeded radiation on those of the seed laser is at the same time a limiting factor. The repetition rate of the state-of-the-art seed lasers used in external seeding is incompatible with the repetition rates of modern high-gain FELs based on superconducting technology. In addition, seeded radiation is a harmonic of the seed laser wavelength, a feature that limits the output wavelength to above a few nanometers and restricts its tunability. To overcome these limitations it is necessary to search for new possibilities in FELs.

The scope of this cumulative thesis is to introduce novel ideas that allow us to achieve high repetition rate and fully coherent radiation at an extended and tunable wavelength range. The three proposals of this thesis aim to reduce the dependence of external seeding schemes on the seed laser source and at the same time, maintain the full coherence of seeded radiation. The first proposal is an optical klystron-based HGHG, which modifies the conventional HGHG beamline in a way that relaxes the stringent requirements on the seed laser power by several orders of magnitude. This way, the repetition rate of the seed laser source can be increased, or seed laser sources of shorter wavelengths can be used instead. The second proposal is an HGHG seeded oscillator-amplifier setup: an optical cavity captures a conventional low repetition rate seed laser pulse and stores it to seed electron bunches at a high repetition rate. The third proposal is an HGHG oscillator-amplifier that eliminates the dependence on external seed lasers. Instead of the external laser, the electrons generate the light pulse themselves, starting from shot noise, and the radiation is stored in the optical cavity to seed electron bunches at high repetition rates. In addition to the high repetition rate, this scheme allows shorter and tunable seeded radiation. This type of radiation has never been possible in the past and can greatly benefit already existing experiments and support new experiments and more discoveries by accelerating the ongoing science at FELs.

Zusammenfassung

High Gain Freie Elektronen Laser (FEL) erzeugen Strahlung von noch nie dagewesener Brillanz und einzigartigen Eigenschaften und haben sich als nützliches Instrument für eine Vielzahl von Studien in Physik, Biologie, Medizin und Chemie erwiesen. Externe Seeding-Techniken wurden experimentell demonstriert und zielen darauf ab, die inhärent geringe zeitliche Kohärenz eines aus dem Schrotrauschen initiierten High-Gain-FEL zu verbessern. Seeding Konzepte wie High Gain Harmonic Generation (HGHG) beruhen auf der Aufwärtskonversion der Fequenz eines externen Seedlasers, der den Prozess im FEL initiiert und die Erzeugung vollständig kohärenter Strahlung ermöglicht. Die Abhängigkeit der Eigenschaften der geseedeten Strahlung von denen des Seedlasers ist jedoch geleichzeitig ein begrenzender Faktor. Die Repetitionsrate der beim externen Seeding verwendeten Seedlaser ist mit den Repetitionsraten moderner high gain FELs, die auf supraleitender Technologie basieren, nicht kompatibel. Darüber hinaus ist die geseedete Strahlung eine höhere Harmonische der Wellenlänge des Seedlasers, sodass die Ausgangswellenlänge auf wenige Nanometer begrenzt und ihre Durchstimmbarkeit eingeschränkt ist. Zur Überwindung dieser Einschränkungen ist es notwendig nach neuen Möglichkeiten für FELs zu suchen.

Im Rahmen dieser Arbeit werden neue Ideen vorgestellt, die es uns ermöglichen eine hohe Repetitionsrate und vollständig kohärente Strahlung in einem erweiterten und durchstimmbaren Wellenlängenbereich zu erreichen. Die drei Vorschläge dieser Arbeit zielen darauf ab, die Abhängigkeit externer Seeding-Systeme von der Seedlaserquelle zu verringern und gleichzeitig die volle Kohärenz der geseedeten Strahlung zu erhalten. Der erste Vorschlag ist ein HGHG, welches auf einem optischen Klystron basiert, und die konventionelle HGHG-Strahlführung so modifiziert, dass die strengen Anforderungen an die Seedlaserleistung um mehrere Größenordnungen reduziert werden. Auf diese Weise kann die Repetitionsrate der Seedlaserquelle erhöht werden, oder es können stattdessen Seedlaserquellen mit kürzeren Wellenlängen verwendet werden. Der zweite Vorschlag ist ein HGHG-geseedeter Oszillator-Verstärker-Aufbau: Ein optischer Resonator fängt einen herkömmlichen SeedLaserpuls mit niedriger Repetitionsrate ein und speichert ihn, um Elektronenpakete mit hoher Repetitionsrate zu seeden. Der dritte Vorschlag ist ein HGHG-Oszillator-Verstärker, der die Abhängigkeit von externen SeedLasern eliminiert. Anstelle des externen Lasers erzeugen die Elektronen, ausgehend vom Schrotrauschen, den Laserpuls selbst, welcher im optischen Resonator gespeichert wird , um Elektronenpakete mit hoher Repitionsrate zu seeden. Neben der hohen Repetitionsrate ermöglicht dieses System eine kürzere und durchstimmbare geseedete Strahlung. Diese Art von Strahlung war in der Vergangenheit noch nie möglich und kann für bereits bestehende Experimente von großem Nutzen sein und neue Experimente sowie weitere Entdeckungen unterstützen, indem sie die laufende Forschung beschleunigt.

Dedicated to Ermis & Lefteris…

Chapter 1

Introduction

1.1 Motivation

Synchrotron radiation was demonstrated for the first time in 1947 in General Electric's research laboratories when accelerated electrons to 70 MeV generated visible light [1]. Initially, it was seen as an effect contributing only to energy losses and thus, as a limiting factor for high-energy physics experiments. As a result, for the first-generation synchrotron light sources, only parasitic operation at accelerators built for high-energy physics experiments was allowed. However, the science community soon realized that the light produced has extraordinary potential for studies of matter, resulting in the second-generation light sources that appeared in the 1970s [2]. These light sources were storage rings and were dedicated sources of radiation that used bending magnets and undulators/wigglers for the generation of light. In the third generation of light sources, the storage rings were designed with dedicated straight sections to insert undulators and wigglers (insertion devices) [2] and improve the properties of the generated radiation. Currently, we exploit the fourth-generation light sources that are diffraction-limited storage rings, such as MAX IV [3] and PETRA IV [4]. Free electron lasers (FELs) are linear-accelerator-based light sources and are by some people perceived as a different class of synchrotron light source and by others as a 4th generation synchrotron light source together with the diffraction-limited storage rings.

The concept of the FEL was first introduced in 1971 by John Madey and was demonstrated soon after that by Madey and colleagues [5, 6]. In most of the initial experiments, oscillators were used to generate light that was amplified in consecutive passes in an undulator enclosed in an optical cavity as the power gain of the light per pass was rather low. Present high-gain FELs are based on the idea that high gain can be achieved in a single-pass. To achieve this, long undulators and high quality electron beams are utilised to reach saturation independently of an optical cavity and mirror availability. This idea was first introduced by Kondratenko and Saldin [7] and soon after that, Bonifacio, Pellegrini, and Narducci [8, 9] described the FEL as a collective instability and formulated a theoretical base to describe it. This new concept opened the possibility to reach shorter wavelengths and to introduce the x-ray FEL (XFEL). FLASH was the first XFEL to start operation in 2005 and covered the XUV/soft x-ray spectral range [10]. Currently, there are several more XFEL user facilities worldwide such as LCLS [11], SACLA [12], FERMI [13], the PAL-FEL [14], the European XFEL [15] and the SwissFEL [16]. Additionally, there are many research and development (R&D) projects for future generations of light sources [17, 18].

A significant figure of merit that characterizes the radiation generated by light sources is the brightness: it describes the number of photons per unit time (flux), per 0.1% bandwidth and per unit phase space area. The radiation generated by FELs provides peak brightness that is up to ten orders of magnitude higher compared to third-generation storage rings, as shown in Fig. 1.1. The FEL radiation is tunable in a wide wavelength range (from millimetre to Ångström), reaches high peak powers (of tens of GW) and ultra-short pulse durations (towards attosecond), and has high purity in terms of transverse coherence, but also longitudinal coherence (transform-limited pulses) under certain conditions .

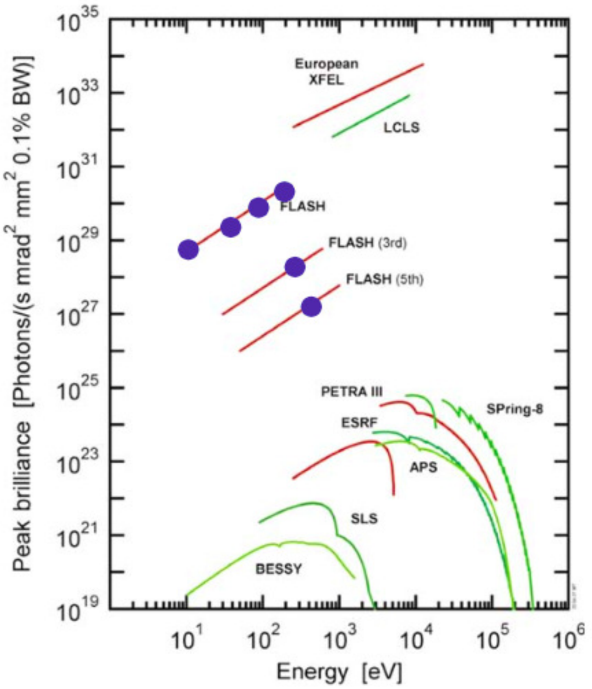

FIGURE 1.1: Comparison of peak brightness of existing FEL sources and synchrotron light sources. Graph taken from [19].

In the most common case of a high-gain FEL, the radiation is generated by a process called self-amplified spontaneous emission (SASE) [9]. SASE depends on the stochastic nature of the synchrotron radiation generated by an electron beam at the upstream part of an undulator and is in detail described in Chapter 2. The initial radiation is amplified along the undulator and as a result, the final FEL radiation has a poor longitudinal coherence. This is reflected in a broad spectrum with various spikes. To improve the longitudinal coherence, several methods are proposed and demonstrated such as the self-seeding [20] and the high brightness SASE [21], for instance. One of the most promising candidates is a family of methods that depend on external seed laser sources and are described under the term external seeding.

With direct external seeding [22], x-ray wavelength range is not accessible since there are no seed laser sources available at this wavelength because of the limitations of the nonlinear up-conversion process of available sources to the extreme ultraviolet (XUV) spectral range [23]. External seeding can alternatively be combined with harmonic generation within the FEL process to achieve shorter wavelengths [24]. In such a scheme, the electron bunch is pre-shaped in one or more short undulators - called modulators - with the help of an intense seed laser pulse before entering a second undulator - called radiator. At the radiator, it emits coherent radiation at a harmonic of the seed laser wavelength, therefore, the high degree of coherence held by lasers is transferred to the final FEL radiation. Two of the most common external seeding schemes are the high gain harmonic generation (HGHG) [24] and the echo enabled harmonic generation (EEHG) [25, 26] and are described in more detail in Chapter 2. In addition to the full coherence of seeded radiation, seeded FELs guarantee synchronization between the seeded FEL and external sources for pump-probe experiments and shot to shot stability due to the deterministic nature of the process. These significant and unique features of seeded radiation have allowed interesting experiments [27, 28] to take place at FERMI, the first fully seeded FEL. In addition to FERMI, more facilities have devoted resources to external seeding research, such as the SDUV-FEL [29], LCLS [30], the Dalian Coherent Light Source [31], SXFEL [32] and FLASH [33]. To take advantage of the opportunities offered with seeded radiation, FLASH is currently undergoing an upgrade, known under the name FLASH2020+ project, that aims at simultaneous operation of a SASE beamline and a seeded beamline that takes advantage of the high repetition rate of superconducting radiofrequency (RF) technology for the first time [34, 35].

Even though external seeded radiation has already considerably increased the opportunities in high gain FELs due to its full coherence and stability, its properties suffer from several limitations that the seed laser introduces:

1. The repetition rate of the seeded FEL radiation cannot be higher than the repetition rate of the seed laser source.
2. The output wavelength of the seeded FEL radiation is a harmonic of the seed laser wavelength, typically limited to a maximum of 100. This limits the:
   (a) Shortest wavelength that can be achieved.
   (b) The tunability of the seeded FEL radiation.

Since with the seeding schemes introduced so far the harmonic conversion is limited, it is desirable to start with a seed laser source of a short wavelength as long as it provides sufficient peak power and stability. For this reason, ultraviolet (UV) lasers are commonly used for external seeding. Current state-of-the-art laser sources fulfilling all requirements in terms of tunability and peak power are typically providing only repetition rates of some tens of Hz. With FLASH2020+, DESY plans to increase this number to up to 6000 pulses per second with a unique burst-mode operation [34, 35]. This is currently the upper limit for the overall repetition rate of external seeding. In addition, the upper limit in wavelength conversion from the seed laser to the output FEL is in the order of 1%, so the shortest possible FEL radiation wavelength is above 2 nm [36]. Finally, these UV sources offer limited wavelength tunability which is typically less than 10% and this implies a limitation in the continuous variation of the seeded FEL wavelength.

Currently, accelerators based on superconducting RF technology can provide electron bunches at MHz repetition rates- a repetition rate that is higher by roughly four orders of magnitude compared to normal conducting accelerators. Burst mode operation, such as the one at FLASH [37] and at the European XFEL [15], provides thousands of electron bunches per second and continuous wave (CW) operation provides million bunches per second. The FELs LCLS II [38] and SHINE [39], currently under-construction, aim at CW operation, showing that there is a clear direction for increased repetition rate in future FELs. In such machines, most of the available electron bunches remain unused in seeded beamlines due to the considerably lower repetition rate of seed lasers.

In order to push the limits of the capabilities of FELs and improve them even further to accommodate the needs of multiple experiments of different purposes, we need to consider that the longitudinal coherence is not always sufficient by itself even though it is an important figure of merit of the FEL radiation for many scientific experiments. The average brightness, which depends on the number of photon pulses generated per second, can be crucial too. Molecular movies benefit from the properties of seeded radiation (purity, intensity, phase and time stability) but require high repetition rate. Similarly, spectroscopic techniques, which aim to resolve the electronic structure of samples, require the high purity that seeding techniques offer but also depend on statistics. In that case, neither SASE nor external seeding can offer a good amount of statistics before, for example, the sample degrades: SASE radiation needs to be monochromatized, which leads to flux reduction and intensity fluctuations, and seeded radiation is currently only available at a low repetition rate despite the MHz repetition rates of electrons bunches. In addition to the repetition rate, extending the wavelength range to shorter than 2 nm would allow new types of experiments that require higher resolution, such as imaging and diffraction, to take advantage of the unique properties of seeded radiation.

In this cumulative thesis, the main goal is to address the limitations described above and propose novel schemes that aim to combine the unique properties of externally seeded radiation with the high repetition rate of superconducting-based FELs. Some of the proposed schemes aim to extend the wavelength range and the wavelength's tunability provided to the experiments, and ultimately the variety of the experiments they address. FEL radiation with these characteristics can significantly accelerate and expand the science taking place at FELs.

1.2 Organization and scope of the thesis

This cumulative thesis is based on three first-author publications. The common thread is the effort to increase the repetition rate of external seeding schemes to make fully coherent x-ray FEL radiation at high repetition rates available for the first time. Additional goals addressed in these schemes are the extension of the wavelength range and its tunability.

I start with the theoretical framework (Chapter 2) needed to understand the results shown in this thesis. In addition to the theory, in Appendix A, I discuss the main simulation codes that have been used to understand the complexity of the physics behind these simulations which is connected to long computational times, and the limitations that may arise based on the mathematical approximations used.

After all the necessary information is introduced, I move on to the main chapters where the publications are presented. I follow an order of ascending complexity of the proposals done in this thesis. Since we have identified the seed laser source to be the main limitation to achieve high repetition rates with seeding schemes, I try step by step to eliminate this dependence with different setups of different complexities. Until now, the weight has been put solely on the seed laser side: seed laser systems are required to become more and more complex and precise. Here, I take a different approach and I act on the FEL scheme itself to eliminate this strong dependence.

In Chapter 3, I present an external seeding scheme, called high gain harmonic generation (HGHG), with the addition of an optical klystron [40]. The optical klystron takes advantage of a low power seed laser source that prepares the electron bunch to be further self-modulated without the need for a high peak power seed laser. This new setup requires much lower seed laser power than conventional seeding schemes. When the seed laser power can be decreased by 2 to 3 orders of magnitude, it is possible to do one of the following:

1. Increase the repetition rate as the optics can withstand these lower power densities.
2. Use seed laser sources of shorter wavelengths which are typically available only at lower powers.

This setup is rather straightforward; the design still depends on a seed laser source and requires a seed pulse for every electron bunch, but the power is much lower so the repetition rate can be increased or the shortest wavelength can be decreased.

Taking one more step away from the dependence of seeding schemes on the seed laser systems, while increasing the complexity, I move on to Chapter 4. Here, I present an HGHG setup based on an oscillator FEL. A low repetition rate external seed laser pulse is first injected into the cavity where it is overlapped with an electron bunch traversing a modulator. Now two processes occur:

1. The electron bunch gets energy-modulated by the laser pulse.
2. The laser pulse gets amplified due to the interaction with the wiggling electron bunch.

While the modulated electron bunch can now be extracted from the cavity, the amplified laser is recirculated to the entrance of the modulator. The following electron bunches are then overlapped with the recirculated light pulse and they maintain the light pulse intensity constant over the bunch train while they are seeded. In this case, we still need a seed laser source to initiate the seeding process, however, this seed laser may:

1. Have a lower intensity since the initial signal can be amplified along the modulator in the cavity.
2. Operate at a low repetition rate since it only needs to initiate the FEL process.

After the initiation, the radiation field is captured and stored in the cavity, enabling high repetition rate seeding.

In the last step in Chapter 5, a scheme completely independent of external seed laser sources is proposed. In this case, I still study an HGHG setup based on an oscillator FEL, but this time, the process starts from shot noise. The electrons themselves in the in-cavity undulator emit radiation which is amplified over the passes in the cavity. When sufficient power is reached, the amplification per pass must be reduced and be replaced by an equilibrium. The advantages are twofold; being completely independent of external seed laser sources we can increase the repetition rate of seeding and reduce the FEL wavelength, in principle with no limitations except for mirror availability. However, in this oscillator starting from shot noise, we have the additional complexity of controlling the power in the cavity to transition from power amplification to power stability, and a monochromator must be used to suppress the initial SASE spectrum.

In the last Chapter 6, I summarize the results shown in the publications and I offer an overview of what has been done, and what else needs to be done and verified before moving to the realization of the studied setups.

Chapter 2

Theory

2.1 Accelerator physics

The field of accelerator physics treats the dynamics of relativistic charged particles experiencing electric and magnetic fields. Since the exact motion of the particles can typically not be solved analytically, it is common to use Taylor-expansions and work with different assumptions and statistical properties of ensembles. This way we can separate the study of linear optics from more complicated nonlinear dynamics and collective effects. Here, I restrict myself to topics that are useful to understand the main results presented in the following chapters. Since we are interested in FELs, we discuss the specific case of electrons and we focus on the main aspects of linear accelerators. For high-gain FELs, it is very important to have high electron density and as a result, the requirements on beam size, divergence and bunch length (which is directly associated to the peak current) are stringent. The control of the beam size and divergence is treated in the transverse beam dynamics, while the bunch compression concept is treated in the longitudinal beam dynamics.

2.1.1 6D phase space

At any position, we can describe an electron in a 6D phase space: $(x, x', y, y', \delta, s)$. The coordinates x and y are the transverse horizontal and vertical displacements respectively, and together with s, the longitudinal intra-bunch coordinate along the trajectory, they define the 3D space. The coordinates x' and y' are the transverse angular displacements and δ is the relative momentum offset. In classical mechanics the conjugate variables are used and we refer to the planes (x, p_x), (y, p_x) as the transverse phase space, where $p_{x/y}$ is the momentum. However, a modified phase space is more common in accelerator physics: (x, x'), (y, y') and (s, δ) are the *horizontal*, *vertical*, and *longitudinal phase space*, respectively. In this 6D phase space, we can define a reference particle that has all coordinates set to zero, $(x = 0, x' = 0, y = 0, y' = 0, \delta = 0, s = 0)$, as it always stays on the design trajectory and has the nominal energy. Following, we summarize the 6 coordinates in a vector, showing the transition from the momentum (canonical conjugate variables) to transverse angular displacements:

$$\begin{pmatrix} x \\ \frac{p_x}{p} \simeq \frac{dx}{dt}\frac{dt}{dz} = x' \\ y \\ \frac{p_y}{p} \simeq \frac{dy}{dt}\frac{dt}{dz} = y' \\ \delta = \frac{\Delta p}{p_o} \\ s \end{pmatrix} \tag{2.1}$$

where p_0 is the reference momentum and t is the time coordinate.

2.1.2 Transverse beam dynamics

In an accelerator, the electron bunch should follow the nominal trajectory. However, the individual electrons diverge within an electron bunch. In order to steer them to the nominal trajectory, we are using transverse magnetic fields. While the Lorentz force accounts for both the electric (**Y**) and magnetic fields (**B**) as:

$$\mathbf{F} = e(\mathbf{Y} + \mathbf{u} \times \mathbf{B}), \tag{2.2}$$

we rewrite the Lorentz force as $F_x = -eu_zB_y$ for an electron of charge e moving with a velocity $\mathbf{u}$ that has only a longitudinal component u_z and is experiencing a magnetic field which has only a vertical component B_y. We assume an equilibrium with the centrifugal force $F_r = m_e u_z^2/R_c$, where R_c is the radius of curvature of the trajectory and m_e the electron rest mass, and by equating these forces we get the *magnetic rigidity* [41]:

$$B_y R_c = \frac{p}{e}. \tag{2.3}$$

Taking only the example of a horizontal deflection, we expand the magnetic field in the vicinity of the nominal trajectory under the assumption that the transverse displacements are very small, and we get a series of multipoles [41]:

$$B_y(x) = B_{y0} + \frac{\partial B_y}{\partial x}x + \frac{1}{2}\frac{\partial^2 B_y}{\partial x^2}x^2 + \frac{1}{3!}\frac{\partial^3 B_y}{\partial x^3}x^3 + \mathcal{O}(x^4) \tag{2.4}$$

Dividing all the terms in Eq. 2.4 with p/e gives:

$$\begin{aligned}\frac{B_y(x)}{p/e} = \frac{B_{y0}}{B_{y0}R_c} + \frac{\partial B_y}{\partial x}\frac{x}{p/e} + \frac{1}{2}\frac{\partial^2 B_y}{\partial x^2}\frac{x^2}{p/e} + \frac{1}{3!}\frac{\partial^3 B_y}{\partial x^3}\frac{x^3}{p/e} + \mathcal{O}(x^4) = \\ \underbrace{\frac{1}{R_c}}_{\text{dipole field}} + \underbrace{\xi x}_{\text{quadrupole field}} + \underbrace{\frac{1}{2}\upsilon x^2}_{\text{sextupole field}} + \underbrace{\frac{1}{3!}\varkappa x^3}_{\text{octupole field}} + \mathcal{O}(x^4)\end{aligned} \tag{2.5}$$

Each of the multipoles appearing in Eq. 2.5 serves a different purpose in an accelerator; when perfectly aligned, dipoles steer the trajectory of all electrons independently of their position, quadrupoles focus and defocus transversely the beam and sextupoles are used to compensate for the so-called chromaticity (referring to the change of linear optics with the beam energy) and for field correction. *Linear beam optics* deal with the two first multipoles; dipoles and quadrupoles.

We can use a matrix formalism to describe how each electron's six coordinates are affected along a transport line in a linear approximation. The coordinates of each electron evolve from an initial set of coordinates $(x_i, x'_i, y_i, y'_i, \delta_i, s_i)$ to a new one $(x_f, x'_f, y_f, y'_f, \delta_f, s_f)$, which can be calculated with the transfer matrix of the elements along the transport line that caused this change. Each of the transfer matrix elements, R_{ij}, describes the correlation between two coordinates and, for instance, R_{56} is the longitudinal dispersion and denotes the correlation between the longitudinal position and the energy of the electrons. These linear matrices are not suitable for non-linear elements such as sextupoles. It is possible to use Taylor expansions to describe higher order terms [42]. For second order terms, the map $T_{\mathrm{i,j,k}}$ is used and for third order terms the map $U_{\mathrm{i,k,j,l}}$ is used and i, j, k, l can take values from 1 to 6, representing the coordinates of the discussed 6D phase space. Nonlinear optics are out of the scope of the thesis, and readers are encouraged to look for more information in [42, 43, 44].

In linear optics, a transfer matrix M describes the transport line and is defined as [41]:

$$M = \begin{pmatrix} R_{11} & R_{12} & R_{13} & R_{14} & R_{15} & R_{16} \\ R_{21} & R_{22} & R_{23} & R_{24} & R_{25} & R_{26} \\ R_{31} & R_{32} & R_{33} & R_{34} & R_{35} & R_{36} \\ R_{41} & R_{42} & R_{43} & R_{44} & R_{45} & R_{46} \\ R_{51} & R_{52} & R_{53} & R_{54} & R_{55} & R_{56} \\ R_{61} & R_{62} & R_{63} & R_{64} & R_{65} & R_{66}. \end{pmatrix} \tag{2.6}$$

With this transfer matrix we can now calculate the new coordinates as:

$$\begin{pmatrix} x_f \\ x'_f \\ y_f \\ y'_f \\ \delta_f \\ s_f \end{pmatrix} = M \begin{pmatrix} x_i \\ x'_i \\ y_i \\ y'_i \\ \delta_i \\ s_i \end{pmatrix}. \tag{2.7}$$

Each element in the accelerator has its characteristic transfer matrix. A number of consecutive elements can be described by a single transfer matrix M_{total}, which is the product of the matrices that describe κ independent elements, with element 1 being upstream of element 2:

$$M_{\text{total}}(1 \to \kappa) = M_\kappa \cdot M_{\kappa-1} \ldots \cdot M_2 \cdot M_1. \tag{2.8}$$

Apart from the single electron trajectories, we are interested in the evolution of the electron bunch so it is useful to define some parameters that characterize the electron bunch as an ensemble instead, when taking a snapshot at a certain longitudinal position z. We define as *emittance*, ε, the area covered by the bunch in the phase space divided by π. Based on the Liouville's theorem, the emittance is a constant of motion when conservative forces are considered. With conservative fields such as the dipole and quadrupole magnetic fields, the emittance remains constant along z. It is useful to express the bunch properties as moments of the particle distribution in phase space. We define the squared rms beam size ${\sigma^2}_x(z) = \langle x^2 \rangle$, the squared rms beam angular divergence $\sigma^2_{x'}(z) = \langle x'^2 \rangle$ and the rms beam correlation $\langle xx' \rangle$. Based on them we define the rms emittance [45], which is a statistical property and is also known as geometric emittance:

$$\varepsilon_x = \sqrt{\langle x^2 \rangle \langle x'^2 \rangle - \langle xx' \rangle^2}, \tag{2.9}$$

Since the geometric emittance describes the area in the phase space, we can define its equation in phase space:

$$\varepsilon = \gamma(z)x^2(z) + 2\alpha(z)x(z)x'(z) + \beta(z)x'^2(z). \tag{2.10}$$

From Eq. 2.10 we can define the Twiss parameters, which describe the shape and orientation of the ellipse formed in the phase space:

$$\begin{aligned} &\beta(z), \\ \alpha(z) &= -\frac{1}{2}\beta'(z) \\ \gamma(z) &= \frac{1+\alpha(z)^2}{\beta(z)}. \end{aligned} \tag{2.11}$$

The *beta function*, $\beta(z)$, is the position-dependent part of the amplitude of the transverse oscillations that each electron performs along the accelerator. Based on the parameters we can define the rms electron beam size σ_x and divergence $\sigma_{x'}$, as illustrated in Fig. 2.1:

$$\begin{aligned} \sigma_x &= \sqrt{\varepsilon_x \beta_x(z)} \\ \sigma_{x'} &= \sqrt{\varepsilon_x \gamma_x(z)} \end{aligned} \tag{2.12}$$

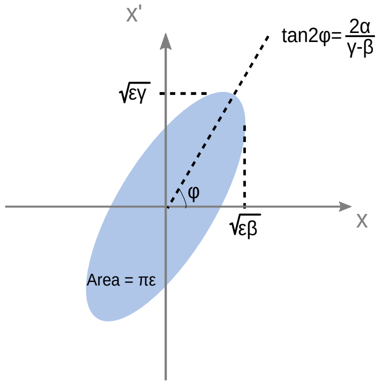

FIGURE 2.1: Beam ellipse in the horizontal phase space at a certain fixed longitudinal position. Here, ϕ is the orientation angle.

Finally, it is common in many cases to refer to the normalized emittance ε_{N}, which is simply normalized to the factor $\beta_{rel}\gamma$, $\varepsilon_{\mathrm{N}} = \varepsilon\beta_{rel}\gamma$ and is conserved during acceleration. Overall, the emittance is a property of the beam that determines the electron beam quality and is very important for the FEL successful operation. The Twiss parameters together with the emittance determine the size and divergence of the electron beam.

2.1.3 Longitudinal beam dynamics and bunch compression

For high gain FELs that aim at generation of short-wavelength radiation the electron beam quality plays an important role. A figure of merit of the quality of the electron beam is the 6D electron beam brightness [46], which is defined as the electron bunch charge divided by the product of the rms horizontal, vertical and longitudinal emittances. Looking at the contribution of the longitudinal component, this means that the electron bunches need to be compressed longitudinally to achieve a high peak current. A high peak current is associated with a larger conversion factor from the beam power to the output FEL radiation power which is in addition obtained in shorter distances (shorter power gain length), as it will be discussed in detail in Section 2.3 that covers the FEL theory. As a result of this longitudinal compression, short electron bunches of 10-100 fs length are achieved [47]. The electron bunch length is in addition, directly associated with the output FEL pulse duration in several FEL schemes.

Magnetic bunch compressors are commonly used in FELs for longitudinal compression. They consist of dipole magnets that deflect the electrons with an energy-dependent angle. For an effective compression the electron bunch needs to traverse the bunch compressor with a linear energy chirp, h, meaning that the energy and longitudinal position of electrons are linearly correlated. An electron bunch with a linear energy chirp is shown in the longitudinal phase on the top right and left corners of Fig. 2.3. For any electron it is possible to express its energy offset δ before the bunch compression as a function of its initial longitudinal intra-bunch coordinate s_i [48]:

$$\delta = \delta_0 + hs_i + h's_i^2 + \mathcal{O}(s^3), \tag{2.13}$$

where δ_0 denotes the uncorrelated energy offset. The linear energy chirp is defined as:

$$h = \frac{dE}{ds}\frac{1}{E}, \tag{2.14}$$

where E is the electron beam energy. In this thesis, we define a positive chirp when the head of the electron bunch has lower energy and the tail has higher energy as shown in Fig. 2.3. A linear energy chirp can be introduced in the linac during the RF acceleration process. The energy gain ΔE_{gain} of the electrons by the RF wave is described with the following equation:

$$\Delta E_{\text{gain}} = eV_{\text{RF}}cos(k_{\text{RF}}s + \phi_{\text{RF}}), \tag{2.15}$$

where V_{RF} is the amplitude of the RF voltage, k_{RF} is the RF wavenumber and ϕ_{RF} is the RF phase. Maximum acceleration occurs when $\phi_{RF} = 0$ and the beam is "on crest", for $\phi_{RF} = \pi$ the beam is "in trough" where maximum deceleration occurs and finally, for $\phi_{RF} = \pi/2$ the beam is at "zero crossing". A schematic representation can be seen in Fig. 2.2. Counter-intuitively, it is not preferred to accelerate the electron bunch when the energy gain is at maximum. Instead, an "off crest" acceleration is needed to get a chirped electron bunch as shown in Fig. 2.3. The possible phases that result in an energy-chirped electron bunch, while it is still accelerated, are either in the region $-\pi/2 < \phi_{RF} < 0$ or $0 < \phi_{RF} < \pi/2$.

In a four dipole chicane illustrated in Fig. 2.3, the electrons of higher energy in the beam travel along the shortest trajectory as they are more "rigid" (see Eq. 2.3). For a bunch chirped properly in the linear accelerator (linac) section before the chicane entrance in which more energetic particles are in the tail of the bunch, an overall bunch compression can be achieved.

An electron of an energy offset δ exits a bunch compressor of a longitudinal dispersion R_{56} with a new longitudinal coordinate s_f [48]:

$$s_f = s_i + R_{56}\delta. \tag{2.16}$$

Subtituting Eq. 2.13 into Eq. 2.16, we get:

$$s_f = s_i(1 + hR_{56}) + R_{56}\delta_0. \tag{2.17}$$

After differentiating, we get the linear compression factor:

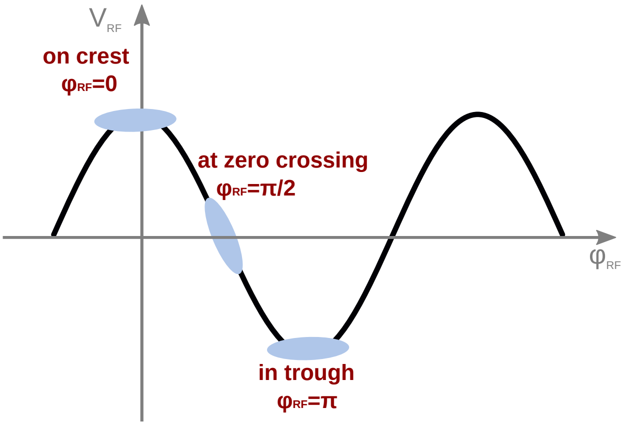
V_{RF}
on crest
$\varphi_{RF}=0$
at zero crossing
$\varphi_{RF}=\pi/2$
in trough
$\varphi_{RF}=\pi$
φ_{RF}

FIGURE 2.2: The electron bunch distribution in the longitudinal phase space is affected by the phase of the RF wave during acceleration. In accordance with Eq. 2.15, maximum acceleration occurs on crest and maximum deceleration occurs in trough.

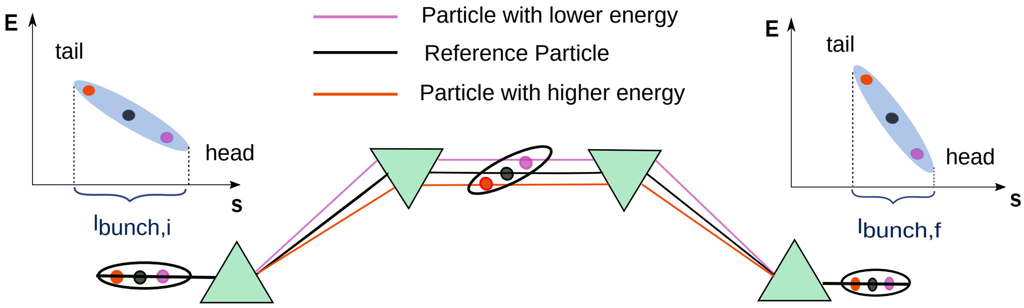
Particle with lower energy
Reference Particle
Particle with higher energy
E
tail
head
s
$l_{bunch,i}$
E
tail
head
s
$l_{bunch,f}$

FIGURE 2.3: Schematic view of bunch compression in a magnetic chicane. An energy-chirped electron bunch transverses the chicane, and the electrons follow different paths based on their energy. The result is that the lower energy electrons follow a longer path and fall behind, while the higher energy electrons follow a shorter path and catch up, reducing the overall length of the bunch. On top left and right I show the electron bunch distribution in the longitudinal phase space. On the left, we can see the linearly chirped electron bunch before compression, and on the right, after compression. The distribution is rotated clockwise, and as a result, the electron bunch gets shorter.

$$C_{BC} = \frac{ds_i}{ds_f} = \frac{l_{\text{bunch,i}}}{l_{\text{bunch,f}}} = (1 + h \cdot R_{56})^{-1}, \tag{2.18}$$

where $l_{\text{bunch,i}}$ and $l_{\text{bunch,f}}$ are the initial and final electron bunch length, respectively. From Eq. 2.18 we see that in order to reduce the bunch length longitudinally, we need an energy chirp and an R_{56} of different signs. The exact signs are a matter of sign convention. In reality, higher order terms are important for RF acceleration and bunch compression. It is possible to use a (decelerating) harmonic cavity [49] or optics linearization with sextupole magnets in arc type bunch compressors to reduce them. This study is out of the scope of the thesis and readers are encouraged to look for more information at Reference [48].

Typically, more than one stages of bunch compression are preferred in FELs because they reduce the sensitivity to RF jitter, they give the possibility to apply the first stage of compression at relatively low electron beam energies, and the second stage at higher energies where the effect of the Coherent Synchrotron Radiation (CSR) on the transverse emittance is less important and space charge forces are minimised. On the other hand, single-stage compression is in favour of minimizing some of the collective effects, such as the microbunching instability [50]. For this reason, even though most FELs operate with two-stage bunch compression, FERMI [13] has been operating in the past with only one bunch compressor in order to minimize the effect of the microbunching instability [51] which plays an important role in seeding [52, 53].

2.2 Synchrotron Radiation

Synchrotron radiation is the radiation emitted by charged particles in the forward direction and tangential to their orbit when their momentum vector is altered. This means that both linear acceleration and circular motion force the charged particle to lose energy in a form of an electromagnetic wave. The power loss of accelerated and non-relativistic charges is described by the so-called Larmor formula which is known since 1897 [41]:

$$P = \frac{q^2}{6\pi\epsilon_0}\frac{1}{m_0^2c^3}(\frac{d\mathbf{p}}{dt})^2, \tag{2.19}$$

where q is the charge of the particle, ϵ_0 is the vacuum permittivity, m_0 is the rest mass of the particle and c is the speed of light. From Eq. 2.19 and for typical accelerator gradients in linear acceleration, such as 60 MV/m, the power loss is negligible so we are going to focus on the generation of synchrotron radiation by relativistic particles, emitted when there is a transverse force with respect to their orbit.

2.2.1 Synchrotron radiation: bending magnets and insertion devices

From Eq. 2.19 it is possible to derive [54] the power loss for circular motion and relativistic particles, known as the Liénard formula [41]:

$$P = \frac{e^2}{6\pi\epsilon_0}\frac{1}{(m_0c^2)^4}\frac{E^4}{R_c^2}, \tag{2.20}$$

In Eq. 2.20 it is clear that it is advantageous to use electrons in light sources instead of protons of the same energy since $P_{\text{electron}}/P_{\text{proton}} \simeq 10^{13}$. For the same reason, protons are preferred in circular colliders. For ultra-relativistic electrons and in the laboratory frame, the synchrotron radiation forms a cone, whose angle is energy-dependent as $\theta = 1/\gamma$ so the higher the electron energy, the more collimated the emitted radiation.

A simple method to obtain synchrotron radiation is to bend an electron in a bending magnet, also known as a dipole. The dipole radiaton's spectrum is broad and it can be described by the *critical frequency* ω_c, which splits the spectrum into two parts of equal integrated power [55]:

$$\omega_c = \frac{3c\gamma^3}{2R_c}. \tag{2.21}$$

In order to achieve higher photon density, after the second generation of synchrotrons, undulators took the main role in the generation of synchrotron radiation instead of dipoles. Undulators are magnetic devices and they belong to the family of insertion devices. They consist of several short dipoles placed one after the other in an alternating polarity with a periodicity of one undulator period λ_u and they consist of two girders facing each other as shown in Fig. 2.4. In such a device, the overall deflection of the electrons is zero.

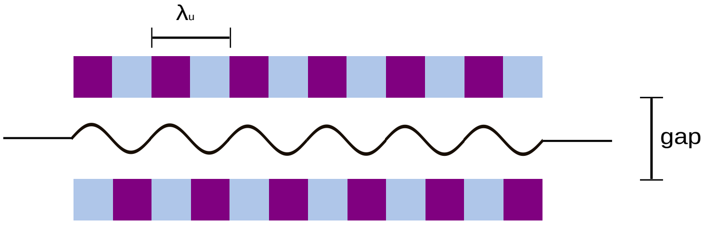

FIGURE 2.4: Simplified schematic representation of an undulator. The undulator period λ_u is the distance between two poles of same polarity and the gap is the distance between the two girders. The black line shows the trajectory of the electrons, which is shown in the same plane as the magnetic field for simplicity, but in reality it lies on the transverse plane of the magnetic field.

In the case of a planar undulator, the vertical field, for instance, varies sinusoidally along z as [56]:

$$B_y = B_0 sin(k_u z), \tag{2.22}$$

where k_u is the wavenumber calculated as $2\pi/\lambda_u$. The transverse velocity of an electron experiencing this magnetic field can be calculated after integration of the equation of motion with the Lorentz force from Eq. 2.2:

$$u_x = \frac{Kc}{\gamma}\cos(k_u z). \tag{2.23}$$

Then the longitudinal velocity can be calculated as $u_z = \sqrt{u^2 - u_x^2}$:

$$u_z = \left(1 - \frac{1}{2\gamma^2}\left(1 + \frac{K^2}{2}\right)\right)c - \frac{cK^2}{4\gamma^2}\cos(2k_u z). \tag{2.24}$$

Due to the small amplitude of the sinus-like path, the radiation cones emitted in each period overlap and constructive interference is possible [2]. The wavelength λ_l of the radiation emitted by a relativistic electron following this motion is [56]:

$$\lambda_l = \frac{\lambda_u}{2n\gamma^2}\left(1 + \frac{K^2}{2} + \gamma^2\theta^2\right), \tag{2.25}$$

where θ is the observation angle and $K = \frac{eB_0}{m_e c k_u} = 0.934 B_0[T]\lambda_u[cm]$ is the dimensionless *undulator parameter*. Constructive interference happens not only at the fundamental wavelength ($n = 1$), but for higher harmonics ($n > 1$) as well which are typically generated with less intensity.

2.3 FEL theory

FELs provide tunable, fully coherent and high peak brightness radiation compared to other types of light sources. The energy exchange between the emitted radiation and the co-propagating electron in an undulator are the baseline of the working principle of FELs. In the undulator, the electromagnetic radiation overpasses the electron bunch by λ_l (the fundamental wavelength radiated in the undulator) for each undulator period λ_u that the electron traverses. This effect is called *slippage*. Depending on the relative phase of the electrons and the electromagnetic wave, an energy exchange takes place between them. Under favourable conditions, the net energy is transferred from the electron bunch to the co-propagating wave and the latter is amplified. It is possible to divide the FELs into a few main categories based on: the power gain in an undulator (high gain and low gain FELs) and the initial conditions (prebunched electron bunch, external co-propagating field or none of these).

2.3.1 Low-gain FELs (Oscillator FEL)

If the energy gain of the electromagnetic wave propagating with the electron beam is relatively small in the order of few per cent in a single-pass in an undulator, then the FEL falls into the category of a low-gain FEL. In this case, optical cavities are employed in an FEL oscillator (FELO) in order to amplify and store the initially small signal during several passes. A common way of defining the power gain in oscillator FEL physics in one pass is $gain = (P_{\text{out}} - P_{\text{in}})/P_{\text{in}}$. This is the definition I adopt in the presentation of my results in the following chapters. Oscillator FELs are limited in the wavelength range that they can support because, for sustainable operation, the power gain in a single pass must exceed the cavity power losses. This puts stringent requirements on the reflectivities of the mirrors. As a result, the FEL oscillators are very common in the THz, infrared (IR), visible and ultraviolet (UV) wavelength range with ELETTRA achieving the shortest recorded wavelength of 190 nm with standard mirrors [57]. Some other examples of well established FEL oscillators are FELIX [58] and the DUKE FEL [59]. An exception for low-gain FELs is the x-ray FEL oscillator (XFELO) [60] which is planned to generate hard x-rays, using crystals (instead of mirrors) which are efficient reflectors at this wavelength range. At the same time, multi-layer mirrors can be considered in shorter wavelength applications as they provide relatively high reflectivities in an extended wavelength range. A simplified sketch of a FELO is shown in Fig. 2.5.

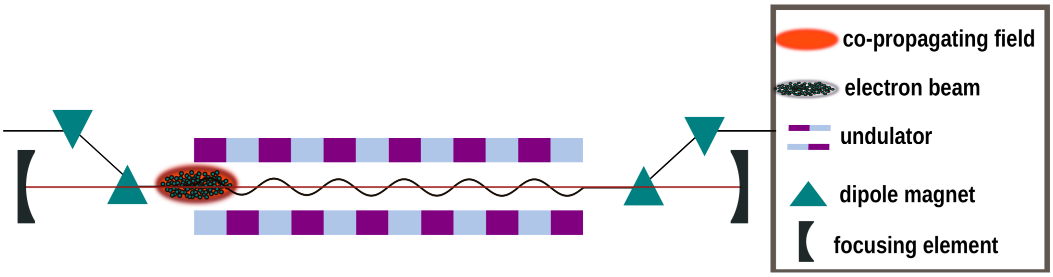

FIGURE 2.5: A simple sketch of an FEL oscillator. An undulator is enclosed in an optical cavity which, in this case, consists of two focusing mirrors. The orange color refers to the stored radiation field which is recirculated in the cavity and it is synchronised to overlap with the electron bunches. With black lines I show the electron bunch path.

In the following, I discuss the low-gain FEL in a more quantitative way, based on references [19, 55]. The fundamental process in FELs is the energy exchange between the electrons and the co-propagating field and here we assume that the co-propagating field is a plane electromagnetic wave [19]:

$$\Upsilon_x(z,t) = \Upsilon_0 \cos\left(k_l z - \omega_l t + \psi_0\right), \tag{2.26}$$

where $k_l = \omega_l / c$ is the wavenumber of the co-propagating wave. With $E = \gamma m_e c^2$ being the electron energy, its derivative is associated with the incremental work:

$$\frac{dE}{dt} = \mathbf{u} \cdot \mathbf{F} = -e u_x \Upsilon_x(t). \tag{2.27}$$

For a negative derivative the light wave gains energy. We consider that the electrons follow a sinusoidal path in an undulator and in addition, their average longitudinal speed is $\overline{u}_z < c$ is:

$$\overline{u}_z = c\left(1 - \frac{2+K^2}{4\gamma^2}\right). \tag{2.28}$$

As a result, the electrons slip behind with respect to the light (slippage). For a sustainable energy transfer from the electrons to the light wave, the electron velocity component that is parallel to the electric field, and the electric field vector have to point in the same direction, and this happens when the light wave moves ahead of the electrons by one optical wavelength for each undulator period.

We can rewrite Eq. 2.27, using Eq. 2.26. We use the approximation that the longitudinal speed of the electrons is constant and equal to the average speed from Eq. 2.28 and get:

$$\begin{aligned} \frac{dE}{dt} &= -\frac{ecK\Upsilon_0}{2\gamma}\cos\psi - \frac{ecK\Upsilon_0}{2\gamma}\cos\chi, \\ \psi &= (k_l + k_u)z - \omega_l t + \psi_0 \\ \chi &= (k_l - k_u)z - \omega_l t + \psi_0, \end{aligned} \tag{2.29}$$

where ψ_0 is an arbitrary initial phase. The argument ψ of the first cosine function of the energy derivative is known as the *ponderomotive phase*. For sustainable and significant energy transfer, we require the ponderomotive phase to be constant. For $d\psi/dt = 0$ it leads to $(k_l + k_u)\overline{u}_z - \omega_l = 0$. Inserting in Eq. 2.28 leads to a *resonance condition*:

$$\lambda_l = \frac{\lambda_u}{2\gamma^2}\left(1 + \frac{K^2}{2}\right). \tag{2.30}$$

The condition for sustained energy transfer from the electrons requires radiation of a wavelength that is the same as the spontaneous undulator radiation of Eq. 2.25. Hence, this radiation can be used as seed radiation in an FEL amplifier. Based on the resonance condition, the exact wavelength of the radiation in an FEL can be tuned either by changing the electron beam energy or by changing the undulator parameter K for fixed undulator period λ_u. The type of polarization can be freely chosen by varying the magnetic field in an undulator. For instance, a sinusoidal trajectory of the electrons in one plane will result in linear polarization and a helical path will lead to elliptical polarization.

Concerning the argument χ of Eq. 2.29, we can rewrite it as $\chi(z) = \psi(z) - 2k_u z$. If $\psi(z) = const$, then $\cos\chi$ performs two oscillations per undulator period and cancels out. For $\psi = 0$ the energy exchange is maximum, for $-\pi < \psi < -\pi/2$ the light wave loses energy, and for $-\pi/2 < \psi < 0$ the light wave gains energy. An interesting aspect of the ponderomotive phase is that it can be related to the intra-bunch longitudinal coordinate as $s = \lambda_l(\psi + \pi/2)/(2\pi)$ [19].

The electrons in a bunch do not always have the exact same reference energy $E_r = \gamma_r m_e c^2$, but there is a relative energy deviation, η, defined as:

$$\eta = \frac{E - E_r}{E_r} = \frac{\gamma - \gamma_r}{\gamma_r} \tag{2.31}$$

For $\gamma \neq \gamma_r$, the ponderomotive phase is not constant, and instead we get [19] :

$$\frac{d\psi}{dt} = 2k_u c\eta. \tag{2.32}$$

From Eq. 2.29 and Eq. 2.31, we get:

$$\frac{d\eta}{dt} = -\frac{eY_0 K}{2m_e c\gamma_r^2}\cos(\psi). \tag{2.33}$$

These two equations (2.32 and 2.33) consist the so-called *FEL pendulum equations*. The ponderomotive phase together with the relative energy deviation define the *longitudinal FEL phase space* and in the case of a low-gain FEL, they completely determine the evolution in the longitudinal FEL phase space. It should be reminded that these are the 1D particle equations of the FEL and that they are valid for low-gain, meaning that the field amplitude Y_0 grows so slowly with z that it can be considered roughly constant along the undulator. The 1D model is an idealised model built on the assumption that the electron beam is monoenergetic (no energy spread), has zero emittance and that it is infinitely long. In addition, the optical diffraction of the co-propagating wave and the electron beam betatron oscillations are not addressed.

We can also derive the energy change of the electrons taking into account their longitudinal oscillations, which was excluded in the previous model. It results that the coupling between the electrons and the co-propagating electromagnetic wave occurs for a slightly modified undulator parameter $\widehat{K}$:

$$\widehat{K} = K \cdot \left[J_0\left(\frac{K^2}{4+2K^2}\right) - J_1\left(\frac{K^2}{4+2K^2}\right)\right], \tag{2.34}$$

therefore the correction factor is the difference between the two Bessel functions J_0 and J_1.

2.3.2 High-gain FELs (The single-pass FEL)

Suppose the change in the magnitude of the optical field in a single pass is significant and comparable to this magnitude. In this case, the explicit evolution of the field along the undulator must be included. Then the FEL works as a high-gain amplifier, and the amplification occurs in a single pass in one long (or several short) undulator [61]. High-gain FELs are the only solution for wavelengths where no mirrors with sufficient reflectivity are available: such as below 200 nm and down to hard X-rays. There are different types of operation for high-gain FELs: the *self-amplified spontaneous emission (SASE)* and the external *seeding* are two of them. In seeding, an external coherent source is used as an input field. In SASE, there is no input field, and instead, the spontaneous emission of the electrons is used as a seed, and as a result, quasi-coherent x-rays can be produced. Another option is to start with no input field but with a pre-bunched electron beam. Finally, it is possible to have high-gain oscillators, which are usually referred to as *Regenerative Amplifier FELs (RAFELs)* [62, 63].

A significant difference compared to low-gain FELs is the *microbunching* structures in an electron bunch that are imprinted as it travels along the undulators. These structures are longitudinal density modulations that appear because of the energy exchange between electrons and light wave: the electrons that gain energy are more rigid to the magnetic field of the undulator compared to those losing energy to the wave. This causes a longitudinal velocity modulation which in turn, results in density modulations around the maximum light amplification positions with a periodicity of one resonant wavelength. The individual microbunches radiate coherently and the power grows exponentially until *saturation* is achieved.

Following, we discuss the 1D theory of high-gain FELs and we consider an input field, whose amplitude is changing along z. We need to consider on top of the Pendulum equations derived for the FEL (see Eq. 2.32 and 2.33) the fact that there are density modulations described by the current density $\mathbf{j}$ and the electric charge density ρ, and the fact that the electric field amplitude of the light wave is not constant. This slightly changes the initial electric field we assumed in Eq. 2.26 to:

$$\Upsilon_x(z,t) = \widetilde{\Upsilon}_x(z)\cos\left(k_l z - \omega_l t\right). \tag{2.35}$$

We use the 1D approximation of the wave equation and the slowly varying envelope approximation (SVA) in which we assume that the amplitude $\widetilde{\Upsilon}_x(z)$ varies very slowly along z and within one undulator period λ_u. As initial condition we assume a uniform density distribution (a DC current characterized by ρ_0 and j_0). A gradual density modulation induced by the interaction with the light wave is described by the charge and current density, respectively:

$$\widetilde{\rho}(\psi,z) = \rho_0 + \widetilde{\rho}_1(z)\exp(i\psi) \tag{2.36a}$$

$$\widetilde{j}(\psi,z) = j_0 + \widetilde{j}_1(z)\exp(i\psi). \tag{2.36b}$$

We get the complete set of coupled first-order equations for the one-dimensional approach of a high-gain FEL for a monoenergetic and on resonance electron beam [55]:

$$\frac{d\psi_\kappa}{dz} = 2k_u\eta_\kappa, \tag{2.37a}$$

$$\frac{d\eta_\kappa}{dz} = -\frac{e}{m_e c^2\gamma_r}\Re\left\{\left(\frac{\widehat{K}\widetilde{\Upsilon}_x}{2\gamma_r} - \widetilde{j}_1\cdot\frac{i\mu_0 c^2}{\omega_l}\right)\exp(i\psi_\kappa)\right\} \tag{2.37b}$$

$$\widetilde{j}_1 = j_0\frac{2}{N}\sum_{\kappa=1}^{N}\exp(-i\psi_\kappa) \tag{2.37c}$$

$$\frac{d\widetilde{\Upsilon}_x}{dz} = -\frac{\mu_0 c\widehat{K}}{4\gamma_r}\cdot\widetilde{j}_1 \tag{2.37d}$$

We use μ_0 for the permeability of free space, and κ for each electron in one longitudinal slice of length λ_l that contains N electrons, each of them characterized by a ponderomotive phase ψ_κ. The two Equations 2.37a and 2.37b are equivalent to the pendulum equations we derived earlier for the low gain FEL. Equation 2.37b includes the electric field amplitude growth, and an additional term that is related to the space charge field that arises due to the density modulation $\widetilde{j}_1$ of Eq. 2.37c.

This way, Eq. 2.37c expresses the modulation current that is developed and that drives the field amplification shown in Eq. 2.37d. Overall, these equations describe the FEL process as follows: the radiation drives energy modulation, the energy modulation drives the density modulation, and finally, the bunching is responsible for the field amplitude growth. Equations 2.37 are a set of 2N+2 number of equations that cannot be solved analytically. To obtain an analytical solution, we make the assumption that the periodic density modulation is small, we can exclude ψ_κ and η_κ for the characterization of the particle dynamics and we solve only the differential equation of the field amplitude evolution. After a number of mathematical operations [19] we get the *third order differential equation of the high-gain FEL*:

$$\frac{\widetilde{Y}'''_x}{\Gamma^3} + 2i\frac{\eta}{\rho_{\mathrm{FEL}}}\frac{\widetilde{Y}''_x}{\Gamma^2} + \left(\frac{k_P^2}{\Gamma^2} - \left(\frac{\eta}{\rho_{\mathrm{FEL}}}\right)^2\right)\frac{\widetilde{Y}'_x}{\Gamma} - i\widetilde{Y}_x = 0. \tag{2.38}$$

Here, we have the new coefficient Γ defined as the gain parameter, and the space charge parameter k_P:

$$\Gamma = \left[\frac{\mu_0 \widehat{K}^2 e^2 k_u n_e}{4\gamma_r^3 m_e}\right]^{1/3}, \tag{2.39}$$

$$k_P = \sqrt{\frac{2k_u \mu_0 n_e e^2 c}{\gamma_r m_e \omega_l}}. \tag{2.40}$$

A fundamental scaling parameter of great importance for FELs is the Pierce parameter [55]:

$$\rho_{\mathrm{FEL}} = \left[\frac{1}{8\pi}\frac{I_{\mathrm{peak}}}{I_A}\left(\frac{\widehat{K}}{1+K^2/2}\right)^2\frac{\gamma\lambda_l^2}{2\pi\sigma_x^2}\right]^{1/3}, \tag{2.41}$$

where $I_A = 17\,\mathrm{kA}$ is the Alfvén current. The Pierce parameter actually characterizes most of the properties in a high-gain FEL. It determines the *power gain length*, $L_{\mathrm{g}0}$, obtained in the 1D theory for a mono-energetic beam and excluding space charge forces:

$$L_{\mathrm{g}0} = \frac{\lambda_u}{4\pi\sqrt{3}\rho_{\mathrm{FEL}}}. \tag{2.42}$$

It expresses the distance over which the power grows by a factor of e. The FEL parameter is a good indication of the natural FEL bandwidth of the high-gain FEL amplifier.

Solving Eq. 2.38 for the case where the FEL is seeded by an external field leads to the solution:

$$\widetilde{Y}_x = \frac{Y_{\mathrm{in}}}{3}\left[\exp((i+\sqrt{3})\Gamma z/2) + \exp((i-\sqrt{3})\Gamma z/2) + \exp(-i\Gamma z)\right]. \tag{2.43}$$

Out of these three terms, the second and third terms describe an exponentially decaying mode and an oscillating mode, respectively, but are insignificant compared to the first term while z increases. The two oscillatory terms are only important for roughly the first two gain lengths in an undulator, a regime often called the *lethargy regime* where the field amplitude remains constant. The FEL process in this regime can be considered identical to the low-gain FEL discussed in the previous section. The first term, describes exponential growth instead. After these two gain lengths, the exponential gain dominates the process and the power grows as:

$$P = \frac{P_0}{9} \exp(z/L_{g0}). \tag{2.44}$$

After roughly 20 gain lengths the region of *saturation* is reached. There, the resonance condition is no longer satisfied as the electrons' energy has been reduced due to the energy transfer. In the FEL phase space, the electrons start moving to a region where they gain energy and as a result the energy is transferred back and forth between the electron bunch and the light wave. This results in an oscillatory behaviour of the power along the undulators. The FEL saturation power depends on the electron beam power:

$$P_{\text{beam}} = \frac{\gamma_r m_e c^2 I_{\text{peak}}}{e}, \tag{2.45}$$

and the efficiency with which the beam power is converted into FEL power is determined by the FEL parameter:

$$P_{\text{sat}} = 1.6 \rho_{\text{FEL}} P_{\text{beam}}. \tag{2.46}$$

The lethargy and the exponential regime of an FEL are often called the *linear regime* of an FEL and can be well described by the third-order FEL equation of Eq. 2.38, while the saturation regime is often described as the *non-linear regime* of the FEL and for its study it is essential to use the coupled equations of Eq. 2.37.

Self-amplified spontaneous emission (SASE)

SASE has been the main method used in high-gain FELs in the past decades to generate FEL light of a wavelength that spans in a range that goes down to Ångström. In SASE, the seed is the incoherent and spontaneous undulator radiation emitted in the first gain lengths. Despite this difference, the behaviour of the FEL in the exponential regime and in saturation is still valid in this case. The Eq. 2.44 still holds true by replacing the input power with the effective noise, which is inversely proportional to the number of electrons in one coherence length [55]. The saturation is reached after roughly 20 gain lengths.

For SASE, the longitudinal cooperation length is defined as $l_c = \lambda_r/(4\pi\rho_{\text{FEL}})$ and expresses the length over which the electrons emit coherently, therefore it is the slippage per gain length. Typically, several cooperation lengths exist within the electron bunch length, so several individual spikes occur in the longitudinal structure of the output FEL. The separation between the spikes is approximately $2\pi l_c$ and therefore, the number of longitudinal modes observed in the frequency domain is $M_f = l_{\text{bunch}}/2\pi l_c$.

Ming-Xie correction for 3D effects

While the discussion of a 3D model for FELs is cumbersome, and we usually use sophisticated numerical simulation codes such as Genesis 1.3 [64] and GINGER [65] for this purpose, here I briefly mention the effects that should be taken into account when moving from the 1D theory to a more accurate calculation. In particular, the electron bunch is described by an energy spread, finite transverse dimensions, an emittance and betatron oscillations along z. In addition, the co-propagating field diverges due to diffraction effects. Based on these effects, Ming-Xie defined some useful three dimensional parameters:

$$\begin{aligned} X_\gamma &= \frac{L_{\mathrm{g}0} 4\pi\sigma_\delta}{\lambda_u} && \text{(2.47a)} \\ X_d &= \frac{L_{\mathrm{g}0}\lambda_l}{4\pi\sigma_r^2} && \text{(2.47b)} \\ X_\varepsilon &= \frac{L_{\mathrm{g}0} 4\pi\varepsilon}{\beta_{\mathrm{avg}}\lambda_l}, && \text{(2.47c)} \end{aligned}$$

where σ_δ is the energy spread relative to the energy and σ_r is transverse rms size of the light beam. The parameters X_γ, X_d and X_ε correct for energy spread, diffraction and emittance effects, respectively. Based on them, a correcting factor $\zeta < 1$ can be calculated which leads to a more realistic gain length $L_g = L_{g0}/\zeta$, and saturation power $P'_{\mathrm{sat}} = \zeta^2 P_{\mathrm{sat}}$ (longer gain length and lower saturation power) [19, 66, 67].

2.4 Seeding theory

So far we have studied the cases where the FEL process is initiated by the spontaneous undulator radiation or an external coherent radiation field that considerably exceeds the shot noise, while the electrons are randomly distributed longitudinally within the bunch. We are going to discuss a different method now: there is no external coherent input field, but the electron bunch is already pre-bunched at the resonant wavelength. The bunching can be achieved by different methods in preparation stages as it will be discussed in the following sections. The most common external seeding methods that take advantage of a pre-bunched electron bunch are the high-gain harmonic generation (HGHG) [24, 68] and the echo-enabled harmonic generation (EEHG) [25, 26].

Independently of the method with which we achieve bunching, we consider a pre-bunched electron bunch and no external laser source for the final amplification. We can quantify the longitudinal density modulation with the bunching factor that is the Fourier component of the density modulation with the resonant wavelength. It can be calculated as a phase average:

$$b_n = \langle e^{-in\psi} \rangle, \tag{2.48}$$

where n is the harmonic number. A pre-bunched electron bunch leads to coherent radiation that evolves as [66]:

$$P_{\mathrm{coh}}(z) = \frac{1}{3}\rho_{\mathrm{FEL}} |b|^2 P_{\mathrm{beam}} \left(\frac{z}{L_g}\right)^2. \tag{2.49}$$

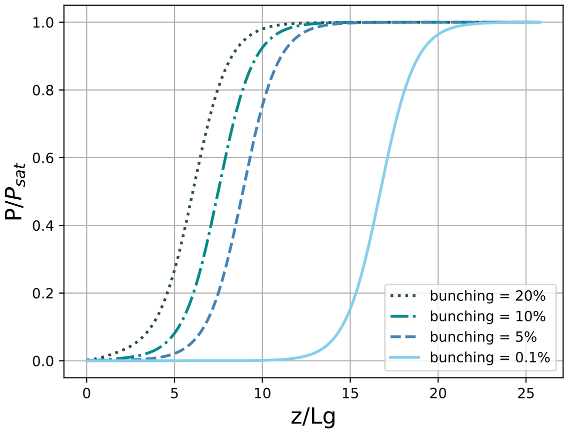

FIGURE 2.6: The power gain curves are demonstrated for different initial bunching factor based on Eq. 2.50. I show the power normalized to the power saturation and the distance z along the undulators normalized to the power gain length.

There is a threshold up to which this equation of quadratic growth is valid. At the transition point, the power is equal to $P_{\text{th}} = \rho_{\text{FEL}}|b|^2 P_{\text{beam}}$. After this transition point, exponential growth takes place as:

$$P(z) = P_{\text{th}} \left[\frac{\frac{1}{3}\left(\frac{z}{L_g}\right)^2}{1+\frac{1}{3}\left(\frac{z}{L_g}\right)^2} + \frac{\frac{1}{2}\exp\left[\frac{z}{L_g} - \sqrt{3}\right]}{1+\frac{P_{th}}{2P^*_{\text{sat}}}\exp\left[\frac{z}{L_g} - \sqrt{3}\right]} \right], \tag{2.50}$$

where $P^*_{\text{sat}} = P_{\text{sat}} - P_{\text{th}}$. In Fig. 2.6, Eq. 2.50 is used to demonstrate the gain curves for a different initial bunching factor. It can be seen that the higher the initial bunching, the faster the saturation is reached. However, the saturation power is always the same. The case of a bunching factor of 0.1% is in the order of shot noise and represents the SASE case. The exact bunching factor in SASE depends on the electron beam parameters and saturation is reached after 20 gain lengths as expected. Seeding methods like HGHG and EEHG are by default deterministic processes and as a result not only highly coherent output FEL pulses are expected, but also highly stable pulses since there are no inherit shot to shot fluctuations expected. This feature is of great importance for energy-resolved experiments.

2.4.1 High-Gain Harmonic Generation

One of the simplest seeding schemes that is based on the amplification of a pre-bunched electron bunch and harmonic conversion is the high-gain harmonic generation, introduced by Yu in 1991 [24, 68]. In HGHG, an external seed laser with a power that exceeds the electron beam shot noise is injected at the entrance of a short undulator. The seed laser overlaps temporally and spatially with the electron bunch along the undulator, which is resonant with the seed laser wavelength. The undulator encodes the phase and amplitude information of the seed laser onto the longitudinal phase space of the electron beam. It results in a sinusoidally energy-modulated electron bunch distribution along the longitudinal axis with a periodicity equal to the seed laser wavelength. For this reason, the undulator is called a *modulator* (see Fig. 2.7) and is typically around two gain lengths long.

The seed laser power has to exceed the shot noise power of the electron beam to eliminate the SASE case. Recalling the theory of a high-gain FEL starting with an external field, based on Eq. 2.44 only one ninth of the input seed laser power is contributing to the exponential growth and on top of this consideration that is based on 1D theory, there is also a reduced contribution due to the transverse coupling [69]. Since the ratio between the two powers determines the contrast between the seeded and the shot noise intensity, it is reasonable to maintain a difference of at least two orders of magnitude. The shot noise power is [66]:

$$P_{\text{shot}} = 3\rho_{\text{FEL}}^2 \omega_r \gamma_r mc^2. \tag{2.51}$$

For typical high-gain FEL parameters it varies around hundreds of Watts to tens of kilowatts. For shorter wavelengths the shot noise power increases, and so do the difficulties in finding high power seed laser sources, making the generation of short wavelengths with external seeding techniques difficult. Commonly used seed laser sources in external seeding are in the ultraviolet (UV) and visible wavelength range, since they are the shortest-wavelength sources that can provide the relatively high powers and stability required at reasonable repetition rates of 10 Hz, for instance.

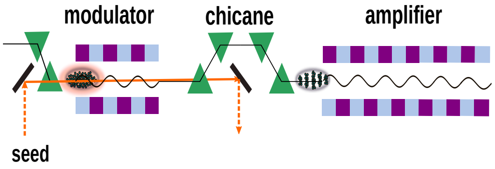

FIGURE 2.7: A simple schematic view of an HGHG setup: the seed laser and electron bunch overlap in the modulator, then the electron bunch continues in the chicane where the bunching is obtained and finally, the pre-bunched electron bunch enters the amplifier to generate radiation at a harmonic of the seed laser wavelength.

A seed laser of power P_{in} and a radius waist w_0 induces an energy modulation ΔE [70]:

$$\Delta E = \sqrt{\frac{P_{\text{in}}}{P_o}} \frac{m_e 2K L_{\text{mod}} \text{JJ}}{\gamma w_0}, \tag{2.52}$$

where $P_0 \approx 8.7\,\text{GW}$, $\text{JJ} = J_0(\xi) - J_1(\xi)$, where $\xi = K^2/(4+2K^2)$ and $J_{0,1}$ the Bessel function of the zeroth and first order and L_{mod} is the modulator length. This result is based on the assumption that the modulator is relatively short and the diffraction and slippage effects do not play an important role. Since this is not always the case in the results presented in this thesis, we consider the case where a longer modulator is employed. In that case, we can no longer ignore the diffraction, the slippage and the power growth since we expand the operation to the exponential power gain regime. In a systematic study of [71], it is shown that for modulators longer than three power gain lengths, the optical field gain should be taken into account. In the case of a modulator $L_{\text{mod}} < 5.2L_g$, an equivalent modulator length can be used in Eq. 2.52:

$$L_{\text{eq}} = L_{\text{mod}} \sqrt{1 + \frac{1}{16} \left(\frac{L_{\text{mod}}}{3.2 L_g} \right)}. \tag{2.53}$$

This correction becomes important for $L_{\text{mod}} > 3.2L_g$. An alternative way to see this correction is to use an equivalent power. Then, instead of the input power P_{in} of

Eq. 2.52 the equivalent power, $P_{\mathrm{eq}} = P_{0.63L_{\mathrm{mod}}}$, so the power established after two thirds of the modulator length, can be used. For longer modulators than 5.2 gain lengths, the exponential growth of Eq. 2.38 is dominant and a higher equivalent power is appropriate [71]. However, this case is not studied further in this thesis.

The energy modulation induced by the interaction with the seed laser can, alternatively, be expressed as an induced energy spread [68]:

$$\Delta E = \sqrt{2}\sqrt{\sigma_E'^2 - \sigma_E^2}\,, \tag{2.54}$$

with σ_E being the uncorrelated energy spread of the electron bunch before the modulator and σ_E' the total energy spread after traversing the modulator. For seeding methods, it is useful to refer to the normalized energy modulation (energy modulation relative to the energy spread) [72]:

$$A = \frac{\Delta E}{\sigma_E}. \tag{2.55}$$

The energy modulation is later converted into a density modulation in a dispersive section of strength R_{56} with a normalized dispersion of [72]:

$$B = \frac{R_{56} k_{\mathrm{seed}} \sigma_E}{E}, \tag{2.56}$$

where E is the reference energy of the electrons and k_{seed} the wavenumber of the seed laser. This density modulation can be easily understood with the bunch compression already discussed. Instead of a macroscopic energy chirp h, the energy modulated electron bunch is described by microscopic energy chirps with a periodicity of the seed laser wavelength. Based on this correlation of the energy and the longitudinal position, the final position z_f of each particle will change from the initial one z_i when passing through a dispersive section of $R_{56} \neq 0$ according to Eq. 2.16. For appropriate choices of energy modulation and R_{56} microbunches are created. These microbunches correspond to current peaks that are equally spaced longitudinally as shown in Fig. 2.8. These current density modulation can be quantified by the bunching factor. In HGHG, the bunching factor of the n-th harmonic can be written as [72]:

$$b_n = |J_n(nAB)| \exp(-\frac{1}{2}n^2B^2) \tag{2.57}$$

where J_n is the n-th Bessel function of its first kind. After achieving the wanted density modulation, the electrons enter an undulator, called a radiator or an amplifier, which is tuned to the desired harmonic of the seed laser wavelength and coherent radiation is generated based on Eq. 2.50.

Another interesting property of the FEL output is its pulse duration, which depends strongly on the seed laser pulse duration σ_ζ in the common case of a shorter seed laser pulse compared to the electron bunch. There is a natural shortening of the FEL pulse when harmonic conversion is involved. In addition, based on [73], the bunching profile affects greatly the pulse characteristics of output FEL. When the argument of the Bessel function of Eq. 2.57, $\chi_n(A,B) = -nAB$, maximizes the Bessel function at $\chi_n^{\max}$, the pulse duration of the FEL, $\sigma_\zeta^{\mathrm{FEL}}$, of the harmonic n will scale with the seed laser pulse duration σ_ζ as:

$$\sigma_\zeta^{\mathrm{FEL}} = \frac{\sigma_\zeta}{\sqrt{n}} \tag{2.58}$$

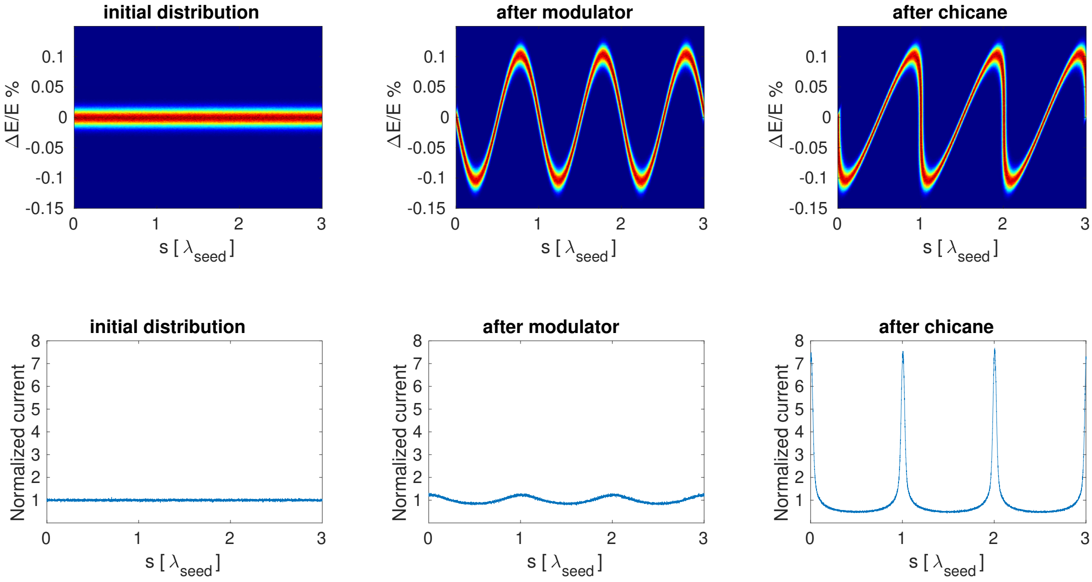

FIGURE 2.8: Electron bunch distribution in the longitudinal phase space (first row) and the related longitudinal current distribution (second row) for an HGHG scheme initially, after the modulator and after the chicane (see Fig. 2.7). The current is normalized to the initial peak current of the electron bunch.

For an argument of the Bessel function that does not maximize it, $\chi_n \neq \chi_n^{\max}$, the scaling is expected to be:

$$\sigma_\zeta^{\mathrm{FEL}} = \frac{6\sigma_\zeta}{7n^{1/3}} \tag{2.59}$$

Increasing the argument of the Bessel function $\chi_n > \chi_{\max}$ would lead to a splitting of the pulse, also informally referred to as *overbunching*.

A single-stage HGHG is limited in the harmonic conversion that can be achieved [26], because two contradicting requirements are posed on the energy spread. For sufficient HGHG bunching the contribution of the exponential term of Eq. 2.57 should be minimized by setting $B \approx 1/n$ while the Bessel function should be maximized. This occurs when $\chi_n \approx n$, which results in the condition $A \approx n$ for the required energy modulation. On the other hand, for exponential amplification in the amplifier the condition $\sigma'_E/E \ll \rho_{\mathrm{FEL}}$ should be satisfied. This means, that there is a trade between the modulation amplitudes that one can achieve for a given initial energy spread. For typical high-gain seeded FEL parameters (around 100 keV uncorrelated energy spread or more and ρ_{FEL} in the order of $10^{-4} - 10^{-3}$), the HGHG scheme is limited to harmonics up to roughly $n = 15$. The dependence of the bunching on the energy modulation and R_{56} is shown in Fig. 2.9, where it is clear that higher harmonics require larger energy modulation and a as a result, a larger induced energy spread. These bunching maps are very useful for the optimization of the HGHG tuning parameters which are the energy modulation and the strength of the chicane.

One solution to achieve shorter wavelengths is to minimize the uncorrelated energy spread [74]. However, the minimum energy spread is limited by space charge effects in the gun and also it is increased in bunch compressors and therefore, it cannot be tuned freely to achieve shorter wavelengths. Another solution would be to

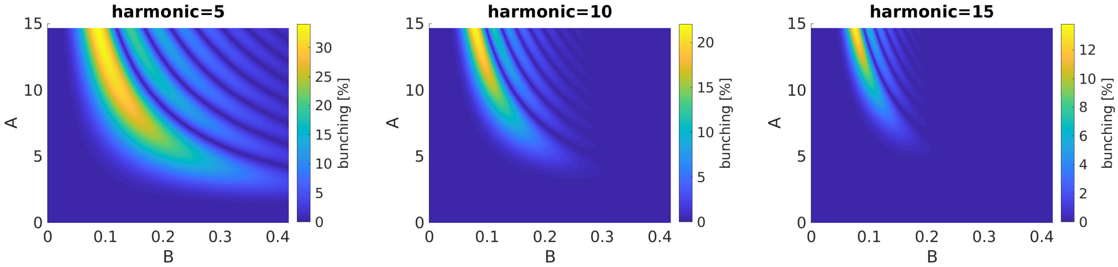

FIGURE 2.9: Bunching maps calculated according to Eq. 2.57 for different harmonics. For this example, typical electron beam parameters of $\sigma_E/E = 10^{-4}$ are used.

use shorter-wavelength seed laser sources, but this is also not an easy task and as already mentioned, the requirements on seed laser power requirements, stability and repetition rate are strict. It is essential to use an alternative scheme to HGHG that can obtain bunching at high harmonics with less energy modulation. The cascaded HGHG (or fresh bunch technique) [75] is one of them, however, its implementation is quite demanding on the electron bunch parameters, the several stages of harmonic conversion can degrade the temporal coherence of the output pulse [76] and the output wavelength can only be a multiple of the harmonics of the two or more individual stages. A widely used alternative scheme for generation of high harmonic is the echo-enabled harmonic generation (EEHG) [25] and it will be briefly introduced later in this section.

2.4.2 The optical klystron

Optical klystrons were first introduced in 1977 [40] to enhance the gain of an oscillator FEL driven by a storage ring, while later, they were used in several other facilities [77, 78]. Their contribution to FELs is significant, yet their working principle is rather simple. An optical klystron consists of (at least) two undulator sections separated by a dispersive section, like a chicane. It is possible to induce an energy modulation before the chicane with or without an external field and use it in a chicane to speed up the process of creating longitudinal density modulations. This way, coherent emission is possible downstream from the chicane and the gain process can be considerably enhanced. More recently, it was used in high-gain FELs in SASE mode to reduce the power gain lengths required to reach saturation. Without the optical klystron, saturation in hard x-rays would require hundreds of meters of undulators. One or more stages of optical klystrons can be used to speed up the FEL process and reduce the saturation length [79]. It is usually efficient to tune all undulators at the same resonance, however there exists a reported example of using subharmonics [80]. A schematic view of an optical klystron is seen in Fig. 2.10. The phase space manipulation is explained with Fig. 2.11.

The optical klystron can be seen as a similar process to HGHG. The difference is that in the first modulator the energy modulation is expected to be much smaller than the one in HGHG and that there is (most of the times) no harmonic conversion.

We can calculate the power gain G_{OK} close to the optimal conditions to enhance the gain and for a cold beam in 1D approach [80]:

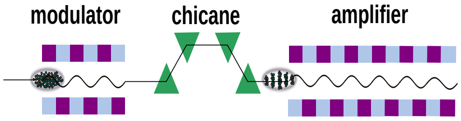

FIGURE 2.10: In the simplest case, the optical klystron consists of two undulators separated by a chicane. The chicane converts the energy modulation induced in the first undulator into a density modulation. This results in increased gain in the second undulator.

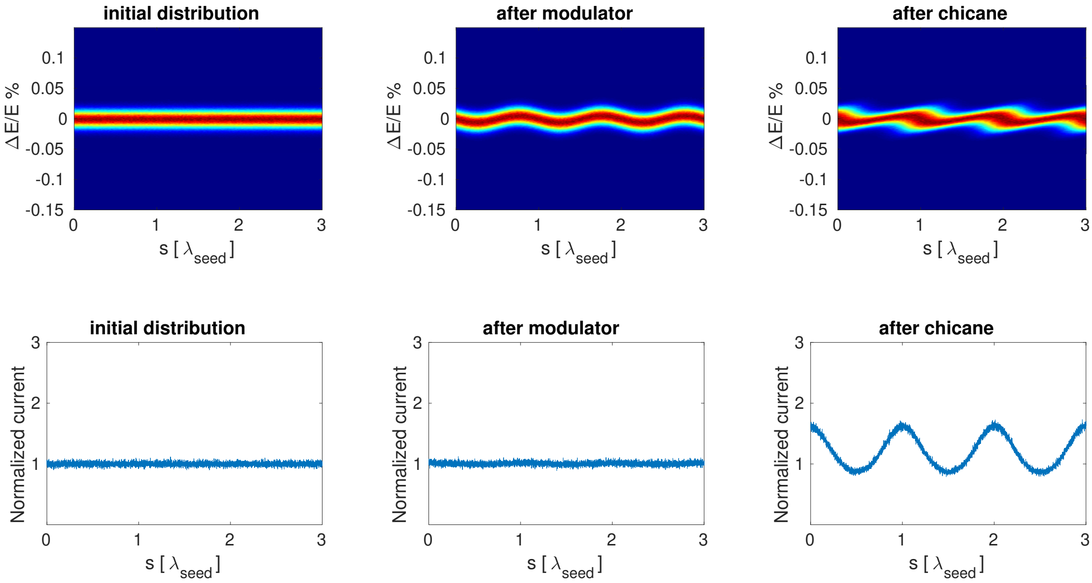

FIGURE 2.11: Electron bunch distribution in the longitudinal phase space (first row) and the corresponding longitudinal current distribution (second row) for an optical klystron scheme initially, after the modulator and after the chicane (see Fig. 2.7). The current is normalized to the initial peak current of the electron bunch.

$$G_{\mathrm{OK}} \approx \frac{1}{9}[5 + D^2 \exp(-D^2\sigma_\delta^2/\rho_{\mathrm{FEL}}^2) + 2\sqrt{3}D \exp(-D^2\sigma_\delta^2/(2\rho_{\mathrm{FEL}}^2))], \tag{2.60}$$

where $D = k_r R_{56} \rho_{\mathrm{FEL}}$ and $\sigma_\delta = \sigma_E/E$ is the relative energy spread. The function shown in Eq. 2.60 is maximised for $D = \rho_{\mathrm{FEL}}/\sigma_\delta$, so when $R_{56} k_r \sigma_\delta = 1$. We get the optimum R_{56}:

$$R_{56} = \frac{\lambda_r}{2\pi\sigma_\delta}. \tag{2.61}$$

It is essential to remember that $\sigma_\delta \ll \rho_{\mathrm{FEL}}$ and to notice the dependence of the optimal performance on the relative uncorrelated energy spread shown in Eq. 2.60. The smaller the uncorrelated energy spread, the higher the gain in Eq. 2.60. These results, however, are only valid when the energy modulation induced before the dispersive section is small, and in the order of the intrinsic energy spread.

For a better understanding, we can consider here the bunching formula of HGHG from Eq. 2.57 that we can rewrite less condensed for the fundamental wavelength as:

$$b_1 = |J_1\left(-R_{56}k_r\frac{\Delta E}{E}\right)|\exp(-\frac{1}{2}\sigma_\delta^2 k_r^2 R_{56}^2) \tag{2.62}$$

For a relatively small energy modulation, the exponential term contribution dominates, and a maximum bunching occurs for $\sigma_\delta k_r R_{56} \approx 1$, in agreement with Eq. 2.61. On the contrary, when the energy modulation becomes significant in comparison with the uncorrelated energy spread, the Bessel function becomes important and maximum bunching occurs at $\frac{\Delta E}{E}k_r R_{56} \approx 1.85$ [80]. Thus, for a larger energy modulation, the optimum R_{56} becomes smaller. It is interesting that apart from oscillator and SASE applications, it has recently been proposed to be exploited in a seeding scheme [81, 82]. In this case the interest is not related to a faster saturation, but the main goal is to obtain the needed energy modulation for seeding with less seed laser power. This case will be further discussed in Chapter 3.

Apart from the already discussed advantages of using an optical klystron it has been reported that it relaxes the emittance requirements [79] and when the R_{56} of the chicane is comparable to the coherence length, it acts as a phase shifter and it can lead to power oscillations that depend on the relative phase between the electron bunch and the light wave [79] that can actually be used to extract the coherence length [83]. Finally, it can be used to calculate the energy spread [84, 85] due to the strong dependence of its performance on this property.

2.4.3 Echo-Enabled Harmonic Generation

The EEHG scheme has proved useful to obtain short wavelengths down to a few nm and stable output FEL and it was proposed by G. Stupakov in 2009 [25, 26]. EEHG aims at overcoming the hurdle of the strong dependence of the bunching at high harmonics on the induced energy spread. This is done in two different stages and each stage employs a modulator followed by a chicane and two separate seed lasers. For the first stage and after the energy modulation in the modulator (characterized by an energy modulation A_1) induced by the first seed laser (seed 1), a relatively strong chicane (characterized by a dispersive strength B_1) often in the order of several mm of $R_{56,1}$ is necessary. This strength is responsible for the over-rotation of the electron distribution in the longitudinal phase as shown in Fig. 2.13. Each horizontal stripe shown in the figure after chicane 1 has a small energy spread. This way, it is possible in the second stage to implement a process equivalent to HGHG (characterized by an energy modulation A_2 and a dispersive strength B_2), with the difference that in this case higher harmonic density modulation can be achieved with reasonable energy modulations, typically $A \ll 10$ induced by the second seed laser (seed 2). As a result, while in HGHG the bunching factor decays exponentially as n^2 with the harmonic number, in EEHG it scales with $m^{-1/3}$ [25] (typically $m = n + 1$ as it will be discussed later in this section) when optimized and high harmonics in the order of ∼100 can be achieved [36]. A schematic view of EEHG is shown in Fig. 2.13.

It is possible to use two seed lasers of different wavelengths, each of them characterized by a wavenumber k_1 and k_2 ($K_{\text{seed}} = k_2/k_1$). The wavenumber of the density modulation after chicane 2 is $k_E = ak_1 + mk_2$, where a is an integer number, typically negative and small, and m is a typically positive and large integer. The two integers determine the harmonic $n = m + a$. For EEHG, the bunching of the nth harmonic is typically maximized at $a = -1$ and can be calculated as follows:

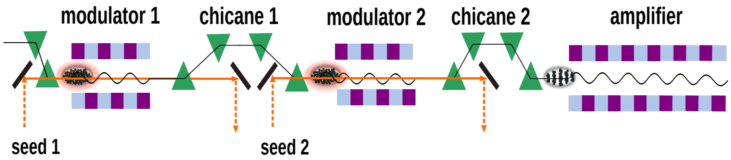

FIGURE 2.12: In an EEHG scheme two seed lasers are needed in the two modulators, each of them followed by a chicane. At the amplifier a high harmonic of the seed laser wavelength can be amplified.

$$\begin{aligned} b_{a,m} = &\,|\exp(-\frac{1}{2}(aB_1 + (K_{\text{seed}}m + a)B_2)^2) \\ &\times J_m(-(K_{\text{seed}}m + a)A_2B_2)J_a(-A_1(aB_1 + (K_{\text{seed}}m + a)B_2))|. \end{aligned} \tag{2.63}$$

In addition to the advantage of extending the wavelength range to shorter wavelengths, EEHG is typically more stable than HGHG in terms of wavelength and pulse energy stability and is reported to be less affected by a linear and nonlinear energy chirp [86, 87, 88]. However, the fragile structure of the narrowly separated bands in the longitudinal phase space and the strong first chicane required are making the bunch more susceptible to collective effects, such as the intrabeam scattering (IBS), the incoherent synchrotron radiation (IS) and the CSR [26, 89, 90, 91]. Even with this very efficient in harmonic conversion method, the harmonic number seems to be limited to a maximum of roughly 100. With the current seed lasers available and suitable for seeding this limits us to wavelengths >2 nm (currently shown down to 2.6 nm [36]). In order to access shorter wavelengths, it is an immediate need to propose different methods.

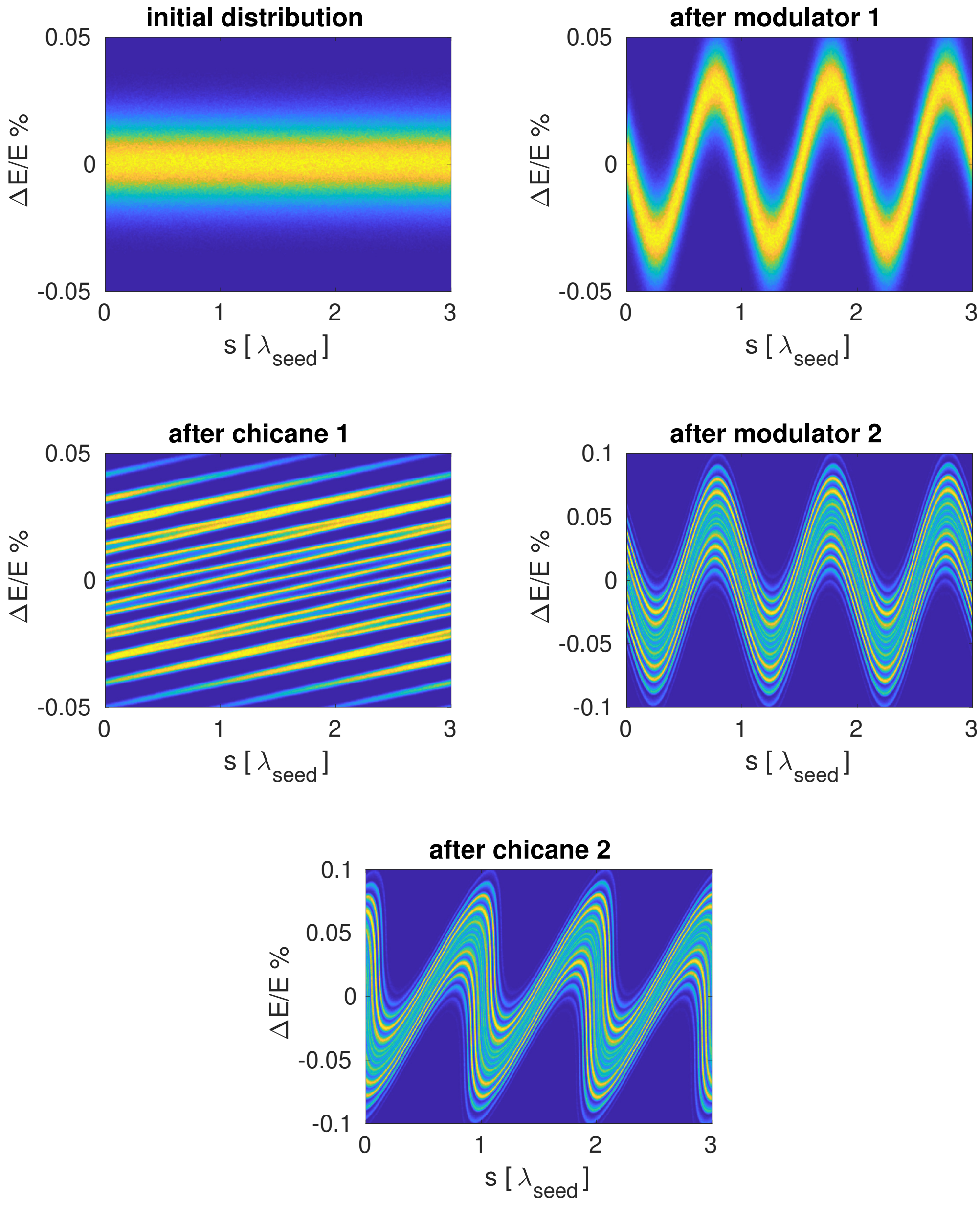

FIGURE 2.13: Electron bunch distribution in the longitudinal phase space for an EEHG scheme. The longitudinal phase space is shown initially, after the first modulator, after the first chicane, after the second modulator and finally, after the second chicane (see Fig. 2.12). Please notice the vertical axis range change in the longitudinal phase space. The longitudinal density can be seen in Fig. 2.14

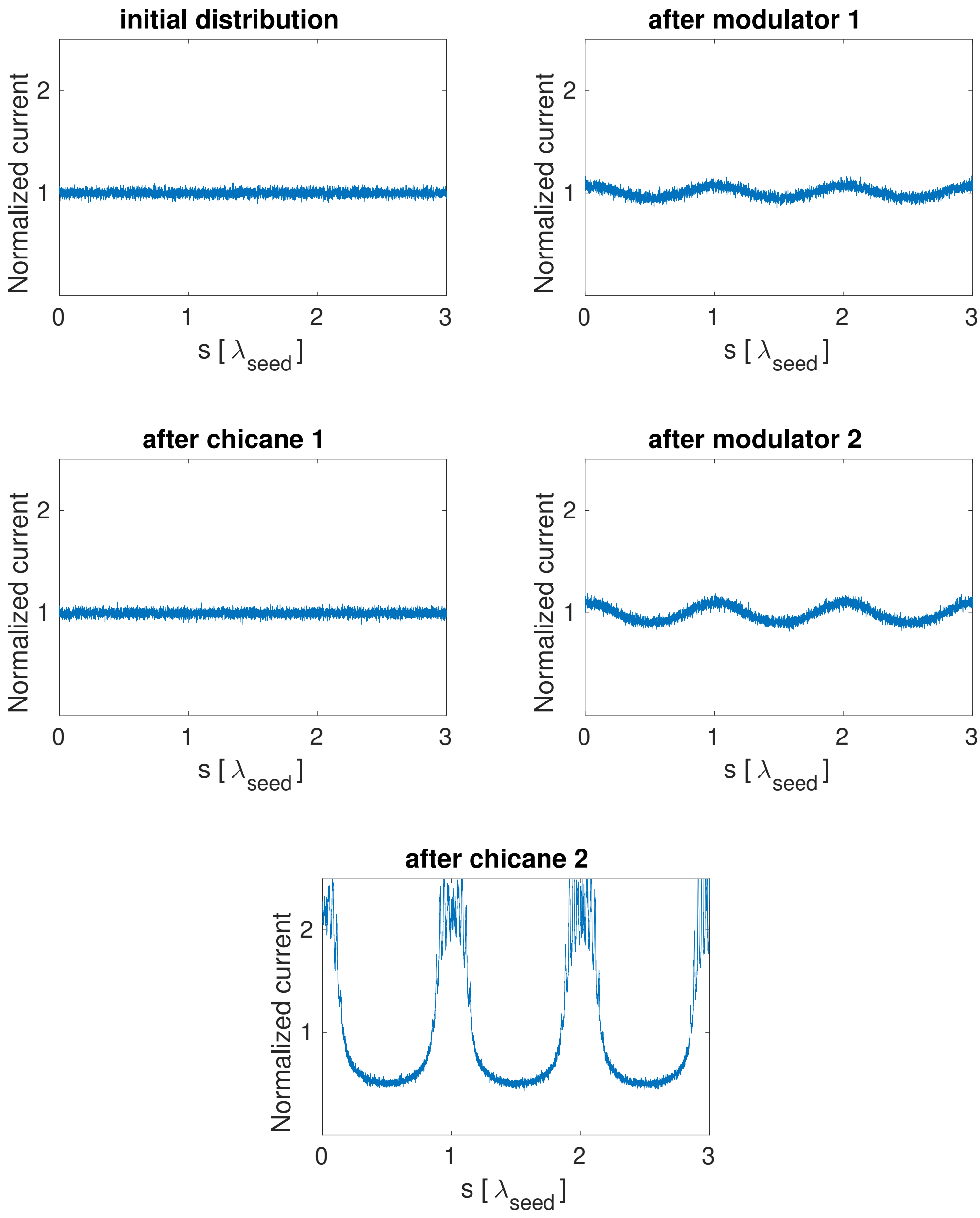

FIGURE 2.14: Longitudinal current distribution for an EEHG scheme. The longitudinal phase space is shown initially, after the first modulator, after the first chicane, after the second modulator and finally, after the second chicane (see Fig. 2.12). The current is normalized to the initial peak current of the electron bunch. The electron density corresponds to the plots of the longitudinal phase space of Fig. 2.13

2.5 Gaussian Optics

2.5.1 Beam properties and propagation

The description of Gaussian beams and their properties is useful not only for the description of the FEL light, but also for the seed laser beams used in seeding techniques. Even though it is an ideal beam, it serves as a good approximation for our case. This subsection is based on the sources [19, 70, 92]. Gaussian beams are a solution of the paraxial Helmholtz equation. For paraxial waves, the variation of the envelope on the longitudinal plane is very small in the scale of one wavelength and hence, it is negligible compared to the transverse oscillations. This equation results in a family of transverse electromagnetic modes (TEM), and the Gaussian beam is the lowest order of the solutions of this equation, also known as the TEM_{00} mode, and its intensity distribution is a Gaussian in both transverse planes. Its wavefronts are approximated as planar close to the waist, and as spherical further away from the waist. A Gaussian beam can be described by its complex amplitude $U(r)$:

$$U(r) = \underbrace{A_0 \frac{w_0}{w(z)} \exp\left(-\frac{r^2}{w^2(z)}\right)}_{\text{Amplitude terms}} \underbrace{\exp\left(-ikz - ik\frac{r^2}{2R_{curv}(z)} + i\zeta(z)\right)}_{\text{Phase terms}}, \tag{2.64}$$

where r is the radial position, which can be associated with the Cartesian coordinates (x, y) as $r^2 = x^2 + y^2$, R_{curv} is the radius of curvature of the wavefront, k is the wavenumber $k = 2\pi/\lambda$ and $\zeta = \arctan(z/z_R)$ is the Gouy phase shift. The smallest radius of a Gaussian beam occurs at the focal point and is called the waist, w_0. Its diameter is referred to as the spot size. A common definition of the waist is the beam radius in which the intensity is larger than $1/e^2$, or 13.5%, of the on axis intensity.

The diffraction of the light results in a transverse spread of the waves when it propagates and the waist radius w depends on the propagation distance from the focal point:

$$w(z) = w_0\sqrt{1 + (z/z_R)^2}, \tag{2.65}$$

where z_R is the Rayleigh length:

$$z_R = \frac{\pi w_0^2}{\lambda}, \tag{2.66}$$

which expresses the distance over which the beam radius spreads by a factor $\sqrt{2}$ and the intensity is halved. At distances $z \gg z_R$, the beam size starts increasing linearly with the distance as $w(z) = w_0 z/z_R$ and at this limit, we define the divergence as the angle associated with this expansion:

$$\theta \simeq tan\theta = \frac{w_0}{z_R} = \frac{\lambda}{\pi w_0}. \tag{2.67}$$

As can be seen in Eq. 2.67, for shorter wavelengths and larger spot sizes the divergence is smaller. The divergence is an important property of the FEL light, because it affects the transportation of the output FEL from the undulators to the experimental hall. Calculating the divergence range for the FEL wavelength range is important in order to arrange the beampipe diameter and the maximum intensity that the optics involved in this transportation of the FEL light can withstand.

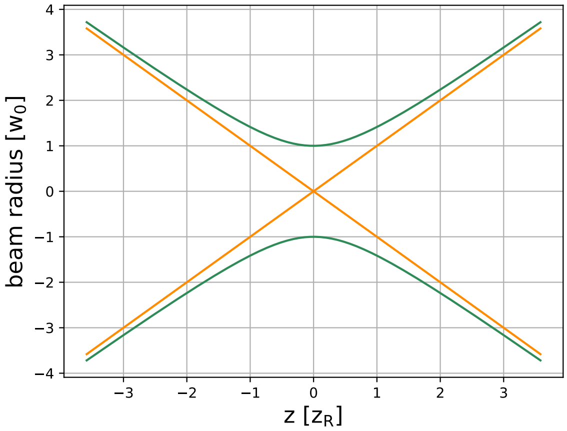

FIGURE 2.15: Beam size evolution for an ideal Gaussian beam. The green lines show the evolution based on Eq. 2.65 and the orange ones define the divergence angle based on Eq. 2.67. The transverse size is normalized to the waist size at focus, and the distance from the focus is normalized to the Rayleigh length.

In the far field, the wavefronts are spherical and the waist scales linearly with z instead. The curvature R_{curv} that the wavefronts acquire at a distance z is defined as:

$$R_{curv}(z) = z\left(1 + \left(\frac{\pi w_0^2}{\lambda z}\right)\right). \tag{2.68}$$

The maximum intensity is on axis ($r = 0$, $z = 0$) and is defined as I_0, and the power of the beam is the integral of the intensity over both transverse planes and therefore [92]:

$$P = \frac{1}{2} I_0 (\pi w_o^2). \tag{2.69}$$

The intensity drops when going off axis, and can be calculated as the square modulus of the complex amplitude, $I(r) = |U(r)|^2$, so from Eq. 2.64 we get:

$$I(r,z) = I_0 \left(\frac{w_0}{w_0(z)}\right)^2 \exp\left(\frac{-2r^2}{w^2(z)}\right). \tag{2.70}$$

Another important property of the Gaussian beam is its phase, which was first introduced in Eq. 2.64:

$$\phi(r,z) = kz - \zeta(z) + \frac{kr^2}{2R_{curv}(z)}. \tag{2.71}$$

The first term refers to the plane wave, while the Gouy phase shift $\zeta(z) = \arctan(z/z_R)$ expresses the additional retardation that Gaussian waves experience in comparison with plane waves. Because of it, a $-\pi$ phase shift occurs at the focus. Finally, the last term of Eq. 2.71 is related to the wavefront bending, thus for $r = 0$ it also goes to zero.

In order to demonstrate these properties of Gaussian beams, here we take a closer look into an example of the propagation of a Gaussian beam along z in Fig. 2.15 and I show how the beam radius increases (Eq. 2.65) and the angle defined by the divergence (Eq. 2.67). For distances $\Delta z \gg z_R$ the beam radius asymptotically approaches the cone of angle that represents the divergence.

Since the Gaussian beam is an idealized beam and all lasers essentially deviate from this model, one can define the M^2 factor as:

$$M^2 = \frac{w_0' \cdot \theta'}{w_0 \cdot \theta} = \frac{w_0' \cdot \theta'}{\lambda/\pi}, \tag{2.72}$$

which is the ratio of the waist diameter-divergence product of the under evaluation beam and the waist diameter divergence product of a Gaussian beam [92]. It is a quality factor that describes the degree of deviation of a laser beam from an ideal Gaussian beam. Since Gaussian beams experience the smallest divergence possible, in all other cases $M^2 > 1$.

2.5.2 Spectral and temporal properties

When interested in temporal and spectral properties of a pulse, it is possible to describe a pulse of a central frequency ω_0 with the complex function

$$U(t) = |A(t)| \exp(i(\omega_0 t + \phi(t))),$$

where $\phi(t)$ is the *temporal phase* and the intensity can be calculated as $I(t) = |U(t)|^2$. We can obtain the complex function in the frequency domain, $V(\nu)$, with a Fourier transformation and calculate the *spectral intensity* as $S(\nu) = |V(\nu)|^2$. The widths of the optical intensity $I(t)$ and spectral intensity $S(\nu)$ determine the pulse width in the time and frequency domain τ_{FWHM} and $\Delta\nu_{\text{FWHM}}$, respectively. Because of the Fourier transformation, these widths are inversely proportional. The pulse's instantaneous angular frequency and frequency are:

$$\begin{aligned} \omega(t) &= \omega_0 + \frac{d\phi}{dt}, \\ \nu(t) &= \nu_0 + \frac{1}{2\pi}\frac{d\phi}{dt}. \end{aligned} \tag{2.73}$$

This means that if the temporal phase is a linear function of time, then the instantaneous frequency will experience a fixed shift in frequency and hence, in wavelength. For a quadratic dependence of the phase on time, we can define a chirp parameter:

$$\alpha = \frac{1}{2}\frac{d^2\phi}{dt^2}. \tag{2.74}$$

A pulse characterized by a temporal phase with a highest order in time being quadratic, is said to be linearly chirped. It is up-chirped and down-chirped for a positive and negative chirp parameter, respectively. This can be seen by using the chirp parameter to calculate the instantaneous angular frequency from Eq. 2.73 as $\omega(t) = \omega_0 + 2\alpha t$. Taking the example of a Gaussian pulse, we can define with the help of the chirp parameter α its complex envelope:

$$A(t) = A_0 \exp(-2\ln 2(t^2/\tau_{\text{FWHM}}^2)) \exp(i(\omega_0 t + \alpha t^2)). \tag{2.75}$$

The FWHM product of this Gaussian pulse is:

$$\tau_{\text{FWHM}} \Delta\nu_{FWHM} = 0.44\sqrt{1+\alpha^2}. \tag{2.76}$$

As a result, the unchirped Gaussian pulse has the smallest time-bandwidth product and is commonly referred to as a *Fourier-transform-limited* pulse. The factor 0.44

is describing Gaussian pulses and for other shapes of pulses this factor should be adjusted.

Depending on the sign of the chirp, it is possible to compress or decompress a pulse, which can be a very useful feature in a group velocity dispersive (GVD) medium. The electron beam together with the undulator can be seen as a GVD medium [93] which adds a small positive chirp. In addition, the electron beam energy chirp can be associated with the chirp of the co-propagating light pulse. A detailed study of the interplay between these three chirps can be found in [93].

2.6 FEL Radiation Properties

Many different ways exist to characterize the output FEL radiation. One of the most useful figures of merit for synchrotron radiation is the *Brightness*. It quantifies the number of photons per second per unit bandwidth and per unit phase space area. It is likely the most important property as it quantifies the radiation quality from many different points of view and there is no optical technique that can further improve the brightness of the FEL radiation. For instance, adding a monochromator can improve the longitudinal coherence but it will reduce the brightness, as the flux will be reduced. Similarly, reducing the vertical size increases the divergence, and adding an aperture decreases the beam size, but it decreases the flux too.

The brightness is calculated as follows:

$$\text{Brightness} = \frac{\Phi}{4\pi^2 \Sigma_x \Sigma_{x'} \Sigma_y \Sigma_{y'}}, \tag{2.77}$$

where Φ is the flux (number of photons per second in 0.1 % bandwidth), $\Sigma_{x/y}$, and $\Sigma_{x'/y'}$ are calculated as the quadratic sum of the electron beam sizes and the photon transverse rms size and divergence, σ_r and $\sigma_{r'}$, respectively:

$$\begin{aligned} \Sigma_{x/y} &= \sqrt{\sigma_{x/y}^2 + \sigma_r^2}, \\ \Sigma_{x'/y'} &= \sqrt{\sigma_{x'/y'}^2 + \sigma_r'^2}. \end{aligned} \tag{2.78}$$

FELs aim at very high peak brightness which typically exceeds the peak brightness of 3rd generation synchrotrons by ten orders of magnitude. The average brightness on the other hand, is the product of the peak brightness, the pulse repetition rate and the pulse duration. The repetition rate of the FEL strongly affects it: normal conducting FELs are usually limited in repetition rates below 100 Hz, while with superconducting technology it is possible to reach repetition rates of several MHz and increase the average brightness by several orders of magnitude.

Breaking down how to achieve high brightness, we focus on the so called *longitudinal coherence*. In a nutshell, it describes the phase correlation of two individual longitudinal points. One way to quantify the longitudinal coherence is to compare the resulting bandwidth to the bandwidth of the transform-limited case that corresponds to the pulse duration measured. Another way to quantify the longitudinal coherence is to calculate the coherence degree with a normalized auto-correlation function [94]:

$$G_{\text{longitudinal}} = \frac{\langle U(t) U^*(t-\tau) \rangle}{\sqrt{\langle |U(t)|^2 \rangle \langle |U(t-\tau)|^2 \rangle}}. \tag{2.79}$$

The range of it is expected to be between 0 and 1. It is also possible to understand the degree of longitudinal coherence held by a pulse by comparing its pulse duration with the coherence time defined earlier in the chapter and is more intuitive. Experimentally, the longitudinal coherence is typically measured with a Michelson interferometer [95, 96]. While for SASE FELs the longitudinal coherence degree is typically very low due to the different longitudinal modes of the output FEL, with seeding the longitudinal coherence is expected to reach the optimum and is typically compared with the Fourier transform limit.

The *transverse coherence* (or spatial coherence) is also an important property of the light that is naturally achieved in free-electron lasers. It describes the degree of correlation of the phase of the wave at two different positions in the transverse plane (r_1 and r_2). Initially in the FEL process, the transverse coherence degree is very low and different modes exist. During the FEL process, diffraction effects take place, but are fortunately counteracted by the *gain guiding*, which describes the effect of the selective amplification of the central part of the co-propagating field which overlaps with the area of high electron density of the bunch. This effect in combination with the diffraction of the co-propagating field that naturally happens lead to *mode selection* and high degree of transverse coherence in FELs. It is possible to quantify the transverse coherence by calculating the transverse coherence degree [94] in a similar way as Eq. 2.79:

$$G_{\text{transverse}} = \frac{\langle U(r_1)U^*(r_2)\rangle}{\sqrt{\langle |U(r_1)|^2\rangle \langle |U(r_2)|^2\rangle}}. \tag{2.80}$$

Even with SASE, the transverse coherence degree exceeds 90% at the end of the linear regime. Deeper in saturation, higher order modes progress and reach saturation with the result of a decreased transverse coherence. The quality of the transverse profile of the beam can also be described by another figure of merit, the M^2 which was already introduced. Experimentally, it is easy to measure the coherence degree with the Young's double slit experiment [97], or ptychography [98].

For FELs and since the fundamental Gaussian mode dominates towards saturation, the electron beam dimensions in Eq. 2.77 are not important and we can rewrite the brightness as Brightness $= 4\Phi/\lambda_r$ [19].

Chapter 3

HGHG seeding with an optical klystron

3.1 High repetition rate seeded FEL with an optical klystron in high-gain harmonic generation

In this chapter, I present simulation results that show the benefits of the addition of an optical klystron [40] in an HGHG [24, 68] seeded beamline. The simulations of the following publication are based on the parameters of the FLASH2020+ project. This project refers to the upgrade of the FLASH FEL at DESY, Hamburg. FLASH was the first FEL to operate in the XUV/soft x-ray spectral regime and has been providing SASE radiation as a user facility since 2005 [10]. One of the unique characteristics of FLASH is the high repetition rate that can be achieved thanks to the linear accelerator that is based on superconducting radiofrequency (RF) technology. FLASH currently provides up to 5000 SASE photon pulses per second to user experiments (up to 1 MHz bursts with a length of up to 0.8 ms at 10 Hz serving two beamlines simultaneously). The upgrade aims at energy upgrade up to 1.35 GeV and a parallel operation of the two beamlines with: high repetition rate externally seeded beamline with new variable gap undulators (FLASH1 beamline), and advanced FEL schemes providing shorter pulses of variable polarization (FLASH2 beamline). A high repetition rate externally seeded beamline requires great efforts to develop a seed laser system that would supply sufficient peak power in burst mode of operation at 100 kHz to 1 MHz. This high repetition rate demands a compromise on the tuning range of the seed laser that is currently foreseen between 297-317 nm. This upgrade will establish FLASH as the first user facility providing high repetition rate seeded FEL.

Following, we consider adding an optical klystron to an HGHG seeding scheme using the parameters of FLASH2020+ in the simulation. The proposal is complementary to the upgrade plans of FLASH and is aiming at relaxing the very demanding requirements posed on the seed laser R&D efforts for FLASH2020+. The study serves as an example applied to the case of FLASH but addresses more facilities. For FELs based on burst mode of operation, the goal is to include the optical klystron and allow seeded operation at their full repetition rate with the additional aid of a reduced requirement on the peak power of the seed laser. For continuous-wave (CW) machines, the requirements on the seed laser repetition rate are even more demanding. While at FLASH a burst mode at 1 MHz requires 5000 seed laser pulses per second for seeding at the full repetition rate, CW machines of 1 MHz require 1 million seed laser pulses, increasing the power density per second by more than two orders of magnitude. An important limitation in the repetition rate of seed lasers arises from the optics involved and the power density they can withstand. This limits the combination of peak power and repetition rate that is accessible and one can trade the one for the other. Since the peak power required in seeding schemes was not negotiable in the past, an increased repetition rate had not been possible so far.

Reducing the seed laser power can be used not only for increasing the repetition rate but also as a feature that allows other types of seed laser sources to be used. In particular, the possible use of HHG sources as a seed would be a game-changer. The main current limitation is that state-of-the-art sources of this type provide powers that are not yet well within the needs of HGHG and EEHG. The advantage of using these sources is that since schemes like HGHG and EEHG are wavelength-limited mainly as a consequence of being harmonic-limited, it will be possible to reach shorter wavelengths at the same harmonic number. The other way around, when wavelengths in the region of 4 nm are achieved as the 70th harmonic of a UV seed laser, they will now be achieved as the 12th harmonic, for instance. In addition, since phase errors and degradation of the bandwidth is increasing with increasing harmonic number [99], this will result in pulses that are closer to the transform limit.

The theoretical background of the optical klystron was introduced in Section 2.4.2. The simulated optical klystron based HGHG scheme utilizes a seed laser of 300 nm. For the simulations, the Genesis 1.3 simulation code, introduced in Appendix A, has been used. We consider a seed laser with a power that induces an energy modulation comparable to the uncorrelated energy spread in the first modulator and as a result, the chicane of the optical klystron is optimized based on Eq. 2.61. After the first modulator the seed laser is out-coupled as it does not play any role in the process anymore. The publication focuses on the 15th harmonic of the seed laser wavelength, which is the upper limit for our parameters in HGHG. We compare a few different sets of parameters (nominal, higher current, longer modulator) to show the dependence of the optical klystron on them. We show that in an optimized setup it is possible to reduce the seed laser power by more than three orders of magnitude and still obtain the same bunching at the harmonic of the seed laser wavelength. We also investigate the sensitivity of the optical klystron on seed laser power jitter and finally, we show results on its sensitivity to the initial shot noise. The manuscript was published in the peer-reviewed journal *Physical Review Accelerators and Beams*. Additional simulation results and considerations are presented in Appendix B.1.

PHYSICAL REVIEW ACCELERATORS AND BEAMS **24,** 120701 (2021)

High repetition rate seeded free electron laser with an optical klystron in high-gain harmonic generation

Georgia Paraskaki,[*] Enrico Allaria, and Evgeny Schneidmiller
Deutsches Elektronen-Synchrotron DESY, Notkestraße 85, 22607 Hamburg, Germany

Wolfgang Hillert
University of Hamburg, Luruper Chaussee 149, 22761 Hamburg, Germany

(Received 26 August 2021; accepted 23 November 2021; published 14 December 2021)

Many high-gain free electron lasers worldwide are planning to incorporate seeding setups into their day-to-day operation. These techniques provide both longitudinal and transverse coherence and extended control of the output free electron laser radiation spectral properties. However, the output wavelength and repetition rate strongly depend on the properties of the seed laser system. With the laser peak power required for successful seeded operation, it is currently not possible to increase their repetition rate to an extent that it matches the electron bunch repetition rate of superconducting accelerators. Here, we investigate the advantages of a modification of standard seeding setups, by combining the seeding with the so-called optical klystron. With this new seeding setup, it is possible to decrease the seed laser power requirements and therefore, seed laser systems can increase their repetition rate at the same wavelength. We show simulation results in a high-gain harmonic generation (HGHG) setup for a range of harmonics (8th to 15th) and we verify the reduction of seed laser power required with an Optical Klystron HGHG scheme. Finally, we comment on the stability of the proposed setup to jitter sources and to shot-to-shot fluctuations and compare to the standard HGHG scheme.

DOI: 10.1103/PhysRevAccelBeams.24.120701

I. INTRODUCTION

High-gain free electron lasers (FELs) have been delivering light characterized by high brightness and wavelength tunability to user experiments for more than a decade [1,2]. At the same time, scientists push the limits in many directions to improve the available flux, the control, and the spectral quality of the output FEL radiation. An interesting milestone to be reached in the near future is to generate stable, fully coherent pulses at high-repetition rate. High repetition rate has been possible with superconducting linacs since 2005, when FLASH started operating at 1 MHz in burst mode [3]. The European X-ray free electron laser (XFEL) is also a burst-mode FEL operating at 4.5 MHz since 2017 [4], while SHINE [5] and LCLS-II [6] aim to be the first continuous wave FELs at 1 MHz.

Even though there is currently no standard method to provide fully coherent pulses at these repetition rates, there has been ongoing research the last decades to increase the repetition rate of fully coherent pulses with a particular interest in oscillator-based solutions. The oscillator can be used either as part of a multistage scheme that is combined with harmonic conversion [7–10] or as a direct source of radiation. The latter oscillator FELs are based on x-ray cavities which provide short wavelengths with full coherence and high repetition rate [11–16].

Self-amplified spontaneous emission (SASE) [17] is one of the standard methods in high-gain FELs to deliver light to experiments. It offers a wide range of wavelength tunability down to hard x rays [18–21] and with high repetition rate [2,4], but it suffers from intrinsic limitations. The output longitudinal coherence of the FEL radiation is poor, as a result of the stochastic initiation of the FEL process, which also leads to shot-to-shot fluctuations of other output FEL pulse properties.

Techniques such as the self-seeding [22–24] and external seeding [25–27] are implemented to improve the longitudinal coherence. Self-seeding has been successfully demonstrated down to the hard x-ray regime with the generation of narrow and single line spectra. However, the shot-to-shot intensity stability still suffers from the SASE fluctuations, and the high repetition rate is challenging due to the heat load of the crystals used [28]. With external seeding techniques, like the echo-enabled harmonic generation (EEHG) [27,29,30] and high-gain harmonic generation (HGHG) [25,31], an external seed laser source is

---

[*] georgia.paraskaki@desy.de

Published by the American Physical Society under the terms of the Creative Commons Attribution 4.0 International license. Further distribution of this work must maintain attribution to the author(s) and the published article's title, journal citation, and DOI.

used to prepare the electron bunches to emit coherently at a harmonic of the seed laser wavelength at the final amplification stage. These methods ensure both longitudinal coherence and shot-to-shot reproducibility and have allowed a great number of interesting experiments to become reality [32–34]. However, the dependence of the output FEL on the seed laser properties comes with a few downsides too, as it limits the shortest wavelength and the highest repetition rate possible.

The most common choices of seed laser systems for external seeding is in the ultraviolet (UV) wavelength range [29,30,35]. These systems offer sufficient pulse energies, wavelength and energy stability with fs duration, and wavelength tunability. Shorter wavelength seed laser systems, such as high-order harmonics generated in gas (HHG) [36], have been used in few direct seeding experiments [37,38] and in harmonic conversion as well [39,40], but have resulted to be unsuitable for user facilities due to the lack of peak power and flexibility. Currently, a conversion of up to two orders of magnitude in wavelength can be foreseen with the most efficient seeding method for this purpose, EEHG. Practically, this limits the shortest wavelength to the soft x-ray regime. At the same time, the UV seed lasers that are currently used for seeding are available at repetition rates of several tens of Hz. The highly demanding parameters at higher repetition rates are not easily achievable, and one of the main limitations is the heat loading due to the peak powers they operate at. As a result, when electron bunches are available at MHz repetition rate, hundreds of thousands of electron bunches remain unused due to the lack of seed laser systems operating at the same repetition rate.

Here, we study in detail an alternative setup that can bridge this gap. This setup is based on the optical klystron (OK) scheme that was first introduced in Ref. [41], and was combined with external seeding only recently [42,43]. An OK can be used in combination with external seeding schemes to reduce the requirements in seed laser power. Our studies show that an optimized setup for this configuration can reduce the power requirements for the seed laser up to a factor of more than one thousand under certain conditions. At the same time, we show that even with a low-seed laser power it is possible to preserve the coherence of the output FEL on a shot-to-shot basis, thus significantly extending the previously reported results [42]. Since the heat load of laser systems is proportional to pulse energy and repetition rate, one can be traded for the other, allowing for higher repetition rate systems with current technology.

Additionally, by using shorter wavelength seed lasers that are available only at lower peak power, the OK-HGHG scheme allows an extension of the tuning range toward shorter wavelengths with respect to the single-stage HGHG scheme. Concerning the implementation of the OK-HGHG scheme, an advantage of this setup is that for facilities designed for EEHG, such as the new FLASH1 beamline proposed in the FLASH2020+ project [44], the existing setup is already sufficient and the OK-HGHG seeding can be implemented with no modifications. Finally, it was recently proposed that an OK-HGHG scheme can take advantage of the energy modulation induced in a dipole with the interaction of the laser beam and electron bunch [45]. A few additional considerations on increasing the repetition rate of seeded FELs can be found in Ref. [46] and an analytical study on several methods that have been proposed for high repetition rate seeded FEL can be found in Ref. [47].

In the following Sec. II, we introduce the OK-HGHG setup. To better understand the opportunities and limitations of the scheme, in Sec. III we simulate an OK-HGHG setup and we investigate the bunching mechanism and its stability to shot-to-shot jitter sources, in comparison with the standard HGHG seeding scheme. In Sec. IV, we select the 15th harmonic of a 300 nm seed laser wavelength and we optimize and present the output FEL. Finally, we discuss the impact of the lower signal to noise ratio on the shot-to-shot stability.

II. MODIFYING AN HGHG SETUP TO INCLUDE AN OPTICAL KLYSTRON

In a standard HGHG setup, an external seed laser source, a short undulator (modulator), a dispersive section, such as a chicane, and a longer undulator (amplifier) are required, as shown in Fig. 1. One seed laser pulse should be injected for each electron bunch, and together they interact along the modulator which is typically around two power gain lengths long. As a result of their interaction, the energy of the electron bunch is sinusoidally modulated in the longitudinal axis with a periodicity of a seed laser wavelength (λ_{seed}). The chicane converts the energy modulation into a longitudinal density modulation. We quantify this density modulation with the so-called bunching factor b_{h} of a harmonic h, defined as

$$b_{\text{h}} = |J_{\text{h}}(-hAB)| \exp\left(-\frac{1}{2}h^2B^2\right), \tag{1}$$

where A is the relative energy modulation, defined as the ratio of the amplitude of the energy modulation ΔE with respect to the uncorrelated energy spread σ_E, and B is the relative dispersive strength of the chicane, $B = 2\pi R_{56}\sigma_E/(\lambda_{\text{seed}}E)$, where E is the electron beam mean energy and R_{56}

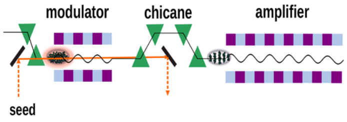

FIG. 1. In a standard HGHG setup, we need one modulator followed by a chicane, before the final FEL amplification at the amplifier. The amplifier is tuned to a harmonic of the seed laser wavelength.

is the longitudinal dispersion of the chicane. Finally, J_h is the Bessel function of the first kind.

For a large B the exponential decay of Eq. (1) minimizes the bunching. As a result, in order to obtain sufficient bunching at a harmonic of the seed laser, a large A is required, and usually we take $A \simeq h$ for the harmonic number h. At the same time, the amplification process in the amplifier depends on the energy spread of the electron bunch upstream from the amplifier (σ'_E) relative to the electron beam energy and should not exceed the FEL parameter ρ [17] upstream from the amplifier, which is typically in the order of 10^{-4}–10^{-3}. For an energy-modulated electron beam, this means that $(\sqrt{\sigma_E'^2 + \Delta E^2/2})/E < \rho$. With a single-stage HGHG, we are typically limited to a highest harmonic of 15, and this number strongly depends on the energy spread of the electron beam [48]. For harmonics up to the 15th, the amplitude of the energy modulation downstream from the modulator is expected to be roughly 5–15 times the uncorrelated energy spread. For typical EUV FEL parameters and since the energy modulation is proportional to the square root of the seed laser power $A \propto \sqrt{P_{\mathrm{seed}}}$ [49], this means that the seed laser power at the modulator should be tens to hundreds of MW. When sufficient bunching is obtained in the order of a few percent, the individual electron microbunches emit radiation in sync at the amplifier downstream and fully coherent radiation at a harmonic of the seed laser wavelength is amplified.

We can reduce the seed laser power requirements with the addition of the OK, as shown in Fig. 2. Optical klystrons have been a useful tool for FELs since the 1970s [41], and have been widely used for gain control in oscillator FELs [50], for energy spread measurements, and to reduce the saturation length in SASE [51–53].

In the case of an OK-HGHG setup, as shown in Fig. 2, we need a seed laser source of a peak power that can induce a low-energy modulation of one to two times the uncorrelated energy spread after traversing the first modulator. Based on Ref. [53], if that is the case, then an optimization according to Eq. (3) is appropriate. This is normally not sufficient for seeding schemes and the generation of higher harmonics, but it is sufficient to increase the bunching at the fundamental wavelength with the right setting of the first chicane $R_{56,1}$. This way, in modulator 2 we no longer need a seed laser, but the initial energy modulation is self-amplified further to an extent that it can be used to increase the bunching at a harmonic of the seed laser wavelength. The expected approximate gain in energy modulation with an optical klystron is [54]

$$G_A = \frac{A_2}{A_1} \simeq \frac{I \times N}{\gamma \sigma_\delta I_A}, \tag{2}$$

where A_1 and A_2 are the energy modulation after the first and second modulator, respectively, $\sigma_\delta = \sigma_E/E$ where σ_E is the uncorrelated energy spread, I is the peak current, γ is the electron beam energy, N is the number of undulator periods of one segment, and $I_A = 17$ kA is the Alfvén current. For this approximation, a thin beam and low gain in a single undulator are assumed and the effect of the emittance on the velocity spread is neglected.

In this setup, since the energy modulation is relatively low, the longitudinal dispersion of chicane 1 is optimized based on the electron beam energy spread as [51,55,56]

$$R_{56,1} = \frac{\lambda_{\mathrm{seed}}}{2\pi\sigma_\delta}. \tag{3}$$

The longitudinal dispersion of chicane 2 is optimized to increase the bunching at a harmonic of the seed laser wavelength based on Eq. (1).

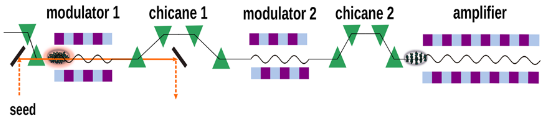

FIG. 2. In an OK-HGHG, we need two pairs of a modulator followed by a chicane. The two modulators are set to the same resonance, chicane 1 is responsible for increasing the bunching at the fundamental wavelength, while chicane 2 is responsible for longitudinal density modulation at a harmonic of the seed laser wavelength. The final FEL amplification of a harmonic of the seed laser wavelength is taking place at the amplifier.

III. GAIN IN SEED LASER POWER WITH AN OPTICAL KLYSTRON

A. Comparing the performance of different setups

In order to verify the benefits of the OK-HGHG, we first looked at the bunching mechanism with single-slice (time-independent) simulations. We used the standard seeding scheme (see Fig. 1), and the one based on an optical klystron (see Fig. 2) to amplify the laser-induced modulation. For this study, we considered the electron beam, seed laser, and undulator parameters shown in Table I. These parameters are typical for EUV FELs and are also used as the basis for the future seeding plans at FLASH1 beamline in the FLASH2020+ upgrade [57]. All simulations shown in this paper were performed with the FEL simulation code GENESIS 1.3, version 4 [58].

The first comparison between the two methods is done by determining the minimum seed laser power required to achieve 8% bunching upstream from the amplifier for different harmonics. This amplitude of bunching is a good trade-off between a higher bunching that requires higher induced energy spread and a lower bunching that increases the saturation length and results in a lower signal to noise ratio. The seed laser wavelength is 300 nm, and we studied the harmonics between the 8th and 15th, thus the output FEL wavelength is between 37.5 nm and 20 nm.

In order to optimize the standard HGHG scheme, we scan the seed laser power and the longitudinal dispersion R_{56} of the chicane. Then, we select the combination of these two parameters with which we can obtain 8% bunching upstream from the amplifier, while the seed laser power (and thus the energy spread upstream from the amplifier σ'_E) is minimum.

For the OK-HGHG, there are three available tuning parameters: the input seed laser power, the strength $R_{56,1}$ and $R_{56,2}$ of the first and second chicane, respectively (see Fig. 2). For low-seed laser power, the optimal setting of $R_{56,1}$ only depends on the electron beam slice energy spread and does not depend on the seed laser properties. Based on Eq. (3), it is set to 482 μm and we keep it constant during our optimization for several harmonics, after verifying that this is the optimal longitudinal dispersion for several cases. Then, we optimize to obtain 8% bunching with minimal energy spread upstream from the amplifier for all harmonics. The remaining available tuning parameters for this purpose are the input seed laser power and the $R_{56,2}$ of the second chicane.

With the OK-HGHG, it is unavoidable to end up with a larger energy spread in order to achieve the same bunching compared to a standard HGHG scheme. This is because, with the OK-HGHG there are two different stages where we rotate the electron bunch distribution in the longitudinal phase space. Due to the intermediate gain, at the end of the second modulator the distribution is not perfectly sinusoidal on the longitudinal axis [Fig. 3(a)] as expected with the standard HGHG setup [Fig. 3(b)]. As a direct consequence, more energy modulation is required to achieve the same bunching. In an equivalent way, the same energy modulation yields smaller bunching for the OK-HGHG.

In Fig. 4, we present the results of this study. In Fig. 4a, we compare the required energy spread upstream from the amplifier (σ'_{E}) to obtain 8% bunching by showing the ratio between the two schemes ($\sigma'_{\mathrm{E,HGHG}}/\sigma'_{\mathrm{E,OK\text{-}HGHG}}$). This way, we capture the anticipated increased energy spread that was demonstrated in Fig. 3. In Fig. 4(b), we show the ratio of the input seed laser power required with the standard HGHG scheme to the input seed laser power required with an OK-HGHG seeding scheme. In the nominal case, we used the parameters shown in Table I, and in all cases, the seed laser power required with the OK-HGHG was 500 to 300 times less than in a standard HGHG setup. The ratio is reduced for higher harmonics, however, even at the highest studied harmonic ($h = 15$), the gain in seed laser power is significant.

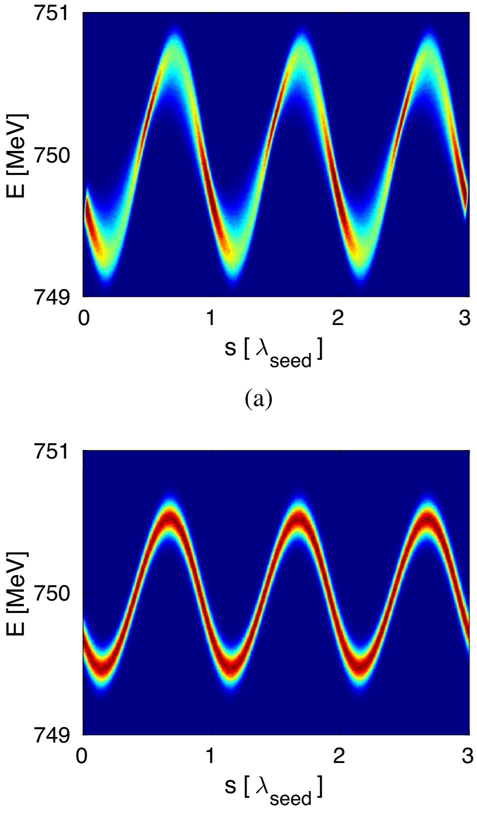

(a)

(b)

FIG. 3. (a) Longitudinal phase space after modulator 2 in an OK-HGHG setup (see Fig. 2). With an $R_{56,2} = 51$ μm, we get $b_{10} = 8\%$. (b) Longitudinal phase space after modulator in a standard HGHG setup (see Fig. 1). With an $R_{56} = 67.25$ μm, we get $b_{10} = 8\%$.

We additionally studied two different configurations to better understand the critical parameters for the OK-HGHG. Initially, we studied the case where the electron beam peak current is increased by 50%, from 500 to 750 A. We assume that the energy spread is increased proportionally during the compression by 50% and is 112.5 keV. The new strength of the first chicane in the OK-HGHG is $R_{56,1} = 318$ μm and it was optimized for the new energy spread value with Eq. (3). In both the OK-HGHG and the standard HGHG setup, the input seed laser power and the strength of the chicane upstream from the amplifier were optimized once more to obtain 8% bunching with the minimum possible seed laser power. The new power ratios are mildly increased, but overall there is no significant difference in the comparison of the two ratios. An increased peak current is directly associated with the decrease of one power gain length (L_{g}), in our case from 0.94 to 0.78 m, thus the ratio of the gain lengths per modulator length (L_{mod}) increases from $L_{\mathrm{mod}}/L_{\mathrm{g}} = 2.6$ to $L_{\mathrm{mod}}/L_{\mathrm{g}} = 3.1$. The increase of the energy spread requires larger energy modulation in both cases. The higher peak current does not significantly affect the gain in the modulator of the standard HGHG setup and the first modulator in the OK-HGHG, since we operate at the lethargy regime. At the second modulator of the OK-HGHG setup, a higher current by itself would allow an increased gain in the second undulator. However, the higher energy spread counteracts this as seen in Eq. (2), and as a result, the ratios are only slightly increased compared to the nominal case.

Finally, we studied a setup with increased modulator length by 20%. This means that the periods of the modulator of the standard HGHG scheme, and of both modulators of the OK-HGHG scheme increased from 30 to 36. This roughly corresponds to an increase of the length of each modulator from 2.48 m to 2.97 m and it directly increases the number of available power gain lengths from $L_{\mathrm{mod}}/L_{\mathrm{g}} = 2.6$ to $L_{\mathrm{mod}}/L_{\mathrm{g}} = 3.2$. For the standard seeding scheme, the energy modulation is increased proportionally with the length of the modulator in a first approximation [59]. With the OK-HGHG, the energy modulation in the first modulator is also increased proportionally to the modulator. However, in this case, we have the additional advantage that the gain is also increased in the second modulator. This led to a power ratio between 1300 and 900 for harmonics between the 8th and 15th as shown in Fig. 4(b), which is significantly increased compared to the previously studied cases. It is worth noticing the essential dependence of the OK setup on the gain lengths. In order for this setup to be beneficial, at least 1.5 to 2 gain lengths are necessary for the second modulator, and the benefits increase strongly when increasing the gain lengths. From Eq. (2) and since $A \propto \sqrt{P_{\mathrm{seed}}}$ [49], the gain in power increases with the square of the undulator periods at low gain. In this last setup studied, the increase of the undulator periods by 25%, more than doubled the gain in power, which implies that there is exponential gain. A few more considerations about the power growth in the second modulator can be found in Ref. [47].

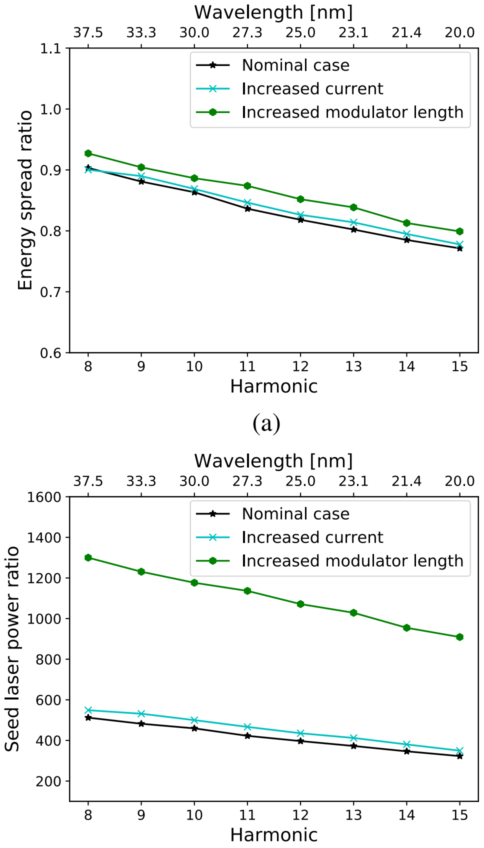

(a)

(b)

FIG. 4. (a) Required energy spread ratio between the two schemes ($\sigma'_{\mathrm{E,HGHG}}/\sigma'_{\mathrm{E,OK\text{-}HGHG}}$) to obtain 8% bunching at different harmonics. In addition to the standard parameters (Table I) also higher peak current and longer undulators are studied. The energy spread (σ'_{E}) is measured upstream from the amplifier. (b) Ratio between the minimum seed laser power required for both schemes ($P_{\mathrm{seed,HGHG}}/P_{\mathrm{seed,OK\text{-}HGHG}}$) to obtain the same bunching for the cases studied in (a).

B. Stability to fluctuations

A significant advantage of seeded FELs is that they generate FEL pulses of great stability which lead to shot-to-shot reproducibility. This is because seeding is a deterministic process, and the large signal to noise ratio eliminates the SASE fluctuations. However, there are still input parameters that fluctuate and that affect the bunching and hence the stability of the output FEL at the amplifier. Here, we investigate the effect of the seed laser power fluctuations and the electron beam compression factor fluctuations which changes both the peak current and the energy spread simultaneously. We compare the impact of these fluctuations on a standard HGHG and on an OK-HGHG setup for the 10th harmonic of a 300 nm seed laser wavelength optimized to obtain 8% bunching, as described in this section. We show the results of this study in Fig. 5.

For the seed laser power fluctuations, once the laser power is optimized, both increasing and decreasing the power causes a decrease of the output bunching, as shown in Fig. 5(a). This bunching decrease is less significant for the OK-HGHG setup, because the energy modulation process only depends partly on the seed laser power which is important for the first modulator. The increase of the amplitude of the energy modulation in the second modulator does not depend anymore on the input seed laser power, and thus the bunching varies less than in a standard seeding HGHG setup. It should be noted that in both cases, a 10% variation of the seed laser power is affecting the bunching by less than 5% and 4% for the standard HGHG and the OK-HGHG setup, respectively.

For the compression factor fluctuations, we change proportionally the peak current and energy spread, while we keep all other parameters constant. In this case as well, the two stages of the OK-HGHG seem to be beneficial for the robustness of the setup. The increased energy spread is naturally affecting the bunching mechanism [see Eq. (1)] for both schemes, however, the increased peak current is only playing a role for the OK-HGHG. In the case of a standard HGHG setup, the modulator is operating at the lethargy regime where the peak current does not play any role on the energy modulation. Therefore, the bunching variation is dominated by the change of the energy spread.

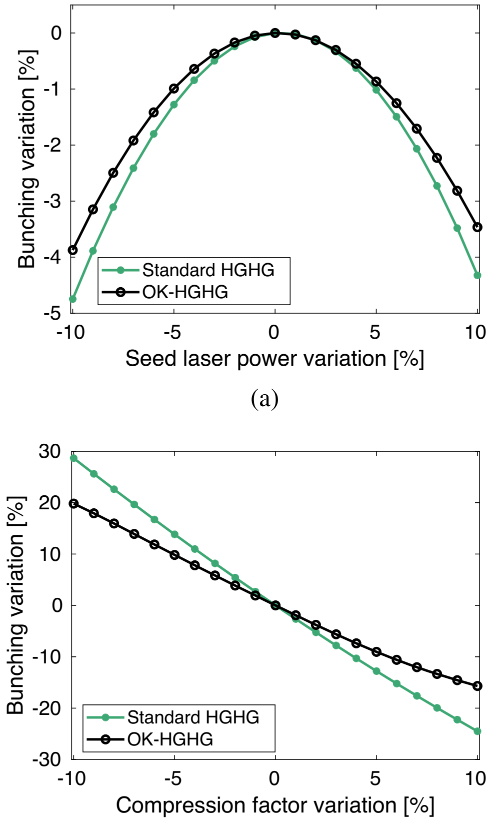

(a)

(b)

FIG. 5. (a) Bunching amplitude response to seed laser power fluctuations for a standard HGHG and an OK-HGHG setup. The nominal seed laser power is 27.7 MW and 54.5 kW for the standard and the OK-HGHG, respectively. (b) Bunching amplitude response to electron beam compression factor fluctuations for a standard HGHG and an OK-HGHG setup. The nominal energy spread and peak current are shown in Table I. They change proportionally when we vary the compression factor.

Instead, the two stages of the optical klystron setup have different responses to the electron beam compression factor fluctuations and thus, its effect on the bunching is milder.

TABLE I. Simulation parameters of the nominal case and for the harmonics between the 8th and 15th harmonic of a 300 nm seed laser wavelength. The seed laser peak power range refers to harmonics between the 8th and 15th. In some simulations, the temporal dependence is not used.

Electron beam	
Energy (E)	750 MeV
Uncorrelated energy spread (σ_E)	75 keV
Current flattop (I)	500 A
Normalized emittance (ϵ_x/ϵ_y)	0.6 mm mrad
Average beta functions (β_x/β_y)	8.4 m/9.8 m
Bunch length (FWHM)	110 fs
Input seed laser	
Wavelength (λ_{seed})	300 nm
rms duration	33 fs
Peak power range (OK-HGHG)	42–265 kW
Peak power range (standard HGHG)	21–85 MW
Waist size	757 μm
Modulator	
Undulator parameter	5.42
Number of periods (N)	30
Undulator period	82.6 mm
Amplifier	
Periods per segment	74
Undulator period	33 mm
Number of segments	4

IV. FEL PERFORMANCE WITH AN OPTICAL KLYSTRON

A. Output FEL

In this section, we show the FEL performance of the OK-HGHG setup in comparison with a standard HGHG setup. We study with three dimensional and time-dependent simulations the performance of one of the most challenging cases; the 15th harmonic of a 300 nm seed laser wavelength, with an output wavelength of 20 nm. At this high harmonic, for an HGHG setup, there are two concerns: (a) the energy spread upstream from the amplifier is relatively high to obtain sufficient bunching and (b) the signal to noise ratio is increased due to the frequency multiplication [60]. The shot noise is expected to contribute quadratically with the harmonic number [61]. Nevertheless, we verified that for our set of parameters the 15th harmonic is still possible and we present here the results.

For both cases, we start with 8% bunching upstream from the amplifier obtained with the minimum possible input seed laser power and we optimize the output FEL separately, in order to get maximum power and good spectral and temporal profile at the end of the amplifier. For both schemes, we follow the same procedure and we optimize the output FEL by fine-tuning the input seed laser power and the undulator parameter of the amplifier, K_{amp}. With this optimization, we keep all amplifier segments tuned at the same resonance and there is no tapering taking place. The simulation parameters used are shown in Table I, while the fine-tuning results in the optimized simulation parameters are shown in Table II. In both cases, the

TABLE II. We list the simulation parameters optimized again for the time-dependent simulations, in addition to the parameters shown in Table I.

	Standard HGHG	OK-HGHG
$R_{56,1}/R_{56,2}$	$-$/38.74 μm	482 μm/32.8 μm
K_{amp}	1.792	1.789
Seed laser power (P_{seed})	61 MW	0.17 MW

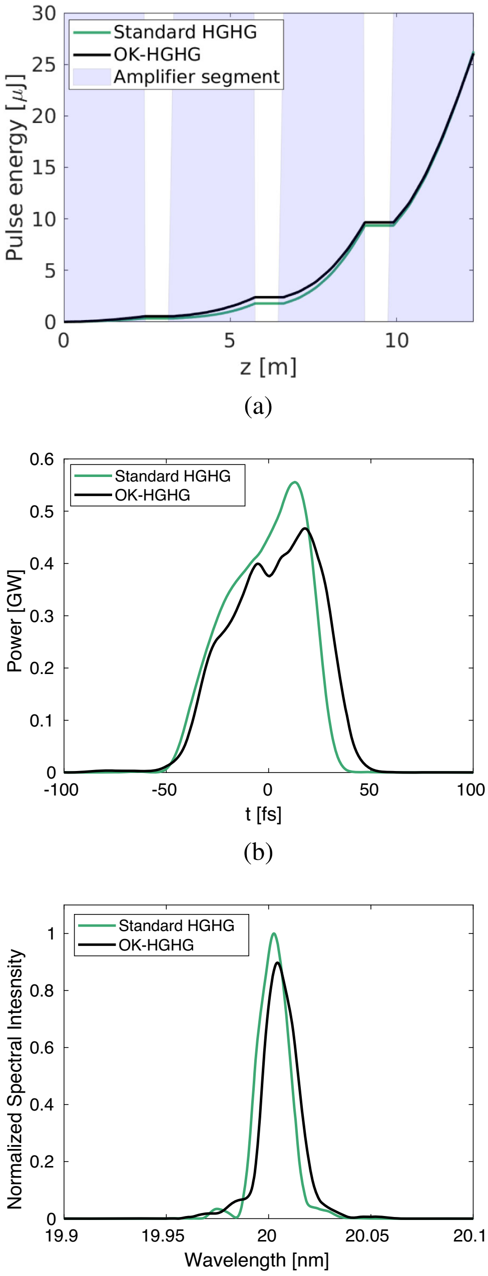

(a)

(b)

(c)

FIG. 6. We compare two fully optimized simulations of a standard HGHG and an OK-HGHG setup for the 15th harmonic of a 300 nm seed laser wavelength. (a) Gain curves in amplifier. (b) Output FEL power profiles. (c) Output FEL spectra normalized to the intensity of the standard HGHG simulation.

obtained bunching at the 15th harmonic after optimization was roughly 7%. Reducing the bunching from 8% to 7% was a result of the optimization and is the consequence of the high gain available within the used length of the amplifier.

The results of the optimization are shown in Fig. 6. The gain curve in the amplifier for both cases is comparable, while the output power profile and spectra after 12.3 m in the amplifier are similar in terms of spectral intensity, bandwidth and power profile. We show in Table III an overview of the pulse properties of the output FEL. The slightly increased pulse duration with the OK-HGHG scheme is justified by the additional slippage in the second modulator.

TABLE III. Comparison of simulation results between a standard HGHG and an OK-HGHG setup. The output wavelength is 20 nm and results as the 15th harmonic of a 300 nm seed laser. The energy spread is calculated upstream from the amplifier.

	Standard HGHG	OK-HGHG
Energy spread at amplifier (σ'_E)	580.9 keV	766.4 keV
FWHM relative bandwidth	9×10^{-4}	9.3×10^{-4}
Pulse energy	26.3 μJ	26 μJ
Pulse duration rms	18.9 fs	21.5 fs
Seed laser power (P_{seed})	61 MW	0.17 MW

B. Shot-to-shot stability

The use of a lower seed laser power in the OK-HGHG setup is expected to decrease the signal to noise ratio because of the shot noise that is unavoidably amplified as well in the amplifier [52,60]. In order to verify the effect of the lower signal to noise ratio, we simulated both schemes several times with different shot noises and we observed if the output FEL is sensitive to this change. As an example study, we use the simulations optimized and discussed above, shown in Fig. 6. We have randomly selected five cases with a different initial shot noise, since larger statistics are computationally time-demanding. For reference, we show in Fig. 7 the SASE background in the temporal domain for these five cases, using the OK-HGHG lattice and the same electron beam parameters, but without a seed laser.

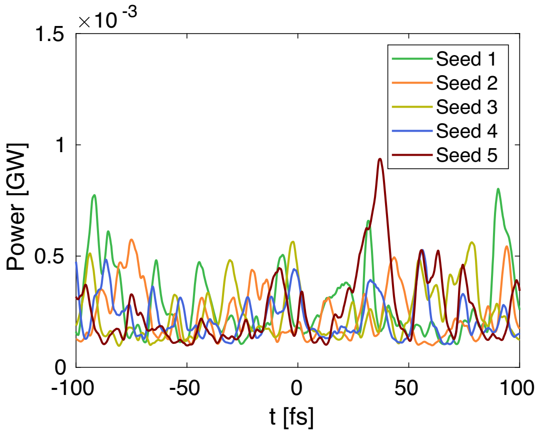

FIG. 7. SASE background in temporal domain for the five initial shot noise cases studied in this section.

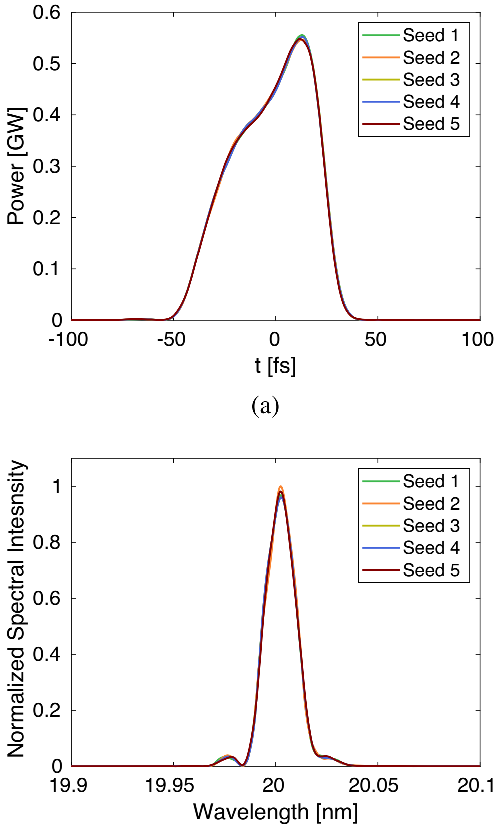

(a)

(b)

FIG. 8. Shot-to-shot fluctuations for a standard HGHG setup, imprinted on the output FEL at 20 nm. (a) Power profile for different initial shot noise. (b) Spectra for different initial shot noise. They are normalized to the highest spectral intensity with Seed 2.

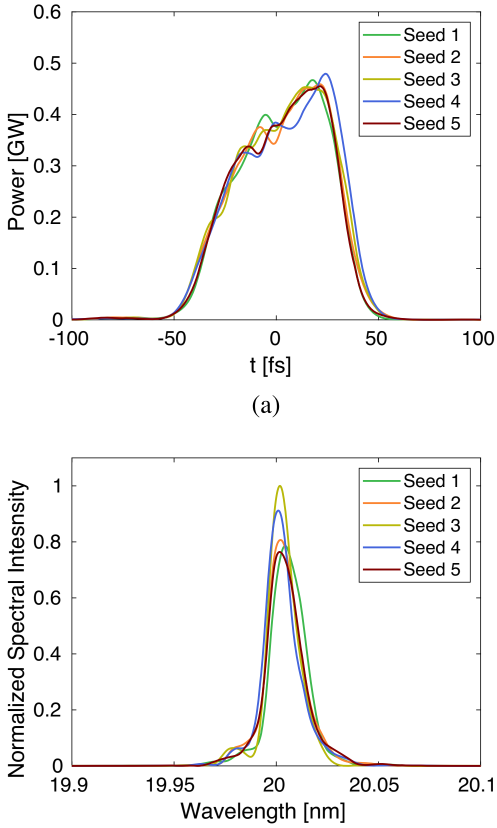

(a)

(b)

FIG. 9. Shot-to-shot fluctuations for an OK-HGHG setup, imprinted on the output FEL at 20 nm. (a) Power profile for different initial shot noise. (b) Spectra for different initial shot noise. They are normalized to the highest spectral intensity with Seed 3.

As expected, the performance of the standard HGHG is not affected at all by the initial shot noise, as it is shown in the spectrum and power profile in Fig. 8. On the contrary, in the OK-HGHG the output FEL properties have small variations on a shot-to-shot basis due to the sensitivity to shot noise, as shown in Fig. 9. Such variations, visible both in the temporal and spectral profiles, are very small in the case of an ideal electron beam as considered here and do not affect the possibility to implement seeding. The standard HGHG completely cancels the SASE background shown in Fig. 7, and the OK-HGHG almost completely cancels it too. The rms wavelength variation for the OK-HGHG results reported in Fig. 9 is 0.001 nm, and even though it is larger than the standard HGHG (0.0001 nm), it still remains significantly smaller than the FEL bandwidth ($\Delta\lambda_{\mathrm{rms}} = 0.14$ nm) and would not affect most experiments. Figure 10 shows that the overall energy per pulse can slightly fluctuate in an OK-HGHG as a result of the shot noise sensitivity, but also in this case the fluctuations are small. This limited sensitivity to shot noise might be partially compensated by the robustness of the OK-HGHG to other parameters' fluctuations as demonstrated in the previous section. All our studies suggest that the OK-HGHG could reliably be used to extend the current capabilities of HGHG in the EUV spectral range.

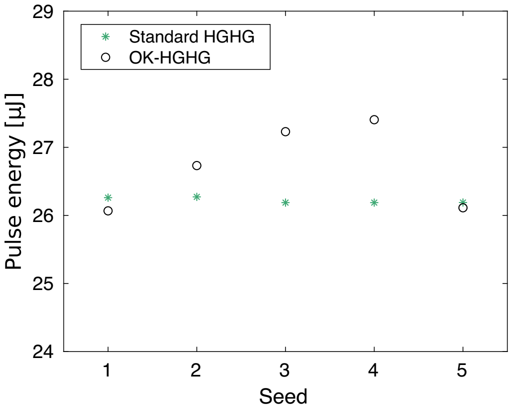

FIG. 10. Shot-to-shot fluctuations of pulse energy for the standard HGHG and the OK-HGHG setup.

V. OUTLOOK

The need to increase the repetition rate of seeded radiation is becoming more and more important. Seeded radiation is nearly Fourier-limited and combines the stability with the control of spectral properties and timing. Being available at high repetition rate with no need for a monochromator will dramatically increase the control and statistics of experiments. Here, we considered an ideal electron beam distribution and we showed that an OK-HGHG scheme can provide a significant reduction for the required seed laser power. This allows seed laser systems to immediately increase their repetition rate and allows the use of other types of short wavelength seed laser sources that are available only with lower peak powers. At the same time, the lower peak power allows operation with a larger laser transverse size which could reduce the sensitivity to the laser alignment. Since the OK-HGHG scheme does not require any additional components compared with an EEHG beamline, in many facilities it is possible to immediately test it and use it in a standard operation.

Complementary to Ref. [42] which presented very valuable experimental results for a single and two-stage HGHG, we have investigated the OK-HGHG setup in a systematic way with simulations. We have shown the strong dependence of the optical klystron on the gain lengths which can result in a reduction of the seed laser power by a factor of up to 1300. We also showed that the two stages of the OK-HGHG scheme can provide increased stability to seed laser power and electron beam compression factor fluctuations. Most importantly, we have verified with time-dependent simulations that the low signal to noise ratio does not deteriorate the coherence properties of the output FEL from shot to shot.

As an outlook, the impact of electron beam imperfections should be studied to verify that they will not diminish its benefits, with a focus on electron beam energy chirp effects and the impact of microbunching which are known to be important for the operation of externally seeded FELs. In that direction, start-to-end simulations with a real electron beam of dedicated facilities would be valuable. Finally, the combination of the optical klystron with more complicated seeding schemes such as the EEHG and the cascaded HGHG should be systematically studied to achieve shorter output wavelengths.

ACKNOWLEDGMENTS

The authors would like to thank the Eugenio Ferrari for supporting the simulation work with Genesis 1.3, Sven Ackermann for a careful proofreading and Maxwell computational resources operated at Deutsches Elektronen-Synchrotron (DESY), Hamburg, Germany. This work was supported by the Impuls- und Vernetzungsfond der Helmholtz-Gemeinschaft e.V. within the CAS-Helmholtz International Laboratory on Free-Electron Laser Science and Technology (CHILFEL), Grant No. InterLabs-0002.

[1] P. R. Ribic and G. Margaritondo, Status and prospects of x-ray free-electron lasers (x-FELs): A simple presentation, J. Phy. D **45**, 213001 (2012).

[2] J. Rossbach, J. R. Schneider, and W. Wurth, 10 years of pioneering x-ray science at the free-electron laser flash at desy, Phys. Rep. **808**, 1 (2019).

[3] B. Faatz *et al.*, Simultaneous operation of two soft x-ray free-electron lasers driven by one linear accelerator, New J. Phys. **18**, 062002 (2016).

[4] D. Nölle, FEL operation at the European XFEL facility, in *Proceedings of International Free Electron Laser Conference (FEL'19), Hamburg, Germany, 2019* (JACoW, Geneva, Switzerland, 2019).

[5] T. Liu, X. Dong, and C. Feng, Start-to-end simulations of the reflection hard X-ray self-aeeding at the SHINE project, in *Proceedings FEL'19, number 39 in Free Electron Laser Conference* (JACoW, Geneva, Switzerland, 2019), pp. 254–257.

[6] E. Hemsing *et al.*, Soft x-ray seeding studies for the SLAC Linac Coherent Light Source II, Phys. Rev. Accel. Beams **22**, 110701 (2019).

[7] P. Gandhi, G. Penn, M. Reinsch, J. S. Wurtele, and W. M. Fawley, Oscillator seeding of a high gain harmonic generation free electron laser in a radiator-first configuration, Phys. Rev. ST Accel. Beams **16**, 020703 (2013).

[8] V. Petrillo, M. Opromolla, A. Bacci, F. Broggi, I. Drebot, G. Ghiringhelli, E. Puppin, M. R. Conti, A. R. Rossi, M. Ruijter, S. Samsam, A. Tagliaferri, G. Rossi, and L. Serafini, Coherent, high repetition rate tender x-ray free-electron laser seeded by an extreme ultra-violet free-electron laser oscillator, New J. Phys. **22**, 073058 (2020).

[9] N. S. Mirian, M. Opromolla, G. Rossi, L. Serafini, and V. Petrillo, High-repetition rate and coherent free-electron laser in the tender x rays based on the echo-enabled harmonic generation of an ultraviolet oscillator pulse, Phys. Rev. Accel. Beams **24**, 050702 (2021).

[10] G. Paraskaki, S. Ackermann, B. Faatz, G. Geloni, T. Lang, F. Pannek, L. Schaper, and J. Zemella, Advanced scheme to generate MHz, fully coherent FEL pulses at nm wavelength, Appl. Sci. **11**, 6058 (2021).

[11] Z. Huang and R. D. Ruth, Fully Coherent X-ray Pulses from a Regenerative-amplifier Free-electron Laser, Phys. Rev. Lett. **96**, 144801 (2006).

[12] K.-J. Kim and Y. V. Shvyd'ko, Tunable optical cavity for an x-ray free-electron-laser oscillator, Phys. Rev. ST Accel. Beams **12**, 030703 (2009).

[13] K. Li and H. Deng, Systematic design and three-dimensional simulation of x-ray fel oscillator for shanghai coherent light facility, Nucl. Instrum. Methods Phys. Res., Sect. A **895**, 40 (2018).

[14] G. Marcus *et al.*, Regenerative amplification for a hard x-ray Free-Electron Laser, in *Proceedings of FEL'19, number 39 in Free Electron Laser Conference* (JACoW Publishing, Geneva, Switzerland, 2019), pp. 118–121.

[15] H. P. Freund, P. J. M. van der Slot, and Y. Shvyd'ko, An x-ray regenerative amplifier free-electron laser using diamond pinhole mirrors, New J. Phys. **21**, 093028 (2019).

[16] M. Opromolla, A. Bacci, M. R. Conti, A. R. Rossi, G. Rossi, L. Serafini, A. Tagliaferri, and V. Petrillo, High repetition rate and coherent free-electron laser oscillator in

the tender x-ray range tailored for linear spectroscopy, Appl. Sci. **11**, 5892 (2021).

[17] E. L. Saldin, E. A. Schneidmiller, and M. V. Yurkov, *The Physics of Free Electron Lasers* (Springer-Verlag, Berlin Heidelber, 2000).

[18] T. Ishikawa *et al.*, A compact x-ray free-electron laser emitting in the sub-ångström region, Nat. Photonics **6**, 540 (2012).

[19] P. Emma *et al.*, First lasing and operation of an ångstrom-wavelength free-electron laser, Nat. Photonics **4**, 641 (2010).

[20] H.-S. Kang *et al.*, Hard x-ray free-electron laser with femtosecond-scale timing jitter, Nat. Photonics **11**, 708 (2017).

[21] E. Prat *et al.*, A compact and cost-effective hard x-ray free-electron laser driven by a high-brightness and low-energy electron beam, Nat. Photonics **14**, 748 (2020).

[22] J. Feldhaus, E. L. Saldin, J. R. Schneider, E. A. Schneidmiller, and M. V. Yurkov, Possible application of x-ray optical elements for reducing the spectral bandwidth of an x-ray SASE FEL, Opt. Commun. **140**, 341 (1997).

[23] G. Geloni, V. Kocharyan, and E. Saldin, A novel self-seeding scheme for hard X-ray FELs, J. Mod. Opt. **58**, 1391 (2011).

[24] J. Amann *et al.*, Demonstration of self-seeding in a hard-x-ray free-electron laser, Nat. Photonics **6**, 693 (2012).

[25] L. H. Yu, Generation of intense UV radiation by subharmonically seeded single-pass free-electron lasers, Phys. Rev. A **44**, 5178 (1991).

[26] G. Stupakov, Using the Beam-Echo Effect for Generation of Short-Wavelength Radiation, Phys. Rev. Lett. **102**, 074801 (2009).

[27] D. Xiang and G. Stupakov, Echo-enabled harmonic generation free electron laser, Phys. Rev. ST Accel. Beams **12**, 030702 (2009).

[28] S. Liu, W. Decking, V. Kocharyan, E. Saldin, S. Serkez, R. Shayduk, H. Sinn, and G. Geloni, Preparing for high-repetition rate hard x-ray self-seeding at the European X-ray Free Electron Laser: Challenges and opportunities, Phys. Rev. Accel. Beams **22**, 060704 (2019).

[29] C. Feng *et al.*, Coherent extreme ultraviolet free-electron laser with echo-enabled harmonic generation, Phys. Rev. Accel. Beams **22**, 050703 (2019).

[30] P. Ribič *et al.*, Coherent soft x-ray pulses from an echo-enabled harmonic generation free-electron laser, Nat. Photonics **13**, 555 (2019).

[31] E. Allaria *et al.*, Highly coherent and stable pulses from the FERMI seeded free-electron laser in the extreme ultraviolet, Nat. Photonics **6**, 699 (2012).

[32] K. Prince *et al.*, Coherent control with a short-wavelength free electron laser, Nat. Photonics **10**, 176 (2016).

[33] P. K. Maroju *et al.*, Attosecond pulse shaping using a seeded free-electron laser, Nature (London) **578**, 386 (2020).

[34] A. Wituschek *et al.*, Tracking attosecond electronic coherences using phase-manipulated extreme ultraviolet pulses, Nat. Commun. **11**, 883 (2020).

[35] C. Lechner *et al.*, Seeding R&D at sFLASH, in *Proceedings of FEL'19, number 39 in Free Electron Laser Conference* (JACoW Publishing, Geneva, Switzerland, 2019), pp. 230–233.

[36] C. Heyl, C. Arnold, A. Couairon, and A. L'Huillier, Introduction to macroscopic power scaling principles for high-order harmonic generation, J. Phys. B **50**, 013001 (2017).

[37] G. Lambert *et al.*, Injection of harmonics generated in gas in a free-electron laser providing intense and coherent extreme-ultraviolet light, Nat. Phys. **4**, 296 (2008).

[38] S. Ackermann *et al.*, Generation of Coherent 19- and 38-nm Radiation at a Free-Electron Laser Directly Seeded at 38 nm, Phys. Rev. Lett. **111**, 114801 (2013).

[39] M. Labat *et al.*, High-Gain Harmonic-generation free-electron laser seeded by harmonics generated in gas, Phys. Rev. Lett. **107**, 224801 (2011).

[40] L. Giannessi *et al.*, Superradiant Cascade in a Seeded Free-Electron Laser, Phys. Rev. Lett. **110**, 044801 (2013).

[41] N. A. Vinokurov and A. N. Skrinsky, About the maximum power of an optical klystron on a storage ring, Preprint of INP 77-59, pp. 77–69, 1977.

[42] J. Yan *et al.*, Self-amplification of Coherent Energy Modulation in Seeded Free-Electron Lasers, Phys. Rev. Lett. **126**, 084801 (2021).

[43] G. Paraskaki, E. Allaria, M. Yurkov, J. Zemella, and E. Schneidmiller, Options for high-repetition-rate seeded FEL, in *EUV and X-ray Optics, Sources, and Instrumentation*, edited by R. Hudec, L. Pina, T. Tschentscher, L. Juha, L. Patthey, K. Tiedtke, M. Zangrando, S. Bajt, and S. Guizard (International Society for Optics and Photonics, SPIE, Czech Republic, 2021), Vol. **11776**, pp. 90–99, 10.1117/12.2589693.

[44] E. Allaria *et al.*, FLASH2020+ plans for a new coherent source at DESY, in *Proceedings of 10th International Particle Accelerator Conference (IPAC'21)* (JACoW Publishing, Geneva, 2021).

[45] J. Yan, N. Huang, H. Deng, B. Liu, D. Wang, and Z. Zhao, First observation of laser-beam interaction in a dipole magnet, Adv. Opt. Photonics **3**, 045003 (2021).

[46] X. Wang, C. Feng, B. Faatz, W. Zhang, and Z. Zhao, Direct-amplification enabled harmonic generation for seeding a high-repetition-rate free-electron laser, https://arxiv.org/abs/2103.11971.

[47] Q. Jia, Analysis of modulation parameters for high repetition rate seeded FEL, Nucl. Instrum. Methods Phys. Res., Sect. A **1015**, 165767 (2021).

[48] G. Penco, G. Perosa, E. Allaria, S. Di Mitri, E. Ferrari, L. Giannessi, S. Spampinati, C. Spezzani, and M. Veronese, Enhanced seeded free electron laser performance with a "cold" electron beam, Phys. Rev. Accel. Beams **23**, 120704 (2020).

[49] L. H. Yu and J. Wu, Theory of high gain harmonic generation: An analytical estimate, Nucl. Instrum. Methods Phys. Res., Sect. A **483**, 493 (2002).

[50] G. Dattoli, L. Giannessi, and P. L. Ottaviani, MOPA optical klystron FELs and coherent harmonic generation, Nucl. Instrum. Methods Phys. Res., Sect. A **507**, 26 (2003).

[51] Y. Ding, P. Emma, Z. Huang, and V. Kumar, Optical klystron enhancement to self-amplified spontaneous emission free electron lasers, Phys. Rev. ST Accel. Beams **9**, 070702 (2006).

[52] G. Penco, E. Allaria, G. De Ninno, E. Ferrari, and L. Giannessi, Experimental Demonstration of Enhanced Self-Amplified Spontaneous Emission by an Optical Klystron, Phys. Rev. Lett. **114**, 013901 (2015).

[53] G. Penco, E. Allaria, G. De Ninno, E. Ferrari, L. Giannessi, E. Roussel, and S. Spampinati, Optical Klystron Enhancement to Self Amplified Spontaneous Emission at FERMI, Photonics **4**, 15 (2017).

[54] E. L. Saldin, E. A. Schneidmiller, and M. V. Yurkov, The free electron laser klystron amplifier concept, in *Proceedings of 26th International Free Electron Laser Conference & 11th FEL Users Workshop (FEL'04)*(JACoW Publishing, Geneva, 2004).

[55] Y. Ding, P. Emma, Z. Huang, and V. Kumar, Optical klystron enhancement to self-amplified spontaneous emission free electron lasers, Phys. Rev. Accel. Beams **9**, 070702 (2006); Phys. Rev. Accel. Beams **23**, 019901(E) (2020).

[56] G. Geloni, M. Guetg, S. Serkez, and E. Schneidmiller, Revision of optical klystron enhancement effects in self-amplified spontaneous emission free electron lasers, Phys. Rev. Accel. Beams **24**, 090702 (2021).

[57] M. Beye, *FLASH2020+: Making FLASH Brighter, Faster and More Flexible: Conceptual Design Report* (Verlag Deutsches Elektronen-Synchrotron, Hamburg, 2020).

[58] S. Reiche, Genesis 1.3: A fully 3d time-dependent fel simulation code, Nucl. Instrum. Methods Phys. Res., Sect. A **429**, 243 (1999).

[59] E. Hemsing, G. Stupakov, D. Xiang, and A. Zholents, Beam by design: Laser manipulation of electrons in modern accelerators, Rev. Mod. Phys. **86**, 897 (2014).

[60] E. L. Saldin, E. A. Schneidmiller, and M. V. Yurkov, Study of a noise degradation of amplification process in a multistage hghg fel, Opt. Commun. **202**, 169 (2002).

[61] W. Brefeld *et al.*, Study of the frequency multiplication process in a multistage HGHG FEL, Nucl. Instrum. Methods Phys. Res., Sect. A **483**, 80 (2002).

Chapter 4

HGHG seeding with an oscillator starting with a low repetition rate seed laser

4.1 Optimization and stability of a high-gain harmonic generation seeded oscillator amplifier

In this Chapter, I present the simulation results of a seeded oscillator for the implementation of an HGHG scheme. Typically, oscillator FELs are associated with low gain and the direct extraction and use of the stored radiation. In the scheme simulated in this Chapter, even though the main aspect of storing a radiation field in a cavity and amplifying it with fresh electron bunches remains, there are some distinct differences between our proposed setup and a low-gain oscillator. One of the main differences is that the power gain per pass is considerable and the FEL operates in high gain. One pass is completed when the radiation field, which is amplified in the in-cavity modulator (as shown in Fig. 4.1), is recirculated back to the entrance of the modulator after following the optical path of the cavity . Another difference is that, even though there is considerable power gain along the in-cavity modulator, the aim is to maintain the same power level per pass. For this reason, the power gain has to be equal to the losses in the cavity (zero net gain). These losses arise in a first approximation due to the reflectivity of the mirrors, however, imperfections may increase them. The stored radiation should not reach saturation, but should be stabilized at a level that is useful for seeding: the power of the stored field at the entrance of the in-cavity modulator should be, in every single pass, analogous to the seed laser sources' power used in seeding methods. Finally, the stored radiation serves the sole purpose of inducing an energy modulation on the electron bunch distribution and is not out-coupled for further use. For this reason, I call the in-cavity undulator a modulator, even though power amplification takes place as well to allow the system to operate. The scheme relies on harmonic conversion and the output FEL is generated at the amplifier placed downstream from the cavity as shown in Fig. 4.2.

In the following publication, I assume the availability of a seed laser source at a low repetition rate, for instance at 10 Hz. For UV seed laser sources, this is not an issue as they are commercially available and widely used at this repetition rate for external seeding experiments. When using such a laser source, the aim of the oscillator is to store and recirculate the initial laser pulse and increase this way its repetition rate to match the electron bunch repetition rate.

An important feature of the in-cavity modulator is that it is relatively long compared to single-pass seeded FELs. Typically, single-pass seeded FELs employ modulators that are less than 3 power gain lengths long and the energy modulation is

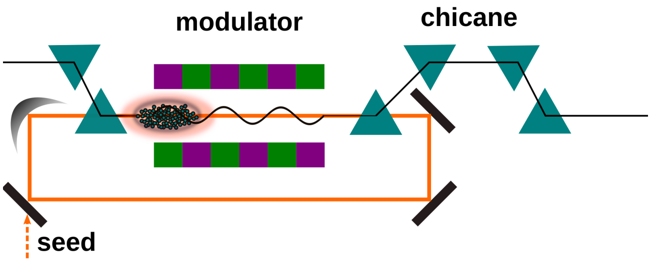

FIGURE 4.1: In the first stage of the seeded oscillator-amplifier, the goal is to maintain a stable power level of the recirculated radiation field in each pass. This stored radiation is used to modulate the energy of the electron bunches.

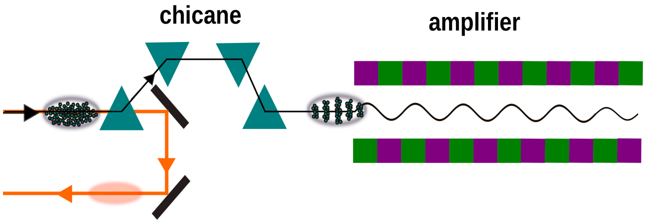

FIGURE 4.2: In the second stage of the seeded oscillator-amplifier, the radiation field does not play any role and is stored in the cavity, while the energy modulated electron bunch is extracted with the chicane. The chicane strength is optimized to introduce bunching at a harmonic of the wavelength of the in-cavity field. This way, coherent emission is possible at that harmonic in the amplifier. In this drawing, the electron bunch and the in-cavity radiation field are considerably separated to emphasize that they are independent at this stage.

achieved in the lethargy regime, where energy exchange occurs with no significant power gain. In the multi-pass case of the oscillator, the power gain is necessary to compensate for the cavity losses. Under these conditions, a lower input power is expected, based on Eq. 2.52 and 2.53. Relaxing the power requirements on the seed laser sources, makes the use of HHG sources as a seed possible. The advantages of implementing seeding with HHG sources were already introduced in Section 2.4.2 and following, it is assumed that an HHG source of 50 nm with 3 MW peak power is available [100]. The simulation results are based on this wavelength as it is the most challenging: the reflectivity in mirrors is considerably lower below 100 nm, while the power gain length is longer for shorter wavelengths. This means that a longer modulator is required for sufficient power gain which comes with the cost of a higher induced energy spread.

I use once more the FLASH2020+ parameters as the study case and I assume that it is possible to generate harmonics up to the 12th with an HGHG setup. The simulations are repeated for a conventional seed laser at 300 nm too. The proposal is to obtain two working points: one between 50 to 100 nm and one between 200 to 300 nm. For the two working points an electron beam energy of 1350 MeV and 750 MeV is used, respectively, in accordance with the FLASH2020+ plans. However, the exact wavelength ranges should be determined by the facility needs and the possible electron beam parameters in combination with the availability in mirrors with sufficient reflectivity.

The simulation work is implemented with the codes Genesis 1.3 version 4 and

Ocelot that are introduced in Appendix A. The simulations' workflow is shown in Fig. 4.3. The initial ideal Gaussian field representing the seed laser is internally generated in Genesis and so is the electron bunch. Then, the interaction of the two of them along the undulators is simulated in Genesis. At the end of the modulator, the amplified radiation field can be extracted and loaded into Ocelot for propagation and focusing. The focused radiation field can be loaded back to Genesis to meet the next electron bunch and start the second pass in the oscillator together. As the simulations are considerably time consuming the optimization is done in several steps:

1. Optimizing a single-pass HGHG of the target wavelength. This determines the lattice parameters, the energy modulation required and the R_{56} of the chicane.
2. Calculating the input seed laser power and waist size based on the required A and B as given in Eq. 2.52 and 2.53.
3. Optimizing cavity design to obtain a stability (reproducible radiation field properties from pass to pass). The optimization excludes the amplifier downstream.
4. Simulating the complete process for a number of consecutive passes and characterizing output FEL.

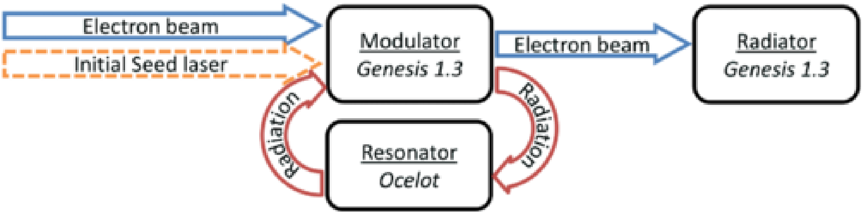

FIGURE 4.3: Flow chart of simulations taken from [101].

The manuscript was published in the peer-reviewed journal *Physical Review Accelerators and Beams*. Additional results and considerations are included in Appendix B.2.

PHYSICAL REVIEW ACCELERATORS AND BEAMS **24,** 034801 (2021)

Review Article

Optimization and stability of a high-gain harmonic generation seeded oscillator amplifier

Georgia Paraskaki,[*] Vanessa Grattoni, Tino Lang, and Johann Zemella
Deutsches Elektronen-Synchrotron DESY, 22607 Hamburg, Germany

Bart Faatz
Shanghai Advanced Research Institute, Chinese Academy of Sciences, Shanghai 201210, China

Wolfgang Hillert
University of Hamburg, 22761 Hamburg, Germany

(Received 14 November 2020; accepted 8 February 2021; published 3 March 2021)

The free-electron laser (FEL) community is interested in taking full advantage of the high-repetition-rates of FELs run by superconducting machines while maintaining the spectral properties achieved with external seeding techniques. Since the feasibility of seed lasers operating at a repetition-rate of MHz and with sufficient energy in a useful wavelength range, such as the ultraviolet (UV) range is challenging, a seeded oscillator-amplifier scheme is proposed instead for generation of fully coherent and high-repetition-rate radiation. The process is triggered by an external seed laser while an optical feedback system feeds the radiation back to the entrance of the modulator where it overlaps with the next electron bunch. Downstream from the feedback system, the electron bunches are then used for harmonic generation. We discuss the optimization of dedicated simulations and we investigate the stability of this scheme with numerical simulations. As a result, we address the control of the reflectivity of the resonator as a key parameter to achieve a stable HGHG seeded radiation. Finally, we show the impact of the power fluctuations in the oscillator on the bunching amplitude with analytical and simulated results. The output FEL radiation wavelengths considered are 4.167 nm and 60 nm.

DOI: 10.1103/PhysRevAccelBeams.24.034801

I. INTRODUCTION

Cavity-based FELs are a well-established technology for generation of radiation in a wide range of wavelengths. Most of the FEL oscillators radiate in the terahertz (THz), infrared (IR), or in the visible wavelength range. Some examples are FELIX in the Netherlands [1], CLIO in France [2], FHI FEL in Germany [3], and FELiChEM in China [4]. There are other examples in different configurations, such as the inverse-Compton interaction compact x-ray source in Hawaii [5] and the storage ring FEL at ELETTRA [6] which has achieved a wavelength down to 190 nm. In addition, several simulation studies have explored low-gain FELs in the past decades [7,8], however, the simulation codes have significantly improved since then, giving the possibility for more detailed studies.

High-gain FEL Oscillators have been demonstrated in the past and are referred to as regenerative amplifier free electron lasers (RAFELs) [9,10]. Initially they addressed longer wavelengths with experimental tests in the IR [11], and later on they were proposed to be used in the x-ray regime as well [12]. A RAFEL requires only a few passes to reach saturation and the requirements on reflectivity are relaxed since it is a high-gain FEL and therefore, it consists of a low Q resonator. Another concept that is under investigation is the FEL oscillator (FELO) in the x-ray wavelength range and down to 0.1 nm [13–15] as a direct source of radiation. There are different driver sources for such an XFELO. Originally, there were studies for an energy recovery linac and therefore, a low-gain FEL. Later, it was adapted to machines like the European XFEL [16] so that the gain could be larger. XFELOs aim at stable and fully coherent x-ray radiation and operate with highly demanding Bragg crystals which require high reflectivity. At the same time there have been studies of schemes that use the oscillator as a source of seed instead of using the generated radiation directly [17–20], and suggestions on combining a RAFEL with harmonic generation as well [21].

---

[*] georgia.paraskaki@desy.de

Published by the American Physical Society under the terms of the Creative Commons Attribution 4.0 International license. Further distribution of this work must maintain attribution to the author(s) and the published article's title, journal citation, and DOI.

In this paper, we describe a setup which uses a cavity-based FEL to imprint the energy modulation onto an electron beam for the implementation of a high-gain harmonic generation (HGHG) [22] seeding setup. The main ingredients of HGHG are a seed laser source, a modulator, a dispersive section, and a radiator. The seed laser interacts with the electron beam along a modulator with the result of modulating the energy of it sinusoidally with a periodicity matching the seed laser wavelength. Then, the dispersive section converts the energy modulation into a density modulation which has a frequency component at a certain harmonic of the seed laser. The prebunched electron beam is traversing the radiator which is tuned to be resonant at the same harmonic of the seed laser.

In single-pass seeded FELs, the seed source for the HGHG scheme is a laser which, when going to high-repetition-rates, determines the repetition-rate of the output seeded FEL radiation. As an example, currently at FLASH [23,24] the seeding experiments are done at a repetition-rate of 10 Hz, in single-bunch operation and at FERMI with a repetition rate of 50 Hz [25]. In the seeded oscillator-amplifier, the optical properties of such a seed laser are retained in a feedback system while the repetition-rate is no longer limited by the seed laser and is determined by the cavity, so it can be increased easily to a MHz and beyond. Seed laser sources with a MHz repetition-rate are currently under development, but are challenging systems. The requirements for tunable sources with tens of μJ of pulse energy, excellent stability, less than 1% rms energy fluctuations and wavelength stability below 1% rms with respect to the spectral bandwidth, make these lasers being considered as beyond the state of the art. Therefore, this scheme is proposed as an alternative solution for generation of high-repetition-rate seeded FEL radiation.

This scheme offers two advantages: the first one is that it can generate seeded FEL radiation at high-repetition-rates beyond the capability of the current seed laser systems exploited to generate ultra short pulses in the UV wavelength range and below. In addition to increasing the repetition-rate of HGHG, this scheme offers the possibility to extend the output wavelength range at this repetition-rate and achieve shorter wavelengths with HGHG. This is due to the amplification of the seed laser input intensity in the modulator which allows the use of shorter wavelength seed lasers of lower intensity. In addition, there are different possibilities offered by this scheme, which are discussed in [26]. In this paper, we show results of an HGHG seeded oscillator-amplifier which generates high-repetition-rate seeded FEL radiation which was first introduced in [27,28]. The simulation results here are more detailed and in addition, the optimization of the simulations is discussed and the stability of this scheme is investigated.

This approach overcomes the limitation of requiring high-repetition-rate seed lasers. This is crucial for pulsed machines, but it is also vital for future continuous wave (CW) machines. Currently, the x-ray user facilities FLASH at DESY, and the European XFEL are the only operating pulsed FELs driven by superconducting linear accelerators, while LCLS-II [29] and SHINE [30] will be CW machines and are under construction. Here, we use FLASH as an example, which operates in a burst-mode. This means that every tenth of a second a 800 μs rf pulse is accelerated, containing a bunch train of 800 bunches. The repetition-rate of FLASH of 1 MHz would require a cavity of 300 m roundtrip length, while for the 4.5 MHz of the European XFEL this would be reduced to 66 m.

II. WORKING PRINCIPLE AND SIMULATION IMPLEMENTATION

A. The HGHG seeded oscillator-amplifier scheme

The goal with the cavity in this scheme is to increase the low-repetition-rate of the seed laser to seed the high-repetition-rate bunches of a superconducting FEL. The process is initiated by a low-repetition-rate seed laser for the first pass, in the case of a burst-mode. The power of the laser is amplified by its interaction with the next electron bunch in the in-cavity undulator, the modulator, and is then stored in an optical cavity in order to seed the next electron bunch arriving at the modulator.

The energy-modulated electron beam exits the modulator and traverses a chicane with a longitudinal dispersion (R_{56}) which induces a density modulation and hence, microbunches with high harmonic content are formed. Downstream of the chicane, an undulator called an amplifier is placed. The amplifier is resonant with the desired harmonic of the seed laser which corresponds to the wavelength of the output seeded FEL radiation. Therefore, this scheme is comparable to a regular single-pass HGHG scheme [31]. The only difference is that it requires a longer modulator in order to amplify the radiation in cavity field to compensate for the power losses that occur in the cavity. A schematic layout of the described HGHG seeded oscillator-amplifier set-up is shown in Fig. 1.

B. Simulation setup and parameter choice

Numerical simulations are implemented by combining two codes for the two different processes: the FEL process in the modulator with Genesis [32] with three-dimensional

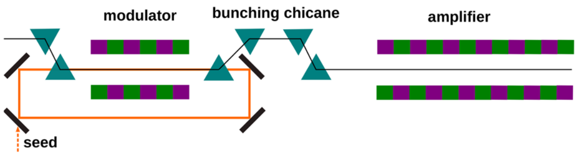

FIG. 1. Simplified schematic view of an HGHG seeded oscillator-amplifier. The orange line represents the path of the light pulse in the cavity and the black one the electron beam trajectory.

time-dependent simulations, and the light propagation in the cavity with ocelot [33]. Genesis simulates the FEL process in the modulator and then, the three-dimensional field at the end of the modulator is extracted and is loaded into ocelot. In our simulations, ocelot is propagating the field along a drift, focuses transversely, and propagates again back to the entrance of the modulator. The field amplitude is reduced to account for cavity losses which are different for the two wavelengths and the longitudinal position of the field is changed so that the roundtrip of the cavity matches the repetition rate of the electron bunches and thus, overlaps optimally with the electron bunches in the modulator. This procedure is repeated for an arbitrary number of passes. Similar three-dimensional and time-dependent simulation approaches have been adopted in other RAFEL designs [21,34].

For the simulations, we use the two electron beam energies (0.75 GeV and 1.35 GeV) that are proposed for the upgrade of FLASH [35] within the FLASH2020+ project [36]. The simulations shown here have been performed for two seed laser wavelengths (300 nm and 50 nm) and their 5th and 12th harmonics respectively. Hence, the output FEL wavelengths are 60 nm and 4.167 nm. This is because these are the longest and shortest foreseen wavelengths in the current design of FLASH2020+ in a seeded operation [36]. For the 50 nm seed laser a high harmonic generation (HHG) source is assumed [37], with state-of-the-art possibilities demonstrated in the extreme ultraviolet (XUV) range [38,39].

The main simulation parameters are summarized in Table I. A flat-top electron beam current distribution is assumed and the modulator parameters are chosen to provide maximum power gain in the steady state region, which refers to the passes in the oscillator in equilibrium state. For the first pass, an ideal Gaussian seed laser pulse is used, which is then propagated and amplified self-consistently during subsequent passes. Since the modulator length is the same for both wavelengths, the input power and reflectivity needed for 50 nm (3 MW and 6% respectively) are higher than those for 300 nm (0.75 MW and 1.01% respectively) since for shorter wavelengths the power gain length is longer [40].

Here we have assumed a simple resonator design that allows us to study in detail the FEL process and does not bound us to a specific optics selection and cavity design that would otherwise be necessary and crucial for the actual implementation of this scheme in an accelerator. We assume that a ring resonator would be a suitable and valid option for the resonator, therefore the total reflectivity applied in each pass accounts for the losses of all 4 elements and the focusing element in ocelot allows us to adjust the properties of the radiation field that would otherwise naturally diverge. As seen in Table I, at 300 nm the total reflectivity is 1.01%, therefore each mirror should have a reflectivity of roughly 30%, while for the 50 nm the total reflectivity is 6% and each mirror should have roughly 50% reflectivity. It should be noted that the exact wavelengths and tunability range for this scheme can be adapted based on availability in seed laser sources and mirrors as the technology advances, therefore the numbers presented here serve as an example study. In addition, the modulator length can be increased to compensate for higher resonator losses in case it is required by mirror availability.

TABLE I. Parameters used for simulations. The rms undulator parameter is referred to as K_{rms}, the number of undulator periods as N_u, and the undulator period as λ_u.

	Electron beam	
Energy	750 MeV	1350 MeV
Uncorrelated energy spread	120 keV	120 keV
Peak current	1 kA	1 kA
Charge	100 pC	100 pC
Normalized Emittance	1 mm mrad	1 mm mrad
	Input seed laser	
Wavelength	300 nm	50 nm
Peak power	0.65 MW	3 MW
Pulse energy	53 nJ	250 nJ
FWHM Duration	78 fs	78 fs
	Modulator	
K_{rms}	4.517	3.248
N_u	90	90
λ_u	60 mm	60 mm
	Cavity	
Reflectivity	1.01%	6%

III. SIMULATION CONSIDERATIONS

In the following section, the most important design considerations during the optimization process are described. The setup of the seeding parameters, the modulator length, and the cavity detuning are presented in Sec. III A, III B, and III C, respectively. In this section, we show results only for a modulator set to resonance with a 50 nm seed laser. This case is presented in more detail because it is one of the most challenging ones compared to longer wavelengths, since the power gain length at this wavelength is the longest, while the cavity losses are the highest and the technology in seed lasers is more limited. For the 300 nm resonant modulator, the optimization steps are the same, while the requirements on laser and mirror technology are more relaxed.

A. Optimization of seeding parameters

Once a stable operation in the longitudinal and transverse plane has been achieved, one can fine-tune the parameters for seeding. The optimal optimization process takes into account the target harmonic, and based on this, the energy modulation at the exit of the modulator is determined. The amplitude ΔE of the energy modulation induced by a field of peak power P_{mod} in the modulator is approximately calculated as [41]:

$$\Delta E = \sqrt{\frac{P_{\mathrm{mod}}}{P_o}} \frac{m_e 2 K L_u \mathrm{JJ}}{\gamma w_0}, \tag{1}$$

where w_0 is the laser waist size, K is the dimensionless undulator parameter, L_u is the undulator length, m_e is the electron mass and $P_0 \approx 8.7$ GW is a constant calculated in [41]. We define JJ as the difference of the Bessel functions, thus $\mathrm{JJ} = J_0(\xi) - J_1(\xi)$, where $\xi = K^2/(4 + 2K^2)$. It should be noted that the simulations are performed with longer modulators than commonly used in seeding schemes, as it will be discussed in Sec. III B. In this case the power level along the modulator cannot be considered constant anymore and diffraction and slippage effects become important. In our case, Eq. (1) is valid with less than 2% error with P_{mod} being the power level established after two thirds of the modulator length $P_{\mathrm{mod},2/3}$. Assuming that the length of the modulator is fixed and the longitudinal and transverse properties of the radiation pulse are stable, one can readjust the power of the radiation field of the input seed laser on its first pass in the modulator to achieve precisely the energy modulation desired in the steady state regime.

After this step, the precise mean energy modulation in the steady state regime is calculated, since at this point the operation of the oscillator is stabilized and fixed. A useful parameter is the normalized energy modulation amplitude which is defined as [41]:

$$A = \frac{\Delta E}{\sigma_{E,i}}, \tag{2}$$

where $\sigma_{E,i}$ is the energy spread upstream the modulator and ΔE is calculated with Eq. (1). Based on the energy modulation we optimize the bunching by adjusting the R_{56}. More commonly, the normalized dispersion is used which is defined as [41]:

$$B = \frac{2\pi R_{56} \sigma_{E,i}}{\lambda_{\mathrm{mod}} E}, \tag{3}$$

where λ_{mod} is the central wavelength of the radiation pulse at the modulator and E is the electron beam energy. The bunching factor, which quantifies the density modulation within the bunch for a specific harmonic number n is defined as [22]:

$$b_n = |J_n(-nAB)| \exp\left(-\frac{1}{2} n^2 B^2\right), \tag{4}$$

where J_n is the Bessel function of the first kind. Based on this formula, the working point, which is defined by the A and B parameters, is determined. As an example, one can aim for 20% of bunching amplitude at the 5th harmonic of a 300 nm seed laser by adjusting the dimensionless parameters A and B.

B. Requirements for modulator length

In this section, we discuss the importance of the length of the modulator and the power level of the radiation field in the cavity. This is because the required normalized energy modulation A can be achieved by varying these two knobs, as shown in Eq. (1).

The upper limit for the modulator length is mainly imposed by the maximum energy spread which can be induced along the modulator while a high-quality beam, suitable for exponential amplification is still maintained. The energy spread of the electron beam upstream from the amplifier, σ_E, as a fraction of the electron beam energy E should be much smaller than the parameter ρ. Therefore, $\sigma_E/E \ll \rho$ [42], where ρ is the dimensionless fundamental FEL parameter [43].

The lower limit is imposed by the energy modulation needed to achieve significant bunching at a certain harmonic of the seed laser, and in addition, by the losses of the resonator. For HGHG, the normalized energy modulation A at the end of the modulator should be approximately equal to the harmonic number in order to efficiently suppress the exponential term and maximize the Bessel function in Eq. (4). However, for higher harmonics it is preferred to deviate from this rule and use smaller energy modulations due to the energy spread limitations discussed above.

The following study for achieving the 12th harmonic of a 50 nm seed source wavelength is based on the previously illustrated principles. Based on this case, the length of the modulator is determined. For longer wavelengths, this length is sufficient and for lower harmonics the peak input power can be decreased to control the energy modulation. The requirements are: (1) For the simulation parameters in Table I, the FEL parameter at the amplifier is $\rho = 1.3 \times 10^{-3}$, therefore the requirement $\sigma_E/E \ll \rho$ leads to $\sigma_E \ll 1.75$ MeV, which is equivalent to $A \ll 14.6$. We set the limit at: $\boldsymbol{A \leq 10}$ for the energy modulation at the end of the modulator. (2) The maximum possible peak power of a seed laser at 50 nm and at 10 Hz is assumed to be 60 MW: $\boldsymbol{P_{\mathrm{seed}}} \leq 60$ MW [37]. (3) The maximum total reflectivity of a resonator for 50 nm is assumed to be 10%: $\boldsymbol{R \leq 10\%}$ [44]. (4) The minimum normalized energy modulation for achieving at least 2% bunching is calculated analytically with Eq. (4) as: $\boldsymbol{A \geq 5.5}$.

Figure 2 shows the possible modulator lengths for different input radiation pulse peak powers, based on simulation results of a single pass in the modulator. As discussed, a maximum input peak power of 60 MW is used. The requirement for $5.5 \leq A \leq 10$, reduces the allowed

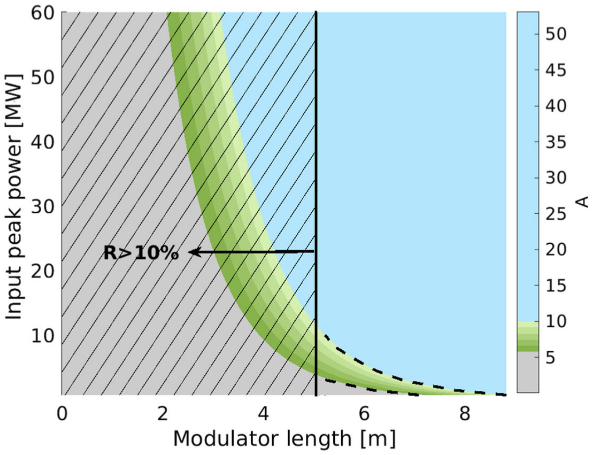

FIG. 2. Overview of possible modulator lengths and seed laser powers. The color bar shows the range of normalized energy modulation that is useful ($5.5 \leq A \leq 10$) in shades of green. The grey and light blue areas of the color bar correspond to non acceptable values of energy modulation. The modulator length for which the power gain is not sufficient to cover resonator losses that are above 90% is also excluded and is shown in the plot with the diagonal black stripes. The small space of input peak power and modulator length combinations that is meeting all the requirements lies in between the two dashed black lines, and the vertical black line. As a result, the minimum possible modulator length is 5 m.

parameter settings to the area indicated by the green band shown in the figure. In order to have enough energy modulation and at the same time achieve the same energy modulation in subsequent passes, the power has to be increased 10 times to compensate for the 90% losses assumed. As a result, the limitation in reflectivity, $R \leq 10\%$, reduces further the allowed parameter settings to the nonstriped area. In the end, there is only a small space available for combinations of seed laser power and modulator length that meet all four requirements, which is the area in between the black dashed lines and the vertical black line. It is concluded that in order to achieve the 12th harmonic of a 50 nm seed laser with reasonable bunching, realistic seed laser power and resonator total reflectivity, the modulator has to be at least 5 m long. Longer modulators can be used in case the reflectivity of 10% cannot be reached, without violating the other 3 conditions. This conclusion is valid for the specific parameters of the study and one can deviate for different simulation parameters, such as the electron beam parameters, or the focusing and waist size of the radiation pulse, for instance.

Based on this study, a modulator of 5.4 m length is chosen with an input seed laser peak power of 3 MW and with total resonator reflectivity of $R = 6\%$ for the 50 nm case. The peak power in the steady state region is stabilized at 3.5 MW. We choose a longer than the minimum required modulator length of 5 m because this way, when there are deteriorations, such as a timing jitter between the seed laser, or a spatial jitter between them, there is still enough power gain to compensate for the resonator losses.

This modulator length is well beyond the traditional approach of using modulators of less than two gain lengths [22]. The consequence is that the modulator operates in the exponential regime, where the system is more sensitive to intensity fluctuations. The calculated power gain length for the simulations based on fitting the Ming-Xie formulas [43] is 1.12 m for the 50 nm resonant modulator and hence, the modulator covers roughly 4.8 gain lengths.

C. Cavity detuning for optimum longitudinal overlap between electrons and stored light pulse

Since the electrons are slower than the photon pulse within the modulator, due to their smaller longitudinal velocity, the laser pulse advances longitudinally in each pass, an effect known as slippage. When the group velocity of the electromagnetic wave is equal to the speed of light [45], the slippage is the product of the number of undulator periods N_u and the resonant wavelength λ_{mod}, therefore $\Delta z = N_u \lambda_{\text{mod}}$. For high-gain FELs in the exponential gain regime, the group velocity is reduced and the slippage drops to $\Delta z = N_u \lambda_{\text{mod}}/3$ as shown in [34,45,46].

In this paper, the zero detuning $\Delta L_{\text{cav}} = 0$ is defined as the length of the cavity for which the light pulse overlaps with the following electron bunch without taking into account the slippage. However, since there is slippage the synchronism of the system is achieved for a cavity length that is longer than the zero-detuning length, so $\Delta L_{\text{cav}} > 0$. Figure 3 shows a detuning curve with the pulse energy and FWHM pulse duration averaged over 30 passes and a modulator resonant with $\lambda_{\text{mod}} = 50$ nm. The cavity detuning can therefore be used to control the pulse duration, bandwidth and pulse energy of the output radiation [4]. In this paper, we are choosing a cavity length which maximizes the gain per pass and the pulse duration, which occurs when $\Delta L_{\text{cav}} \approx 54\lambda_{\text{mod}}$. The width of the

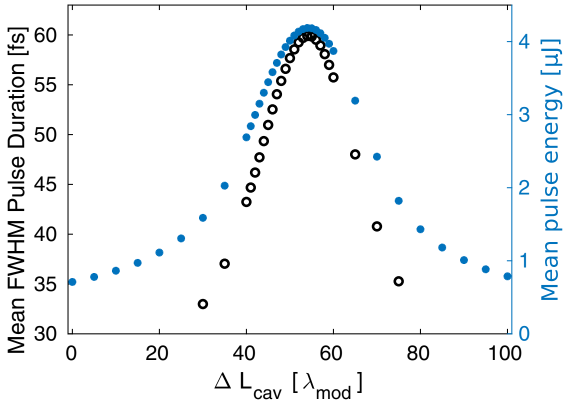

FIG. 3. Mean pulse energy and pulse duration over 30 passes in the oscillator for different cavity detuning ΔL_{cav} length. The modulator is tuned to $\lambda_{\text{mod}} = 50$ nm.

cavity detuning curve depends on the seed laser pulse duration and the electron bunch length which in this case is a 100 fs flat-top bunch.

IV. SIMULATION RESULTS

A. Transverse properties of light pulse in the cavity

It results from the simulations that not only the longitudinal plane, but also the transverse plane of the radiation field plays an important role in the stability of the resonator, making the use of 3-dimensional codes such as Genesis of utmost importance. Changing the waist size and/or waist position within the modulator in one pass affects the gain of the system significantly. The Rayleigh length depends on the waist size, and its relation with the power gain length affects the energy exchange and amplification process in FELs when the diffraction effect cannot be suppressed [43]. In addition, the energy modulation depends on the effective power that overlaps temporally and spatially with the electron beam. In the transverse plane, the field has to be reasonably larger than the electron beam size, while it is usually desired to be shorter longitudinally.

The waist size in the modulator per pass is simulated and calculated with chi23d [47]. The M^2 [48] and waist size in the steady state region (here we assume from pass 30 to pass 100) for both horizontal and vertical planes along with their rms fluctuations and for resonators suitable for 50 nm and 300 nm are summarized in Table II. It should be noted, that the focusing has been optimized separately for the two wavelengths. The waist size w_0 is defined as the radius of the beam when the intensity drops to $1/e^2$ of the on-axis intensity, and at focus position when propagating in a drift section. For the first pass, the seed laser is an ideal Gaussian pulse. The field stabilizes transversely in terms of intensity and waist size with very low fluctuations over the course of passages. We conclude that the radiation pulse has properties which depend on the design of the cavity. This has the advantage of compensating initial fluctuations and leading to a self-stabilized working point.

B. Output seeded FEL radiation

In this section we present the simulation results for 2 different cases: (i) The 5th harmonic of a modulator resonant with 300 nm, (ii) and the 12th harmonic of a modulator resonant with 50 nm. The stability per pass in frequency domain for the output FEL is shown in Fig. 4(a) and 5(a). As an example, the spectra of the passes 20, 40, 60, 80, 90, 100 for both cases are shown in Fig. 4(b) and 5(b) and the power profiles for the same passes in Fig. 4(d) and 5(d) are shown separately. The evolution of the power profile for 100 passes is shown in Fig. 4(c) and 5(c).

TABLE II. Transverse properties of stored radiation pulse: waist size and M^2 on horizontal (x) and vertical (y) plane and their rms fluctuations in the steady state region.

	50 nm	300 nm
M^2 x	1.859 ± 0.002	1.538 ± 0.002
M^2 y	1.576 ± 0.002	1.339 ± 0.001
Waist size x	(267.9 ± 0.3) μm	(589.4 ± 0.5) μm
Waist size y	(250.3 ± 0.3) μm	(681.1 ± 0.6) μm

For both output FEL wavelengths (4.167 nm and 60 nm), the spectrum is longitudinally coherent from the first pass already and shows wavelength and coherence stability, proving that one can use this scheme to generate fully coherent high-repetition rate seeded FEL radiation. For the 4.167 nm case, we see in Fig. 5(a) that there is a red shift in the spectrum which is less than 0.03%, and depending on the experiment, can be tolerated. Finally, Fig. 5(c) shows a pulse shortening of the FEL pulse duration caused by the development of an FEL frequency chirp along the modulator with the number of passes. The pulse duration can be restored with a grating if required by the experiment. The timing for both cases seems to be reliable. Some of the basic parameters that characterize the final FEL pulses are shown in Table III as an average.

V. STABILITY OF THE SYSTEM

In this section, we investigate the stability of an HGHG seeded oscillator-amplifier. In Sec. V A we study the effect of fluctuations of the input seed laser power, the tolerances in the total reflectivity of the resonator, the effect of relative timing offset between the injected seed laser and the electron bunch in the first pass and the charge jitter. In all cases, the stability is examined with simulated results in terms of power gain G and normalized energy modulation A from the 30th pass and up to 100 passes in the oscillator, so in the steady state regime.

The power gain is defined as $G = (P_f - P_i)/P_i$, where P_i is the peak power upstream from the modulator and P_f is the peak power downstream of it. The results shown refer to a 50 nm resonant modulator and optical feedback system, since the 300 nm resonant modulator is operating at the exponential region as well and analogous results are observed in the simulations.

In Sec. V B, we discuss the effect of the oscillator power fluctuations on the energy modulation and the bunching amplitude, which is crucial for implementing the HGHG seeding. In this case, both the 300 nm and the 50 nm cases are considered and analytical derivations are compared to simulation results. Similarly to the previous section, we show the results for the 5th harmonic of a 300 nm seed laser and the 12th harmonic of a 50 nm seed laser.

A. Impact of input seed laser peak power, resonator reflectivity, laser-electron beam timing offset and charge jitter

Shot-to-shot fluctuations of the input seed laser power at the first pass can affect the stability of the stored power in

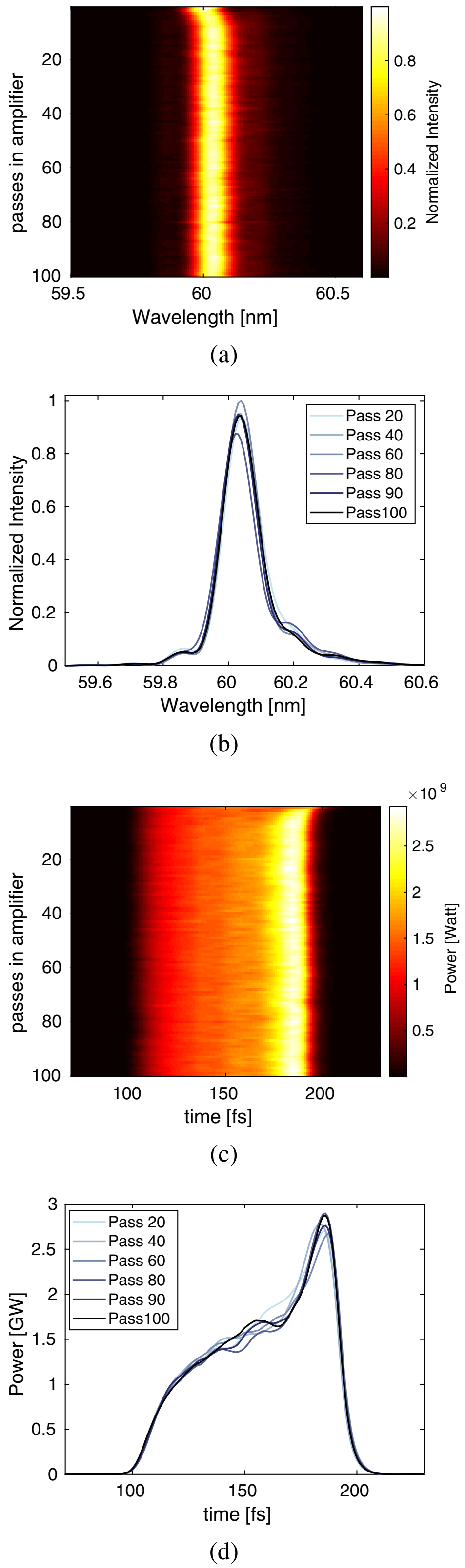

FIG. 4. 5th harmonic of a 300 nm seed light pulse. (a) Output spectrum per pass at amplifier. (b) Output spectrum for selected passes. (c) Power per pass in amplifier along the intrabeam coordinate s. (d) Output power profile for selected passes.

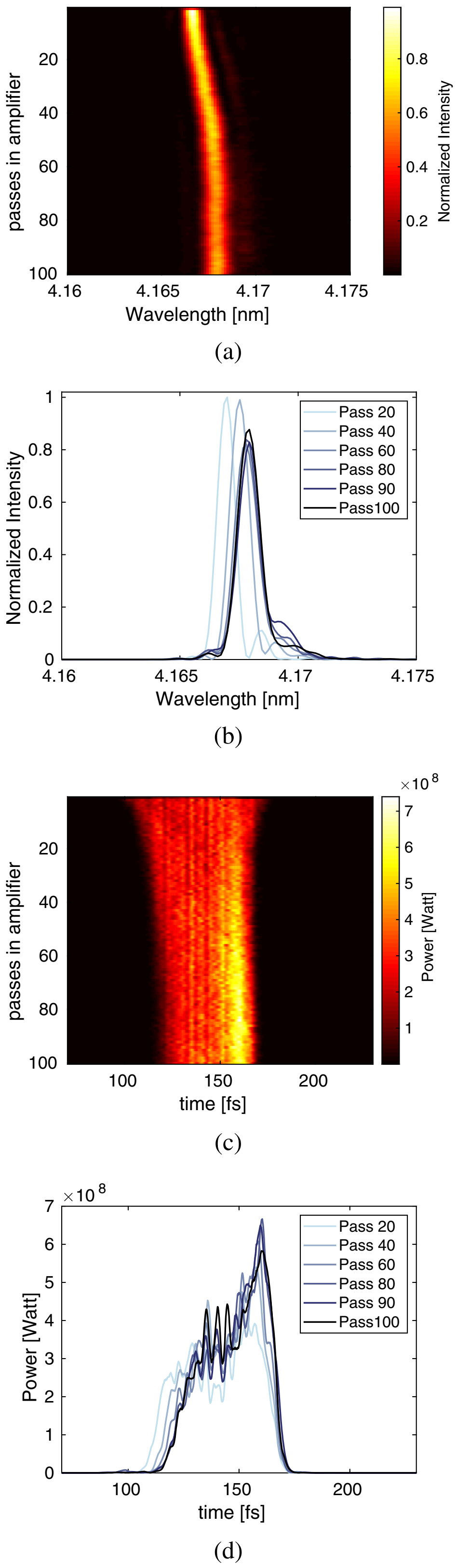

FIG. 5. 12th harmonic of a 50 nm seed light pulse. (a) Output spectrum per pass at amplifier. (b) Output spectrum for selected passes. (c) Power per pass in amplifier along the intrabeam coordinate s. (d) Output power profile for selected passes.

TABLE III. Properties of FEL output radiation.

	4.167 nm	60 nm
Pulse energy	18.2 μJ	150 μJ
rms pulse duration	13.4 fs	25.2 fs
$\Delta\lambda_{\mathrm{rms}}/\lambda$	2.8×10^{-4}	1.8×10^{-3}

the feedback system per pass. In Fig. 6(a) the effect of the input seed laser power is shown for a 5% and 10% offset, which is considerably larger than the power stability of current seed laser systems which are often expected to be within 1% rms. Since a deviation of 10% in the seed laser power affects the energy modulation by less than 4% and the power gain considerably less than 0.01%, it is concluded that the seed laser power fluctuations are not critical for the stability of the HGHG seeded oscillator-amplifier. This result relaxes the requirements on the seed laser source.

The reflectivity of the optical feedback system can vary either due to static effects or due to dynamic effects. Some of the effects that can degrade the operation of the cavity are the thermal loading, the slow degradation of the mirrors or the thermal effects on the mirror holders which can cause a cavity misalignment. Higher reflectivity, and therefore more power, leads to more instability as shown in Fig. 6(b). Increasing the power level of the radiation in the feedback system for a fixed modulator length results in a different working point on the gain curve which is closer to the saturation. In the reflectivity study case, the effect on both the relative energy modulation and the relative power gain is much stronger than in the seed power fluctuation study [Fig. 6(a)], since in this case the reflectivity offset is acting in every single pass and the effect is amplified with the number of passes.

It results that the reflectivity has to be carefully controlled and thermal effects have to be studied to secure a stable operation, since a 2% relative deviation in reflectivity can affect the energy modulation to an extent that HGHG is no longer possible. However, a careful design of the mirrors, and a feedback system that counteracts the degradation of the mirrors can ensure that the reflectivity changes are limited to acceptable ranges, which in our case should be $< 1\%$, and achieve active control.

Figure 6(c) shows the effect of a ±40 fs timing offset between the electron bunch and the seed laser which is injected in the first pass. The timing jitter should be better than 40 fs with optically locked seed lasers and assuming that feedback systems can prevent slow drifts. The simulations are implemented with a 100 fs flat-top electron bunch, since this bunch length is sufficient to simulate the overlap between the electron bunch and the radiation pulse, taking into account the slippage with accurate simulation results. This allows reducing the demanding required computational time needed for such simulations that run in several passes. However, only for this study, we have extended the electron bunch length to a 300 fs flat-top current distribution, for realistic results of time jitter. In all cases, the energy modulation is not affected more than 4%, therefore the timing between the electron bunch and the seed laser injected in the first pass is not crucial when the electron bunch is sufficiently long and uniform.

In addition, we simulated the effect of charge jitter up to ±1% [49] by adjusting the peak current of the flat-top. The simulation results showed that even with the maximum offset, the energy modulation is affected by less than 4% and the gain by less than 0.2% within the error bars. It is concluded that a moderate charge jitter is not critical for the implementation of the scheme under study. In the following section, we extend the study to understand how the normalized energy modulation fluctuations affect the formation of the bunching amplitude and eventually, the seeding process.

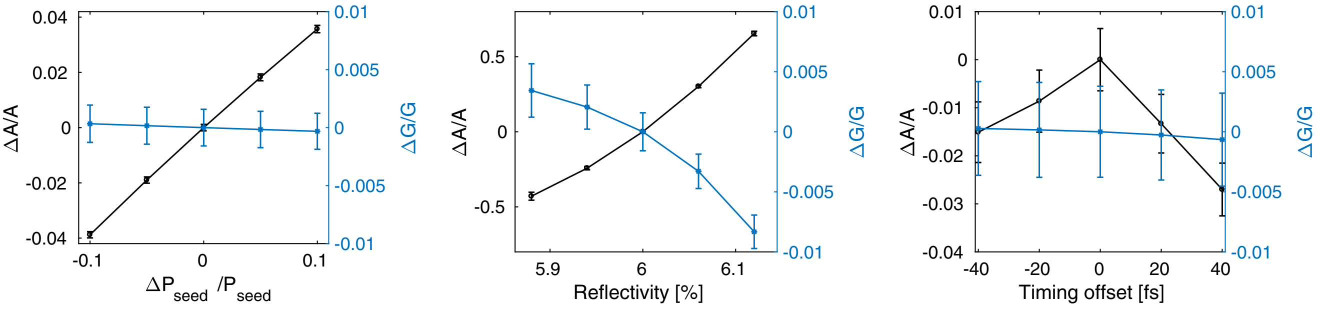

(a) (b) (c)

FIG. 6. Overview of the stability study. In (a) the effect of seed laser peak power, P_{seed}, fluctuation up to ±10% is shown, in (b) the reflectivity tolerances for up to ±2% and (c) the effect of timing offset between the external seed laser pulse and the electron beam for up to ±40 fs. In all cases we show the effect on the relative normalized energy modulation $\Delta A/A$, achieved at the steady state in the oscillator (passes between 30 and 100), and on the right axis, the effect on the relative power gain, $\Delta G/G$ as an average over the same passes. The error bars indicate the standard error on the mean values calculated at the steady state region.

B. Sensitivity of bunching amplitude on power fluctuations

As discussed in the previous section, there are several factors that can cause fluctuations in the power level, and hence the energy modulation achieved at the modulator. After exiting the chicane, the prebunched electron bunches arrive at high-repetition-rates and enter the amplifier. At this second stage, the amplifier, the only input parameter is the prebunched electron bunch. For this reason, it is essential to study the sensitivity of the bunching factor on the power fluctuations in the oscillator. Starting from Eq. (1), and Eq. (2), the sensitivity of the normalized energy modulation A to the power per pass P_{mod} of the stored radiation pulse in the cavity is

$$\frac{\Delta A}{A} = \frac{1}{2}\frac{\Delta P_{\mathrm{mod}}}{P_{\mathrm{mod}}}. \tag{5}$$

The rms power fluctuations and rms normalized energy modulation fluctuations are shown in Table IV and they are consistent with Eq. (5). In addition, Table V summarizes the seed laser pulse properties at the exit of the modulator, where the peak power maximizes. The peak power that reaches the mirror downstream will be less than the several MW reported here due to diffraction.

Based on Eq. (1), (2), and (4), the power fluctuations in the oscillator translate into bunching fluctuations for the electron beam that enters the amplifier. In turn, the power level P_{th} when the power growth is transitioning to exponential in the amplifier is correlated with the bunching amplitude as: $P_{\mathrm{th}} \propto |b_n|^2$ [50]. This means that for a fixed radiator length and sufficient initial bunching at the amplifier, the bunching fluctuations can affect the final FEL power depending on whether or not saturation has been reached at this point.

TABLE IV. The Table summarizes the mean normalized energy modulation A and the mean power in the cavity P_{mod} over 100 passes with their rms fluctuations. In addition, the normalized dispersive strength B used for the analytical calculations in this section is shown.

	300 nm-5th harmonic	50 nm-12th harmonic
A	7.24	7.11
A rms fluctuations	1.66%	1.93%
P_{mod} rms fluctuations	3.12%	4.31%
B	0.17	0.14

TABLE V. Summary of laser pulse properties at the exit of the modulator.

	300 nm-5th harm.	50 nm-12th harm.
P_{mod}	51.4 MW	56 MW
Pulse energy	3.4 μJ	2.7 μJ
rms pulse duration	25 fs	17.8 fs
Beam radius x	228 μm	147 μm
Beam radius y	192 μm	120 μm

We calculate the sensitivity of the bunching amplitude on energy modulation deviation for an HGHG scheme [51] as:

$$\frac{\Delta b_n}{b_n} = n^2 B^2 \frac{\Delta A}{A} - \frac{1}{2}\left[n^2(B^2 + B^2 A^2 - 1)\right]\frac{\Delta A^2}{A^2}. \tag{6}$$

One can easily extract the sensitivity of the bunching amplitude on the power fluctuations in the oscillator from Eq. (5) and (6).

Figure 7 shows how Eq. (6) relates to the simulation data for all 100 passes shown in Fig. 4 and 5. Table IV shows the exact parameters used in Eq. (6), with the normalized dispersion B being calculated by taking into account the chicane strength and the longitudinal dispersion added along the long modulator [52]. The power fluctuations in the oscillator affect the bunching amplitude of higher harmonics more severely, based on Eq. (6) and the simulation results. We have extended the analytical study for up to a 40% deviation in A, in order to cover the effects studied in Sec. V A. These analytical calculations can be used to minimize the effect of the fluctuations in the oscillator on the bunching amplitude.

Finally, the bunching maps of the 5th harmonic of a 300 nm and the 12th harmonic of 50 nm seed laser are shown in Fig. 8(a) and 8(b). The peak to peak energy modulation fluctuations which occur in the first 100 passes are shown with a double arrow on the bunching maps The color bar indicates the analytically calculated bunching amplitude fluctuations expected for the calculated energy modulation fluctuations observed in the simulations and for

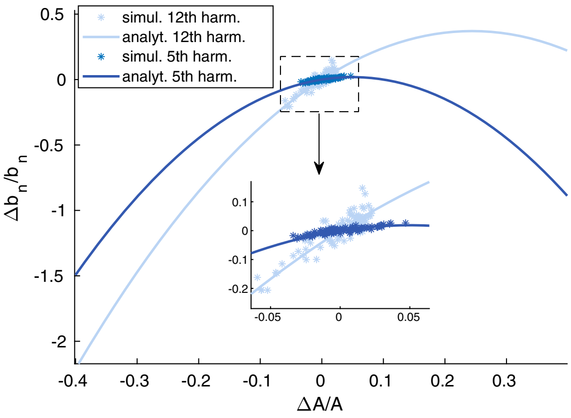

FIG. 7. Sensitivity of bunching amplitude on energy modulation fluctuations downstream from the modulator. The solid lines are calculated with Eq. (6), while the stars show the simulation results for 100 passes. The dark blue and the light blue color represent the 5th harmonic of a 300 nm resonant modulator and the 12th harmonic of a 50 nm resonant modulator, respectively. In the inset, we show the range of the fluctuations observed in the simulations in more detail.

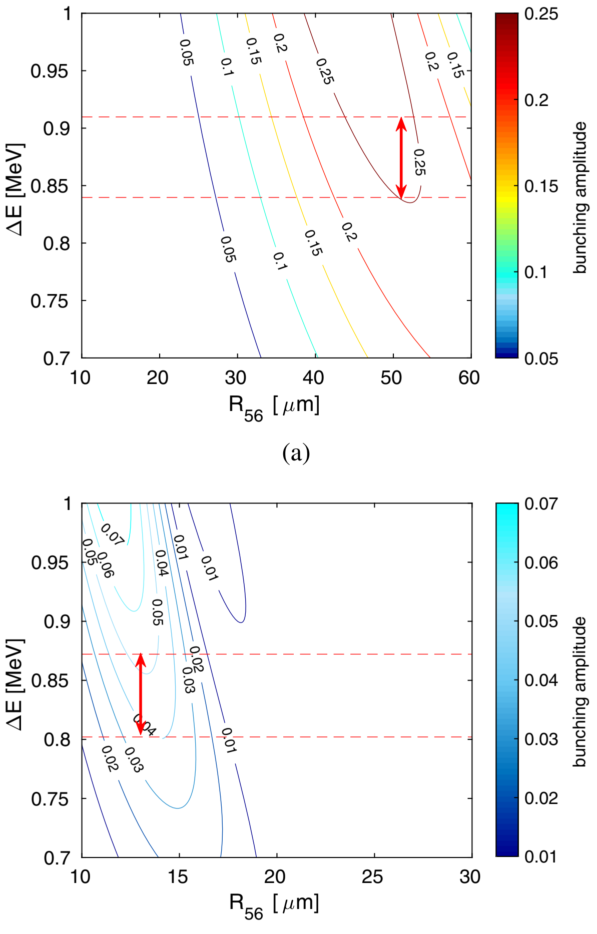

(a)

(b)

FIG. 8. Analytically calculated bunching maps [see Eq. (4)]. The red horizontal dashed lines show the peak to peak fluctuations calculated for 100 passes in the oscillator and the red double arrow indicates the bunching fluctuations for the R_{56} used in the simulations. (a) 5th harmonic of 300 nm. (b) 12th harmonic of 50 nm.

the R_{56} set in the simulations. For increasing harmonic number the bunching maps become more constricted which illustrates the increasing sensitivity to fluctuations. One can use this type of plots to optimize for minimum bunching fluctuations, or for maximum bunching amplitude.

VI. CONCLUSIONS

In this paper, we presented the optimization process of an HGHG seeded oscillator-amplifier. The modulator length was determined based on the requirements for the implementation of HGHG seeding and the technology available for this setting, and the seeding parameters were optimized. An overview of the output seeded FEL radiation per pass in time and frequency domain for 100 passes from initiation proves that fully coherent light can be generated almost immediately with a seeded oscillator-amplifier scheme.

Since the oscillator is partially operating in the exponential regime, the stability of the power per pass in the oscillator is more crucial compared to conventional FEL oscillators operating close to saturation. The seed laser power fluctuations at the first pass can be tolerated up to 10%, which relaxes the requirements on the seed laser. In addition, a timing jitter between electron and laser beam up to ±40 fs and a charge jitter up to ±1% can be tolerated, indicating the feasibility of the scheme. The reflectivity seems to be the main challenge since it should deviate considerably less than 1% from the nominal value for reliable results. This can be achieved with appropriate mirror choice and the use of feedback systems. An active control on the reflectivity is crucial, since it is the main tuning knob for compensation of other fluctuations and for system stability.

Finally, we show how the power fluctuations in the oscillator affect the fluctuations in energy modulation which in turn determine the fluctuations in bunching amplitude. Simulation results were compared with analytical expressions in good agreement and can be used to determine a stable working point.

ACKNOWLEDGMENTS

The authors would like to thank Sven Ackermann, Enrico Allaria, Francesca Curbis, Gianluca Geloni, Lucas Schaper, Takanori Tanikawa for their useful insights and Svitozar Serkez for his support with ocelot. We would like to thank Saša Bajt, Elke Plönjes, and Rolf Treush for information on mirrors. This work was supported by the Impuls- und Vernetzungsfond der Helmholtz-Gemeinschaft e.V. within the CAS-Helmholtz International Laboratory on Free-Electron Laser Science and Technology (CHILFEL), Grant No. InterLabs-0002 and by the Maxwell computational resources operated at Deutsches Elektronen-Synchrotron (DESY), Hamburg, Germany.

[1] D. Oepts, A. van der Meer, and P. van Amersfoort, The free-electron-laser user facility FELIX, Infrared Physics & Technology **36**, 297 (1995).

[2] J. M. Ortega, The CLIO infrared FEL facility, Synchrotron Radiat. News **9**, 20 (1996).

[3] W. Schöllkopf, S. Gewinner, H. Junkes, A. Paarmann, G. von Helden, H. P. Bluem, and A. M. M. Todd, The new IR and THz FEL facility at the Fritz Haber Institute in Berlin, in *Advances in X-ray Free-Electron Lasers Instrumentation III*, Vol. 9512, edited by S. G. Biedron, International Society for Optics and Photonics, Prague, Czech Republic (SPIE, 2015), pp. 238–250, https://spie.org/eoo/conferencedetails/euv-x-ray-optics?utm_id=reoo21scpw.

[4] Z.-Y. Zhao, H.-T. Li, and Q.-K. Jia, Effect of cavity length detuning on the output characteristics for the middle infrared FEL oscillator of FELiChEM, Chin. Phys. C **41**, 108101 (2017).

[5] P. Niknejadi, J. M. Kowalczyk, M. R. Hadmack, B. T. Jacobson, I. Howe, S. Kan, S. Smith, E. B. Szarmes,

G. Varner, and J. M. Madey, Free-electron laser inverse-Compton interaction x-ray source, Phys. Rev. Accel. Beams **22**, 040704 (2019).

[6] M. Trovò, J. Clarke, M. Couprie, G. Dattoli, D. Garzella, A. Gatto, L. Giannessi, S. Günster, N. Kaiser, M. Marsi, M. Poole, D. Ristau, and R. Walker, Operation of the European storage ring FEL at ELETTRA down to 190 nm, Nucl. Instrum. Methods Phys. Res., Sect. A **483**, 157 (2002).

[7] G. Dattoli, B. Faatz, L. Giannessi, and P. L. Ottaviani, The tandem FEL dynamic behavior, IEEE J. Quantum Electronics **31**, 1584 (1995).

[8] G. Dattoli, L. Giannessi, and P. Ottaviani, Oscillator-amplifier free electron laser devices with stable output power, J. Appl. Phys. **95**, 3211 (2004).

[9] B. Faatz, J. Feldhaus, J. Krzywinski, E. Saldin, E. Schneidmiller, and M. Yurkov, Regenerative FEL amplifier at the TESLA test facility at DESY, Nucl. Instrum. Methods Phys. Res., Sect. A **429**, 424 (1999).

[10] H. P. Freund, P. J. M. van der Slot, and Y. Shvyd'ko, An x-ray regenerative amplifier free-electron laser using diamond pinhole mirrors, New J. Phys. **21**, 093028 (2019).

[11] D. C. Nguyen, R. L. Sheffield, C. M. Fortgang, J. C. Goldstein, J. M. Kinross-Wright, and N. A. Ebrahim, First lasing of the regenerative amplifier FEL, Nucl. Instrum. Methods Phys. Res., Sect. A **429**, 125 (1999).

[12] Z. Huang and R. D. Ruth, Fully Coherent X-Ray Pulses from a Regenerative-Amplifier Free-Electron Laser, Phys. Rev. Lett. **96**, 144801 (2006).

[13] K.-J. Kim, Y. Shvyd'ko, and S. Reiche, A Proposal for an X-Ray Free-Electron Laser Oscillator with an Energy-Recovery Linac, Phys. Rev. Lett. **100**, 244802 (2008).

[14] J. Zemella, J. Rossbach, C. Maag, H. Sinn, and M. Tolkiehn, Numerical simulations of an XFELO for the european XFEL driven by a spent beam, in *FEL 2012—34th International Free Electron Laser Conference*, 429 (JACoW Publishing, Nara, Japan, 2012), https://accelconf.web.cern.ch/FEL2012/papers/wepd29.pdf.

[15] P. Rauer, I. Bahns, W. Decking, W. Hillert, J. Roßbach, and H. Sinn, Integration of an XFELO at the European XFEL facility, in *Proc. FEL'19*, Free Electron Laser Conference No. 39 (JACoW Publishing, Geneva, Switzerland, 2019), pp. 62–65, https://doi.org/10.18429/JACoW-FEL2019-TUP009.

[16] D. Nölle, FEL operation at the European XFEL facility, in *Proc. of International Free Electron Laser Conference (FEL'19), Hamburg, Germany, August 26-30, 2019*, International Free Electron Laser Conference No. 39 (JACoW, Geneva, Switzerland, 2019).

[17] P. Gandhi, G. Penn, M. Reinsch, J. Wurtele, and W. Fawley, Oscillator seeding of a high gain harmonic generation free electron laser in a radiator-first configuration, Phys. Rev. Accel. Beams **16**, 020703 (2013).

[18] V. Petrillo, A. Bacci, A. R. Rossi, L. Serafini, I. Drebot, M. R. Conti, M. Ruijter, M. Opromolla, S. Samsam, F. Broggi, G. Ghiringhelli, E. Puppin, G. Rossi, and A. tagliaferri, Coherent, high repetition rate tender X-ray Free-Electron Laser seeded by an Extreme Ultra-Violet Free-Electron Laser Oscillator, New J. Phys. **22**, 073058 (2020).

[19] K. Li, J. Yan, C. Feng, M. Zhang, and H. Deng, High brightness fully coherent x-ray amplifier seeded by a free-electron laser oscillator, Phys. Rev. Accel. Beams **21**, 040702 (2018).

[20] F. Ciocci, G. Dattoli, A. Angelis, F. Garosi, L. Giannessi, P. Ottaviani, and A. Torre, Design elements of a high-power VUV free electron laser, Il Nuovo Cimento Soc. Ital. Fis. **106A**, 1757 (1993).

[21] B. W. J. McNeil, N. R. Thompson, D. J. Dunning, J. G. Karssenberg, P. J. M. van der Slot, and K.-J. Boller, A design for the generation of temporally-coherent radiation pulses in the VUV and beyond by a self-seeding high-gain free electron laser amplifier, New J. Phys. **9**, 239 (2007).

[22] L. H. Yu and J. Wu, Theory of high gain harmonic generation: an analytical estimate, Nucl. Instrum. Methods Phys. Res., Sect. A **483**, 493 (2002).

[23] J. Rossbach, J. R. Schneider, and W. Wurth, 10 years of pioneering X-ray science at the Free-Electron Laser FLASH at DESY, Phys. Rep. **808**, 1 (2019), 10 years of pioneering X-ray science at the Free-Electron Laser FLASH at DESY.

[24] B. Faatz, M. Braune, O. Hensler, K. Honkavaara, R. Kammering, M. Kuhlmann, E. Ploenjes, J. Roensch-Schulenburg, E. Schneidmiller, S. Schreiber, K. Tiedtke, M. Tischer, R. Treusch, M. Vogt, W. Wurth, J. Zemella, and M. Yurkov, The FLASH facility: Advanced options for FLASH and future perspectives, Appl. Sci. **7**, 1114 (2017).

[25] P. Ribič, A. Abrami, L. Badano, M. Bossi, H.-H. Braun, N. Bruchon, F. Capotondi, D. Castronovo, M. Cautero, P. Cinquegrana, M. Coreno, M. Couprie, I. Cudin, M. Danailov, D. N. Giovanni, A. Demidovich, S. Di Mitri, B. Diviacco, W. Fawley, and E. Allaria, Coherent soft X-ray pulses from an echo-enabled harmonic generation free-electron laser, Nat. Photonics **13**, 555 (2019).

[26] S. Ackermann, B. Faatz, V. Grattoni, M. M. Kazemi, T. Lang, C. Lechner, G. Paraskaki, J. Zemella, G. Geloni, S. Serkez, T. Tanikawa, and W. Hillert, Novel method for the generation of stable radiation from free-electron lasers at high repetition rates, Phys. Rev. Accel. Beams **23**, 071302 (2020).

[27] G. Paraskaki, S. Ackermann, B. Faatz, V. Grattoni, C. Lechner, M. Mehrjoo, G. Geloni, S. Serkez, T. Tanikawa, and W. Hillert, Study of a seeded oscillator-amplifier FEL, in *Proc. of International Free Electron Laser Conference (FEL'19), Hamburg, Germany, August 26-30, 2019*, International Free Electron Laser Conference No. 39 (JACoW, Geneva, Switzerland, 2019).

[28] S. Ackermann, B. Faatz, V. Grattoni, C. Lechner, G. Paraskaki, G. Geloni, S. Serkez, T. Tanikawa, and W. Hillert, High-repetition-rate seeding schemes using a resonator-amplifier setup, in *Proc. of International Free Electron Laser Conference (FEL'19), Hamburg, Germany, August 26-30, 2019*, International Free Electron Laser Conference No. 39 (JACoW, Geneva, Switzerland, 2019).

[29] A. Brachmann, M. Dunham, and J. Schmerge, LCLS-II - Status and upgrades, in *Proc. FEL'19*, Free Electron Laser Conference No. 39 (JACoW Publishing, Geneva, Switzerland, 2019), pp. 772–775, https://doi.org/10.18429/JACoW-FEL2019-FRA02.

[30] T. Liu, X. Dong, and C. Feng, Start-to-end simulations of the reflection hard X-ray self-seeding at the SHINE project, in *Proc. FEL'19*, Free Electron Laser Conference No. 39 (JACoW Publishing, Geneva, Switzerland, 2019), pp. 254–257, https://doi.org/10.18429/JACoW-FEL2019-TUP087.

[31] L.-H. Yu, M. Babzien, I. Ben-Zvi, L. F. DiMauro, A. Doyuran, W. Graves, E. Johnson, S. Krinsky, R. Malone, I. Pogorelsky, J. Skaritka, G. Rakowsky, L. Solomon, X. J. Wang, M. Woodle, V. Yakimenko, S. G. Biedron, J. N. Galayda, E. Gluskin, J. Jagger, V. Sajaev, and I. Vasserman, High-gain harmonic-generation free-electron laser, Science **289**, 932 (2000).

[32] S. Reiche, GENESIS 1.3: a fully 3D time-dependent FEL simulation code, Nucl. Instrum. Methods Phys. Res., Sect. A **429**, 243 (1999).

[33] I. Agapov, G. Geloni, S. Tomin, and I. Zagorodnov, OCELOT: A software framework for synchrotron light source and FEL studies, Nucl. Instrum. Methods Phys. Res., Sect. A **768**, 151 (2014).

[34] H. P. Freund, D. C. Nguyen, P. A. Sprangle, and P. J. M. van der Slot, Three-dimensional, time-dependent simulation of a regenerative amplifier free-electron laser, Phys. Rev. Accel. Beams **16**, 010707 (2013).

[35] J. Zemella and M. Vogt, Optics & compression schemes for a possible FLASH upgrade, in *Proc. 10th International Particle Accelerator Conference (IPAC'19), Melbourne, Australia, 19-24 May 2019*, International Particle Accelerator Conference No. 10 (JACoW Publishing, Geneva, Switzerland, 2019), pp. 1744–1747, https://doi.org/10.18429/JACoW-IPAC2019-TUPRB026.

[36] M. Beye, *FLASH2020+: Making FLASH brighter, faster and more flexible: Conceptual Design Report* (Verlag Deutsches Elektronen-Synchrotron, Hamburg, 2020), pp. 1–126.

[37] E. Takahashi, Y. Nabekawa, and K. Midorikawa, Generation of 10-μJ coherent extreme-ultraviolet light by use of high-order harmonics, Opt. Lett. **27**, 1920 (2002).

[38] C. Heyl, C. Arnold, A. Couairon, and A. L'Huillier, Introduction to macroscopic power scaling principles for high-order harmonic generation, J. Phys. B **50**, 013001 (2017).

[39] I. Makos, I. Orfanos, A. Nayak, J. Peschel, B. Major, I. Liontos, E. Skantzakis, N. Papadakis, C. Kalpouzos, M. Dumergue, S. Kühn, K. Varju, P. Johnsson, A. L'Huillier, P. Tzallas, and D. Charalambidis, A 10-gigawatt attosecond source for non-linear XUV optics and XUV-pump-XUV-probe studies, Sci. Rep. **10**, 3759 (2020).

[40] P. Schmüser, M. Dohlus, and J. Rossbach, *Ultraviolet and Soft X-Ray Free-Electron Lasers: Introduction to Physical Principles, Experimental Results, Technological Challenges*, 1st ed. (Springer Publishing Company, New York, 2008).

[41] E. Hemsing, G. Stupakov, D. Xiang, and A. Zholents, Beam by design: Laser manipulation of electrons in modern accelerators, Rev. Mod. Phys. **86**, 897 (2014).

[42] S. Reiche, Overview of seeding methods for FELs, in *Proceedings of the 4th International Particle Accelerator Conference, IPAC-2013, Shanghai, China, 2013* (JACoW, Shanghai, China, 2013), p. 2063.

[43] M. Xie, Design optimization for an X-ray free electron laser driven by SLAC LINAC, in Proceedings, 16th Particle Accelerator Conference and International Conference on High-Energy Accelerators, HEACC 1995: Dallas, USA, May 1-5, 1995, *Conf. Proc.* C950501, 183 (1996).

[44] M. Vidal-Dasilva, M. Fernández-Perea, J. A. Méndez, J. A. Aznárez, and J. I. Larruquert, Narrowband multilayer coatings for the extreme ultraviolet range of 50–92 nm, Opt. Express **17**, 22773 (2009).

[45] H. Freund and T. Antonsen, *Principles of Free-Electron Lasers* (Springer, New York, 2018), pp. 328–330.

[46] X. Yang, N. Mirian, and L. Giannessi, Postsaturation dynamics and superluminal propagation of a superradiant spike in a free-electron laser amplifier, Phys. Rev. Accel. Beams **23**, 010703 (2020).

[47] T. Lang, A. Harth, J. Matyschok, T. Binhammer, M. Schultze, and U. Morgner, Impact of temporal, spatial and cascaded effects on the pulse formation in ultra-broadband parametric amplifiers, Opt. Express **21**, 949 (2013), available at www.chi23D.com.

[48] S. Ackermann, B. Faatz, and V. Miltchev, Modal analysis of a seeded free-electron laser, Phys. Rev. Accel. Beams **16**, 100702 (2013).

[49] T. Kozak, B. Steffen, S. Pfeiffer, S. Schreiber, and A. Napieralski, Fast intra bunch train charge feedback foρ FELs based on photo injector laser pulse modulation, IEEE Trans. Nucl. Sci. **64**, 2904 (2017).

[50] L. Giannessi, Seeding and harmonic generation in free-electron lasers (Synchrotron Light Sources and Free-Electron Lasers: Accelerator Physics, Instrumentation and Science Applications, 2016), pp. 195–223.

[51] E. Hemsing, B. Garcia, Z. Huang, T. Raubenheimer, and D. Xiang, Sensitivity of echo enabled harmonic generation to sinusoidal electron beam energy structure, Phys. Rev. Accel. Beams **20**, 060702 (2017).

[52] R. Molo, Investigation of short-pulse radiation sources at DELTA based on coherent harmonic generation and echo-enabled harmonic generation, Master's thesis, Technical University Dortmund, DELTA, 2011.

Chapter 5

HGHG seeding with an oscillator starting from shot noise

5.1 Advanced Scheme to Generate MHz, Fully Coherent FEL Pulses at nm Wavelength

In external seeding, harmonics of a seed laser source are amplified and as a result the wavelength range of the output FEL is restricted by the fundamental wavelength of the seed laser source. This limits the shortest output wavelength that can be achieved and in addition, it limits the tuning range that is not continuous but instead, wavelength gaps within this range are common. To address these two limitations, it is important not only to reduce the fundamental wavelength but also to be able to tune it freely. In this last section of the results of this thesis, I take one more step forward to completely abandon the dependence of seeding on external seed lasers and address these limitations. With the proposed HGHG scheme that depends on a cavity-based FEL that starts from shot noise there are three independent advantages:

1. The fundamental wavelength at the modulator can be decided at wish. This means that it is possible to start from a relatively short wavelength in the order of few to tens of nm, depending on mirror availability. Starting with such a short wavelength can expand the wavelength range of the output FEL to very short wavelengths, which was never possible before with external seeding and harmonic conversion.

2. As the wavelength of the seed in the modulator can be tuned as desired, the problem of the wavelength tunability is solved. A continuous and wide wavelength range is generated and offered to experiments.

3. Similarly with the seeded oscillator amplifier discussed in Section 4, the repetition rate can be adjusted to match the electron bunch repetition rate. The only adjustment is, in principle, the cavity length.

These advantages come with two additional challenges that are thoroughly discussed in this Section. In the proposed setup:

1. A SASE spectrum is expected when starting the FEL process from shot noise and this must be suppressed by a monochromator that will increase the estimated losses in the cavity.

2. A positive net gain is required initially to amplify the power of the stored radiation in the cavity. When the required for seeding power level is reached, the net gain must be reduced back to zero to achieve equilibrium.

Regarding the first challenge, the additional losses due to the monochromator have to be carefully be taken into account in addition to the mirror reflectivity losses. To be able to compensate for these losses, a higher power gain is required in the cavity. Concerning the second challenge of the transition from positive gain to zero net gain, a number of different approaches is suggested and simulated in the following publication. The common thread is that in order to reduce the power gain a very fast feedback is required in the order of the electron bunch repetition rate. Here, CW machines have a natural advantage: since the number of consecutive electron bunches is in principle unlimited, it is possible to reduce the gain slowly and in several passes, reducing this way the requirements on the feedback system. On the other hand, burst mode machines have the inherent difficulty of a finite number of consecutive electron bunches within a flat top. This number of bunches must be used for amplification of the power, for reduction of the power gain with a fast feedback and finally, for the main operation at equilibrium.

In this publication, I again work on the example of a 50 nm fundamental wavelength for consistency, and I use for the simulations the same electron bunch parameters and the same optimized beamline of Chapter 4. The following manuscript was published in the peer-reviewed journal *MDPI Applied Sciences* and as part of the Special Issues *Oscillator-Amplifier Free Electron Lasers an Outlook to Their Feasibility and Performances*. The published manuscript reviews several methods to obtain gain control by showing simulation results and includes analytical calculations for the optimization of the setup and the estimation of the power density that the cavity mirrors should withstand.

applied sciences

MDPI

Article

Advanced Scheme to Generate MHz, Fully Coherent FEL Pulses at nm Wavelength

Georgia Paraskaki [1], Sven Ackermann [1], Bart Faatz [2], Gianluca Geloni [3,*], Tino Lang [1], Fabian Pannek [4], Lucas Schaper [1] and Johann Zemella [1]

[1] Deutsches Elektronen-Synchrotron DESY, Notkestraße 85, 22607 Hamburg, Germany; georgia.paraskaki@desy.de (G.P.); sven.ackermann@desy.de (S.A.); tino.lang@desy.de (T.L.); lucas.schaper@desy.de (L.S.); johann.zemella@desy.de (J.Z.)

[2] Shanghai Advanced Research Institute, Chinese Academy of Sciences, Haike Road 99, Shanghai 201210, China; faatzbart@sari.ac.cn

[3] European XFEL, Holzkoppel 4, 22869 Schenefeld, Germany

[4] Institute for Experimental Physics, University of Hamburg, Luruper Chaussee 149, 22761 Hamburg, Germany; fabian.pannek@desy.de

* Correspondence: gianluca.geloni@xfel.eu

Abstract: Current FEL development efforts aim at improving the control of coherence at high repetition rate while keeping the wavelength tunability. Seeding schemes, like HGHG and EEHG, allow for the generation of fully coherent FEL pulses, but the powerful external seed laser required limits the repetition rate that can be achieved. In turn, this impacts the average brightness and the amount of statistics that experiments can do. In order to solve this issue, here we take a unique approach and discuss the use of one or more optical cavities to seed the electron bunches accelerated in a superconducting linac to modulate their energy. Like standard seeding schemes, the cavity is followed by a dispersive section, which manipulates the longitudinal phase space of the electron bunches, inducing longitudinal density modulations with high harmonic content that undergo the FEL process in an amplifier placed downstream. We will discuss technical requirements for implementing these setups and their operation range based on numerical simulations.

Keywords: seeded FEL; oscillator; amplifier; high repetition rate

check for updates

Citation: Paraskaki, G.; Ackermann, S.; Faatz, B.; Geloni, G.; Lang, T.; Pannek, F.; Schaper, L.; Zemella, J. Advanced Scheme to Generate MHz, Fully Coherent FEL Pulses at nm Wavelength. *Appl. Sci.* **2021**, *11*, 6058. https://doi.org/10.3390/app11136058

Academic Editors: Giuseppe Dattoli, Alessandro Curcio and Danilo Giulietti

Received: 25 May 2021
Accepted: 19 June 2021
Published: 29 June 2021

Publisher's Note: MDPI stays neutral with regard to jurisdictional claims in published maps and institutional affiliations.

Copyright: © 2021 by the authors. Licensee MDPI, Basel, Switzerland. This article is an open access article distributed under the terms and conditions of the Creative Commons Attribution (CC BY) license (https://creativecommons.org/licenses/by/4.0/).

1. Introduction

Free-electron lasers (FELs) have been making enormous improvements during the past decades, delivering high-brightness radiation to users all over the world at wavelengths from mm to hard x-rays, covering a wide range of experiments. At the same time, many experiments, for instance, those that depend on spectroscopic techniques to resolve electronic structure, require full coherence and high statistics, which can only be fulfilled with fully coherent radiation at high repetition rate. These two requirements are becoming important for scientific applications and are driving new FEL developments. Currently, superconducting accelerators are capable of providing thousands of bunches per second at MHz repetition rate. This potential is currently exploited in self-amplified spontaneous emission (SASE) mode [1]. However, in this case, the FEL process starts from random fluctuations of the electron beam charge density distribution [2] leading to a limited temporal coherence, which impacts the peak brightness. The longitudinal coherence can be improved by self-seeding [3,4] and single-mode [5,6] lasing schemes which are based on the SASE process. As a consequence, the stochastic nature of SASE is imprinted on the final FEL pulse as intensity fluctuations even though improved longitudinal coherence is achieved.

At wavelengths in the nanometer range and longer, alternatives to generate fully coherent radiation are based on external seeding. In this case, a seed laser of typically several tens MW of power is used to prepare an initial signal for a final FEL amplifier, usually tuned at a harmonic of its wavelength, thus imprinting its coherence properties upon the output FEL pulse. Many interesting experiments and methods are allowed due to the unique properties of seed radiation [7–10]. Two chief examples of external seeding schemes are the high-gain harmonic generation (HGHG) [11,12] and the echo-enabled harmonic generation (EEHG) [13–15]. As the harmonic conversion of seeding schemes is limited, it is advantageous to use short wavelength seed lasers. Currently, ultraviolet (UV) seed lasers are the most suitable candidates for such setups [14–16]. However, the requirements put on these laser systems in terms of peak power limit their repetition rate, which is usually in the kHz regime. As seeded radiation pulses can be generated at a maximum repetition rate defined by the seed laser repetition rate, not all electron bunches generated in superconducting accelerators can be seeded. This leads to high peak brightness FEL pulses, but limited average flux, in contrast to the number of electron bunches available. In order to address this limitation, alternatives have been recently studied to increase the repetition rate of seeding schemes by reducing the seed laser power requirements [17,18], and in this paper, we propose an oscillator–amplifier setup.

Here, we review and further discuss a scheme which can generate FEL pulses of both high peak brightness, compared to SASE, and of high average flux compared to standard seeding schemes, by generating high repetition rate seeded radiation pulses [19–22]. In this scheme, an FEL oscillator is employed and acts as a feedback system which recirculates a seed pulse, and seeds the electron bunches at high repetition rate. In this case, one may either use a low repetition rate seed laser, or start from shot noise. Starting from shot noise lets us be independent of seed laser systems both in terms of repetition rate and wavelength. Oscillator FELs are a well-studied topic, and their technology has been established for a long time. There is a wide range of oscillator FELs that were operated during the past decades, and detailed simulation studies were performed almost two decades ago [23–25]. These studies led, more recently, to the development of other ideas such as XFELOs [26] and Regenerative Amplifier Free-Electron Lasers (RAFELs) [27–30] (high-gain oscillators). Both these schemes aim at Angstrom radiation with Bragg crystals instead of conventional mirrors, and no harmonic conversion is used. However, at wavelengths in the nanometer range, where crystal optics cannot be used, mirror technology strongly limits the generation of wavelengths below the 190 nm demonstrated at ELETTRA [31]. In order to reach shorter wavelengths, one can exploit a resonator at a longer wavelength, together with harmonic conversion. Such cascades have been proposed in [32–35]. Earlier work on resonators in the EUV regime can be found in [36].

An overview of the seeding schemes that can employ an oscillator to increase the repetition rate of the FEL radiation is given in Section 2, together with comments on its implementation in continuous wave and burst-mode accelerators. Considerations on the implementation of a resonator and a simple model which can be used for its design are provided in Section 3. In Section 4, we introduce the methods used in simulations for power gain control in the cavity, when the start-up of the FEL process is based on random fluctuations of the initial electron beam distribution. In Section 5, we compare these results to the case of an oscillator where the start-up of the FEL process is based on a low repetition rate external seed laser, to the case of standard single-pass seeding, and to SASE simulations.

2. Overview of Methods

2.1. Employing an Oscillator in Standard Seeding Schemes

In this section, we review different schemes that can be implemented with an oscillator in order to provide high repetition rate seed pulses. In standard seeding techniques, an external seed laser is used to modulate the energy of the electron beam as a result of their interaction along an undulator (modulator). In this case, one seed laser pulse needs to be injected for each electron bunch. The purpose of adding an optical cavity to a seeding scheme is to replace the need for an external seed laser, because the cavity can recirculate a radiation pulse and maintain its peak power and pulse properties. In this case, in addition to the energy modulation process which happens along the modulator, an amplification process must also occur. This is important because the power gain is used to compensate for unavoidable cavity losses. Here, we define as net gain the difference between the peak power at the beginning of a pass n + 1 and the peak power at the beginning of pass n, divided by the peak power at pass n. If the power gain compensates exactly for the losses and the net gain is zero, the peak power per pass remains constant as long as the pulse properties remain stable. In this way, the seed pulse is reproducible and can support seeding schemes at high repetition rates.

In this paper we consider two approaches to generate and store a seed laser pulse in cavity.

1. An oscillator-FEL starting with an external seed laser pulse. An external seed laser initiates the modulation of the first electron bunch and the bunch amplifies the seed pulse to compensate for the power losses in the cavity. The optical cavity feeds back the seed pulse which is used to modulate the following bunches. The shortest wavelength of the modulator is determined by the low repetition rate seed laser source and by the mirror availability.
2. An oscillator-FEL starting from shot-noise. An electron bunch generates radiation along the modulator, which is amplified with the number of passes. This process can be divided into two phases. The "build-up regime", where the net gain per pass needs to be positive to build up the peak power required for seeding, and the "steady-state regime" where the net gain needs to go back to zero so that the resonator losses are equal to the power gain. In order to transition between these two phases, an active control on the gain per pass is required. In addition, starting from noise means that a SASE spectrum is generated. This needs to be monochromatized. In this case, the shortest wavelength of the modulator is determined by the mirror availability.

In the following, we consider the implementation of an oscillator-based FEL in support to HGHG and EEHG seeding schemes in order to further extend the tuning range to shorter wavelength and higher repetition rate.

2.1.1. High-Gain Harmonic Generation (HGHG)

HGHG is a method to achieve fully coherent and stable seeded radiation in high-gain FELs and was introduced in [11]. The components needed are a modulator, a seed laser resonant to the wavelength of the modulator, a dispersive section, and an FEL amplifier tuned at a harmonic of the seed laser wavelength. The seed laser is overlapped with the electron bunch in the modulator, and their interaction results in a longitudinal sinusoidal energy modulation along the electron bunch with the periodicity of the resonant wavelength. In the dispersive section placed downstream, the energy modulation is converted into density modulation that includes relevant harmonic content. The dispersive section is characterized by the R_{56} matrix element of the transfer matrix, which describes the evolution of the 6-D phase space (x, x′, y, y′,δ_γ, z) of the electrons. The R_{56} is closely related with the presence of longitudinal dispersion. When a correlation between the longitudinal position (z) and a relative energy offset (δ_γ) is established in the modulator, it is possible to choose an R_{56} to rotate the longitudinal phase space, and convert the energy modulation into longitudinal density modulation. The same matrix element is responsible for the so called bunch compression in accelerators, where we exploit an electron beam with an energy-longitudinal position correlation (electron beam energy chirp) to compress it longitudinally and increase its peak current. After the dispersive section, the bunched electron beam then enters the amplifier and emits coherent radiation. In the case of an HGHG oscillator-amplifier, an optical cavity which encloses the modulator is added as shown in Figure 1. Instead of injecting a seed laser pulse for each consecutive electron bunch, the optical cavity stores a radiation pulse which acts as a seed laser source. Because, as discussed above, a certain amount of power gain is required at each pass, the modulator is longer than in a conventional HGHG scheme.

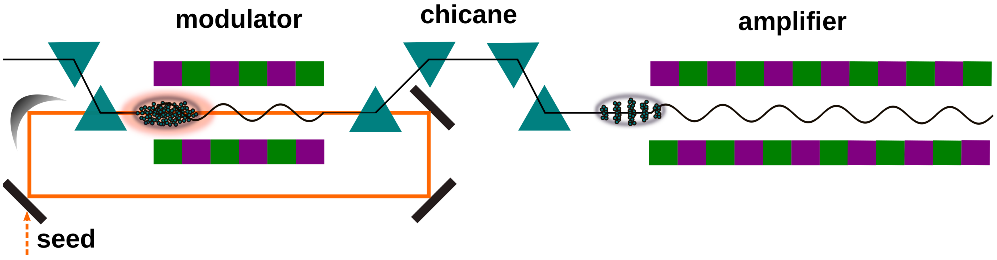

Figure 1. In an oscillator-based HGHG scheme, an optical cavity is added and encloses the modulator. The optical cavity acts as a feedback system which maintains the peak power of the stored radiation field and, under perfect synchronism, this field is used to seed consecutive electron bunches arriving from the linac upstream the cavity. Note that in reality, the optical cavity design will be more complex than this simplified sketch.

2.1.2. Echo-Enabled Harmonic Generation (EEHG)

HGHG schemes are characterized by a limited up-frequency conversion efficiency due to the fact that the nth harmonic requires the energy modulation to be n times larger than the slice energy spread to maximize the bunching. This is typically limiting the conversion to $n = 15$ and critically depends on the energy spread [37]. The EEHG scheme [13–15] was proposed to overcome this limitation, achieve higher harmonics and, thus, shorter wavelengths. In this scheme, there are two seed lasers with two modulators, two dispersive sections, and one radiator. The first modulator and seed laser are used to induce an energy modulation, and then the first dispersive section, which has a large longitudinal dispersion, shreds the longitudinal phase space of the electron beam creating thin energy bands. Each of these bands has a lower energy spread than the initial one, and this way a lower energy modulation is required in the second modulator compared to HGHG. The second dispersive section is weaker and compresses the energy bands. Similarly to what happens in HGHG, it converts the energy modulation from the second modulator into a density modulation, which in this case can have higher harmonic content.

In a regular single-pass EEHG, two modulators and two seed lasers are needed. In order to convert the classic scheme to a high repetition rate cavity-FEL, one possibility is to include two cavities, one for each modulator. In the case of two cavities, the wavelength can be chosen independently and the high repetition rate is secured. Another solution is to feed one modulator with an external seed laser and place the other modulator in a cavity. In this case, the repetition rate of the external seed laser source determines the overall repetition rate. This seed laser should have a longer wavelength which is at present already available at high repetition rate. Then, the other modulator which is enclosed in the optical cavity is resonant to a shorter wavelength.

It is important to investigate if it is more advantageous to have the shortest wavelength at the first or the second modulator. We study the specific case of a combination of two seed laser wavelengths of 300 nm and 50 nm by using an electron beam with a nominal energy of 1.35 GeV, energy spread of 120 keV, and energy modulation amplitudes of $A_1 = 3$ and $A_2 = 5$ times the energy spread in the first and second modulator, respectively. These parameters fit the choices of the FLASH2020+ project [38]. The resulting maximum bunching factor b [13] for final wavelengths between 2 nm and 6 nm is shown in Figure 2a. Using a seed with a wavelength of 50 nm in the first modulator and 300 nm in the second modulator is not beneficial in terms of bunching compared to the classic scheme with two seed lasers with a wavelength of 300 nm, whereas much higher bunching can be achieved by utilizing the shorter seed in the second modulator. Both 50 nm configurations drastically reduce the required longitudinal dispersion of the first chicane, as can be seen in Figure 2b. As the second chicane converts the energy modulation from the second modulator, a seed wavelength of 50 nm in this modulator results in an approximately six times smaller optimum dispersive strength than the one needed for a 300 nm seed.

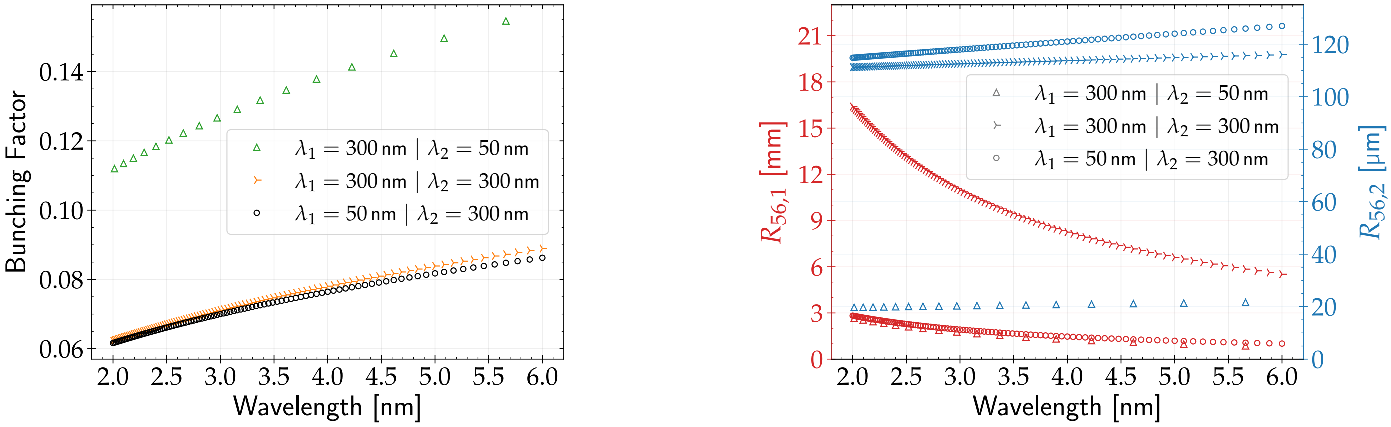

(**a**) (**b**)

Figure 2. (**a**) Maximum bunching factor for different combinations of seed laser wavelengths. (**b**) Optimum setup of the chicanes to maximize the bunching factor. The working point resulting in a lower $R_{56,1}$ is shown for each configuration.

A tunable seed around 50 nm in the second modulator would allow to overcome the limitations of the wavelength separation of the harmonics and provide access to a continuous wavelength range and high bunching. For example, a final target wavelength of 4 nm with more than 13 % bunching could be achieved either by a 47.4 nm or a 51.3 nm seed. The preferred setup with the second modulator enclosed in a cavity and thus being resonant to a shorter seed is shown in Figure 3. As a final remark, we note that one cavity could be employed for both modulators, which would be preferred in terms of cavity length requirements. However, in this case, the peak power of the radiation cannot be tuned independently at the two modulators which is an important aspect of the optimization of EEHG.

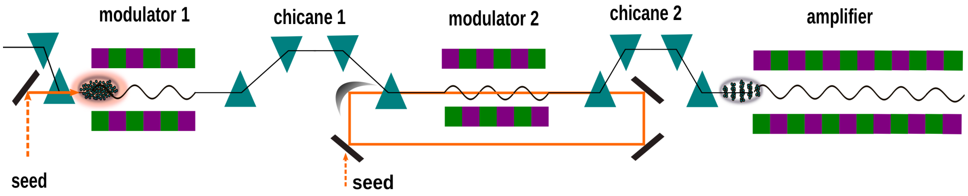

Figure 3. In an oscillator-based EEHG scheme, one or two optical cavities can be attached. In this figure, the first modulation occurs with a conventional external seed laser, while the second energy modulation is achieved by employing an optical cavity around the second modulator. The optical cavity is fed by a seed laser and maintains its properties in order to seed consecutive electron bunches.

To demonstrate the feasibility of the proposed EEHG configuration, a single-pass full simulation with the FEL code Genesis 1.3 [39] is carried out. The wavelengths of the first and the second seed laser are 300 nm and 50 nm, respectively. The electron beam parameters are the same as those used in the already presented analytical calculations above, and in addition, the normalized emittance is 0.6 mm mrad, the electron bunch length is 314 fs full width at half max (FWHM), and the current profile is Gaussian with a peak of 500 A. The duration of the Gaussian seed laser pulses is set to 150 fs and 50 fs FWHM for the first and second seed laser, respectively. The simulation is optimized for an output wavelength of 2.013 nm with longitudinal dispersions of $R_{56,1} = 2.649$ mm and $R_{56,2} = 17.50$ μm. The radiator has a period length of $\lambda_u = 19$ mm and is tuned to the output wavelength. The bunching along the electron bunch upstream from the radiator, the evolution of the FEL peak power along the radiator, as well as the spectrum and power profile at the same position in the radiator are presented in Figure 4. The bunching amplitude is approximately 9.5% and thus slightly smaller than the 11.2% predicted by the simple analytical model (see Figure 2a), but still more than sufficient for an efficient amplification in the radiator.

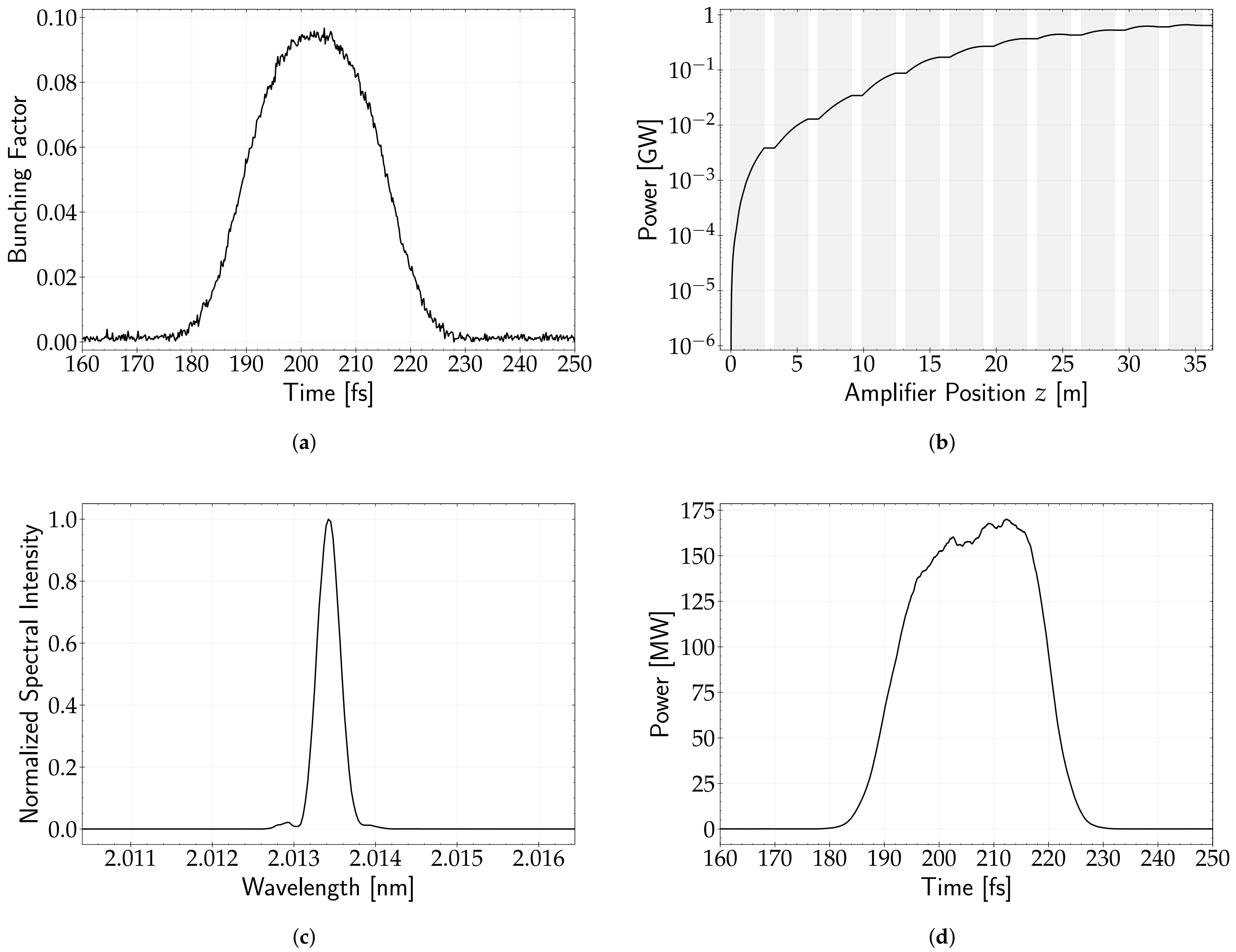

(**a**) (**b**)

(**c**) (**d**)

Figure 4. (**a**) Bunching along the electron bunch. (**b**) FEL peak power along the amplifier modules (gray). (**c**) Spectrum after the 5 modules of the amplifier. (**d**) Power profile after 5 modules of the amplifier.

2.2. Employing an Oscillator-Based Seeding Scheme in an Accelerator in Continuous-Wave or Burst-Mode Operation

A seeded oscillator-amplifier scheme is suitable for accelerators that can generate electron bunches at high repetition rates, as it requires a cavity length which matches the electron bunch repetition rate. The cavity roundtrip length should be $L_{cav} = c/(m \cdot f_{rep})$, where f_{rep} refers to the electron bunch separation and m is an integer which represents the number of roundtrips of the radiation before it meets again an electron bunch. For instance, when the electron bunches arrive with a frequency of 1 MHz, the total roundtrip cavity length should be $L_{cav} \approx 300$ m for $m = 1$. Alternatively, the radiation pulse can perform more than one roundtrip in between two consecutive bunches. However, in this case the total resonator reflectivity decreases with the number of passes m as R^m.

A superconducting accelerator can run in continuous wave (CW) or burst-mode operation. At FLASH [40,41], which operates in burst-mode, the bunch trains arrive with a repetition rate of 10 Hz with a flattop of 800 µs and a bunch spacing of 1 µs (1 MHz repetition rate). With a pulsed operation at 10 Hz as well, the flattop of the European XFEL is 600 µs with a 0.22 µs bunch separation (4.5 MHz) [42]. The exact number of bunches available depends on the operation mode and the sharing of those bunches among different undulator beamlines. In the case of burst-mode operation, there is a specific number of bunches available to build-up the peak power and stability needed to deliver seeded FEL pulses. This is not an issue when the process starts with a low repetition rate seed laser source because the steady-state regime is reached within a few passes [22] as shown in Figure 5a, but it is critical when starting from shot noise, as we show in Figure 5b. The build-up regime is marked with a green background color. During this process, there must be positive net gain, and the peak power in each pass increases. The steady-state regime is marked with blue color in the same figure, and refers to the passes in the oscillator where the net gain is zero and the peak power per pass is constant. Comparing Figure 5a,b, there are more power fluctuations in the case where we start with a seed laser. This might be due to the fact that in this case we do not use a monochromator.

In burst-mode operation, the more bunches are used during the build-up process, the less bunches will be part of the steady-state regime when seeded radiation is generated. The steady-state can be maintained for a maximum number of passes defined by the difference between the available bunches in one bunch train and the number of bunches used during the build-up process. Taking as an example FLASH and the build-up regime shown in Figure 5b, we would need 18 bunches to take part in the build-up of the power, and the remaining 782 bunches would be part of the steady-state regime where the seeded radiation is generated.

A machine operated in CW mode offers a continuous number of bunches with a constant separation between them. For instance, SHINE in Shanghai will be operated in a CW mode and is expected to provide bunches with a continuous 1 MHz repetition rate [43]. The same repetition rate is planned for LCLS-II [44] as well. In this case, the build-up time needed becomes less important. It is possible to increase the number of passes in the build-up regime and ensure a smooth transition to the steady state. However, it becomes more important to verify how long the steady-state regime can be maintained before the process needs to be initiated again.

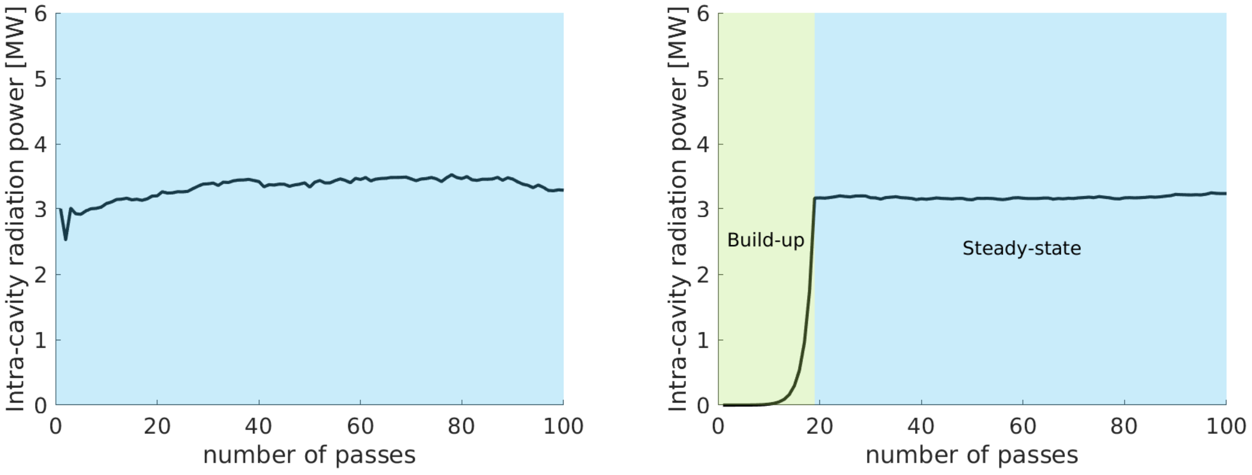

(**a**) (**b**)

Figure 5. (**a**) Example of the peak power per pass in an oscillator starting with a low repetition rate seed laser. From the first pass already the net gain should be zero. In practice, it takes a few passes for the system to self-stabilize. (**b**) Example of the peak power per pass in an oscillator starting from shot-noise. For 19 passes the build-up regime where the net gain is positive is highlighted with a green color. At pass 19, the desired peak power level is reached and the steady state regime is entered, marked with a blue color. From this pass and onward, the net gain is reduced to zero and the peak power level is maintained in each pass.

3. Resonator Considerations

3.1. A Simple Model for the Reflectivity Requirements and Estimated Power Level in the Cavity

The transition between the build-up and the steady-state regime in the case of start-up from shot noise is discussed in more detail in Section 4, while here we focus on the steady-state operation of the modulator-amplifier. We maintain the generality of the discussion by using approximations to build a simple model that can be used to investigate the parameter space for the design requirements. In the steady-state regime, there is a number of conditions that need to be fulfilled:

- The input seed power needs to exceed the shot noise power of the electron beam by several orders of magnitude; otherwise, the SASE is not suppressed and the seeding process is not successful. Only a part of the seed power contributes to the exponential growth. Using for estimation the 1D cold FEL model this fraction amounts to 1/9. Assuming an excess of 3 orders of magnitude, the minimum input seed laser pulse peak power needs to be at least several 10 kW to 100 kW, depending on the exact electron beam parameters [45]. In addition, for seeding techniques it is required to induce an energy modulation of several times the initial energy spread which depends on the target harmonic to be amplified, the exact seeding scheme and the modulator length for given electron beam parameters. Typically, this requires a peak power that is larger than 100 kW.
- The saturation power downstream of the modulator needs to be well below the "natural" saturation to avoid large induced energy spread, which would suppress the amplification process at the amplifier. As a general rule, the energy spread downstream of the modulator σ_E relative to the electron beam energy E, should be considerably less than the FEL parameter of the amplifier ρ_{amp} [46], thus $\sigma_E/E \ll \rho_{amp}$ [45]. The maximum acceptable seed peak power after amplification in the modulator strongly depends on the length of the modulator with respect to the gain length, and thus on the power amplification and on the energy spread increase. For the sake of avoiding a specific parameter set, here we assume that saturation at the seed laser wavelength yields between 1 GW to several 10 GW. Assuming a margin of 3 orders of magnitude to avoid "heating" of the beam, the seed peak power after amplification needs to be limited to not more than several tens of MW.

The gain from shot noise to saturation of an FEL is around 9 orders of magnitude, which corresponds to about 20 power gain lengths (L_g). This means that there are 3 orders of magnitude between the minimum input peak power (P_{in}) and the maximum output peak power which are allowed to be lost in the cavity. Otherwise, either the minimum power is too close to shot noise or the maximum power too close to saturation. It is clear that these boundaries are not very strict and should only be seen as an approximation. It is known that the power along z develops as [46]:

$$P(z) = \frac{P_{in}}{9} \cdot e^{z/L_g}\,. \tag{1}$$

With a roundtrip reflectivity R, the power after a modulator length of L_{mod} should be $P(L_{mod}) = P_{in}/R$. This leads to

$$\frac{P_{in}}{R} = \frac{P_{in}}{9} \cdot e^{L_{mod}/L_g} \rightarrow L_{mod} = L_g \cdot \ln(\frac{9}{R}) \tag{2}$$

For the first approximately three power gain lengths we expect no FEL power amplification, and this is referred to as the lethargy regime. Assuming three orders of magnitude for the maximum allowed power amplification, the maximum modulator length is $9 \cdot L_g$ to compensate losses. The same equation can be used for design considerations; for instance, for a total reflectivity of 6%, the modulator should be roughly $5 \cdot L_g$. This result is independent of the input seed laser power, however, in practice, the energy modulation process depends on both the input seed peak power and the length of the modulator as [47]:

$$\Delta E = \sqrt{\frac{P_{in}}{P_o}} \frac{m_e 2 K L_{mod} \mathrm{JJ}}{\gamma w_0}, \tag{3}$$

where w_0 is the seed waist size, K is the dimensionless undulator parameter, m_e is the electron mass in keV, $P_0 \approx 8.7\,\mathrm{GW}$ [47], $\mathrm{JJ} = J_0(\xi) - J_1(\xi)$, where $\xi = K^2/(4+2K^2)$ and $J_{0,1}$ the Bessel function of the zeroth and first order. As the modulator is used both for energy modulation and amplification, both these aspects need to be taken into account for the exact design. Let us consider an example of these analytical estimations by means of a reasonable set of parameters: $\lambda_{seed} = 50\,\mathrm{nm}$, $K = 3.25$, $w_0 = 286\,\mu\mathrm{m}$, $\gamma = 2641.9$, $L_g = 1.12\,\mathrm{m}$. In Figure 6, we show the expected energy modulation for a combination of seed laser peak power and modulator length, calculated with Equation (3). In the same figure, we show the reflectivity required as expected by the 1D cold theory and Equation (1) with the dashed black vertical lines, as it is independent of the input seed laser power. It is clear that while the modulator length is fixed and is used to determine the amplification, for a given modulator length, it is still possible to use the seed laser peak power as a knob to adjust the energy modulation. In turn, the energy modulation is related to the energy spread which affects the FEL process in the amplifier, as already discussed. Note that while Equations (1) and (3) are well established approximations valid in the 1D case, diffraction effects should be also taken into account and the exact dependencies may deviate from this result.

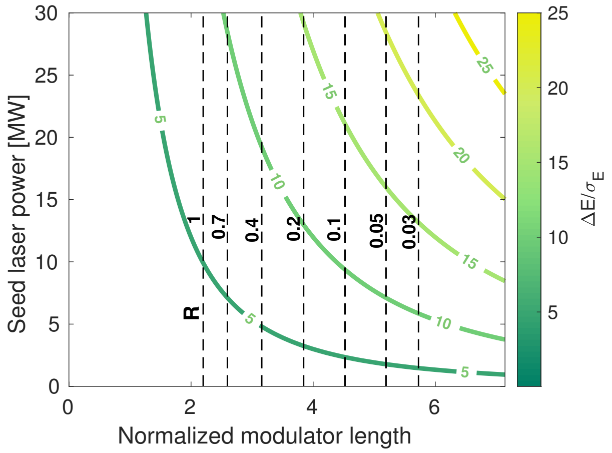

Figure 6. The color bar indicates the energy modulation achieved for combinations of seed laser peak powers (P_{in}) and modulator lengths (L_{mod}) and is calculated with Equation (3). The horizontal axis shows the normalized modulator length to the gain length (L_{mod}/L_g). The vertical dashed lines show the reflectivity R required for equilibrium between amplification and losses for different normalized modulator lengths, and is calculated with Equation (2).

3.2. Cavity Design Considerations

The numbers quoted so far are needed for the system to work, and should be complementary with a discussion on the technical feasibility of the resonator. The important questions here are if the downstream mirror, which will have the maximum power density, will be able to withstand it, and if mirrors with the required properties actually exist. We consider two operation regimes for the resonator: one at a wavelength between 200 nm and 300 nm, and one between 50 nm and 100 nm.

Regarding the reflectivity requirements, we expect that for wavelengths around 300 nm, the mirror choice will not pose an issue as there are options to choose from. Optics in this wavelength regime are used for current laser systems, such as dielectric mirrors, with reflectivity and damage threshold that guarantee sustainable operation and have been studied for other storage ring FELs in the past as well [48]. The main challenge is faced for the working point in the XUV range between 100 nm and 50 nm, where no commonly used options are available. Here, we consider the upper limit in gain, where the roundtrip loss should not exceed a factor 1000 to avoid electron beam heating. Under normal incidence, this means that each mirror should reflect at least $1/\sqrt{1000} \approx 1/33$ or 3%. In case of a ring resonator with mirrors at 45 degree incidence angle, each should reflect more than $1/\sqrt{\sqrt{1000}} \approx 1/5.6$ or 18%. For example, we consider Molybdenum mirrors. At normal incidence, the reflectivity at 40 nm is ~6%, at 45 degree around 40% [49]. Both values exceed the requirements. Note that a gain of 1000 is an upper limit that would require a relatively long modulator. However, it is preferred to operate at a lower gain if the reflectivity of mirrors allows it.

Here, we consider simple estimations in order to calculate the power density for a Gaussian beam. Assuming a Gaussian beam with a waist at the end of the undulator, the size of the spot at the mirror is [47]:

$$w^2(L) = w_0^2\left(1 + \left(\frac{L}{\ell}\right)^2\right), \tag{4}$$

where L is the distance from the undulator to the mirror, w_0 is the spotsize at the waist and ℓ is the Rayleigh length. With the distance to the mirror much larger than the Rayleigh length and remembering that for a Gaussian beam $\pi w_0^2 = \lambda\ell$ with λ the radiation wavelength, the dependence of the beam radius on the distance becomes nearly linear and we can rewrite Equation (4) as

$$w^2(L) \approx \left(\frac{L\lambda}{\pi w_0}\right)^2 \approx \left(\frac{L\lambda}{\pi\sigma_b}\right)^2, \tag{5}$$

where we have approximated the spotsize of the radiation with the electron beam size σ_b. Since the mirror has an angle with respect to the radiation in one plane only, the area of the radiation on the mirror for a transversely symmetric beam can be approximated as:

$$S \approx \left(\frac{L\lambda}{\pi\sigma_b}\right)^2 \frac{1}{\sin\alpha}, \tag{6}$$

with α the glancing angle.

Assuming that the fraction of the pulse energy that is not reflected by the mirror is in fact absorbed, the power density P_d absorbed is

$$P_d = \frac{E_p}{S} \cdot (1 - R) = E_p(1 - R)\sin\alpha\left(\frac{\pi\sigma_b}{L\lambda}\right)^2, \tag{7}$$

with E_p the pulse energy.

Here, we take the example of FLASH2 and the existing mirrors commonly used in FLASH operation to demonstrate a feasible working point. For a wavelength of 15 nm with a mirror 15 m downstream of the undulator under a glancing angle of 1 degree, from Equation (6) the spot size is approximately 0.3 cm^2, assuming a 100 µm beam size. With a reflectivity of 99% ($R = 0.99$) and 1 mJ of pulse energy per second for a single pulse, the power density is around 1 mW/0.3 cm^2, or up to 17 W/cm^2 for a pulse train of 5000 pulses per second. Under these assumptions and taking into account the reflectivity, the absorbed power of FLASH2 on the mirror is up to 170 mW/cm^2 for 15 nm.

For a modulator with the mirror at normal incidence at the same distance of 15 m, the same electron beam size and a wavelength of 50 nm, the spot is from Equation (5) approximately 2.4 by 2.4 mm. Assuming again Molybdenum mirrors with 95% absorption, the pulse energy should not exceed 2 µJ in order to avoid an absorbed power density higher than 170 mW/cm^2. At 45 degrees with 60% absorption, the pulse energy would be approximately 5 µJ. Assuming a typical pulse duration of 100 fs, the peak power is therefore 20 MW (or 50 MW for the 45 degree mirror case), which is consistent with the values mentioned earlier for FLASH. For a CW-FEL, the numbers are more critical because of the larger number of bunches per second.

Finally, we would like to comment on the geometry of the optical feedback system. There is a number of components needed in order to maintain a stable operation and diagnose the radiation field properties. The intensity of the seed laser, which in this case is the intensity inside the resonator, needs to be regulated and therefore measured for a large wavelength range without significant distortion of the radiation field. Furthermore, with the system starting from noise, the noise needs to be suppressed, which is best done with a grating. Finally, the radiation needs to be refocused in the middle of the modulator. Therefore, the actual resonator will have a more complicated geometry than depicted earlier. A ring resonator could include all needed elements, but other geometries should be considered and compared depending on the wavelength requirements and space constraints of a specific facility. The technical design and specifications are, however, beyond the scope of this paper.

4. Simulation Results and Implementation Considerations for Oscillator-Based Seeding Starting from Shot Noise

In this section, we focus on an HGHG-based oscillator scheme as shown in Figure 1 and more specifically, in the case of an oscillator-FEL starting from shot noise. As shown in Figure 5b, when the process in the cavity starts from shot noise, there are two separate operation regimes to be considered. For a transition from positive net gain (“build-up”) to zero net gain (“steady-state”), the gain has to be reduced. Here, we discuss different methods that could be applied in order to achieve control over the power gain in the resonator. In all cases we use the same set of simulation parameters, which is summarized in Table 1, and the modulator is resonant with 50 nm wavelength. For the sake of simplicity, here we restrict ourselves to the case of a relative energy modulation $A = \Delta E/\sigma_E = 7$, meaning that the amplitude of the energy modulation ΔE after the modulator is seven times larger than the initial energy spread σ_E in the steady-state regime. As seen in Equation (3), for given lattice, electron beam parameters and constant waist size, the energy modulation is stabilized if the input peak power in the modulator P_{in} is stable too. All simulations here are done with Genesis 1.3 for the FEL process [39], while the radiation field in the cavity is treated with ocelot [50], which accounts for the slippage, reflectivity, focusing, and monochromatization.

Table 1. Electron beam parameters used in simulations.

Electron Beam Parameters	
Energy	1350 MeV
Energy spread	120 keV
Peak current	1 kA (flat-top)
Pulse duration	300 fs
Normalized Emittance	1 mm · mrad

4.1. Reflectivity Adjustment

The most direct way to control the net gain is to adjust the resonator reflectivity. In this case, initially the reflectivity ($R_{build-up}$) is as high as possible to enable a fast build-up of the power and then, when the desired peak power level is reached, the reflectivity has to drop to the value R_{equil}, which ensures equilibrium between losses and power gain. The reflectivity applied during the build-up process, $R_{build-up}$, is determined by the maximum total reflectivity allowed by the mirrors, and the maximum change in reflectivity that can be supported by a filter within the time separation of two consecutive bunches. The larger the difference in reflectivity $\Delta R = R_{build-up} - R_{equil}$ is, the higher the net gain and the faster the steady-state regime will start, as shown in Figure 7a. For the present setup of resonator and beam parameters shown in at Table 1, the reflectivity at equilibrium is $R_{equil} = 10.6\%$, including the losses in the monochromator. With $R_{build-up} = 14\%$, 46 passes are required in the build-up regime in order to reach a relative energy modulation of $A = 7$, while a reflectivity of $R_{build-up} = 12\%$ requires 99 passes. It is also possible to apply the reflectivity change in steps if a fast change is not possible. For instance, for the reflectivity change required as shown in Figure 7b, it is possible to apply the $\Delta R = 3.4\%$ (from $R_{build-up} = 14\%$ to $R_{equil} = 10.6\%$) in steps of $\Delta R = 0.34\%$ in 10 passes. In the case of a burst-mode of operation, the number of steps must be reasonably small compared to the number of bunches at the steady-state. In the case of a continuous wave operation, these steps can be as small as required by the hardware limitations.

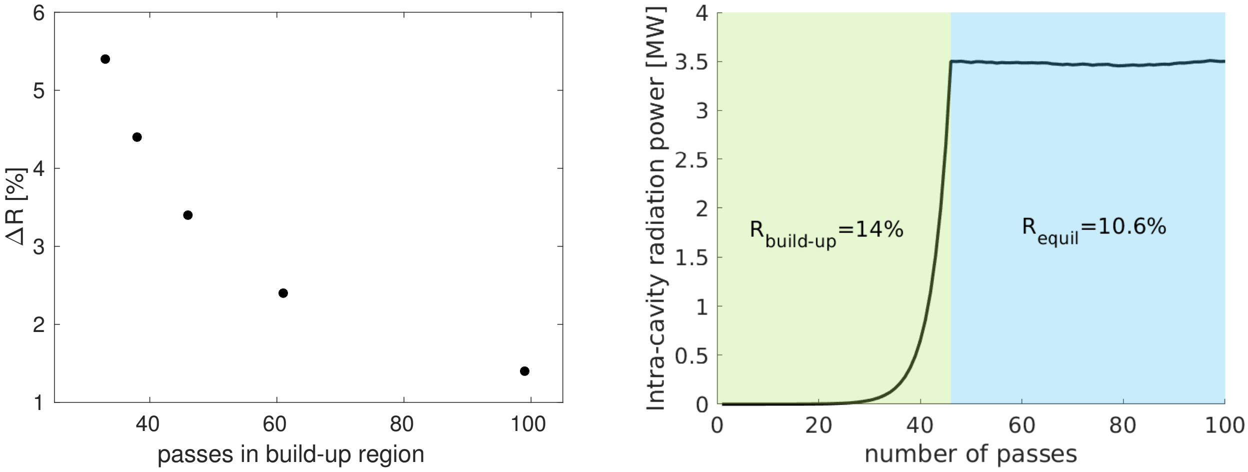

(a)

(b)

Figure 7. (**a**) In this plot, the number of passes needed to reach steady-state as function of reflectivity change, $\Delta R = R_{build-up} - R_{equil}$, is shown. We assume that the build-up process is over when the energy modulation is at least A = 7. (**b**) Example of $\Delta R = 3.4\%$. For the first 46 passes the reflectivity is set to $R_{build-up} = 14\%$ and from the 47th pass onward the reflectivity drops to $R_{equil} = 10.6\%$ and the net gain is zero. As a result, the peak power is stabilized.

In practice, the reflectivity change can be implemented by adding a filter in the return path of the radiation field. A total reflectivity change of several percent is currently not possible to be applied within 1 μs, but would be possible in several steps during a transition time. For this reason, this method would be an option in CW machines, as it is currently unlikely to function in burst-mode in view of time constraints.

4.2. Longitudinal Overlap between Electron Bunch and the Recirculating Light Pulses

Another method to obtain gain control is by affecting the longitudinal overlap between the electron bunch and the stored radiation field. A change in cavity length would change the arrival time of the radiation pulse, a procedure known as cavity detuning. The exact amount of the detuning or delay needed to transition between positive net gain and zero net gain depends on the electron bunch length. Here, we have assumed a 300 fs flat-top current distribution for the electron bunch as an example study.

For all passes, the reflectivity is set to a value R_{set} which is larger than R_{equil}, namely, the reflectivity, which leads to zero net gain when the longitudinal synchronism between the electron bunches and the recirculated seed pulse is optimum. Here, we define the cavity length L_{cav} for which the detuning is zero ($\Delta L_{cav} = 0$), as the cavity length for perfect synchronism between the radiation pulses and consecutive electron bunches for no slippage, thus it is the cold cavity length. Due to slippage effects, perfect synchronism is achieved for longer cavity lengths ($\Delta L_{cav} > 0$) that allow the longitudinally advanced radiation pulse to be delayed. As in this case we assume that the reflectivity cannot be reduced, we keep the reflectivity constant over all passes and we de-tune the cavity by ΔL_{cav} to reduce the net gain in the steady-state regime. The detuning and the reflectivity are two complementary knobs. The larger the reflectivity difference $\Delta R = R_{set} - R_{equil}$ is, the longer the detuning is needed.

In Figure 8a, a cavity detuning is simulated for a range of set reflectivities R_{set} between 11% and 15% . The cavity detuning curve for each reflectivity shows how much the length of the cavity should be shifted to move from the maximum net gain (shown with the vertical arrow), to zero net gain (intersections between the horizontal dashed line and detuning curve). The cavity detuning for maximum power gain is independent of the total reflectivity as expected, as it depends on the total slippage per pass, which is in turn dependent on the wavelength, the periods of the modulator and the group velocity of the field. Taking again the example of $R_{set} = 14\%$, in Figure 7a we need 46 passes to reach the desired in-cavity peak power level with the optimum detuning of $\Delta L_{cav} = 2.7\,\mu\text{m}$, and from Figure 8b we see that a detuning of $\Delta L_{cav} = -14.1\,\mu\text{m}$ keeps the in-cavity peak power level constant. The result is shown in Figure 8b, where the cavity length is shifted by 16.8 µm and equilibrium is reached and maintained.

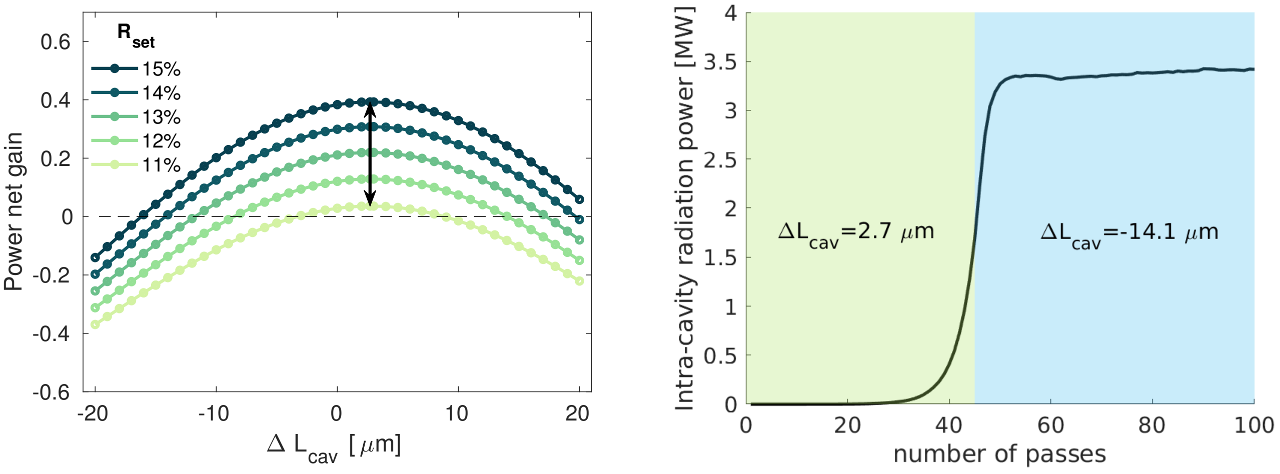

(**a**) (**b**)

Figure 8. (**a**) Detuning curves for a 300 fs flat-top electron beam. The optimum detuning length is at $\Delta\lambda = 2.7\,\mu\text{m}$, for all set reflectivities, as shown with the vertical arrow. The zero net gain point shown with the horizontal dashed line, shows the detuning that needs to be applied to reach equilibrium for each total reflectivity R_{set}. Keeping the reflectivity constant and changing the cavity length can transition the system from positive to zero net gain. We remind the readers that the power net gain has no units as it is the difference between the peak power at the beginning of pass n + 1 and at pass n, divided by the peak power at pass n. (**b**) With an oscillator starting from the random fluctuation of the electron beam distribution, a transition between amplification of the power and maintenance of the peak power is achieved by detuning the cavity length from $\Delta L_{cav} = 2.7\,\mu\text{m}$ to $\Delta L_{cav} = -14.1\,\mu\text{m}$. For all passes the reflectivity is $R_{set} = 14\%$.

For the implementation of this technique there are different options that can be considered. When detuning the cavity length, the position of one or more mirrors needs to be adjusted within µm and with a MHz repetition rate. This depends heavily on the mirror choice and mirror size and weight. As an alternative solution, in the past a similar dynamic cavity desynchronization was considered for FELIX [51] in order to control the growth rate and the final power at saturation and the fluctuations in power [52,53]. It was proposed that instead of mechanically adjusting the mirrors, it is preferable to ramp the electron bunch repetition rate frequency by Δf_{rep} to achieve a cavity detuning of $\Delta L_{cav} = L\Delta f_{rep}/f_{rep}$ [53]. In this case, a dynamic desynchronization along the bunch train is important.

As a final remark, it is important to point out that the cavity detuning results in a change in the temporal and spectral distribution of the stored FEL pulse. This has been extensively discussed in FEL oscillators in the past [54–56]. The consequences on the properties of the output FEL should be carefully considered before applying this method for power gain control.

4.3. Optical Klystron

Another well-established method of gain control in FELs is the use of an Optical Klystron (OK), first introduced in [57]. It was originally introduced for gain control in oscillator FELs [58], but its application has been expanded. It has been used as a method to speed up the FEL process in SASE operation, when the total amplifier length is not sufficient for a given wavelength [59–61]. In addition, it is used in a seeding scheme when the seed laser peak power is not sufficient to increase the energy modulation required in seeding [17]. The simplest configuration of an optical klystron consists of two undulators tuned at the same resonant wavelength and a dispersive section in between them. The electron beam travels in the first undulator starting from some initial conditions (noise, or external seed) and a relatively weak energy modulation is induced. Then, the dispersive element modifies the electron beam phase space. This way, the bunching at this fundamental wavelength is increased, and the bunched electron beam generates coherent emission in the second undulator with increased gain. The dependence of the power gain on the longitudinal dispersion is a useful knob for our setup.

In an oscillator, the two modulator sections separated by the dispersive section are in the resonator as shown in Figure 9. A 1D theory of optical klystron is discussed in [61] and a recent revision can be found in [62]. The optimum longitudinal dispersion depends on the energy spread and in our case can be estimated as

$$R_{56,1} = \frac{\lambda_{res}}{2\pi\delta}, \tag{8}$$

where δ is the relative energy spread. With the studied parameter space, the optimum longitudinal dispersion is predicted as $R_{56,1}$ = 89 µm. Note that the sum of the length of modulator 1 and modulator 2 in Figure 9 is equal to the length of the modulator in Figure 1, so the power gain increase is introduced by chicane 1 only, and not by increasing the length of the modulator.

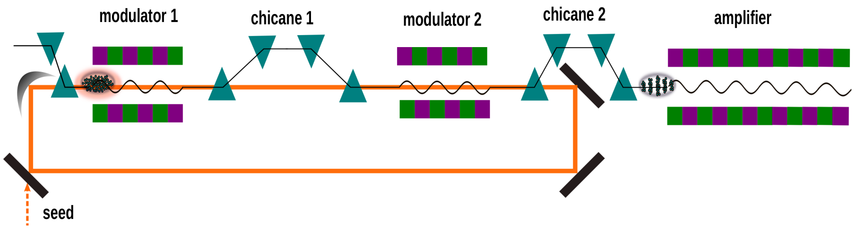

Figure 9. In an oscillator-based HGHG scheme, an optical klystron can be employed. To do so, the cavity contains two modulators separated by a chicane. This way this chicane can be tuned to control the gain per pass.

In order to transition to the zero net gain regime, the $R_{56,1}$ should initially be set to a value close to the optimal, and later on tuned to another value which would reduce the gain in the second modulator. In Figure 10a, we show the net gain achieved for different reflectivities and $R_{56,1}$. The $R_{56,1}$ at the steady state is determined by the intersection of the curves and the horizontal dashed line, which shows the zero net gain. We are interested in the range $R_{56,1} < 75$ µm, because a too large $R_{56,1}$ would cause an over-rotation of the longitudinal phase space which is not useful, as we still need to increase the bunching at a harmonic of the seed wavelength with the $R_{56,2}$. The optimum longitudinal dispersion appears at around $R_{56,1} = 73$ µm, which is approximately in agreement with Equation (8). Note, here, that the reflectivities required with the optical klystron are dramatically reduced, by more than an order of magnitude, when we compare to Figure 8a. As an example, with a reflectivity $R_{set} = 0.38\%$, we can build-up the peak power needed for seeding with $R_{56,1} = 42.5$ µm, and after 19 passes change the longitudinal dispersion of the first chicane to $R_{56,1} = 30$ µm to achieve zero net gain, and stable peak power of the radiation field per pass as shown in Figure 10b. Note, here, that the input peak power is considerably lower in the order of 120 kW compared to the roughly 3.5 MW needed in all other gain-control methods presented already, to achieve the same energy modulation $A = 7$. In addition, the reflectivity required, $R_{set} = 0.38\%$, which considerably relaxes the requirements on the mirror specifications.

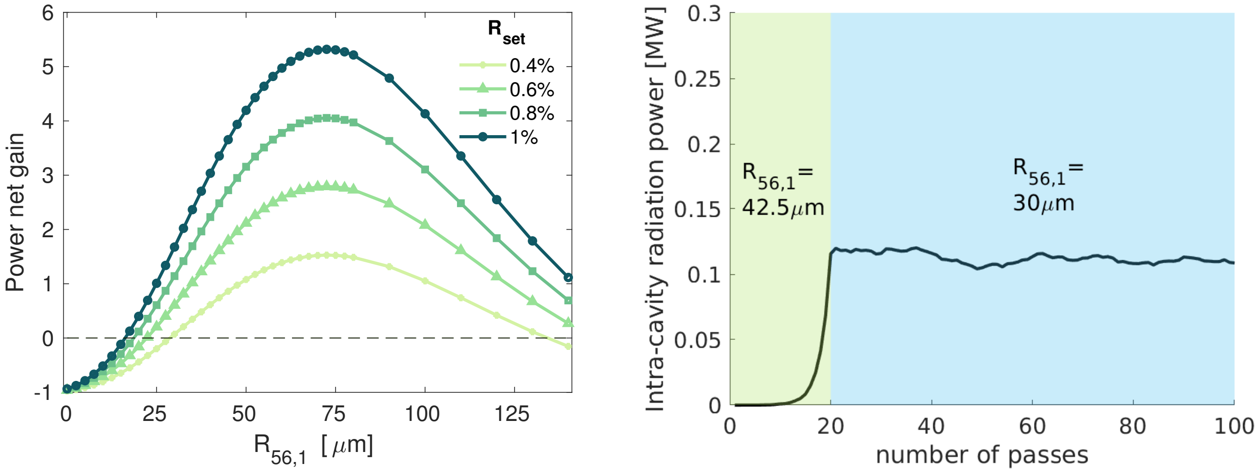

(**a**) (**b**)

Figure 10. (**a**) Changing the $R_{56,1}$ of the chicane affects drastically the gain in power. Here we show the net power gain for selected set reflectivities R_{set}, between 0.4% and 1%. The horizontal line shows the zero net gain. (**b**) With a reflectivity $R_{set} = 0.38\%$, it is possible to transition from positive gain to zero gain by adjusting the longitudinal dispersion of chicane1 as shown in Figure 8, from $R_{56,1} = 42.5\,\mu\text{m}$ to $R_{56,1} = 30\,\mu\text{m}$, respectively.

The optical klystron has many advantages. As already explained, the first one is that it makes the transition from positive to zero net gain possible. In addition, it increases the gain both in the positive gain regime and in the zero net gain regime as $R_{56,1} \neq 0$ as well. This relaxes significantly the requirements in mirror reflectivity in the XUV range. Moreover, the optical klystron could be used as an active tuning tool to adjust the gain per pass and absorb different sources of jitter which contribute to gain changes. Concerning technical requirements, a chicane consisting of fast kickers for this purpose should be able to change the R_{56} by several µm and with a MHz repetition rate. Stripline fast kickers are already standard technology and are, for instance, used at the European XFEL for extracting individual electron bunches with up to 4.5 MHz repetition rate [63,64]. Let us assume that a change of 10 µm is sufficient to transition from positive net gain to zero net gain. The longitudinal dispersion of the chicane is approximately $R_{56} \approx L\theta^2$, where L is the distance between the first and second dipole of a chicane and θ is the bending angle of the first dipole. A kicker adds an angle

$$\Delta\theta[\mu\text{rad}] = L_{kicker}[\text{cm}]B_{kicker}[\text{Gauss}]/E_b[\text{GeV}],$$

with L_{kicker} and B_{kicker} being the length and field of the kicker and E_b the electron beam energy. With these kickers, a kick angle of 0.6 mrad can be achieved with $E_b = 1\,\text{GeV}$ and the change of R_{56} shown in Figure 10b would be possible within 1 µs. It is important to ensure that implementing this change in R_{56} will not affect the stability of the system. Using the kickers only in the build-up regime would ensure stability during the steady-state regime. For the build-up regime, the stability is not so important, as long as the peak power is reached, since during these passes no seeded radiation is generated.

5. Comparison of Simulation Results

Until now, we have only discussed about the process in the modulator and resonator. In this section, we compare simulation results at a final wavelength of 4.167 nm, reached with different schemes and this time we show the final FEL pulses generated at the amplifier. For the HGHG simulations, this wavelength is the 12th harmonic of a 50 nm resonant modulator. We consider the following four cases:

- A SASE setup, starting from shot noise and without changing any electron beam parameters. The FEL pulse is extracted at the same position as the seeding simulations.
- A single-pass standard HGHG setup, starting with an ideal Gaussian seed laser pulse instead.
- An HGHG seeded oscillator-amplifier starting with a low repetition rate seed laser. This scheme was discussed in detail in [22]. For the first electron bunch an external seed laser pulse is injected, and then the seed pulse is stored in the cavity.
- An HGHG seeded oscillator-amplifier system starting from shot noise. This was described in detail in Section 4. A reflectivity change from $R_{build-up} = 14\%$ to $R_{equil} = 10.6\%$ was used to transition from positive to zero net gain.

In Table 2, we have summarized the main simulation results for the four different cases, and in Figure 11 we show the final spectra for the four different cases with the same final wavelength of 4.167 nm. In addition, for completeness, we have added the pulse properties of the output FEL at 2 nm with the EEHG simulations discussed in Section 2.1.2. The output FEL is shown in Figure 4. Note that the peak power is comparable for all HGHG seeded pulses as expected; however, as the resulting pulse duration differs, the bandwidth cannot be directly compared. It is important to emphasize that a single-spike spectrum was generated in all seeded schemes. The power spectral density in the multi-pass HGHG starting with a seed laser, and in the standard single-pass HGHG are almost identical, while the multi-pass HGHG starting from shot noise seems to have almost an order of magnitude higher spectral density as shown in Figure 11d. In this case, we have used a monochromator with an rms bandwidth of $\Delta\lambda/\lambda = 2.5 \cdot 10^{-4}$ in the resonator, which stretches the radiation pulses and filters the radiation in the frequency domain. Because of this, the result in Figure 11d deviates compared to the other two HGHG cases.

Table 2. Simulation results for final FEL pulse at the same position along amplifier. For the multi-pass simulations, we examine the FEL pulse after 100 passes. For the SASE, we calculate based on the average over 50 simulations with different shot noise. For EEHG, we consider the simulation results of a 2 nm output FEL shown in Figure 4.

	Peak Power	$\Delta\lambda_{FWHM}/\lambda$	rms Pulse Duration
SASE	3 MW	2×10^{-3}	75 fs
Standard HGHG	1.2 GW	1.6×10^{-4}	20 fs
multi-pass HGHG (seed)	1.2 GW	2×10^{-4}	27 fs
multi-pass HGHG (shot-noise)	1.1 GW	5×10^{-5}	60.6 fs
single-pass EEHG	0.18 GW	1.6×10^{-4}	11.35 fs

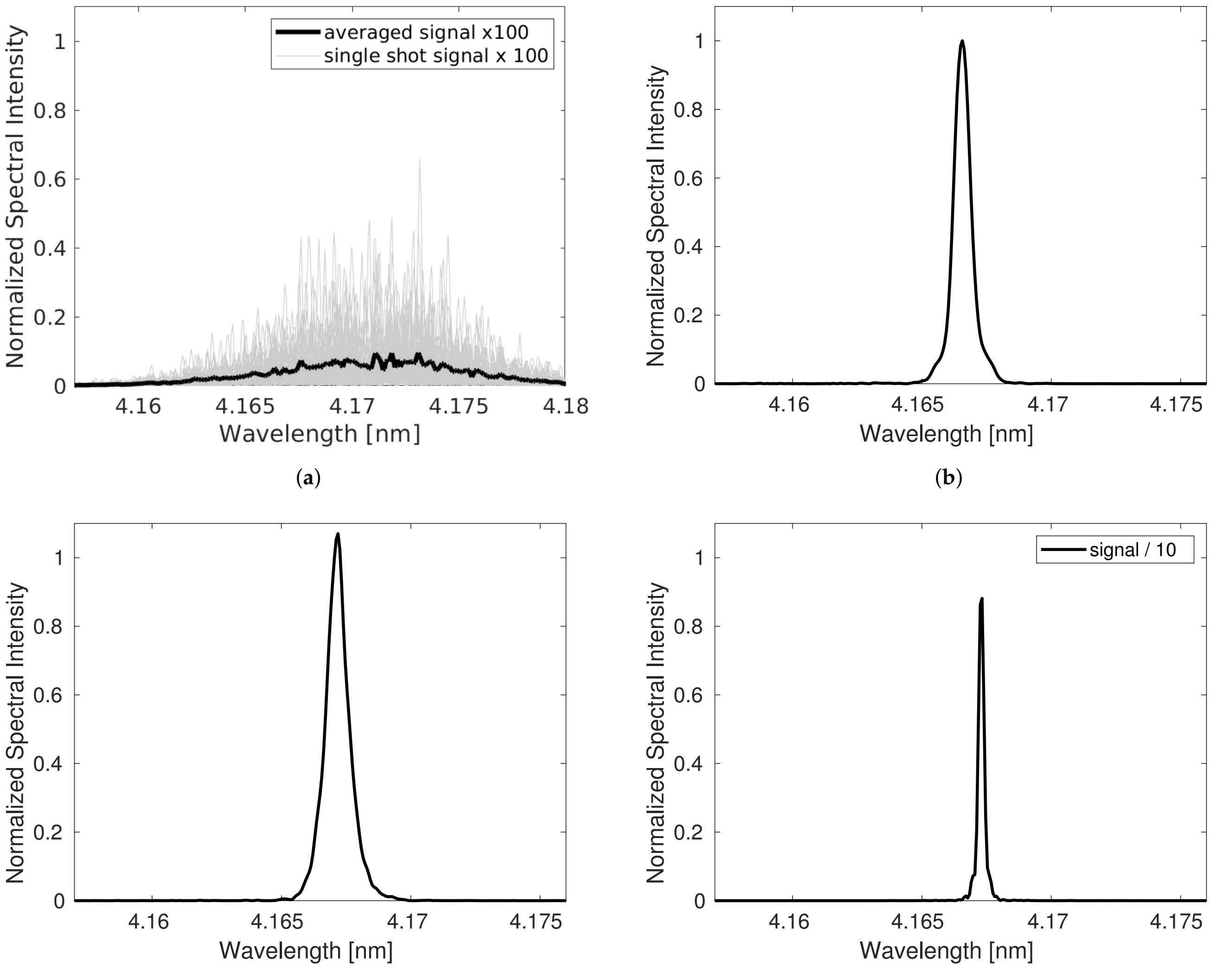

(**a**) (**b**)

(**c**) (**d**)

Figure 11. Spectra of final FEL pulse at the same position at the amplifier and with the same electron beam parameters shown at Table 1. The spectral intensity is normalized to the peak intensity calculated at the standard single-pass HGHG simulation. (**a**) SASE. Please notice the extended horizontal axis. The average SASE spectrum over 50 shots is shown with the black line. (**b**) Standard HGHG in a single-pass. (**c**) Oscillator-FEL starting with an external seed laser pulse. (**d**) Oscillator-FEL starting from shot-noise.

6. Discussion

In this paper, we described different seeding schemes that can benefit by employing an oscillator setup to increase the repetition rate of a seeded FEL. We presented an overview of simulations and requirements for its implementation. We developed a simple model to estimate the amplification and modulation process in the modulator. This gave an insight into the design of the resonator in terms of modulator length, resonator requirements, and feasibility of the implementation of this scheme. Then, we focused on simulation results of an HGHG scheme. We showed that there is a number of methods that could be used to dynamically control the power gain in the resonator when the process starts from shot-noise and we compared the performance of a single pass HGHG, a multi-pass HGHG starting with a low repetition rate seed laser and of SASE, which is to be considered as our background.

Where so far the wavelength range mentioned here could only be reached with an EEHG scheme, the use of a resonator now would make it possible to reach the same wavelength with an HGHG scheme. Alternatively, starting with a shorter wavelength in an EEHG scheme, the use of the resonator could push the minimum wavelength beyond the water window and transition metals, making seeding in this important wavelength range possible. These options will be studied in future studies.

In addition, there are still a number of considerations that need to be addressed as we are moving towards more detailed studies for the realization of this scheme. Even though first stability studies were presented in [22], it is still crucial to study the stability of this scheme over several passes with a non-ideal electron beam, including imperfections and energy chirp effects. In addition, there are other important questions related to its implementation, such as how the repetition rate can be adjusted when experiments need a lower repetition rate, the space constraints to insert mirrors when the longitudinal dispersion required for seeding at short wavelengths is small, the requirements in terms of diagnostics for the recirculating radiation field, and realizing wavelength tunability. These are expected to be addressed in future work.

Author Contributions: Conceptualization, B.F.; data curation, G.P. and F.P.; validation, G.P., B.F. and G.G.; formal analysis, G.P.; writing—Original draft preparation, G.P.; writing—Review and editing, G.P., S.A., B.F., G.G., T.L., F.P., L.S. and J.Z.; project administration, G.P. and G.G. All authors have read and agreed to the published version of the manuscript.

Funding: This work was supported by the Impuls- und Vernetzungsfond der Helmholtz-Gemeinschaft e.V. within the CAS-Helmholtz International Laboratory on Free-Electron Laser Science and Technology (CHILFEL), grant number InterLabs-0002.

Institutional Review Board Statement: Not applicable.

Informed Consent Statement: Not applicable.

Data Availability Statement: Not applicable.

Acknowledgments: The authors would like to thank Fred Bijkerk for consultation regarding mirrors in the EUV, Frank Obier for information on kickers, Enrico Allaria and Pardis Niknejadi for useful discussions, and the Maxwell computational resources operated at Deutsches Elektronen-Synchrotron (DESY), Hamburg, Germany. Finally the authors thank Chao Feng, and Elke Ploenjes-Palm for a careful proofreading of the manuscript.

Conflicts of Interest: The authors declare no conflict of interest.

References

1. Saldin, E.L.; Schneidmiller, E.A.; Yurkov, M.V. *The Physics of Free Electron Lasers*; Springer: Berlin/Heidelberg, Germany, 2000.
2. Saldin, E.; Schneidmiller, E.; Yurkov, M. Statistical Properties of Radiation from VUV and X-ray Free Electron Laser. *Opt. Commun.* **1998**, *148*, 383–403. doi:10.1016/S0030-4018(97)00670-6.
3. Amann, J.; Berg, W.; Blank, V.; Decker, F.J.; Ding, Y.; Emma, P.; Feng, Y.; Frisch, J.; Fritz, D.; Hastings, J.; et al. Demonstration of self-seeding in a hard-X-ray free-electron laser. *Nat. Photonics* **2012**, *6*, 693–698. doi:10.1038/nphoton.2012.180.
4. Geloni, G.; Kocharyan, V.; Saldin, E. A novel self-seeding scheme for hard X-ray FELs. *J. Mod. Opt.* **2011**, *58*, 1391–1403. doi:10.1080/09500340.2011.586473.
5. Rosenzweig, J.; Alesini, D.; Andonian, G.; Boscolo, M.; Dunning, M.; Faillace, L.; Ferrario, M.; Fukusawa, A.; Giannessi, L.; Hemsing, E.; et al. Generation of ultra-short, high brightness electron beams for single-spike SASE FEL operation. *Nucl. Instrum. Methods Phys. Res. Sect. Accel. Spectrometers Detect. Assoc. Equip.* **2008**, *593*, 39–44. doi:10.1016/j.nima.2008.04.083.
6. Marinelli, A.; MacArthur, J.; Emma, P.; Guetg, M.; Field, C.; Kharakh, D.; Lutman, A.; Ding, Y.; Huang, Z. Experimental demonstration of a single-spike hard-X-ray free-electron laser starting from noise. *Appl. Phys. Lett.* **2017**, *111*, 151101. doi:10.1063/1.4990716.
7. Prince, K.; Allaria, E.; Callegari, C.; Cucini, R.; Giovanni, D.N.; Di Mitri, S.; Diviacco, B.; Ferrari, E.; Finetti, P.; Gauthier, D.; et al. Coherent control with a short-wavelength Free Electron Laser. *Nat. Photonics* **2016**, *10*, 176–179. doi:10.1038/nphoton.2016.13.
8. Gauthier, D.; Ribič, P.R.; De Ninno, G.; Allaria, E.; Cinquegrana, P.; Danailov, M.B.; Demidovich, A.; Ferrari, E.; Giannessi, L. Generation of Phase-Locked Pulses from a Seeded Free-Electron Laser. *Phys. Rev. Lett.* **2016**, *116*, 024801. doi:10.1103/PhysRevLett.116.024801.
9. Gauthier, D.; Allaria, E.; Coreno, M.; Cudin, I.; Dacasa, H.; Danailov, M.; Demidovich, A.; Di Mitri, S.; Diviacco, B.; Ferrari, E.; et al. Chirped pulse amplification in an extreme-ultraviolet free-electron laser. *Nat. Commun.* **2016**, *7*, 13688. doi:10.1038/ncomms13688.
10. Gorobtsov, O.; Mercurio, G.; Capotondi, F.; Skopintsev, P.; Lazarev, S.; Zaluzhnyy, I.; Danailov, M.; Dell'Angela, M.; Manfredda, M.; Pedersoli, E.; et al. Seeded X-ray free-electron laser generating radiation with laser statistical properties. *Nat. Commun.* **2018**, *9*, 4498. doi:10.1038/s41467-018-06743-8.

11. Yu, L.H.; Babzien, M.; Ben-Zvi, I.; DiMauro, L.F.; Doyuran, A.; Graves, W.; Johnson, E.; Krinsky, S.; Malone, R.; Pogorelsky, I.; et al. High-Gain Harmonic-Generation Free-Electron Laser. *Science* **2000**, *289*, 932–934, doi:10.1126/science.289.5481.932.
12. Allaria, E.; Cinquegrana, P.; Cleva, S.; Cocco, D.; Cornacchia, M.; Craievich, P.; Cudin, I.; D'Auria, G.; Dal Forno, M.; Danailov, M.; et al. Highly coherent and stable pulses from the FERMI seeded free-electron laser in the extreme ultraviolet. *Nat. Photonics* **2012**, *6*, 699–704. doi:10.1038/nphoton.2012.233.
13. Xiang, D.; Stupakov, G. Echo-enabled harmonic generation free electron laser. *Phys. Rev. ST Accel. Beams* **2009**, *12*, 030702. doi:10.1103/PhysRevSTAB.12.030702.
14. Feng, C.; Deng, H.; Zhang, M.; Wang, X.; Chen, S.; Liu, T.; Zhou, K.; Gu, D.; Wang, Z.; Jiang, Z.; et al. Coherent extreme ultraviolet free-electron laser with echo-enabled harmonic generation. *Phys. Rev. Accel. Beams* **2019**, *22*, 050703. doi:10.1103/PhysRevAccelBeams.22.050703.
15. Ribič, P.; Abrami, A.; Badano, L.; Bossi, M.; Braun, H.H.; Bruchon, N.; Capotondi, F.; Castronovo, D.; Cautero, M.; Cinquegrana, P.; et al. Coherent soft X-ray pulses from an echo-enabled harmonic generation free-electron laser. *Nat. Photonics* **2019**, *13*, 1–7. doi:10.1038/s41566-019-0427-1.
16. Lechner, C.; Ackermann, S.; Azima, A.; Aßmann, R.; Biss, H.; Drescher, M.; Faatz, B.; Grattoni, V.; Hartl, I.; Hartwell, S.; et al. Seeding R&D at sFLASH. In Proceedings of the FEL'19, Geneva, Switzerland, 26–30 August 2019; Number 39 in Free Electron Laser Conference; pp. 230–233. doi:10.18429/JACoW-FEL2019-TUP076.
17. Yan, J.; Gao, Z.; Qi, Z.; Zhang, K.; Zhou, K.; Liu, T.; Chen, S.; Feng, C.; Li, C.; Feng, L.; et al. Self-Amplification of Coherent Energy Modulation in Seeded Free-Electron Lasers. *Phys. Rev. Lett.* **2021**, *126*, 084801. doi:10.1103/PhysRevLett.126.084801.
18. Wang, X.; Feng, C.; Faatz, B.; Zhang, W.; Zhao, Z. Direct-Amplification Enabled Harmonic Generation for Seeding a High-Repetition-Rate Free-Electron Laser. 2021. Available online: http://xxx.lanl.gov/abs/2103.11971 (accessed on 10 May 2021).
19. Ackermann, S.; Faatz, B.; Grattoni, V.; Lechner, C.; Paraskaki, G.; Geloni, G.; Serkez, S.; Tanikawa, T.; Hillert, W. High-Repetition-Rate Seeding Schemes Using a Resonator-Amplifier Setup. In Proceedings of the International Free Electron Laser Conference (FEL'19), Hamburg, Germany, 26–30 August 2019; Number 39 in International Free Electron Laser Conference; JACoW: Geneva, Switzerland, 2019; doi:10.18429/JACoW-FEL2019-TUP073.
20. Paraskaki, G.; Ackermann, S.; Faatz, B.; Grattoni, V.; Lechner, C.; Mehrjoo, M.; Geloni, G.; Serkez, S.; Tanikawa, T.; Hillert, W. Study of a Seeded Oscillator-Amplifier FEL. In Proceedings of the International Free Electron Laser Conference (FEL'19), Hamburg, Germany, 26–30 August 2019; Number 39 in International Free Electron Laser Conference; JACoW: Geneva, Switzerland, 2019; doi:10.18429/JACoW-FEL2019-TUP077.
21. Ackermann, S.; Faatz, B.; Grattoni, V.; Kazemi, M.M.; Lang, T.; Lechner, C.; Paraskaki, G.; Zemella, J.; Geloni, G.; Serkez, S.; et al. Novel method for the generation of stable radiation from free-electron lasers at high repetition rates. *Phys. Rev. Accel. Beams* **2020**, *23*, 071302. doi:10.1103/PhysRevAccelBeams.23.071302.
22. Paraskaki, G.; Grattoni, V.; Lang, T.; Zemella, J.; Faatz, B.; Hillert, W. Optimization and stability of a high-gain harmonic generation seeded oscillator amplifier. *Phys. Rev. Accel. Beams* **2021**, *24*, 034801. doi:10.1103/PhysRevAccelBeams.24.034801.
23. Dattoli, G.; Giannessi, L.; Ottaviani, P.; Torre, A. Dynamical behavior of a free-electron laser operating with a prebunched electron beam. *Phys. Rev.. E Stat. Phys. Plasmas Fluids Relat. Interdiscip. Top.* **1994**, *49*, 5668–5678. doi:10.1103/PhysRevE.49.5668.
24. Dattoli, G.; Faatz, B.; Giannessi, L.; Ottaviani, P.L. The tandem FEL dynamic behavior. *IEEE J. Quantum Electron.* **1995**, *31*, 1584–1590. doi:10.1109/3.400416.
25. Dattoli, G.; Giannessi, L.; Ottaviani, P. Oscillator-amplifier free electron laser devices with stable output power. *J. Appl. Phys.* **2004**, *95*, 3211. doi:10.1063/1.1645649.
26. Kim, K.J.; Shvyd'ko, Y.; Reiche, S. A Proposal for an X-Ray Free-Electron Laser Oscillator with an Energy-Recovery Linac. *Phys. Rev. Lett.* **2008**, *100*, 244802. doi:10.1103/PhysRevLett.100.244802.
27. Nguyen, D.C.; Sheffield, R.L.; Fortgang, C.M.; Goldstein, J.C.; Kinross-Wright, J.M.; Ebrahim, N.A. First lasing of the regenerative amplifier FEL. *Nucl. Instrum. Methods Phys. Res. A* **1999**, *429*, 125–130. doi:10.1016/S0168-9002(99)00090-X.
28. Faatz, B.; Feldhaus, J.; Krzywinski, J.; Saldin, E.; Schneidmiller, E.; Yurkov, M. Regenerative FEL amplifier at the TESLA test facility at DESY. *Nucl. Instrum. Methods Phys. Res. Sect. A Accel. Spectrometers Detect. Assoc. Equip.* **1999**, *429*, 424–428. doi:10.1016/S0168-9002(99)00123-0.
29. Huang, Z.; Ruth, R.D. Fully Coherent X-ray Pulses from a Regenerative-Amplifier Free-Electron Laser. *Phys. Rev. Lett.* **2006**, *96*, 144801. doi:10.1103/PhysRevLett.96.144801.
30. Freund, H.P.; van der Slot, P.J.M.; Shvyd'ko, Y. An X-ray regenerative amplifier free-electron laser using diamond pinhole mirrors. *New J. Phys.* **2019**, *21*, 093028. doi:10.1088/1367-2630/ab3f72.
31. Trovò, M.; Clarke, J.; Couprie, M.; Dattoli, G.; Garzella, D.; Gatto, A.; Giannessi, L.; Günster, S.; Kaiser, N.; Marsi, M.; et al. Operation of the European storage ring FEL at ELETTRA down to 190 nm. *Nucl. Instrum. Methods Phys. Res. Sect. A Accel. Spectrometers Detect. Assoc. Equip.* **2002**, *483*, 157–161. doi:10.1016/S0168-9002(02)00303-0.
32. Gandhi, P.; Penn, G.; Reinsch, M.; Wurtele, J.; Fawley, W. Oscillator seeding of a high gain harmonic generation free electron laser in a radiator-first configuration. *Phys. Rev. Spec. Top. Accel. Beams* **2013**, *16*, 020703.
33. Li, K.; Yan, J.; Feng, C.; Zhang, M.; Deng, H. High brightness fully coherent x-ray amplifier seeded by a free-electron laser oscillator. *Phys. Rev. Accel. Beams* **2018**, *21*, 040702. doi:10.1103/PhysRevAccelBeams.21.040702.

34. Petrillo, V.; Bacci, A.; Rossi, A.R.; Serafini, L.; Drebot, I.; Conti, M.R.; Ruijter, M.; Opromolla, M.; Samsam, S.; Broggi, F.; et al. Coherent, high repetition rate tender X-ray Free-Electron Laser seeded by an Extreme Ultra-Violet Free-Electron Laser Oscillator. *New J. Phys.* **2020**, *22*, 073058.
35. Mirian, N.; Opromolla, M.; Rossi, G.; Serafini, L.; Petrillo, V. High-repetition rate and coherent free-electron laser in the tender x rays based on the echo-enabled harmonic generation of an ultraviolet oscillator pulse. *Phys. Rev. Accel. Beams* **2021**, accepted.
36. Newnam, B.E. Extreme ultraviolet free-electron laser-based projection lithography systems. *Opt. Eng.* **1991**, *30*, 1100–1108. doi:10.1117/12.55914.
37. Penco, G.; Perosa, G.; Allaria, E.; Di Mitri, S.; Ferrari, E.; Giannessi, L.; Spampinati, S.; Spezzani, C.; Veronese, M. Enhanced seeded free electron laser performance with a "cold" electron beam. *Phys. Rev. Accel. Beams* **2020**, *23*, 120704. doi:10.1103/PhysRevAccelBeams.23.120704.
38. Beye, M. *FLASH2020+: Making FLASH Brighter, Faster and More Flexible : Conceptual Design Report*; Verlag Deutsches Elektronen-Synchrotron: Hamburg, Germany, 2020; pp. 1–126. doi:10.3204/PUBDB-2020-00465.
39. Reiche, S. GENESIS 1.3: A fully 3D time-dependent FEL simulation code. *Nucl. Instrum. Methods Phys. Res. Sect. A Accel. Spectrometers Detect. Assoc. Equip.* **1999**, *429*, 243–248. doi:10.1016/S0168-9002(99)00114-X.
40. Faatz, B.; Plönjes, E.; Ackermann, S.; Agababyan, A.; Asgekar, V.; Ayvazyan, V.; Baark, S.; Baboi, N.; Balandin, V.; von Bargen, N.; et al. Simultaneous operation of two soft x-ray free-electron lasers driven by one linear accelerator. *New J. Phys.* **2016**, *18*, 062002. doi:10.1088/1367-2630/18/6/062002.
41. Rossbach, J.; Schneider, J.R.; Wurth, W. 10 years of pioneering X-ray science at the Free-Electron Laser FLASH at DESY. *Phys. Rep.* **2019**, *808*, 1–74.
42. Nölle, D. FEL Operation at the European XFEL Facility. In Proceedings of the International Free Electron Laser Conference (FEL'19), Hamburg, Germany, 26–30 August 2019; Number 39 in International Free Electron Laser Conference; JACoW: Geneva, Switzerland, 2019; doi:10.18429/JACoW-FEL2019-FRA01.
43. Liu, T.; Dong, X.; Feng, C. Start-to-end Simulations of the Reflection Hard X-Ray Self-Seeding at the SHINE Project. In Proceedings of the FEL'19, Geneva, Switzerland, 26–30 August 2019; Number 39 in Free Electron Laser Conference; pp. 254–257. doi:10.18429/JACoW-FEL2019-TUP087.
44. Hemsing, E.; Marcus, G.; Fawley, W.M.; Schoenlein, R.W.; Coffee, R.; Dakovski, G.; Hastings, J.; Huang, Z.; Ratner, D.; Raubenheimer, T.; et al. Soft X-ray seeding studies for the SLAC Linac Coherent Light Source II. *Phys. Rev. Accel. Beams* **2019**, *22*, 110701. doi:10.1103/PhysRevAccelBeams.22.110701.
45. Reiche, S. Overview of Seeding Methods for FELs. In Proceedings of the 4th International Particle Accelerator Conference, Shanghai, China, 12–17 May 2013.
46. Xie, M. Design optimization for an X-ray free electron laser driven by SLAC LINAC. *Conf. Proc.* **1996**, *C950501*, 183–185. doi:10.1109/PAC.1995.504603.
47. Hemsing, E.; Stupakov, G.; Xiang, D.; Zholents, A. Beam by design: Laser manipulation of electrons in modern accelerators. *Rev. Mod. Phys.* **2014**, *86*, 897–941. doi:10.1103/RevModPhys.86.897.
48. Guenster, S.; Ristau, D.; Gatto, A.; Kaiser, N.; Trovo, M.; Danailov, M.; Sarto, F. VUV Optics Development for the Elettra Storage Ring FEL. In Proceedings of the 26th International Free Electron Laser Conference & 11th FEL Users Workshop, Trieste, Italy, 29 August–3 September 2004.
49. Henke, B.; Gullikson, E.; Davis, J. X-ray Interactions: Photoabsorption, Scattering, Transmission, and Reflection at E = 50-30,000 eV, Z = 1-92. *At. Data Nucl. Data Tables* **1993**, *54*, 181–342. doi:10.1006/adnd.1993.1013. Available online: https://henke.lbl.gov/optical_constants/mirror2.html (accessed on 10 May 2021).
50. Agapov, I.; Geloni, G.; Tomin, S.; Zagorodnov, I. OCELOT: A software framework for synchrotron light source and FEL studies. *Nucl. Instrum. Methods Phys. Res. A* **2014**, *768*, 151–156. doi:10.1016/j.nima.2014.09.057.
51. Oepts, D.; van der Meer, A.; van Amersfoort, P. The Free-Electron-Laser user facility FELIX. *Infrared Phys. Technol.* **1995**, *36*, 297–308. doi:10.1016/1350-4495(94)00074-U.
52. Jaroszynski, D.; Oepts, D.; Van Der Meer, A.; Van Amersfoort, P.; Colson, W. Consequences of short electron-beam pulses in the FELIX project. *Nucl. Instrum. Methods Phys. Res. Sect. A Accel. Spectrometers Detect. Assoc. Equip.* **1990**, *296*, 480–484. doi:10.1016/0168-9002(90)91254-9.
53. Knippels, G.M.H.; Bakker, R.J.; van der Meer, A.F.G.; Jaroszynski, D.A.; Oepts, D.; van Amersfoort, P.W.; Hovenier, J.N. Dynamic cavity desynchronisation in FELIX. *Nucl. Instrum. Methods Phys. Res. A* **1994**, *341*, ABS26–ABS27. doi:10.1016/0168-9002(94)90425-1.
54. MacLeod, A.M.; Yan, X.; Gillespie, W.A.; Knippels, G.M.H.; Oepts, D.; van der Meer, A.F.G.; Rella, C.W.; Smith, T.I.; Schwettman, H.A. Formation of low time-bandwidth product, single-sided exponential optical pulses in free-electron laser oscillators. *Phys. Rev. E* **2000**, *62*, 4216–4220. doi:10.1103/PhysRevE.62.4216.
55. Zhao, Z.Y.; Li, H.T.; Jia, Q.K. Effect of cavity length detuning on the output characteristics for the middle infrared FEL oscillator of FELiChEM. *Chin. Phys. C* **2017**, *41*, 108101. doi:10.1088/1674-1137/41/10/108101.
56. Kiessling, R.; Colson, W.B.; Gewinner, S.; Schöllkopf, W.; Wolf, M.; Paarmann, A. Femtosecond single-shot timing and direct observation of subpulse formation in an infrared free-electron laser. *Phys. Rev. Accel. Beams* **2018**, *21*, 080702. doi:10.1103/PhysRevAccelBeams.21.080702.

57. Vinokurov, N.A.; Skrinsky, A.N. *About the Maximum Power of an Optical Klystron on a Storage Ring*; Report No. BINP 77-67; Budker Institute for Nuclear Physics: Novossibirsk, Russia, 1977.
58. Dattoli, G.; Giannessi, L.; Ottaviani, P. MOPA optical klystron FELs and coherent harmonic generation. *Nucl. Instrum. Methods Phys. Res. Sect. A Accel. Spectrometers Detect. Assoc. Equip.* **2003**, *507*, 26–30. doi:10.1016/S0168-9002(03)00828-3.
59. Penco, G.; Allaria, E.; Ninno, G.D.; Ferrari, E.; Giannessi, L. Experimental Demonstration of Enhanced Self-Amplified Spontaneous Emission by an Optical Klystron. *Phys. Rev. Lett.* **2015**, *114*, 013901.
60. Penco, G.; Allaria, E.; De Ninno, G.; Ferrari, E.; Giannessi, L.; Roussel, E.; Spampinati, S. Optical Klystron Enhancement to Self Amplified Spontaneous Emission at FERMI. *Photonics* **2017**, *4*, 15. doi:10.3390/photonics4010015.
61. Ding, Y.; Emma, P.; Huang, Z.; Kumar, V. Optical klystron enhancement to self-amplified spontaneous emission free electron lasers. *Phys. Rev. ST Accel. Beams* **2006**, *9*, 070702; Erratum in **2020**, *23*, 019901.
62. Geloni, G.; Guetg, M.; Serkez, S.; Schneidmiller, E. A Revision of Optical Klystron Enhancement Effects in SASE FELs. *Phys. Rev. Accel. Beams*. **2021**, submitted.
63. Keil, B.; Baldinger, R.; Ditter, R.; Gloor, M.; Koprek, W.; Marcellini, F.; Marinkovic, G.; Roggli, M.; Rohrer, M.; Stadler, M.; et al. Status of The European XFEL Transverse Intra Bunch Train Feedback System. In Proceedings of the International Beam Instrumentation Conference (IBIC2015), Melbourne, Australia, 13–17 September 2015; Number 4 in International Beam Instrumentation Conference; JACoW: Geneva, Switzerland, 2016; pp. 492–496. doi:10.18429/JACoW-IBIC2015-TUPB064.
64. Obier, F.; Decking, W.; Hüning, M.; Wortmann, J. Fast Kicker System for European XFEL Beam Distribution. In Proceedings of the 39th International Free-Electron Laser Conference, Hamburg, Germany, 26–30 August 2019; JACoW Publishing: Geneva, Switzerland, 2019; p. 4. doi:10.18429/JACoW-FEL2019-WEP013.

Chapter 6

Conclusions and Outlook

This thesis is motivated by the limitations that external seeding techniques suffer from because of the, otherwise fundamentally important, seed laser systems: their coherence is transferred to the output FEL radiation but at the same time they limit its maximum repetition rate, shortest possible wavelength and tunability in wavelength. This way, many experiments that would benefit by the full coherence and timing stability of seeded radiation are excluded. In addition, the low repetition rate of seeded radiation limits the statistics obtained in experiments and excludes the observation of very fast processes. In Chapters 3, 4 and 5 I showed published and detailed simulation results of three setups that allow us to manoeuvre around these limitations and generate high repetition rate radiation while maintaining the unique properties of external seeding techniques. All of them primarily aim to increase the repetition rate, secondarily to reduce the shortest wavelength of seeded radiation and in some cases to extend the wavelength tunability.

The first proposal was an optical-klystron based HGHG scheme presented in Chapter 3. With our work, we have demonstrated that with this setup it is possible to reduce the required seed laser power by two to three orders of magnitude and yet, maintain the properties of seeded radiation even at the 15th harmonic of the seed laser wavelength. As the seed laser power is significantly reduced, it is possible to increase the repetition rate or use seed laser systems of shorter wavelengths. While the first proof of principle experiment has already taken place [81], it is still important to study in more detail and systematically the advantages and limitations of this setup. It is crucial to verify the effect of a linear and quadratic energy chirp: in a standard HGHG setup, a wavelength shift is anticipated with the linear chirp and bandwidth broadening with the quadratic energy chirp. With the optical klystron, it is expected that the wavelength shift will be more significant due to the two individual stages with chicanes. As a result, a different optimization depending on the electron bunch energy profile is required. In addition, the micro-bunching instability has proven to be a significant limitation in seeded FELs and its impact on an optical klystron based HGHG should be verified. This systematic study will allow further experiments that can be optimized based on the observations from simulations. Since the setup is rather simple and resembles EEHG beamlines, this scheme could be part of the standard operation of high repetition rate FELs in the near future.

The second proposal was an HGHG seeded oscillator-amplifier, using a low repetition rate seed laser to initiate the process, and an optical cavity to store it and seed consecutive electron bunches (Chapter 4). This solution is attractive because it allows high repetition rate seeding while using seed lasers in low repetition rate. While the simulations published were quite extended, to be able to design a first proof of principle experiment there are further considerations that can be made. Concerning the electron bunch, it is important to incorporate in the simulations its expected energy chirp. As the energy chirp translates into a chirp of the amplified field, the several passes in the resonator are expected to gradually enhance this chirp. A start to end electron bunch should be used to verify that it does not affect significantly the stability of the setup. Concerning technical considerations, the in-coupling of the seed laser in the cavity needs to be designed and the reflectivity of mirrors at wavelengths between 50-100 nm must be experimentally determined since there is little available data in this region of interest. In addition, it is important to verify the position that the first mirror after the in-cavity modulator should be placed at. While the chicane seems to be a natural choice, short wavelengths in the order of 50 nm and typical electron bunch properties require a longitudinal dispersion in the order of tens of micrometres. Such a small R_{56} is a limiting factor when space is needed for a mirror insertion. Different considerations need to be taken into account to solve this issue. For instance, the optical klystron discussed above can be a solution: since the chicane in between the two undulator sections increases the bunching at the fundamental wavelength, the longitudinal dispersion is typically larger. Another solution is to directly implement an EEHG setup with an oscillator as a larger dispersion is more common compared to an HGHG setup. Both solutions are briefly discussed in the publication of Chapter 5. Finally, the optical cavity is very long and in the order of 300 m for 1 MHz repetition rate and reducing further the repetition rate is not straightforward. If sufficient reflectivity is provided by the mirrors, one solution would be to let the stored radiation pulse perform more than one roundtrip in the cavity in between two consecutive electron bunches.

In Chapter 5 it was proposed to become completely independent of seed laser sources . The additional advantage compared with the setup discussed above is that the fundamental wavelength can be chosen independently of availability in seed laser sources, making extended wavelength tunability and shorter wavelengths possible. While all the considerations discussed above for the seeded oscillator hold true for this setup as well (except for the in-coupling of the seed laser), here the considerations to plan a first proof of principle experiment are extended. First of all, it is crucial to identify a fast feedback that will allow a smooth transition between power amplification and power equilibrium. Several methods were proposed in the publication and all of them are calling for near state-of-the-art solutions, therefore experimentally testing the different solutions to identify the technical limitations is of utmost importance. Out of the proposed solutions, the fast kicker chicane has the natural advantage that it is "off" during the steady-state, and "on" during the amplification of the power when the stability of the chicane does not matter as the radiation is not yet used at experiments. To be able to transition from the positive net gain to a steady-state there must be a fast feedback that can measure the power at the return path and identify the pass that the transition should take place. In simulations, it is easy to identify after how many passes the power of interest is reached, however, since it starts from shot noise and the electron beam parameters fluctuate from bunch to bunch the number of passes required to reach the power of interest is expected to vary from one bunch train to the next one. This feedback is also important to be able to identify other abnormalities such as when one electron bunch is lost and the gain needs to be readjusted to compensate for the additional losses.

Last but not least, as a monochromator is required, the losses would increase further and the requirements on mirror reflectivity become more and more important. Another issue that arises when the seed laser is completely omitted, is that the synchronization with the pump-probe laser is lost and a fast feedback with a femtosecond synchronisation system is required instead to synchronise the FEL pulses and the pump-probe laser. The different advantages and disadvantages vary depending on the type of operation of the FEL. CW operation allows a smoother transition from the power amplification to the equilibrium state due to the, in principle, unlimited number of bunches compared to a burst mode of operation. On the other hand, a burst mode of operation fulfills a much lower threshold of power density that the mirrors in the cavity can withstand compared to the many more photon pulses per second generated by a CW FEL. As a result, different machines need to study the cavity geometry and the technical challenges based on the special features of each FEL.

Appendix A

Numerical methods

In this section, I introduce the FEL code Genesis 1.3 [64], which is the main tool for all FEL simulations shown in this thesis, and the multi-package Ocelot [102], which is used for the treatment of the radiation fields when there is no interaction with the electrons. Following, the main features of these codes are introduced.

A.1 Simulating the FEL process with Genesis 1.3

Simulation codes that model the FEL process (interaction of electrons with an optical field in an undulator) are of utmost importance for the understanding and accurate design of FELs. As discussed in the Theory chapter of this thesis (Chapter 2), an analytical solution for the FEL process is not possible, so numerically solving the FEL equations is the most promising approach for reliable results. Many different applications of FELs exist and call for different approximations, so different codes offer different solutions of one dimensional or three dimensional approach, averaging or not the undulator orbit, using time dependence or not, using a slow varying amplitude approximation. Different simulation codes exist to serve the different requirements within the FEL community and few of them that are commonly used are Genesis 1.3 [64], Ginger [65], MINERVA [103], MEDUSA [104], FAST [105], PUFFIN [106] and more.

The results shown in this thesis depend on the simulation code Genesis 1.3 version 4 [107] which is a time-dependent and three-dimensional simulation code that is based on a slowly varying envelope approximation (SVEA) and undulator period-averaged equations of motion. An electron bunch consists of a large number of electrons, typically in the range $10^9 - 10^{11}$. Simulating all these electrons can be very demanding computationally and requires several hours of simulations. While in most simulation codes (including the previous version of Genesis) the electrons are represented by macro-particles, which are sample particles used to reduce memory requirements and speed-up the simulations, in this 4th version of Genesis it is possible to simulate all electrons in an *one4one* mode. This means that each electron is treated individually in the simulations. In Genesis, the electron bunch consists of longitudinal slices with each of them being one resonant wavelength long and the radiation field is described in a 2D grid that is also treated in longitudinal slices. In Genesis v4, the electrons are allowed to move from the one longitudinal slice to another, as the complete electron bunch and radiation field are kept in the memory. This feature is particularly useful for electron bunches with a significant energy chirp traversing a chicane, or schemes like EEHG where strong chicanes are needed to reshuffle the electrons in the longitudinal phase space. This version of Genesis is written in C++.

This highly accurate model requires the use of clusters and parallel computing, and all simulation results based on Genesis are, for this thesis, obtained this way and with the help of the Maxwell cluster resources operated at DESY. In Chapter 3, the optical klystron based HGHG is simulated in an one4one mode, so with a realistic number of electrons, unless otherwise stated. In a few cases, it is explicitly stated that steady-state simulations (no longitudinal dependence of properties) was chosen to scan parameters faster. The oscillator-FEL is a rather more computationally demanding FEL scheme since the simulations run in several passes. For this reason, a "macro-particle" approached was preferred when simulating the results shown in Chapter 4 and 5.

A.2 Radiation field treatment with Ocelot

Ocelot is an open source multiphysics simulation toolkit based on python that addresses light sources such as FELs [102]. In an FEL, it covers a wide range of its physics as it is possible to optimize the electron beam dynamics, import the lattice to FEL simulation codes such as Genesis and perform pre/post-processing, export the FEL radiation field for characterization and propagation in a beamline. In addition, it offers online optimization tools for FEL tuning [108]. In the results shown in this thesis, I use Ocelot for FEL radiation propagation and characterization of the field properties. More specifically, Ocelot was used for the oscillator FEL simulation results shown in Chapters 4 and 5. Adaptors from Genesis to Ocelot and vice versa already exist in Ocelot.

When the radiation field is loaded into Ocelot, a number of actions is possible to simulate the transportation of the radiation field in the cavity. The radiation field can be converted to the appropriate domain for the desired operation and it can be propagated along drift sections while the mesh size can be readjusted to allow optimum resolution with no numerical reflections due to the grid size. In addition, it is possible to focus the radiation field which is done by adding a quadratic curvature to the wavefront. Another feature that was used in the simulations presented in the thesis is the monochromatisation. For this, a Gaussian transfer function can be defined to filter the radiation field in the frequency domain at the desired wavelength and bandwidth. Other useful tools offer: plotting the radiation field, plotting the Wigner distribution, adding group delay dispersion, calculating the coherence degree, identifying the waist size and position of the radiation field, back-propagating it, reflecting it on mirrors with height errors.

Finally, for this thesis many self-written tools were used but also a few more tools that were generously shared: elegant [109] was used for the electron beam optics matching, chi23d [110] was used for post-processing of the in-cavity radiation field and params, an excel tool developed by B. Faatz, was used on several occasions to obtain estimations and optimize the design of the FEL.

Appendix B

Additional simulation results

B.1 HGHG seeding with an optical klystron

For the simulation results shown in this section, I consider the simulation parameters and results shown in the publication of Chapter 3. I use the same simulation parameters but in this case, I optimize for the 10th harmonic of the seed laser wavelength. In a similar optimization method, $R_{56,1}$ remains the same as it does not depend on the input seed laser power, but only on the uncorrelated energy spread. I aim at a bunching of 8% at the 10th harmonic with the minimum seed laser power possible. To achieve this, the input seed laser power and the $R_{56,2}$ are tuned. The optimized parameters for the optical klystron HGHG (OK HGHG) and the standard HGHG are shown in Table B.1.

With these parameters, the bunching at the fundamental wavelength after chicane 1 in the optical klystron HGHG is equal to $b_1 = 16\%$. Based on Eq. 2.49, a pre-bunched electron bunch can almost immediately start emitting coherent radiation with no need for an external seed laser. For relatively shorter modulators, the power in the second modulator grows quadratically, while for longer modulators it grows exponentially (see Eq. 2.50), following the already introduced FEL process starting with a pre-bunched electron bunch. As shown in Fig. 2.6, the power increases rapidly if there is sufficient bunching. I compare the rise of energy modulation along the modulators with the chicane at the optimized $R_{56,1} = 482\,\mu\text{m}$ and the chicane off. I show the energy modulation along the modulators shown in power gain lengths in Fig. B.1. It is clear that without the chicane, it is not beneficial to use two modulators. The energy modulation increases more considerably after the first gain length in modulator 2.

TABLE B.1: I list the simulation parameters optimized for the time-dependent simulations.

	Standard HGHG	**OK-HGHG**
$R_{56,1}$ / $R_{56,2}$	-/67.6 µm	482 µm/50 µm
K_{amp}	1.7	1.7
Seed laser power (P_{seed})	25 MW	0.048 MW

The optimization of the output FEL for the standard HGHG and the optical klystron HGHG (OK-HGHG) resulted in comparable results, shown in Fig. B.2. The pulse properties and energy spread of the electron beam are shown in Table B.2. The results of the OK-HGHG were achieved with a seed laser power that is reduced by a factor of more than 500 compared to the standard HGHG (see Table B.1).

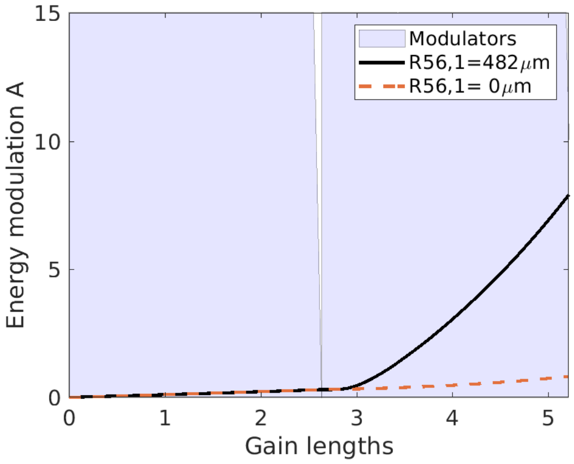

FIGURE B.1: Energy modulation along the two modulators with the chicane on and off. The modulator length is shown in power gain lengths and, for an easier understanding, I have excluded the drifts, the quadrupole and the chicane in between the two modulators since the energy modulation is not affected while the electron bunch traverses these elements.

TABLE B.2: Comparison of simulation results between a standard HGHG and an OK-HGHG setup. The output wavelength is 30 nm and results as the 10th harmonic of a 300 nm seed laser. The energy spread is calculated upstream from the amplifier.

	Standard HGHG	**OK-HGHG**
Energy spread at amplifier (σ_E')	373.3 keV	407.3 keV
FWHM relative bandwidth	$1.1 \cdot 10^{-3}$	$1.1 \cdot 10^{-3}$
Pulse energy	63.8 µJ	64.8 µJ
Pulse duration rms	20.2 fs	20.7 fs

I repeat the same simulations shown in Fig. B.2 but this time I change the initial shot noise in each of these simulations. The random seeds that initiate the simulations are the same as the ones used for the 15th harmonic shown in the publication of Section 2.4.2.

The results of the 10th harmonic and the 15th harmonic of a 300 nm seed laser wavelength are both very encouraging for the implementation of an OK HGHG scheme. The potential issues are that the noise amplification depends quadratically on the harmonic number, which could affect the higher harmonic, and that the 10th harmonic requires only 48 kW of input power which translates into a lower input signal to noise ratio. However, in both harmonics I showed with time dependent and 3D simulations that:

1. The seed laser power can be reduced by two orders of magnitude.

2. The output FEL radiation shows an insignificant sensitivity to the initial shot noise, while the output pulse properties remain comparable to the standard HGHG results.

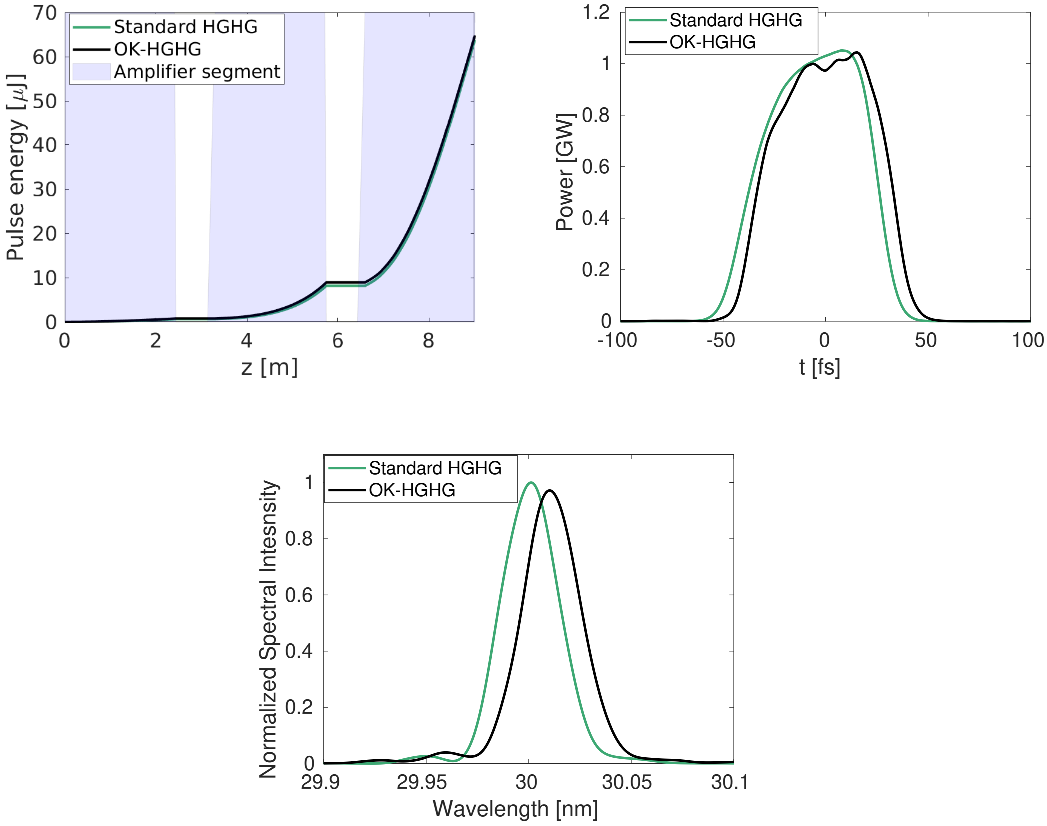

FIGURE B.2: I compare two fully optimized simulations of a standard HGHG and an OK-HGHG setup for the 10th harmonic of a 300 nm seed laser wavelength. In the first row I show the gain curves in amplifier and the output FEL power profiles. At the bottom, I show the output FEL spectra normalized to the intensity of the standard HGHG simulation.

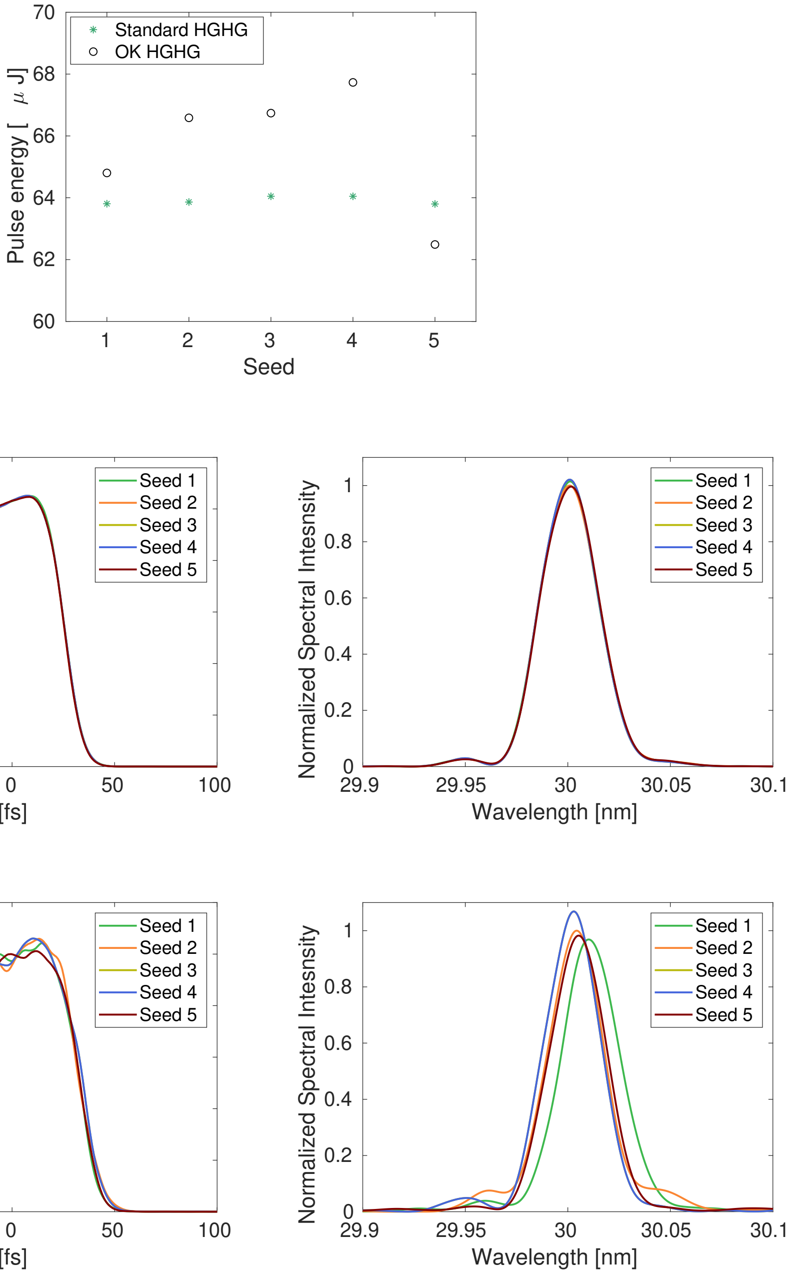

FIGURE B.3: I repeat the simulations of Fig. B.2 with a different initial shot noise of the simulation. In the first row I show the shot to shot pulse energy fluctuations, in the second row I show the output FEL power and spectrum for a standard HGHG scheme and at the bottom I show the power profile and spectrum of the output FEL for the OK HGHG scheme.

B.2 HGHG seeding with an oscillator starting with a low repetition rate seed laser

In this section, I have included additional material that is complementary to the publication shown in Section 4. The focus here remains on the 50 nm resonant modulator and the amplification of the 12th harmonic. Initially, I discuss in more detail the optimization of the oscillator, shown in Fig. 4.1. As a first step, the lattice parameters are chosen. This means that the undulator parameter should be decided and a reasonable optics matching should be achieved by adjusting the quadrupoles' strength. While the undulator parameter is typically calculated from the resonance condition of Eq. 2.30, 3D effects that are included in our simulations may result in a different optimum K. Scanning the undulator parameter of the modulator (in-cavity undulator) in a single pass and in several passes in the oscillator results in different power gain as shown in Fig. B.4. The K for an optimum gain is shifted to lower K values compared to a single-pass.

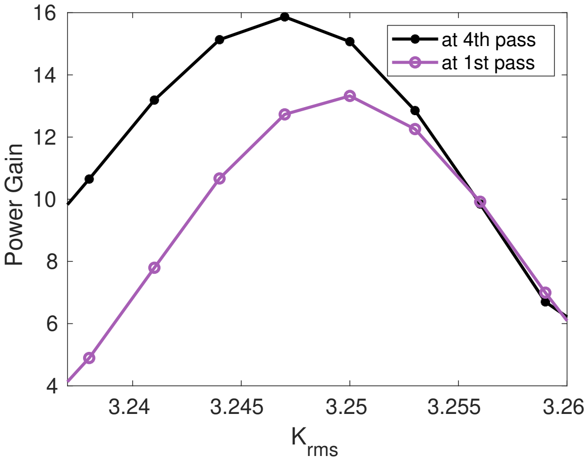

FIGURE B.4: Power gain in the first pass of the oscillator and in the fourth pass for different undulator parameters K.

The beta functions in the modulator are shown in Fig. B.5. Based on this, the rms electron beam size varies between 32 µm-85 µm horizontally and between 50 µm-80 µm vertically. Even at focus, the radiation field is larger than the electron beam size, ensuring a good overlap between the two. The waist size (in a definiton of $1/\exp^2$) is shown in Fig. B.6. It should be pointed out that due to the gain guiding the radiation field is typically smaller transversely than anticipated by propagating it in a drift section. To demonstrate this I take the radiation field at the 60th pass and I first propagate this along the actual beamline and I plot the intensity profile at several positions (see Fig. B.7), and then I propagate the same radiation field along a drift of the same length (see Fig. B.8). It is clear that while the radiation field along a drift reaches the minimum waist size at focus and then starts diverging again, along the modulator the gain guiding plays an important role; since the FEL interaction occurs where the electron density is significant, the dominant mode of the radiation is kept at the central part of the electron bunch where the amplification takes place and as a result, the transverse size of the radiation is smaller compared to its size when diffraction occurs without guiding.

The optimization of the longitudinal overlap has already been discussed in the publication in Section 4 and the optimum detuning is extracted from the detuning

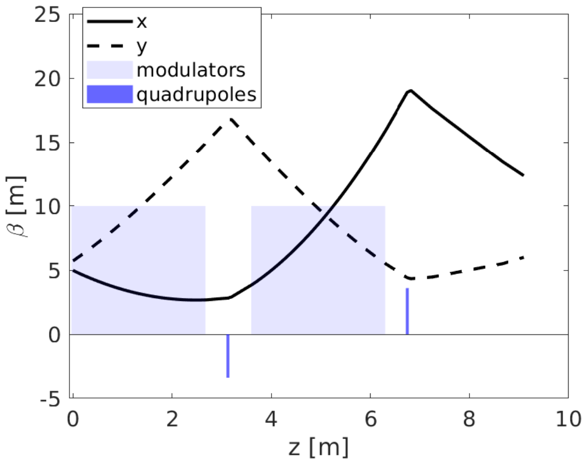

FIGURE B.5: Optics matching along the modulators and the chicane. The elements of the beamline can be seen in Fig. 4.1.

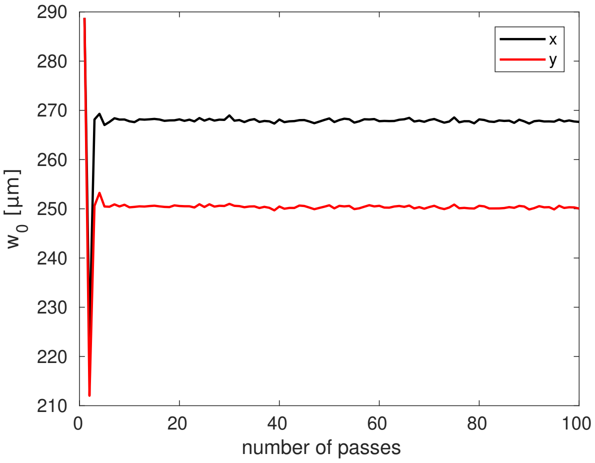

FIGURE B.6: Waist size of radiation field stored in the cavity. It is calculated by propagating the input field along a drift and identifying its waist size.

curve of Fig. 3. Using the suggested cavity detuning of $\Delta\lambda = 54\lambda_{seed}$, I show the stability of the longitudinal position of the radiation field with respect to the electron bunch position per pass in Fig. B.9. The time window of the simulation is 80 μm and it is fixed to follow the electron bunch. On the left, the power profile is shown with respect to the electron bunch current distribution at the 1st pass of the oscillator and at the entrance of the modulator. On the right, I show the position of the peak of the Gaussian power profile of the radiation field at the entrance and at the exit of the modulator. As it can be seen, the radiation field is shifted along the modulator due to slippage, but an optimum cavity detuning corrects for this slippage and allows optimum overlap for all 100 passes.

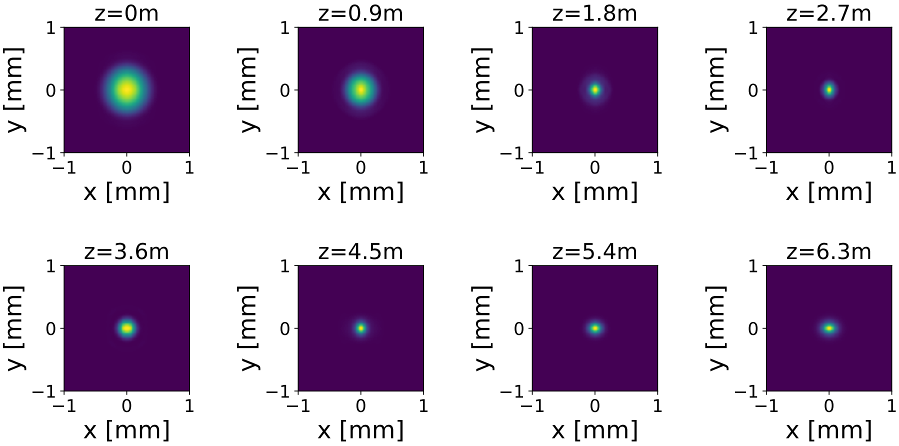

FIGURE B.7: Projected intensity of the radiation field on the transverse plane. Position $z = 0\,\mathrm{m}$ shows the intensity at the entrance of the modulator at the 60th pass. At $z = 2.7\,\mathrm{m}$ the first modulator segment ends, and two drift sections separated by a quadrupole follow, as shown in Fig. B.5. Between $z = 3.6\,\mathrm{m}$ and $z = 6.3\,\mathrm{m}$ the second modulator segment is placed. In this case, amplification takes place and leads to gain guiding.

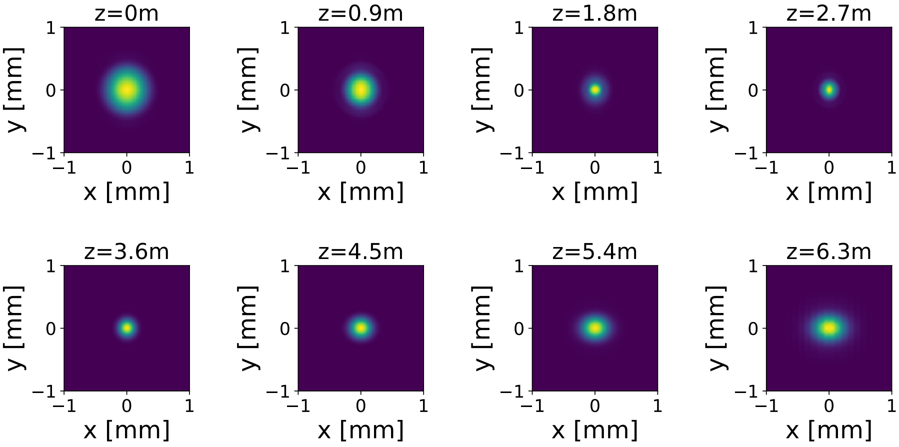

FIGURE B.8: Projected intensity of the radiation field on the transverse plane. Position $z = 0\,\mathrm{m}$ shows the intensity at the entrance of the modulator at the 60th pass. The radiation field is propagated along a drift section and the focal point occurs after roughly $3\,\mathrm{m}$. In this case, there is no amplification of the radiation field so the propagation leads to diffraction.

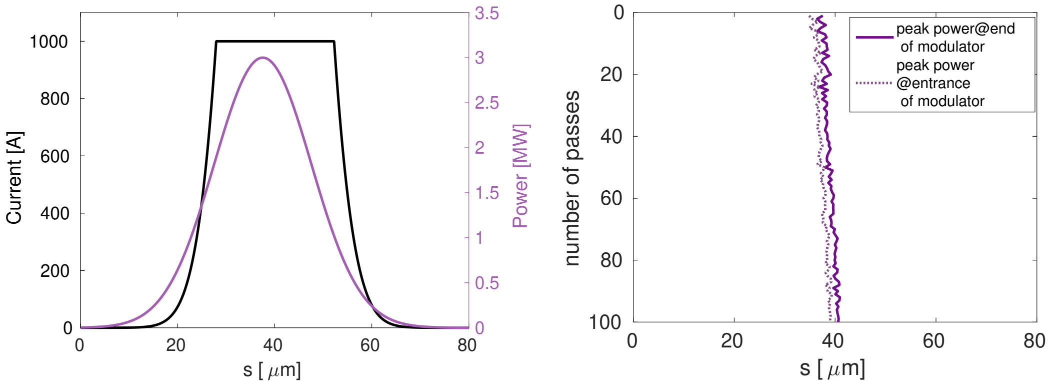

FIGURE B.9: On the left, I show the overlap of the electron bunch current distribution and the radiation field power profile at the entrance of the modulator and at the first pass in the oscillator. On the right, I show the position of the peak of the power profile at the entrance and at the exit of the modulator, with respect to the electron bunch position that is fixed in the time window. These two positions are shown per pass.

In the second part of the setup (see Fig. 4.2), the energy-modulated electron bunch traverses the bunching chicane to obtain sufficient bunching at the 12th harmonic of the seed laser wavelength. The R_{56} of the chicane is tuned to achieve maximum bunching. Comparing the theoretical prediction for R_{56} there is a discrepancy (a lower R_{56} was used in the simulation). This difference results due to the relatively long modulator used of 5.4 m. Since the modulator is characterized by a longitudinal dispersion, this should be subtracted when setting the R_{56} of the chicane.

The results of the output FEL shown in the publication of Section 4 were obtain with the undulator parameter of the amplifier set based on the resonance condition of Eq. 2.30. A scan of the undulator parameter can, however, further enhance the output FEL as shown in Fig. B.10. These results were obtained by reducing the theoretically calculated undulator parameter by 0.2%.

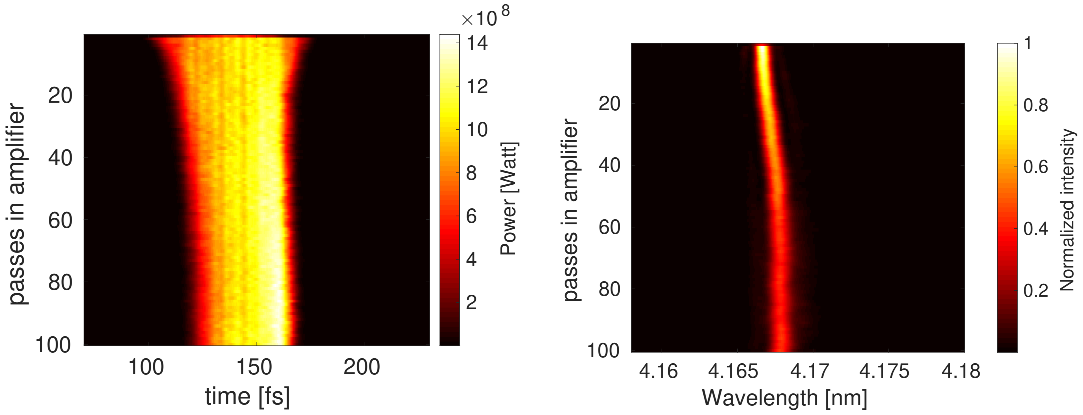

FIGURE B.10: The output of the FEL amplifier in time and frequency domain for one 100 passes. This results as the 12th harmonic of a 50 nm wavelength laser. These results can be compared to the Fig. 4 and 5 of the publication shown in Chapter 4. The difference between these results is that here I have reduced the K parameter of the amplifier by 0.2%.

For completeness I have added the electron optics in the amplifier section in Fig. B.11.

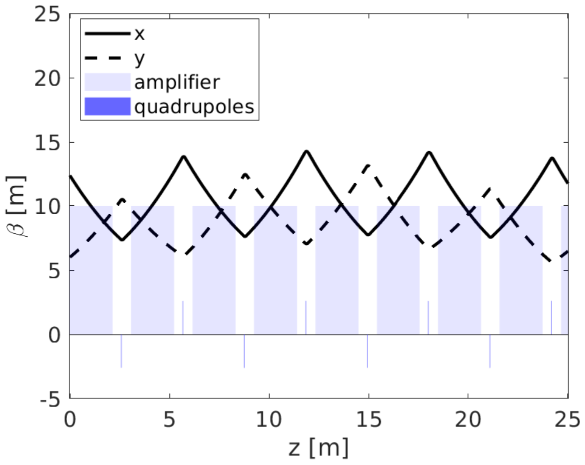

FIGURE B.11: Optics matching along the amplifier. The elements of the beamline can be seen in Fig. 4.2.

List of Figures

1.1 Comparison of peak brightness of existing FEL sources and synchrotron light sources. Graph taken from [19]. 2

2.1 Beam ellipse in the horizontal phase space at a certain fixed longitudinal position. Here, ϕ is the orientation angle. 10
2.2 The electron bunch distribution in the longitudinal phase space is affected by the phase of the RF wave during acceleration. In accordance with Eq. 2.15, maximum acceleration occurs on crest and maximum deceleration occurs in trough. 12
2.3 Schematic view of bunch compression in a magnetic chicane. An energy-chirped electron bunch transverses the chicane, and the electrons follow different paths based on their energy. The result is that the lower energy electrons follow a longer path and fall behind, while the higher energy electrons follow a shorter path and catch up, reducing the overall length of the bunch. On top left and right I show the electron bunch distribution in the longitudinal phase space. On the left, we can see the linearly chirped electron bunch before compression, and on the right, after compression. The distribution is rotated clockwise, and as a result, the electron bunch gets shorter. 12
2.4 Simplified schematic representation of an undulator. The undulator period λ_u is the distance between two poles of same polarity and the gap is the distance between the two girders. The black line shows the trajectory of the electrons, which is shown in the same plane as the magnetic field for simplicity, but in reality it lies on the transverse plane of the magnetic field. 14
2.5 A simple sketch of an FEL oscillator. An undulator is enclosed in an optical cavity which, in this case, consists of two focusing mirrors. The orange color refers to the stored radiation field which is recirculated in the cavity and it is synchronised to overlap with the electron bunches. With black lines I show the electron bunch path. 15
2.6 The power gain curves are demonstrated for different initial bunching factor based on Eq. 2.50. I show the power normalized to the power saturation and the distance z along the undulators normalized to the power gain length. 22
2.7 A simple schematic view of an HGHG setup: the seed laser and electron bunch overlap in the modulator, then the electron bunch continues in the chicane where the bunching is obtained and finally, the pre-bunched electron bunch enters the amplifier to generate radiation at a harmonic of the seed laser wavelength. 23

2.8 Electron bunch distribution in the longitudinal phase space (first row) and the related longitudinal current distribution (second row) for an HGHG scheme initially, after the modulator and after the chicane (see Fig. 2.7). The current is normalized to the initial peak current of the electron bunch. 25
2.9 Bunching maps calculated according to Eq. 2.57 for different harmonics. For this example, typical electron beam parameters of $\sigma_E/E = 10^{-4}$ are used. 26
2.10 In the simplest case, the optical klystron consists of two undulators separated by a chicane. The chicane converts the energy modulation induced in the first undulator into a density modulation. This results in increased gain in the second undulator. 27
2.11 Electron bunch distribution in the longitudinal phase space (first row) and the corresponding longitudinal current distribution (second row) for an optical klystron scheme initially, after the modulator and after the chicane (see Fig. 2.7). The current is normalized to the initial peak current of the electron bunch. 27
2.12 In an EEHG scheme two seed lasers are needed in the two modulators, each of them followed by a chicane. At the amplifier a high harmonic of the seed laser wavelength can be amplified. 29
2.13 Electron bunch distribution in the longitudinal phase space for an EEHG scheme. The longitudinal phase space is shown initially, after the first modulator, after the first chicane, after the second modulator and finally, after the second chicane (see Fig. 2.12). Please notice the vertical axis range change in the longitudinal phase space. The longitudinal density can be seen in Fig. 2.14 30
2.14 Longitudinal current distribution for an EEHG scheme. The longitudinal phase space is shown initially, after the first modulator, after the first chicane, after the second modulator and finally, after the second chicane (see Fig. 2.12). The current is normalized to the initial peak current of the electron bunch. The electron density corresponds to the plots of the longitudinal phase space of Fig. 2.13 31
2.15 Beam size evolution for an ideal Gaussian beam. The green lines show the evolution based on Eq. 2.65 and the orange ones define the divergence angle based on Eq. 2.67. The transverse size is normalized to the waist size at focus, and the distance from the focus is normalized to the Rayleigh length. 33

4.1 In the first stage of the seeded oscillator-amplifier, the goal is to maintain a stable power level of the recirculated radiation field in each pass. This stored radiation is used to modulate the energy of the electron bunches. 52
4.2 In the second stage of the seeded oscillator-amplifier, the radiation field does not play any role and is stored in the cavity, while the energy modulated electron bunch is extracted with the chicane. The chicane strength is optimized to introduce bunching at a harmonic of the wavelength of the in-cavity field. This way, coherent emission is possible at that harmonic in the amplifier. In this drawing, the electron bunch and the in-cavity radiation field are considerably separated to emphasize that they are independent at this stage. 52
4.3 Flow chart of simulations taken from [101]. 53

B.1 Energy modulation along the two modulators with the chicane on and off. The modulator length is shown in power gain lengths and, for an easier understanding, I have excluded the drifts, the quadrupole and the chicane in between the two modulators since the energy modulation is not affected while the electron bunch traverses these elements. . 98

B.2 I compare two fully optimized simulations of a standard HGHG and an OK-HGHG setup for the 10th harmonic of a 300 nm seed laser wavelength. In the first row I show the gain curves in amplifier and the output FEL power profiles. At the bottom, I show the output FEL spectra normalized to the intensity of the standard HGHG simulation. 99

B.3 I repeat the simulations of Fig. B.2 with a different initial shot noise of the simulation. In the first row I show the shot to shot pulse energy fluctuations, in the second row I show the output FEL power and spectrum for a standard HGHG scheme and at the bottom I show the power profile and spectrum of the output FEL for the OK HGHG scheme. 100

B.4 Power gain in the first pass of the oscillator and in the fourth pass for different undulator parameters K. 101

B.5 Optics matching along the modulators and the chicane. The elements of the beamline can be seen in Fig. 4.1. 102

B.6 Waist size of radiation field stored in the cavity. It is calculated by propagating the input field along a drift and identifying its waist size. 102

B.7 Projected intensity of the radiation field on the transverse plane. Position $z = 0$ m shows the intensity at the entrance of the modulator at the 60th pass. At $z = 2.7$ m the first modulator segment ends, and two drift sections separated by a quadrupole follow, as shown in Fig. B.5. Between $z = 3.6$ m and $z = 6.3$ m the second modulator segment is placed. In this case, amplification takes place and leads to gain guiding. 103

B.8 Projected intensity of the radiation field on the transverse plane. Position $z = 0$ m shows the intensity at the entrance of the modulator at the 60th pass. The radiation field is propagated along a drift section and the focal point occurs after roughly 3 m. In this case, there is no amplification of the radiation field so the propagation leads to diffraction. 103

B.9 On the left, I show the overlap of the electron bunch current distribution and the radiation field power profile at the entrance of the modulator and at the first pass in the oscillator. On the right, I show the position of the peak of the power profile at the entrance and at the exit of the modulator, with respect to the electron bunch position that is fixed in the time window. These two positions are shown per pass. . 104

B.10 The output of the FEL amplifier in time and frequency domain for one 100 passes. This results as the 12th harmonic of a 50 nm wavelength laser. These results can be compared to the Fig. 4 and 5 of the publication shown in Chapter 4. The difference between these results is that here I have reduced the K parameter of the amplifier by 0.2%. 105

B.11 Optics matching along the amplifier. The elements of the beamline can be seen in Fig. 4.2. 106

List of Tables

B.1 I list the simulation parameters optimized for the time-dependent simulations. . . . 97

B.2 Comparison of simulation results between a standard HGHG and an OK-HGHG setup. The output wavelength is 30 nm and results as the 10th harmonic of a 300 nm seed laser. The energy spread is calculated upstream from the amplifier. . . . 98

List of Symbols

A	normalized energy modulation
b	bunching factor
B	normalized dispersion
B_x, B_y	magnetic field
c	speed of light
C_{BC}	linear compression factor
e	electron charge
E	energy
$G_{\text{longitudinal}}$	longitudinal coherence degree
G_{OK}	optical klystron power gain factor
$G_{\text{transverse}}$	transverse coherence degree
h	electron beam linear energy chirp parameter
I_A	Alfvén current
I_0	on axis intensity
I	light intensity
I_{peak}	electron beam peak current
J	Bessel function
j_0	dc electron beam current density
$\widetilde{j}$	modulated electron beam current density
K	undulator parameter
$\widehat{K}$	modified undulator parameter
k_l	FEL radiation wavenumber
k_P	space charge parameter
k_{RF}	RF wavenumber
K_{seed}	seed laser wavenumber ratio
k_{seed}	seed laser wavenumber
k_u	undulater period wavenumber
l_{bunch}	electron bunch length
l_c	coherence/cooperation length
L_{g0}	1D power gain length
L_{g}	3D power gain length
L_{mod}	modulator length
M	transfer matrix
M^2	M^2 quality factor
M_f	longitudinal modes
m_0	rest mass
m_e	electron rest mass
n	harmonic number
N_u	number of undulator periods
P_{beam}	electron beam power
P_{coh}	coherent power of pre-bunched electron beam
P_{in}	input power

P_{sat}	saturation power
P_{shot}	shot noise power
P_{th}	transition power of pre-bunched electron beam
P	power
p	momentum
r	radial coordinate
R_c	radius of curvature of particle trajectory
R_{curv}	radius of curvature of wavefronts
R_{56}	longitudinal dispersion
S	spectral intensity
s	longitudinal intra-bunch coordinate
t	time coordinate
U	wave complex amplitude
$u_{z/x/y}$	longitudinal/horizontal/vertical velocity
V_{RF}	RF voltage amplitude
w_0	waist size of radiation field at focus
$w(z)$	waist size of radiation field
X_γ	energy spread parameter
X_d	diffraction parameter
X_ε	angular spread parameter
x/y	transverse displacement
x'/y'	transverse angular displacement
z	longitudinal position
z_R	Rayleigh length

α	laser chirp parameter
$\alpha(z)$	alpha function (twiss parameter)
A	normalized energy modulation
$\beta(z)$	beta function (twiss parameter)
β_{avg}	average beta function
β_{rel}	velocity relative to speed of light
Γ	gain parameter
$\gamma(z)$	gamma function (twiss parameter)
γ	electron beam energy
δ	relative momentum offset
ΔE_{gain}	electron beam energy gain
ΔE	energy modulation
$\Delta\nu_{\text{FWHM}}$	FWHM frequency bandwidth
ε	emittance
ϵ_0	vacuum perimittivity
ε_N	normalized emittance
ζ	Gouy phase shift
η	relative energy deviation
λ_l	undulator wavelength/FEL wavelength
λ_r	reference wavelength
λ_u	undulator period
μ_0	permeability of free space
ν	instantaneous frequency
ρ_{FEL}	FEL or Pierce parameter
ρ_0	dc electric charge density
$\widetilde{\rho}$	modulated electric charge density

σ_r	photon beam rms transvserse size
$\sigma_{r'}$	photon beam rms angular size
$\sigma_{x/y}$	electron beam rms transvserse size
$\sigma_{x'/y'}$	electron beam rms angular divergence
σ_δ	relative energy spread
σ_E	uncorrelated energy spread
$\sigma_{E'}$	energy spread upstream from amplifier
$\sigma_\zeta^{\mathrm{FEL}}$	FEL rms pulse duration
σ_ζ	seed laser rms pulse duration
τ_{FWHM}	FWHM pulse duration
Υ	electric field
Φ	flux
ψ	ponderomotive phase
ω	angular frequency

Acknowledgements

I want to deeply thank everyone who has supported me in completing my PhD and everyone who has proofread parts of my dissertation. First of all, I would like to thank my supervisor Wolfgang Hillert who offered me the possibility to pursue this PhD and steered my direction to the very interesting field of FEL physics and for his excitement and faith in my PhD topic. I would also like to thank my first supervisor Bart Faatz for all the long and interesting physics discussions we've had together that have evolved me a lot as a physicist and for being a mentor even after he left, and Johann Zemella who accepted with no hesitation to take over my supervision, and always offered a different and interesting point of view on my work.

I would also like to thank a lot my colleagues Lucas Schaper, Pardis Niknejadi, Sven Ackermann, Velizar Miltchev, Mehdi Kazemi, Tino Lang, Sheida Mahmoodi and Jiaan Zheng. Each of them has contributed in a very different, yet important way to my journey in Physics and I am grateful for that. I thank my FLASH colleagues and operators and in particular Mathias Vogt, Elke Ploenjes-Palm, Martin Beye, Siggi Schreiber and my European XFEL colleagues Christoph Lechner, Gianluca Geloni and Takanori Tanikawa for being available to discuss with me and share their knowledge and Eugenio Ferrari, Sven Reiche and Svitozar Serkez for their kind support in simulations. I thank Najmeh Mirian for our coffee breaks and discussions that effortlessly save the day. I also thank warmly Evgeny Schneidmiller and Enrico Allaria for allowing me to work on their ideas which ended up being a very enjoyable project that gave me a lot of new knowledge. A special thanks to Enrico Allaria for always being available to provide his physics insights and mentoring and for always reviving my enthusiasm for research.

I am grateful to the students Margarit Asatrian, Hauke Biss, Sam Hartwell, Fabian Pannek, Mihai Pop, Dmitrii Samoilenko, Andreas Thiel for the mutual support and our interesting discussions. I want to express my gratitude to Vanessa Grattoni, my office mate and my good friend. Our mutual support and knowledge sharing was a fundamental ingredient during this PhD. I also thank the dynaMENT members and my mentor for honest discussions and for guiding me to take the most out of my PhD. I am grateful to the co-members of GWiS for letting me be part of their family-like community and explore science communication and the importance of honest and open communities in science. A warm tack så mycket to Francesca Curbis and Sverker Werin from MAX IV for their support and willingness to provide help.

Last but not least I want to thank my friends, my beloved sister and parents for our unconditional love which can't be affected by the distance. A very warm ευχαριστώ and lots of love to Ermis and Lefteris who have been by my side for the last decade and are my definition of "feeling like home" even in Hamburg.

Bibliography

[1] F. R. Elder et al. "Radiation from Electrons in a Synchrotron". In: *Phys. Rev.* 71 (11 June 1947), pp. 829–830. DOI: 10.1103/PhysRev.71.829.5. URL: https://link.aps.org/doi/10.1103/PhysRev.71.829.5.

[2] Arthur L. Robinson. "History of Synchrotron Radiation". In: *Synchrotron Radiation News* 28.4 (2015), pp. 4–9. DOI: 10.1080/08940886.2015.1059228. URL: https://doi.org/10.1080/08940886.2015.1059228.

[3] Pedro F. Tavares et al. "The MAXIV storage ring project". In: *Journal of Synchrotron Radiation* 21.5 (Sept. 2014), pp. 862–877. DOI: 10.1107/S1600577514011503. URL: https://doi.org/10.1107/S1600577514011503.

[4] I. V. Agapov et al. "Status of the PETRA IV project". In: *Proc. 10th Int. Particle Accelerator Conf. (IPAC'19)* (Melbourne, Australia). JACoW Publishing, May 2019, pp. 1404–1407. DOI: doi:10.18429/JACoW-IPAC2019-TUPGW011. URL: http://accelconf.web.cern.ch/ipac2019/papers/TUPGW011.pdf.

[5] Luis R. Elias et al. "Observation of Stimulated Emission of Radiation by Relativistic Electrons in a Spatially Periodic Transverse Magnetic Field". In: *Phys. Rev. Lett.* 36 (13 Mar. 1976), pp. 717–720. DOI: 10.1103/PhysRevLett.36.717. URL: https://link.aps.org/doi/10.1103/PhysRevLett.36.717.

[6] D. A. G. Deacon et al. "First Operation of a Free-Electron Laser". In: *Phys. Rev. Lett.* 38 (16 Apr. 1977), pp. 892–894. DOI: 10.1103/PhysRevLett.38.892. URL: https://link.aps.org/doi/10.1103/PhysRevLett.38.892.

[7] Kondratenko A.M and Saldin E.L. "Generation of coherent radiation by a relativistic electron beam in an ondulator". In: *Particle Accelerators* 10.3-4 (1980), pp. 207–216. ISSN: 0031-2460. URL: https://inis.iaea.org/search/search.aspx?orig_q=RN:12582046.

[8] R. Bonifacio, F. Casagrande, and G. Casati. "Cooperative and chaotic transition of a free electron laser Hamiltonian model". In: *Optics Communications* 40.3 (Jan. 1982), pp. 219–223. DOI: 10.1016/0030-4018(82)90265-6.

[9] R. Bonifacio, C. Pellegrini, and L.M. Narducci. "Collective instabilities and high-gain regime in a free electron laser". In: *Optics Communications* 50.6 (1984), pp. 373–378. ISSN: 0030-4018. DOI: https://doi.org/10.1016/0030-4018(84)90105-6. URL: https://www.sciencedirect.com/science/article/pii/0030401884901056.

[10] Jörg Rossbach, Jochen R. Schneider, and Wilfried Wurth. "10 years of pioneering X-ray science at the Free-Electron Laser FLASH at DESY". In: *Physics Reports* 808 (2019). 10 years of pioneering X-ray science at the Free-Electron Laser FLASH at DESY, pp. 1–74. ISSN: 0370-1573. DOI: https://doi.org/10.1016/j.physrep.2019.02.002. URL: https://www.sciencedirect.com/science/article/pii/S0370157319300663.

[11] P. Emma et al. “First lasing and operation of an ångstrom-wavelength free-electron laser”. English (US). In: *Nature Photonics* 4.9 (Sept. 2010), pp. 641–647. ISSN: 1749-4885. DOI: `10.1038/nphoton.2010.176`.

[12] T. Ishikawa et al. “A compact X-ray free-electron laser emitting in the sub-ångström region”. In: *Nature Photonics* 6 (2012), pp. 540–544. DOI: `https://doi.org/10.1038/nphoton.2012.141`.

[13] L. Giannessi et al. “Status and Perspectives of the FERMI FEL Facility (2019)”. In: *Proc. 39th Int. Free Electron Laser Conf. (FEL’19)* (Hamburg, Germany). JACoW Publishing, Sept. 2019, pp. 742–745. DOI: `doi:10.18429/JACoW-FEL2019-THP079`.

[14] Heung-Sik Kang et al. “Hard X-ray free-electron laser with femtosecond-scale timing jitter”. In: *Nature Photonics* 11 (Nov. 2017). DOI: `10.1038/s41566-017-0029-8`.

[15] D. Nölle. “FEL Operation at the European XFEL Facility”. In: *Proc. of International Free Electron Laser Conference (FEL’19), Hamburg, Germany, August 26-30, 2019*. International Free Electron Laser Conference 39. Geneva, Switzerland: JACoW, 2019. DOI: `doi:10.18429/JACoW-FEL2019-FRA01`.

[16] Eduard Prat et al. “A compact and cost-effective hard X-ray free-electron laser driven by a high-brightness and low-energy electron beam”. In: *Nature Photonics* 14 (Dec. 2020), pp. 1–7. DOI: `10.1038/s41566-020-00712-8`.

[17] Ralph Assmann et al. “EuPRAXIA Conceptual Design Report”. In: *The European Physical Journal Special Topics* 229 (Dec. 2020), pp. 3675–4284. DOI: `10.1140/epjst/e2020-000127-8`.

[18] Sarah Schröder et al. “High-resolution sampling of beam-driven plasma wakefields”. In: *Nature Communications* 11 (Nov. 2020). DOI: `10.1038/s41467-020-19811-9`.

[19] Peter Schmüser, Martin Dohlus, and Jörg Rossbach. *Ultraviolet and Soft X-Ray Free-Electron Lasers: Introduction to Physical Principles, Experimental Results, Technological Challenges*. 1st. Springer Publishing Company, Incorporated, 2008. ISBN: 3540795715.

[20] J. Feldhaus et al. “Possible application of X-ray optical elements for reducing the spectral bandwidth of an X-ray SASE FEL”. In: *Optics Communications* 140.4 (1997), pp. 341–352. ISSN: 0030-4018. DOI: `https://doi.org/10.1016/S0030-4018(97)00163-6`.

[21] B. W. J. McNeil, N. R. Thompson, and D. J. Dunning. “Transform-Limited X-Ray Pulse Generation from a High-Brightness Self-Amplified Spontaneous-Emission Free-Electron Laser”. In: *Phys. Rev. Lett.* 110 (13 Mar. 2013), p. 134802. DOI: `10.1103/PhysRevLett.110.134802`. URL: `https://link.aps.org/doi/10.1103/PhysRevLett.110.134802`.

[22] G. Lambert et al. “Injection of harmonics generated in gas in a free-electron laser providing intense and coherent extreme-ultraviolet light”. In: *Nature Physics* 4 (2008), pp. 296–300. DOI: `10.1038/nphys889`.

[23] Christoph Heyl et al. “Introduction to macroscopic power scaling principles for high-order harmonic generation”. In: *Journal of Physics B: Atomic, Molecular and Optical Physics* 50 (Jan. 2017), p. 013001. DOI: `10.1088/1361-6455/50/1/013001`.

[24] L. H. Yu. “Generation of intense uv radiation by subharmonically seeded single-pass free-electron lasers”. In: *Phys. Rev. A* 44 (8 Oct. 1991), pp. 5178–5193. DOI: `10.1103/PhysRevA.44.5178`. URL: `https://link.aps.org/doi/10.1103/PhysRevA.44.5178`.

[25] G. Stupakov. “Using the Beam-Echo Effect for Generation of Short-Wavelength Radiation”. In: *Phys. Rev. Lett.* 102 (7 Feb. 2009), p. 074801. DOI: `10.1103/PhysRevLett.102.074801`. URL: `https://link.aps.org/doi/10.1103/PhysRevLett.102.074801`.

[26] Dao Xiang and Gennady Stupakov. “Echo-enabled harmonic generation free electron laser”. In: *Phys. Rev. ST Accel. Beams* 12 (3 Mar. 2009), p. 030702. DOI: `10.1103/PhysRevSTAB.12.030702`. URL: `https://link.aps.org/doi/10.1103/PhysRevSTAB.12.030702`.

[27] Kevin Prince et al. “Coherent control with a short-wavelength Free Electron Laser”. In: *Nature Photonics* 10 (Feb. 2016), pp. 176–179. DOI: `10.1038/nphoton.2016.13`.

[28] Praveen Kumar Maroju et al. “Attosecond pulse shaping using a seeded free-electron laser”. In: *Nature* 578 (2020), pp. 386–391. DOI: `https://doi.org/10.1038/s41586-020-2005-6`.

[29] Z. T. Zhao et al. “First lasing of an echo-enabled harmonic generation free-electron laser”. In: *Nature Photonics* 6.6 (June 2012), pp. 360–363. DOI: `10.1038/nphoton.2012.105`.

[30] Erik Hemsing et al. “Echo-enabled harmonics up to the 75th order from precisely tailored electron beams”. In: *Nature Photonics* 10 (2016), pp. 512–515. DOI: `https://doi.org/10.1038/nphoton.2016.101`.

[31] G. L. Wang. “Commissioning Status of the Dalian Cohernet Light Source”. In: *Proc. 8th Int. Particle Accelerator Conf. (IPAC'17)* (Copenhagen, Denmark). https://doi.org/10.18429/JACoW-IPAC2017-WEPAB058. JACoW Publishing, May 2017, pp. 2709–2712. DOI: `doi:10.18429/JACoW-IPAC2017-WEPAB058`. URL: `https://jacow.org/ipac2017/papers/WEPAB058.pdf`.

[32] Chao Feng et al. “Coherent extreme ultraviolet free-electron laser with echo-enabled harmonic generation”. In: *Phys. Rev. Accel. Beams* 22 (5 May 2019), p. 050703. DOI: `10.1103/PhysRevAccelBeams.22.050703`. URL: `https://link.aps.org/doi/10.1103/PhysRevAccelBeams.22.050703`.

[33] C. Lechner et al. “Seeding R&D at sFLASH”. In: *Proc. 39th Int. Free Electron Laser Conf. (FEL'19)* (Hamburg, Germany). https://doi.org/10.18429/JACoW-FEL2019-TUP076. JACoW Publishing, Sept. 2019, pp. 230–233. DOI: `doi:10.18429/JACoW-FEL2019-TUP076`. URL: `https://jacow.org/fel2019/papers/TUP076.pdf`.

[34] Martin Beye. *FLASH2020+: Making FLASH brighter, faster and more flexible : Conceptual Design Report*. Hamburg: Verlag Deutsches Elektronen-Synchrotron, 2020, pp. 1–126. ISBN: 9783945931301. DOI: `10.3204/PUBDB-2020-00465`. URL: `https://bib-pubdb1.desy.de/record/434950`.

[35] Lucas Schaper et al. “Flexible and Coherent Soft X-ray Pulses at High Repetition Rate: Current Research and Perspectives”. In: *Applied Sciences* 11.20 (2021). ISSN: 2076-3417. DOI: `10.3390/app11209729`. URL: `https://www.mdpi.com/2076-3417/11/20/9729`.

[36] Primož Ribič et al. “Coherent soft X-ray pulses from an echo-enabled harmonic generation free-electron laser”. In: *Nature Photonics* 13 (Aug. 2019), pp. 1–7. DOI: `10.1038/s41566-019-0427-1`.

[37] Bart Faatz et al. “The FLASH Facility: Advanced Options for FLASH2 and Future Perspectives”. In: *Applied Sciences* 7.11 (2017), p. 1114. ISSN: 2076-3417. DOI: `10.3390/app7111114`. URL: `http://bib-pubdb1.desy.de/record/393961`.

[38] E. Hemsing et al. “Soft x-ray seeding studies for the SLAC Linac Coherent Light Source II”. In: *Phys. Rev. Accel. Beams* 22 (11 Nov. 2019), p. 110701. DOI: `10.1103/PhysRevAccelBeams.22.110701`. URL: `https://link.aps.org/doi/10.1103/PhysRevAccelBeams.22.110701`.

[39] T. Liu, X. Dong, and C. Feng. “Start-to-end Simulations of the Reflection Hard X-Ray Self-Seeding at the SHINE Project”. In: *Proc. FEL’19* (Hamburg, Germany). Free Electron Laser Conference 39. https://doi.org/10.18429/JACoW-FEL2019-TUP087. JACoW Publishing, Geneva, Switzerland, Nov. 2019, pp. 254–257. ISBN: 978-3-95450-210-3. DOI: `doi:10.18429/JACoW-FEL2019-TUP087`. URL: `http://jacow.org/fel2019/papers/tup087.pdf`.

[40] N. A. Vinokurov and A. N. Skrinsky. In: *Preprint of INP 77- 59* (1977), INP 77–69.

[41] Klaus Wille. *The physics of particle accelerators*. Oxford Univ. Press, 2000. URL: `https://catalogue.library.cern/literature/ct722-yam11`.

[42] Werner Herr and Etienne Forest. “Non-linear Dynamics in Accelerators”. In: *Particle Physics Reference Library : Volume 3: Accelerators and Colliders*. Ed. by Stephen Myers and Herwig Schopper. Cham: Springer International Publishing, 2020, pp. 51–104. ISBN: 978-3-030-34245-6. DOI: `10.1007/978-3-030-34245-6_3`. URL: `https://doi.org/10.1007/978-3-030-34245-6_3`.

[43] David C. Carey. *THE OPTICS OF CHARGED PARTICLE BEAMS*. Harwood-Academic Publisher, 1987. ISBN: 978-3-7186-0545-3.

[44] Helmut Wiedemann. *Particle accelerator physics; 3rd ed.* Berlin: Springer, 2007. DOI: `10.1007/978-3-540-49045-6`. URL: `https://cds.cern.ch/record/1083415`.

[45] Wolfgang Hillert. *Transverse Linear Beam Dynamics*. 2021. arXiv: `2107.02614 [physics.acc-ph]`.

[46] Simone Di Mitri. “On the Importance of Electron Beam Brightness in High Gain Free Electron Lasers”. In: *Photonics* 2.2 (2015), pp. 317–341. ISSN: 2304-6732. DOI: `10.3390/photonics2020317`. URL: `https://www.mdpi.com/2304-6732/2/2/317`.

[47] C. Behrens and DESY. “Characterization and control of femtosecond electron and X-ray beams at free-electron lasers.” Universität Hamburg, Diss., 2012. Dr. Hamburg: Universität Hamburg, 2012. DOI: `10.3204/DESY-THESIS-2012-038`. URL: `https://bib-pubdb1.desy.de/record/139966`.

[48] Yipeng Sun et al. “X-band rf driven free electron laser driver with optics linearization”. In: *Phys. Rev. ST Accel. Beams* 17 (11 Nov. 2014), p. 110703. DOI: `10.1103/PhysRevSTAB.17.110703`. URL: `https://link.aps.org/doi/10.1103/PhysRevSTAB.17.110703`.

[49] Klaus Floettmann, Thorsten Limberg, and Philippe Piot. *Generation of Ultrashort Electron Bunches by Cancellation of Nonlinear Distortions in the Longitudinal Phase Space*. Tech. rep. TESLA FEL 2001-06. abstract kopieren geht nicht. 2001, p. 15. URL: https://bib-pubdb1.desy.de/record/409209.

[50] S. Di Mitri and S. Spampinati. "Microbunching instability study in a linac-driven free electron laser spreader beam line". In: *Phys. Rev. Accel. Beams* 20 (12 Dec. 2017), p. 120701. DOI: 10.1103/PhysRevAccelBeams.20.120701. URL: https://link.aps.org/doi/10.1103/PhysRevAccelBeams.20.120701.

[51] M Cornacchia et al. "Running fermi with one-stage compressor: advantages, layout,performance". In: (May 2007). DOI: 10.2172/929314. URL: https://www.osti.gov/biblio/929314.

[52] E. Ferrari et al. "Impact of Non-Gaussian Electron Energy Heating upon the Performance of a Seeded Free-Electron Laser". In: *Phys. Rev. Lett.* 112 (11 Mar. 2014), p. 114802. DOI: 10.1103/PhysRevLett.112.114802. URL: https://link.aps.org/doi/10.1103/PhysRevLett.112.114802.

[53] N. S. Mirian et al. "Characterization of soft x-ray echo-enabled harmonic generation free-electron laser pulses in the presence of incoherent electron beam energy modulations". In: *Phys. Rev. Accel. Beams* 24 (8 Sept. 2021), p. 080702. DOI: 10.1103/PhysRevAccelBeams.24.080702. URL: https://link.aps.org/doi/10.1103/PhysRevAccelBeams.24.080702.

[54] John David Jackson. *Classical electrodynamics*. 3rd ed. New York, NY: Wiley, 1999. ISBN: 9780471309321. URL: http://cdsweb.cern.ch/record/490457.

[55] Kwang-Je Kim, Zhirong Huang, and Ryan Lindberg. *Synchrotron Radiation and Free-Electron Lasers: Principles of Coherent X-Ray Generation*. Cambridge University Press, 2017. DOI: 10.1017/9781316677377.

[56] Zhirong Huang and Kwang-Je Kim. "Review of x-ray free-electron laser theory". In: *Phys. Rev. ST Accel. Beams* 10 (3 Mar. 2007), p. 034801. DOI: 10.1103/PhysRevSTAB.10.034801. URL: https://link.aps.org/doi/10.1103/PhysRevSTAB.10.034801.

[57] M. Trovò et al. "Operation of the European storage ring FEL at ELETTRA down to 190nm". In: *Nuclear Instruments and Methods in Physics Research Section A: Accelerators, Spectrometers, Detectors and Associated Equipment* 483.1 (2002). Proceedings of the 23rd International Free Electron Laser Confere nce and 8th FEL Users Workshop, pp. 157–161. ISSN: 0168-9002. DOI: https://doi.org/10.1016/S0168-9002(02)00303-0. URL: http://www.sciencedirect.com/science/article/pii/S0168900202003030.

[58] D. Oepts, A.F.G. van der Meer, and P.W. van Amersfoort. "The Free-Electron-Laser user facility FELIX". In: *Infrared Physics & Technology* 36.1 (1995), pp. 297–308. ISSN: 1350-4495. DOI: https://doi.org/10.1016/1350-4495(94)00074-U. URL: http://www.sciencedirect.com/science/article/pii/135044959400074U.

[59] Paul Wang et al. "Status report on the Duke FEL facility". In: vol. 4. Feb. 2001, 2819–2820 vol.4. ISBN: 0-7803-7191-7. DOI: 10.1109/PAC.2001.987920.

[60] Kwang-Je Kim, Yuri Shvyd'ko, and Sven Reiche. "A Proposal for an X-Ray Free-Electron Laser Oscillator with an Energy-Recovery Linac". In: *Phys. Rev. Lett.* 100 (24 June 2008), p. 244802. DOI: 10.1103/PhysRevLett.100.244802. URL: https://link.aps.org/doi/10.1103/PhysRevLett.100.244802.

[61] Primoz Rebernik Ribic and G Margaritondo. “Status and prospects of x-ray free-electron lasers (X-FELs): a simple presentation”. In: *Journal of Physics D: Applied Physics* 45.21 (May 2012), p. 213001. DOI: 10.1088/0022-3727/45/21/213001. URL: https://doi.org/10.1088/0022-3727/45/21/213001.

[62] B. Faatz et al. “Regenerative FEL amplifier at the TESLA test facility at DESY”. In: *Nuclear Instruments and Methods in Physics Research Section A: Accelerators, Spectrometers, Detectors and Associated Equipment* 429.1 (1999), pp. 424–428. ISSN: 0168-9002. DOI: https://doi.org/10.1016/S0168-9002(99)00123-0. URL: http://www.sciencedirect.com/science/article/pii/S0168900299001230.

[63] H P Freund, P J M van der Slot, and Yu Shvyd’ko. “An x-ray regenerative amplifier free-electron laser using diamond pinhole mirrors”. In: *New Journal of Physics* 21.9 (Sept. 2019), p. 093028. DOI: 10.1088/1367-2630/ab3f72. URL: https://doi.org/10.1088%2F1367-2630%2Fab3f72.

[64] S. Reiche. “GENESIS 1.3: a fully 3D time-dependent FEL simulation code”. In: *Nuclear Instruments and Methods in Physics Research Section A: Accelerators, Spectrometers, Detectors and Associated Equipment* 429.1 (1999), pp. 243–248. ISSN: 0168-9002. DOI: https://doi.org/10.1016/S0168-9002(99)00114-X. URL: http://www.sciencedirect.com/science/article/pii/S016890029900114X.

[65] William M. Fawley. “A user manual for GINGER and its post-processor XPLOT-GIN”. In: *Lawrence Berkeley National Laboratory* (2002).

[66] Luca Giannessi. “Seeding and Harmonic Generation in Free-Electron Lasers”. In: Synchrotron Light Sources, Free-Electron Lasers: Accelerator Physics, Instrumentation, and Science Applications, Jan. 2016, pp. 195–223. ISBN: 978-3-319-14393-4. DOI: 10.1007/978-3-319-14394-1_3.

[67] M. Xie. “Design optimization for an X-ray free electron laser driven by SLAC LINAC”. In: *Conf. Proc.* C950501 (1996), pp. 183–185. DOI: 10.1109/PAC.1995.504603.

[68] Li Hua Yu and Juhao Wu. “Theory of high gain harmonic generation: an analytical estimate”. In: *Nuclear Instruments and Methods in Physics Research Section A: Accelerators, Spectrometers, Detectors and Associated Equipment* (May 2002), pp. 493–498. DOI: 10.1016/S0168-9002(02)00368-6.

[69] S. Reiche. “Overview of Seeding Methods for FELs”. In: *Proc. 4th Int. Particle Accelerator Conf. (IPAC’13)* (Shanghai, China). JACoW Publishing, May 2013, pp. 2063–2067. URL: https://jacow.org/IPAC2013/papers/WEZB102.pdf.

[70] Erik Hemsing et al. “Beam by design: Laser manipulation of electrons in modern accelerators”. In: *Rev. Mod. Phys.* 86 (3 July 2014), pp. 897–941. DOI: 10.1103/RevModPhys.86.897. URL: https://link.aps.org/doi/10.1103/RevModPhys.86.897.

[71] Qika Jia. “Analysis of modulation parameters for high repetition rate seeded FEL”. In: *Nuclear Instruments and Methods in Physics Research Section A: Accelerators, Spectrometers, Detectors and Associated Equipment* 1015 (2021), p. 165767. ISSN: 0168-9002. DOI: https://doi.org/10.1016/j.nima.2021.165767. URL: https://www.sciencedirect.com/science/article/pii/S016890022100752X.

[72] Chao Feng. “Basic Theory of FEL”. In: Dec. 2016, pp. 9–17. ISBN: 978-3-662-49064-8. DOI: 10.1007/978-3-662-49066-2_2.

[73] Paola Finetti et al. “Pulse Duration of Seeded Free-Electron Lasers”. In: *Physical Review X* 7.2 (June 2017), p. 021043. ISSN: 2160-3308. DOI: 10.1103/PhysRevX.7.021043.

[74] G. Penco et al. “Enhanced seeded free electron laser performance with a “cold” electron beam”. In: *Phys. Rev. Accel. Beams* 23 (12 Dec. 2020), p. 120704. DOI: 10.1103/PhysRevAccelBeams.23.120704. URL: https://link.aps.org/doi/10.1103/PhysRevAccelBeams.23.120704.

[75] Li-Hua Yu and Ilan Ben-Zvi. “High-gain harmonic generation of soft X-rays with the “fresh bunch” technique”. In: *Nuclear Instruments and Methods in Physics Research Section A: Accelerators, Spectrometers, Detectors and Associated Equipment* 393.1 (1997). Free Electron Lasers 1996, pp. 96–99. ISSN: 0168-9002. DOI: https://doi.org/10.1016/S0168-9002(97)00435-X. URL: https://www.sciencedirect.com/science/article/pii/S016890029700435X.

[76] E.L Saldin, E.A Schneidmiller, and M.V Yurkov. “Study of a noise degradation of amplification process in a multistage HGHG FEL”. In: *Optics Communications* 202.1 (2002), pp. 169–187. ISSN: 0030-4018. DOI: https://doi.org/10.1016/S0030-4018(02)01091-X. URL: https://www.sciencedirect.com/science/article/pii/S003040180201091X.

[77] A.S. Artamonov et al. “The first experiments with an optical klystron installed on the VEPP-3 storage ring”. In: *Nuclear Instruments and Methods* 177.1 (1980), pp. 247–252. ISSN: 0029-554X. DOI: https://doi.org/10.1016/0029-554X(80)90557-1. URL: https://www.sciencedirect.com/science/article/pii/0029554X80905571.

[78] Vladimir N Litvinenko et al. “Operation of the OK-4/Duke storage ring FEL below 200nm”. In: *Nuclear Instruments and Methods in Physics Research Section A: Accelerators, Spectrometers, Detectors and Associated Equipment* 475.1 (2001). FEL2000: Proc. 22nd Int. Free Electron Laser Conference and 7th F EL Users Workshop, pp. 195–204. ISSN: 0168-9002. DOI: https://doi.org/10.1016/S0168-9002(01)01559-5. URL: https://www.sciencedirect.com/science/article/pii/S0168900201015595.

[79] Yuantao Ding et al. “Optical klystron enhancement to self-amplified spontaneous emission free electron lasers”. In: *Phys. Rev. ST Accel. Beams* 9 (7 July 2006), p. 070702. DOI: 10.1103/PhysRevSTAB.9.070702. URL: https://link.aps.org/doi/10.1103/PhysRevSTAB.9.070702.

[80] Giuseppe Penco et al. “Optical Klystron Enhancement to Self Amplified Spontaneous Emission at FERMI”. In: *Photonics* 4.4 (Mar. 2017), p. 15. ISSN: 2304-6732. DOI: 10.3390/photonics4010015.

[81] Jiawei Yan et al. “Self-Amplification of Coherent Energy Modulation in Seeded Free-Electron Lasers”. In: *Phys. Rev. Lett.* 126 (8 Feb. 2021), p. 084801. DOI: 10.1103/PhysRevLett.126.084801. URL: https://link.aps.org/doi/10.1103/PhysRevLett.126.084801.

[82] Georgia Paraskaki et al. “High repetition rate seeded free electron laser with an optical klystron in high-gain harmonic generation”. In: *Phys. Rev. Accel. Beams* 24 (12 Dec. 2021), p. 120701. DOI: 10.1103/PhysRevAccelBeams.24.120701. URL: https://link.aps.org/doi/10.1103/PhysRevAccelBeams.24.120701.

[83] Gianluca Geloni et al. “Revision of optical klystron enhancement effects in self-amplified spontaneous emission free electron lasers”. In: *Phys. Rev. Accel. Beams* 24 (9 Sept. 2021), p. 090702. DOI: `10.1103/PhysRevAccelBeams.24.090702`. URL: `https://link.aps.org/doi/10.1103/PhysRevAccelBeams.24.090702`.

[84] Chao Feng et al. “Measurement of the average local energy spread of electron beam via coherent harmonic generation”. In: *Phys. Rev. ST Accel. Beams* 14 (9 Sept. 2011), p. 090701. DOI: `10.1103/PhysRevSTAB.14.090701`. URL: `https://link.aps.org/doi/10.1103/PhysRevSTAB.14.090701`.

[85] G. Penco et al. “Experimental Demonstration of Enhanced Self-Amplified Spontaneous Emission by an Optical Klystron”. In: *Phys. Rev. Lett.* 114 (1 Jan. 2015), p. 013901. DOI: `10.1103/PhysRevLett.114.013901`. URL: `https://link.aps.org/doi/10.1103/PhysRevLett.114.013901`.

[86] “Study of the Energy Chirp Effects on Seeded FEL Schemes at SDUV-FEL”. In: *IPAC2012 TUPPP056* 12 (3 Mar. 2009), p. 030702. DOI: `10.1103/PhysRevSTAB.12.030702`. URL: `https://link.aps.org/doi/10.1103/PhysRevSTAB.12.030702`.

[87] Guanglei Wang et al. “Beam energy chirp effects in seeded free-electron lasers”. In: *Nuclear Instruments and Methods in Physics Research A* 753 (July 2014), pp. 56–60. DOI: `10.1016/j.nima.2014.03.015`.

[88] B. W. Garcia et al. “Echo-Enabled Harmonic Generation Results with Energy Chirp”. In: *Proc. 38th Int. Free Electron Laser Conf. (FEL’17)* (Santa Fe, NM, USA). JACoW Publishing, Sept. 2017, pp. 64–67. DOI: `doi:10.18429/JACoW-FEL2017-MOP017`.

[89] G. V. Stupakov. “Effect of Coulomb Collisions on Echo-Enabled Harmonic Generation (EEHG)”. In: *Proc. 33rd Int. Free Electron Laser Conf. (FEL’11)* (Shanghai, China). JACoW Publishing, Sept. 2011, pp. 49–52. URL: `https://jacow.org/FEL2011/papers/MOPB20.pdf`.

[90] D. Samoilenko et al. “Discussion on CSR instability in EEHG Simulation”. In: *Proc. 12th Int. Particle Accelerator Conf. (IPAC’21)* (Campinas, Brazil). JACoW Publishing, May 2021, pp. 1622–1625. DOI: `doi:10.18429/JACoW-IPAC2021-TUPAB103`. URL: `https://jacow.org/ipac2021/papers/TUPAB103.pdf`.

[91] F. Pannek et al. “Mitigation of Beam Instabilities in the Echo-Enabled Harmonic Generation Beamline for FLASH2020+”. In: *Proc. 12th Int. Particle Accelerator Conf. (IPAC’21)* (Campinas, Brazil). https://doi.org/10.18429/JACoW-IPAC2021-FRXA06. JACoW Publishing, May 2021, pp. 4514–4517. DOI: `doi:10.18429/JACoW-IPAC2021-FRXA06`. URL: `https://jacow.org/ipac2021/papers/FRXA06.pdf`.

[92] Bahaa E A Saleh and Malvin Carl Teich. *Fundamentals of photonics; 2nd ed.* Wiley series in pure and applied optics. New York, NY: Wiley, 2007. Chap. 3. URL: `https://cds.cern.ch/record/1084451`.

[93] Juhao Wu et al. “Interplay of the chirps and chirped pulse compression in a high-gain seeded free-electron laser”. In: *Journal of the Optical Society of America B Optical Physics* 24.3 (Mar. 2007), pp. 484–495. DOI: `10.1364/JOSAB.24.000484`.

[94] E. Saldin, E. Schneidmiller, and M. V. Yurkov. "Transverse and Longitudinal Coherence Properties of the Radiation from X-Ray SASE FELs". In: *Proc. 28th Int. Free Electron Laser Conf. (FEL'06)* (Berlin, Germany). JACoW Publishing, Sept. 2006, pp. 206–209. URL: `https://jacow.org/f06/papers/MOPPH069.pdf`.

[95] B. Liu et al. "Demonstration of a widely-tunable and fully-coherent high-gain harmonic-generation free-electron laser". In: *Phys. Rev. ST Accel. Beams* 16 (2 Feb. 2013), p. 020704. DOI: `10.1103/PhysRevSTAB.16.020704`. URL: `https://link.aps.org/doi/10.1103/PhysRevSTAB.16.020704`.

[96] Vinzenz Hilbert et al. "An extreme ultraviolet Michelson interferometer for experiments at free-electron lasers". In: *The Review of scientific instruments* 84 (Sept. 2013), p. 095111. DOI: `10.1063/1.4821146`.

[97] F. Capotondi et al. "Invited Article: Coherent imaging using seeded free-electron laser pulses with variable polarization: First results and research opportunities". In: *Review of scientific instruments* 84.5 (2013), pp. 051301–11. ISSN: 0034-6748. DOI: `10.1063/1.4807157`.

[98] Konstantin Kharitonov et al. "Flexible ptychography platform to expand the potential of imaging at free electron lasers". In: *Opt. Express* 29.14 (July 2021), pp. 22345–22365. DOI: `10.1364/OE.426931`. URL: `http://www.osapublishing.org/oe/abstract.cfm?URI=oe-29-14-22345`.

[99] D. Ratner et al. "Laser phase errors in seeded free electron lasers". In: *Phys. Rev. ST Accel. Beams* 15 (3 Mar. 2012), p. 030702. DOI: `10.1103/PhysRevSTAB.15.030702`. URL: `https://link.aps.org/doi/10.1103/PhysRevSTAB.15.030702`.

[100] Eiji Takahashi, Yasuo Nabekawa, and Katsumi Midorikawa. "Generation of 10-µJ coherent extreme-ultraviolet light by use of high-order harmonics". In: *Opt. Lett.* 27.21 (Nov. 2002), pp. 1920–1922. DOI: `10.1364/OL.27.001920`. URL: `http://ol.osa.org/abstract.cfm?URI=ol-27-21-1920`.

[101] Sven Ackermann et al. "High-Repetition-Rate Seeding Schemes Using a Resonator-Amplifier Setup". In: *Proc. of International Free Electron Laser Conference (FEL'19), Hamburg, Germany, August 26-30, 2019*. International Free Electron Laser Conference 39. Geneva, Switzerland: JACoW, 2019. DOI: `doi:10.18429/JACoW-FEL2019-TUP073`.

[102] Ilya Agapov et al. "OCELOT: A software framework for synchrotron light source and FEL studies". In: *Nuclear instruments & methods in physics research / A* 768 (2014), pp. 151–156. ISSN: 0168-9002. DOI: `10.1016/j.nima.2014.09.057`.

[103] P. J. M. van der Slot and H. Freund. "Three-dimensional, Time-dependent Simulation of Free-Electron Lasers". In: *Proc. 37th Int. Free Electron Laser Conf. (FEL'15)* (Daejeon, Korea). JACoW Publishing, Sept. 2015, pp. 331–333. DOI: `doi:10.18429/JACoW-FEL2015-TUP004`. URL: `https://jacow.org/FEL2015/papers/TUP004.pdf`.

[104] Henry P. Freund and Li-Hua Yu. "Comparison of the non-wiggler-averaged code MEDUSA and the wiggler-averaged code TDA3D". In: *Free-Electron Laser Challenges*. Ed. by Patrick G. O'Shea and Harold E. Bennett. Vol. 2988. International Society for Optics and Photonics. SPIE, 1997, pp. 108–111. DOI: `10.1117/12.274373`. URL: `https://doi.org/10.1117/12.274373`.

[105] E.L. Saldin, E.A. Schneidmiller, and M.V. Yurkov. “FAST: a three-dimensional time-dependent FEL simulation code”. In: *Nuclear Instruments and Methods in Physics Research Section A: Accelerators, Spectrometers, Detectors and Associated Equipment* 429.1 (1999), pp. 233–237. ISSN: 0168-9002. DOI: https://doi.org/10.1016/S0168-9002(99)00110-2.

[106] L. T. Campbell and B. W. J. McNeil. “Puffin: A Three Dimensional, Unaveraged Free Electron Laser Simulation Code”. In: *Proc. 34th Int. Free Electron Laser Conf. (FEL’12)* (Nara, Japan). JACoW Publishing, Sept. 2012, pp. 73–76. URL: https://jacow.org/FEL2012/papers/MOPD12.pdf.

[107] S. Reiche. “Update on the FEL Code Genesis 1.3”. In: *Proc. 36th Int. Free Electron Laser Conf. (FEL’14)* (Basel, Switzerland). JACoW Publishing, Sept. 2014, pp. 403–407. URL: https://jacow.org/FEL2014/papers/TUP019.pdf.

[108] S. I. Tomin et al. “On-line Optimization of European XFEL with OCELOT”. In: *Proc. 16th Int. Conf. on Accelerator and Large Experimental Physics Control Systems (ICALEPCS’17)* (Barcelona, Spain). https://doi.org/10.18429/JACoW-ICALEPCS2017-WEAPL07. JACoW Publishing, Oct. 2017, pp. 1038–1042. DOI: doi:10.18429/JACoW-ICALEPCS2017-WEAPL07. URL: https://jacow.org/icalepcs2017/papers/WEAPL07.pdf.

[109] M. Borland et al. “Recent Progress and Plans for the Code ELEGANT”. In: *Proc. 10th Int. Computational Accelerator Physics Conf. (ICAP’09)* (San Francisco, CA, USA). JACoW Publishing, Sept. 2009, pp. 111–116. URL: https://jacow.org/ICAP2009/papers/WE3IOPK02.pdf.

[110] T. Lang et al. “Impact of temporal, spatial and cascaded effects on the pulse formation in ultra-broadband parametric amplifiers”. In: *Opt. Express* 21.1 (Jan. 2013), pp. 949–959. DOI: 10.1364/OE.21.000949. URL: www.chi23D.com.